



UNIVERSIDAD  
DE CANTABRIA

ESCUELA TÉCNICA SUPERIOR DE INGENIEROS  
INDUSTRIALES Y DE TELECOMUNICACIÓN

**TESIS DOCTORAL**

**Sensores ópticos para  
estructuras inteligentes**

Autor: **LUIS RODRÍGUEZ COBO**  
Directores: **JOSÉ MIGUEL LÓPEZ HIGUERA**  
**ADOLFO COBO GARCÍA**

SANTANDER, 2013

UNIVERSIDAD DE CANTABRIA

ESCUELA TÉCNICA SUPERIOR DE INGENIEROS  
INDUSTRIALES Y DE TELECOMUNICACIÓN

DEPARTAMENTO DE TECNOLOGÍA ELECTRÓNICA,  
INGENIERÍA DE SISTEMAS Y AUTOMÁTICA

TESIS DOCTORAL

Presentada por: Luis Rodríguez Cobo  
Ingeniero de Telecomunicación

Para acceder al título de: Doctor por la Universidad de Cantabria

Dirigida por: José Miguel López Higuera  
Doctor Ingeniero de Telecomunicación

Adolfo Cobo García  
Doctor Ingeniero de Telecomunicación

Santander, 2013

Tesis Doctoral: **Sensores ópticos para estructuras inteligentes.**

Autor: **Luis Rodríguez Cobo**  
Aspirante a Doctor Ingeniero de Telecomunicación

Director: **José Miguel López Higuera**  
Catedrático de Universidad  
Universidad de Cantabria  
**Adolfo Cobo García**  
Profesor titular de Universidad  
Universidad de Cantabria

Tribunal que juzgó la Tesis Doctoral:

Presidente: .....  
.....  
Vocal 1: .....  
.....  
Vocal 2: .....  
.....  
Vocal 3: .....  
.....  
Secretario: .....  
.....

El tribunal acuerda otorgarle la calificación de:.....

Santander, a ..... de ..... de 2013

---

*Insanity: doing the same thing over and over again  
and expecting different results.*

*Albert Einstein*



# Reconocimientos

Esta tesis ha sido desarrollada en el Grupo de Ingeniería Fotónica del departamento de Tecnología Electrónica Ingeniería de Sistemas y Automática de la Universidad de Cantabria. Me gustaría expresar mi gratitud a los supervisores de esta tesis, José Miguel López Higuera y Adolfo Cobo García por su valiosa supervisión durante estos estudios. Además, también me gustaría agradecer a todos mis compañeros del grupo de investigación su apoyo y colaboración.

Asimismo, también me gustaría reconocer todo el trabajo realizado en colaboración con nuestros compañeros de la Universidad Pública de Navarra, liderados por el Prof. Manuel López Amo, que siempre nos han brindado su apoyo y colaboración.

Por otro lado, también me gustaría agradecer el soporte proporcionado durante los meses de estancia en el INESC Porto (Portugal) al Prof. José Luis Santos y a mi supervisor directo, Dr. Orlando Frazão, así como al resto de compañeros del INESC.

Los trabajos de investigación recogidos en esta tesis doctoral han sido posibles gracias a la beca de Formación de Personal Universitario del Ministerio de Educación (AP2009-1403), así como a las contribuciones de los proyectos de I+D en los que se ha enmarcado. Particularmente al TEC20120-20224-C02 financiado por el Ministerio de Ciencia y Tecnología así como al proyecto “Palas Inteligentes” financiado por la compañía Aeroblade.



# Agradecimientos

**A mi familia**, por todo el respaldo y ánimo que siempre me han dado

**A Sa**, por estar siempre ahí y aguantar mis locuras

**A mis compañeros del GIF**, porque siempre se puede aprender algo

**A mis amigos**, porque es importante tener alguien con quien desconectar



# Resumen

Una estructura inteligente puede entenderse como aquella que, siendo consciente de su estado actual, es capaz de reaccionar a cambios tanto en su entorno como en sí misma. Para realizar este cometido, la estructura debe adaptarse para compensar las influencias externas, alcanzando un estado apropiado de funcionamiento. Este tipo de estructuras tienen que realizar tres tareas principales durante su adaptación al entorno: recopilar información sobre su estado actual; procesar dicha información y decidir las posibles actuaciones y, finalmente, materializar dichas decisiones, adaptando la estructura al entorno. En resumen, una estructura inteligente debe reunir tres capacidades principales: medir, decidir y actuar.

Durante el transcurso de esta tesis doctoral, han sido desarrolladas diversas contribuciones a la decisión y medida mediante técnicas ópticas, así como a la “inteligencia” y a los medios de actuación requeridos en este tipo de estructuras. La mayor parte de trabajos están centrados en el desarrollo de nuevos dispositivos y técnicas de medida, empleando principalmente tres tecnologías de fibra óptica para cuantificar diferentes parámetros como deformación, temperatura o vibración, entre otros.

El primer grupo de sensores se centra en redes de difracción de período corto (FBGs). Partiendo de estos elementos, se ha desarrollado una nueva técnica de procesado para obtener la deformación interna de estos transductores. Además, se han desarrollado nuevos dispositivos para medir diferentes parámetros (tanto típicos como nuevos), combinando FBGs con diferentes materiales. Aplicando estos nuevos dispositivos al área de los materiales compuestos, se pueden obtener nuevos puntos de vista que aportan información valiosa en el desarrollo de modelos estructurales más avanzados.

Asimismo, basándose en fibras ópticas de plástico (POFs), se han desarrollado varios sensores de bajo coste y altas prestaciones. Empleando este tipo

---

de dispositivos basados en interferometría Speckle en fibras de plástico multimodo y nuevos algoritmos de procesamiento, se han medido numerosos parámetros físicos, mostrando su posible aplicación para la monitorización estructural y de la salud.

Intentando aumentar la sensibilidad y aplicación remota de los sensores de fibra óptica, también se han abordado sensores basados en láseres en fibra. Este tipo de sensores generan una fuerte señal local dentro de la cabeza sensora que puede ser muy útil para aumentar la distancia de interrogación manteniendo las ventajas de los FBGs. Para ello, se han empleado fibras ópticas comerciales dopadas con Erblio para fabricar sensores láser. Empleando diferentes técnicas de filtrado óptico, se han diseñado y probado varios sensores láser monomodo.

Nuevos materiales también han sido estudiados para desarrollar sensores híbridos y dispositivos de actuación. Empleando dos tecnologías maduras como los FBGs y las aleaciones con efecto memoria (SMA), varios esquemas han sido propuestos y verificados tanto para detectar y medir como para actuar. En concreto se han desarrollado y probado un sensor de temperatura y un material inteligente auto-estabilizado basados en dicha combinación.

Con el fin de determinar la reacción de la estructura, es necesario tomar decisiones en tiempo real basándose en los datos en “crudo” de los sensores. Puesto que la complejidad de las estructuras está aumentando, esta tarea también se ha complicado. En un intento de compensar este incremento de complejidad, varias estrategias de aprendizaje máquina se han evaluado para aportar la “inteligencia” a la estructura. Se han procesado datos de una aplicación real de una estructura mediante estos algoritmos, demostrando las ventajas del modelado sin conocimiento a-priori cuando se trabaja con datos reales.

En resumen, en el transcurso de esta tesis, se han desarrollado varias contribuciones para cada una de las tres partes de una estructura inteligente (medida, decisión y actuación). Los resultados obtenidos intentan mejorar el estado del conocimiento y de la técnica actual, facilitando el desarrollo de sensores de fibra óptica para estructuras inteligentes.

Los resultados obtenidos han sido validados por la comunidad científica internacional con la publicación de 1 patente, 15 artículos en revistas internacionales y más de 40 publicaciones en conferencias. Además, varios artículos han sido enviados recientemente para su publicación.

# Abstract

In a simple way, a Smart Structure can be understood as one that is aware of its self-state and also is able to react to changes in the environment and/or in its own condition. In order to correct these changes, the structure must reach a situation that compensates these influences, leaving the structure in a suitable state. A Smart Structure must be able to perform three main tasks to achieve this reaction: to collect information regarding its state; to process the collected information and to take a decision and, finally, to make actuations according to this decision. Based on this definition, three main sub-parts constitute a Smart Structure: sensing, “intelligence” and actuation.

Several contributions to sensing, using optical fiber technologies, to “intelligence” and also to actuation have been addressed during this thesis. The main contributions are centered on new sensing devices and techniques and in the obtention of inner parameters such as strain, temperature and vibration, employing three different optical fiber technologies.

The first group of sensors has been centered on Fiber Bragg Gratings (FBG), where a new technique to achieve intragrating resolution has been proposed. In addition, new sensing heads for traditional and new measurands have been developed, by combining FBGs with different materials. Employing composite materials as the main application target, these devices provide useful high level information for the development of improved structural models.

Different sensors based on Polymer Optical Fiber (POF) technologies have been developed, offering very cost-effective devices. Combining Speckle interferometry in multimode POFs with new processing schemes, several approaches have been proposed and demonstrated, being capable of measuring physical parameters for health care and for structural integrity applications.

Different contributions to Fiber Laser Sensors have been also addressed during this work, trying to improve the sensitivity of Optical Fiber Sensors and

their remote operation. This kind of Fiber Laser Sensors generates locally a strong laser signal within the sensing head that can be very useful for improving the interrogation distance while keeping the linear response of FBGs to strain and temperature. Based on commercial Erbium-doped fibers, different sensing heads have been developed employing a simple filtering technique to manufacture short linear lasers operating in the Single Longitudinal Regime.

In order to develop new hybrid sensing schemes and actuation devices, different materials have been studied. Different approaches have been proposed and demonstrated for both sensing and actuation purposes, by merging two widely employed technologies, FBGs and Shape Memory Alloys (SMA). Particularly, a temperature level fiber sensor and a smart material (self-stabilized) have been proposed and experimentally demonstrated.

Based on the raw data measured by the sensing system, on-line decisions must be taken to determine the reaction to be completed. With the growing complexity of structures, this task becomes more and more difficult. Different Machine Learning approaches have been employed as the “intelligence” of a real structure, trying to address this challenge, exhibiting the benefits of blind modeling when working with real data and complex structures.

In summary, several contributions to the three main parts of Smart Structures (sensing, decision and actuation) have been addressed during this thesis. The reported work tries to improve the actual technology and knowledge, enabling a more feasible development of OFS-based Smart Structures. The achieved results have been validated by the international sensing community with the publication of 15 papers in international Journals and more than 40 communications in international conferences. Several papers also have been recently submitted.

# Acronyms

- **ANN:** Artificial Neural Network
- **CCD:** Charge-Coupled Device
- **CFRP:** Carbon-Fiber Reinforced Plastic
- **CNC:** Computer Numerical Control
- **DBR:** Distributed Bragg Reflector
- **EDFA:** Erbium Doped Fiber Amplifier
- **EDFRL:** Erbium Doped Fiber Ring Laser
- **EFPI:** Extrinsic Fabry-Perot Interferometer
- **ESA:** Electrical Spectrum Analyzer
- **FBG:** Fiber Bragg Grating
- **FEA:** Finite Element Analysis
- **FLS:** Fiber Laser Sensor
- **FRP:** Fiber Reinforced Plastic
- **FSS:** Fiber Specklegram Sensor
- **FWHM:** Full Width at Half Maximum
- **GFRP:** Glass-Fiber Reinforced Plastic
- **HTM:** Hierarchical Temporal Memory
- **ICT:** Information and communication technology

- **ML:** Machine Learning
- **NDT:** Non-Destructive Testing
- **OE:** Opto-Electronic
- **OFS:** Optical Fiber Sensor
- **OSA:** Optical Spectrum Analyzer
- **OSNR:** Optical Signal to Noise Ratio
- **OTDR:** Optical Time-Domain Reflectometer
- **PID:** Proportional, Integral, Derivative
- **PMMA:** Poly(methyl methacrylate)
- **POF:** Polymer Optical Fiber
- **PSO:** Particle Swarm Optimization
- **PWM:** Pulse Width Modulation
- **PZT:** Piezoelectric Transducer
- **SDM:** Space-Division Multiplexing
- **SFBG:** Sampled Fiber Bragg Grating
- **SHM:** Structural Health Monitoring
- **SLM:** Single Longitudinal Mode
- **SMA:** Shape Memory Alloy
- **TDM:** Time-Division Multiplexing
- **TLS:** Tunable Light Source
- **VaRI:** Vacuum-assisted Resin Infusion
- **VaRTM:** Vacuum-assisted Resin Transfer Molding
- **WDM:** Wavelength-Division Multiplexing

# Contents

<b>Abstract</b>	<b>ix</b>
<b>Acronyms</b>	<b>xi</b>
<b>I. Preliminary</b>	<b>3</b>
<b>1. Introduction: Motivation of OFS in Smart Structures</b>	<b>5</b>
<b>2. State of the art: OFS in Smart Structures</b>	<b>9</b>
2.1. Optical Fiber Sensors and structures . . . . .	10
2.1.1. Optical Fiber Sensors technologies . . . . .	10
2.1.2. Optical Fiber Sensors and composite materials . . . . .	14
2.1.3. Cost reduction on Optical Fiber Sensors . . . . .	18
2.2. Remote Optical Fiber Sensors . . . . .	20
2.3. Data managing . . . . .	21
2.4. Challenges of Optical Fiber Sensors in Smart Structures . . . . .	23
2.5. Conclusions . . . . .	24
<b>3. Objectives</b>	<b>27</b>
<b>II. Contributions</b>	<b>31</b>
<b>4. Sensors based on FBG technology</b>	<b>33</b>
4.1. Intragrating distributed technique . . . . .	34
4.1.1. Sampled FBGs . . . . .	35
4.1.2. Uniform FBGs . . . . .	50
4.1.3. Summary . . . . .	56

4.2.	Designs for temperature-strain discrimination . . . . .	57
4.2.1.	Strain and temperature sensors . . . . .	58
4.2.2.	Temperature-independent strain sensor . . . . .	63
4.2.3.	Plates manufacture . . . . .	64
4.2.4.	Experimental response . . . . .	65
4.2.5.	Error analysis . . . . .	70
4.2.6.	Summary . . . . .	74
4.3.	Embedded transducers for laminated composites . . . . .	74
4.3.1.	Bonding transducer . . . . .	76
4.3.2.	Compaction pressure transducer . . . . .	88
4.3.3.	Embedded strain transducer . . . . .	97
4.3.4.	Field demonstrations . . . . .	103
4.3.5.	Summary . . . . .	114
4.4.	Conclusions . . . . .	115
<b>5.</b>	<b>Speckle based sensors using POF</b>	<b>119</b>
5.1.	Sensing principle . . . . .	120
5.2.	Vibration sensing . . . . .	122
5.2.1.	Differential processing . . . . .	122
5.2.2.	Experiments and results . . . . .	123
5.2.3.	Heart rate detection . . . . .	128
5.2.4.	Seismic sensor . . . . .	129
5.2.5.	Summary . . . . .	131
5.3.	Strain sensing . . . . .	132
5.3.1.	Morphological processing . . . . .	133
5.3.2.	Experiments and results . . . . .	136
5.3.3.	Summary . . . . .	139
5.4.	Radial speckle . . . . .	140
5.4.1.	Radial processing . . . . .	141
5.4.2.	Experiments and results . . . . .	142
5.4.3.	Summary . . . . .	144
5.5.	Conclusions . . . . .	145

<b>6. Fiber laser sensors</b>	<b>147</b>
6.1. FBG spectral evolution in active fibers . . . . .	148
6.1.1. Spectral narrowing principle . . . . .	149
6.1.2. Experiments . . . . .	151
6.1.3. Summary . . . . .	154
6.2. Filtering technique based on spectral overlapping . . . . .	155
6.2.1. Spectral overlapping . . . . .	156
6.2.2. Simulations . . . . .	157
6.2.3. Experiments . . . . .	159
6.2.4. Summary . . . . .	162
6.3. Single Longitudinal Mode Lasers . . . . .	163
6.3.1. Laser manufacturing . . . . .	163
6.3.2. Laser characterization . . . . .	164
6.3.3. Summary . . . . .	168
6.4. Conclusions . . . . .	169
<b>7. Hybrid FBG-SMA techniques</b>	<b>171</b>
7.1. Shape Memory Alloy . . . . .	172
7.2. Hybrid temperature level transducer . . . . .	173
7.2.1. Transducer architecture . . . . .	174
7.2.2. Experiments . . . . .	175
7.2.3. Quasi-distributed transducer . . . . .	177
7.2.4. Summary . . . . .	178
7.3. Smart material based on SMA . . . . .	178
7.3.1. Material description . . . . .	179
7.3.2. Experiments . . . . .	180
7.3.3. Summary . . . . .	183
7.4. Conclusions . . . . .	183
<b>8. Data managing and decision making</b>	<b>185</b>
8.1. Machine learning approaches . . . . .	187
8.2. Application to Smart Structures: Impact detection . . . . .	190
8.2.1. Application scenario . . . . .	190
8.2.2. Experiments . . . . .	191
8.2.3. Results . . . . .	194

8.2.4. Summary . . . . .	198
8.3. Conclusions . . . . .	198
<b>III. Conclusions and future lines</b>	<b>201</b>
<b>9. Summary and Conclusions</b>	<b>203</b>
<b>10. Open Future Lines</b>	<b>209</b>
<b>IV. References</b>	<b>213</b>
<b>11. References by chapter</b>	<b>215</b>
11.1. References of Chapter 2 . . . . .	215
11.2. References of Chapter 4 . . . . .	232
11.3. References of Chapter 5 . . . . .	238
11.4. References of Chapter 6 . . . . .	240
11.5. References of Chapter 7 . . . . .	242
11.6. References of Chapter 8 . . . . .	244
<b>12. References in alphabetical order</b>	<b>247</b>
<b>13. List of publications</b>	<b>277</b>
13.1. Close related to the PhD work . . . . .	277
13.1.1. International Journals . . . . .	277
13.1.2. International conferences . . . . .	278
13.1.3. Industrial Publications . . . . .	280
13.2. Other contributions . . . . .	281
13.2.1. International Journals . . . . .	281
13.2.2. National Journals . . . . .	281
13.2.3. International conferences . . . . .	282
13.2.4. National conferences . . . . .	283
13.3. Submitted contributions . . . . .	284
13.3.1. Journal articles close related to the PhD work . . . . .	284
13.3.2. Other journal articles . . . . .	285





# Part I.

## Preliminary

Based on the research field of structural monitoring, a brief definition and motivation of Smart Structures and their improvement through Optical Fiber Sensors has been described in this part. Centered on this combination, a state-of-the-art revision has been also included to identify present challenges on Optical Fiber Sensors for Smart Structures. Finally, different objectives have been established trying to contribute to the challenges previously identified. The chapters included in this section are:

- Chapter 1: Introduction: Motivation of OFS in Smart Structures
- Chapter 2: State of the art: OFS in Smart Structures
- Chapter 3: Objectives



# Chapter 1

---

## Introduction: Motivation of Optical Fiber Sensors in Smart Structures

---

Human beings have always tried to improve their living environment by modifying their surrounding nature. From the prehistoric stone axe to the new energy production systems, a lot of examples of human inventions that have changed their lifestyle can be cited. Most of these tools and structures were based on mimicking nature; however, as the human understanding about structural engineering improved, these structures evolved in very different ways.

Since the first reported studies about structures made by Leonardo da Vinci in the 15th century, science has tried to explain the response of new materials and structures, applying this new techniques to solve particular challenges. This understanding has experienced a remarkable improvement during the 18th century, when structures became a very important factor on society and economics, evolving from being a technology limited to great monuments to impulse industry and economy during the Industrial Revolution.

By developing new modeling techniques and with the improvement on building materials, structural engineering has become a very active research field

during the last century. Within this area, new measuring and Non-Destructive Testing (NDT) techniques arose, helped by the emerging Information and Communication Technologies (ICTs). These measuring and NDT methods help designers to overcome new challenges, obtaining different properties of the employed materials or by identifying weak points within each design.

Mainly due to price reduction on ICTs, different sensing technologies have been widely incorporated to structures during the last decades. Examples such as electrical strain gauges or thermocouples are employed today as reference methods to characterize materials. Despite the help offered by these sensing technologies during design and manufacture processes, this concept has evolved the last years to allow the collecting of measurements during the working life of structures. A new research field, known as Structural Health Monitoring (SHM), has arisen, combining new sensing methods with feedback processes that respond to the detected changes.

Technically, SHM can be defined as the integration of sensing and, possibly also actuation devices, to allow the loading and damaging conditions of a structure to be recorded, analyzed, localized and even predicted in a way where non-destructive testing becomes an integral part of the structure. There are different levels in SHM according to the literature, although all of them are based on three key factors: the first one lies in the acquisition of an entire knowledge about the present (and historical) status of the different structural parts by means of sensing systems and data acquisition tools. Based on this data, several decisions about the overall structure condition and possible actuation have to be taken (e. g. one part has collapsed so the structure has to stop). Finally, at higher levels of SHM (Self-Healing), some actuation means have to be included to allow the structure to react according to the chosen decision. An structure combining these three factors (sensing, decision making and actuation) can be understood as a *Smart Structure* able to alter its configuration, form or properties in response to changes in the environment or in its condition.

SHM and smart structures are two relatively new concepts within structural engineering, being the most challenging subject in this regard is the interdisciplinarity required to cover all the key factors: a specific kind of expertise about mechanics and materials is required to understand how the structure is

---

working. Some metrology aspects have also to be considered to obtain reliable measurements. The recorded data also require a carefully designed algorithm capable of reaching some decision regarding the structure. Finally, mechanics is also reached when some kind of actuation is required to follow the algorithm output.

Smart structures are usually based on the latest developed materials and techniques. These new materials have to be characterized before reaching a working structure, so NDT methods are usually employed to determine its properties, relating certain sensing technologies to new materials. Within smart structures of specific fields, the combination between Fiber Reinforced Plastics (FRP) and Optical Fiber Sensors has become relevant these years. Both technologies have proved mechanically compatible, exhibiting the advantage of adding sensing capabilities to the host structure.

Although both technologies have been widely addressed, several improvements regarding the science of materials and structures as well as in sensing capabilities are required to lead SHM to its highest levels, achieving a truly smart structure. Regarding these requirements, Optical Fiber Sensors are playing a key role in these structures, working properly on a wide range of field scenarios, enabling the quick development of new materials and structures.

All the topics addressed in this document have been grouped into four main parts:

- **Part I:** Preliminary (Chapters 1-3)
- **Part II:** Contributions (Chapters 4-8)
- **Part III:** Conclusions and future lines (Chapters 9-10)
- **Part IV:** References (Chapter 11)



# Chapter 2

---

## State of the art: Optical Fiber Sensors in Smart Structures

---

Smart structures [1] can be understood as a huge research field where many different technologies can be merged to reach the final objectives: sensing, decision making and actuation. However, independently of the employed technologies, the first step always lies in the determination of how the structure and its environment behave. Even within the sensing scenario, there are also lots of different kinds of measurands that can be also measured in many different ways. This set of measurements usually can be complemented with environmental information such as temperature, wind speed or humidity. Although there are many sensing techniques available for SHM tasks, some automatic decision has to be taken using the available data. This decision is usually taken by an algorithm implemented into a computer, what implies that measurements (algorithm input data) must be translated to electronic means. Nevertheless, there are still lots of electronic and optoelectronic means to obtain these measurements.

Another key factor when working on smart structures is to be able to get

useful data when the structure is in operation. Trying to retrieve useful data during the operation of a structure can be a real challenge for some sensing techniques. Optical Fiber Sensors (OFS) have proved to be a reliable solution to obtain measurements even within harsh environments. Although OFSs are not the only option to be chosen, these technologies have become more accessible during last years, and have been widely tested in many different host structures (composite materials, metallic structures, concrete...).

A deep study of the current state of the art has been performed to identify open challenges and needs, that guide the following work. This research tries to contribute and develop useful devices and techniques for real situations, covering specific identified needs. The state of the art has been mainly centered on Optical Fiber Sensors applied to structural monitoring, being the basis of smart structures and new SHM models. A very brief summary and conclusions of the mentioned review have been included in the next sections.

## **2.1. Optical Fiber Sensors and structures**

A very wide set of parameters can be measured using optical fiber sensors [2], both mechanical and chemical. However, mechanical properties such as strain or temperature are useful for present SHM models and have been more studied in the literature. Although there are many reported applications, a brief description of the most successful techniques applied to SHM is detailed in the following sections.

### **2.1.1. Optical Fiber Sensors technologies**

Optical fiber sensors can be classified according to very different rules. Particularly, in this description, they have been grouped depending on their sensing range. Each category has its advantages and drawbacks for any given application.

#### **2.1.1.1. Local optical fiber sensors**

Many intensity based sensors, such as microbend sensors [3, 4], and most of the interferometric OFSs, are local sensors that can measure changes at specified local points in a given structure. Interferometric OFSs are the most

commonly used punctual sensors since they offer the best sensitivity [5]. This sensing technique is based primarily on detecting the optical phase change induced in the light as it propagates along the optical fiber. Light from a source is equally divided into two fiber-guided paths (one is used as reference). The beams are then recombined to be coherently mixed and form a “fringe pattern”, which is directly related to the optical phase difference experienced between the two optical beams. The most common configurations of such interferometric sensors are the Mach-Zehnder, Michelson and Fabry-Perot OFSs [6]. Among them, the Fabry-Perot (F-P cavity) OFS and the so-called long gauge OFS are the two types of local sensors commonly utilized in civil engineering.

Since the first reported examples such as the measurement of the deformation over a concrete block using Michelson interferometry [7] or employing Fabry-Perot interferometers to characterize a steel tendon of a prestressed bridge [8], punctual sensors have been developed to cover field applications by measuring very different parameters such as curing processes, vibration or strain [9].

Although the described interferometric technologies have been the most widely applied solution for field measurements, there also exist other punctual technologies successfully validated. Detecting corrosion in bridges and railways using an absorption sensor [10] or quantifying vehicle weights using polarimetric sensors [11] are some examples of punctual FOSs applied to structural monitoring.

The detailed techniques exhibit certain benefits in comparison to other sensing techniques, however, since the appearance of quasidistributed sensors based on Fiber Bragg Gratings, their field application was limited to very specific applications where extremely sensitivity was required.

#### **2.1.1.2. Quasidistributed sensors: Fiber Bragg Gratings**

Optical fiber gratings are one of the most intensively studied optical structures because of their great possibilities to create devices for both sensing and telecommunication applications [12, 13]. Fiber gratings can be defined as a periodic variation of the refractive index in the optical fiber core that filters particular wavelengths (Fig. 2.1). In sensing, both short period (Fiber Bragg

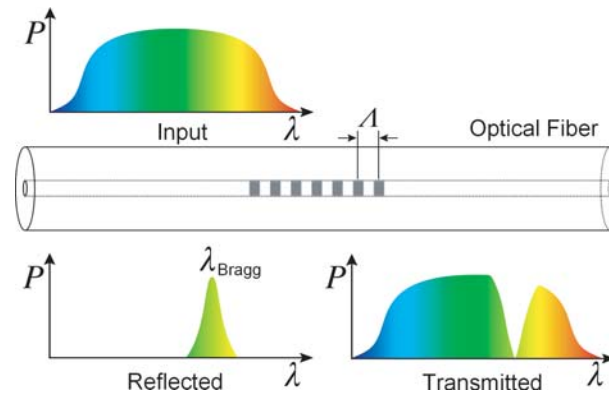


**Fig. 2.1.:** Basis of a Fiber Bragg Grating

Gratings, FBGs) and long period (Long Period Gratings, LPGs) are used. A grating period can be considered short (FBG), when it is comparable to the wavelength of the light and long (LPG) when it is much longer. FBGs are used because of their capability to measure both strain and temperature (and an ample variety of indirect measurands) of the structure [14]. Long-period gratings (LPGs) are used, mainly, because of their high sensitivity to the cladding modes [15].

In a simple way, FBGs work as follows: when light within a fiber reaches the periodic variation, a constructive interference between the forward wave and the contra-propagating light wave leads to narrowband back-reflection of light when the Bragg condition is satisfied ( $\lambda_{Bragg} = 2n_{eff}\Lambda$ ). A Fiber Bragg Gating can serve as an intrinsic sensor, given that any local strain or temperature changes alter the refraction index within the core ( $n_{eff}$ ) and/or the grating period ( $\Lambda$ ) followed by changes in the wavelength of the reflected light ( $\lambda_{Bragg}$ ). Wavelength changes can be detected by an interrogator that employs, among others, edge filters, tunable lasers or CCD spectrometers [16–18], which are commercially available nowadays and capable of operating in harsh environments.

FBG transducers exhibit a unique property over other OFSs: they encode the wavelength, that is an absolute parameter and does not suffer from disturbances of the light paths. FBG transducers could be particularly useful when gratings with different periods are arranged along an optical fiber. Each of the reflected signals will have a unique Bragg wavelength and can be easily monitored, thus achieving multiplexing of the outputs of multiple sensing

points using a single fiber (Fig. 2.1). Although there are several approaches for sensor multiplexing [19] such as SDM [20] or TDM [21, 22], WDM [16, 23] techniques are widely employed in structural monitoring. Nowadays, several tens of FBGs (depending on the expected deformations) can be wavelength-multiplexed (WDM) in a single fiber, allowing quasi-distributive measurement of strain, simplifying the interrogation requirements.

FBG transducers are preferred in many SHM applications and have been successfully employed in several full-scale structures requiring multiple-point sensing or distributed sensing over a long range. Bridges, especially those made of concrete, are the most monitored civil structures using FBGs [24–27]. However, FBGs have been employed also to monitor concrete foundations [28]; railway condition such as deformation [29] or imbalance [30]; historical buildings [31] and even state-of-the-art facilities [32], high-performance vessels [33–35] and aerospace prototypes [36].

FBG transducers are the most employed sensing technology for structural monitoring due to their multiplexing capabilities and the relatively simplicity of their interrogation. There are also several scenarios where more sensing points are required, what inspires distributed technologies.

### **2.1.1.3. Distributed Sensors**

Distributed sensors are most suitable for structural and environmental monitoring of large structures. Since all the segments of an optical fiber act as sensors, the perturbations within various segments of the fiber can be sensed. Distributed sensors are based on the modulation of light intensity in the fiber. Fracture losses or local damages in a structure cause light intensity variations. Two major distributed sensor methodologies are the optical time domain reflectometry (OTDR) and the Brillouin and Raman scattering. In the OTDR [37, 38], Rayleigh [39] and Fresnel scatterings are used for sensing structural perturbations. On the other hand, Brillouin scattering [40] detects the Doppler shift in light frequency which is related to the measurands.

Particularly, hybrid systems of Brillouin-Raman scattering can address both strain and temperature sensing, that are the main measurands for structural monitoring [41]. However, high resolution distributed systems have not found widespread usage in structural applications and the main reason lies in the

complexity of the interrogation equipment, that limits the application scenarios of these techniques.

All in all, there are still some examples in structural monitoring such as retrieving strain distribution along a repaired concrete bridge [42] or a metallic structure [43, 44] using BOTDR techniques. The same sensing scheme has been also applied to monitor underground structures such as foundations [45], tunnels [46, 47], an active mine [48] or to carry out soil studies [49]. Despite BOTDR is the most popular distributed sensing method for structural monitoring, other distributed sensing techniques such as Brillouin Optical Fiber Time Domain Analysis (BOTDA) [50] or Brillouin Optical Frequency Domain Analysis (BOFDA) [51] have been also reported in field applications. Although non linear techniques have been widely applied to structural monitoring, other distributed approaches based on new interferometric devices are currently developed for their application in SHM fields [14].

### **2.1.2. Optical Fiber Sensors and composite materials**

In recent years, high-performance composite materials have been widely used in industries such as aviation, aerospace, automobile and civil engineering. It is extremely important to ensure the reliability of these structures that are easy to degenerate or be damaged in harsh environments.

Several constituent elements can be combined to obtain a final material with properties different from the individual components. These kinds of combinations are known as composite materials and are usually associated with Fiber Reinforced Plastics (FRPs). These specific composite materials are made of a polymer matrix (i.e. epoxy or polyester) reinforced with fibers of different materials such as glass, carbon or aramid.

Several sensing methods based on OFSs have been successfully applied to composite materials to monitor their properties or even employing them in smart structures. These examples exhibit the potential to satisfy the characterization requirements, even by embedding OFSs during the fabrication stage without affecting the integrity of the structure.

FBGs are the most extended OFS technique for composite material monitoring [52]; however, other OFS techniques have been also applied. There are examples in this regard such as EFPI punctual sensors to monitor the manu-

facturing process [53] and strain response of FRP plates [54, 55]. Distributed techniques have been also reported to study composite materials by analyzing their curing process using Brillouin [56, 57] or by detecting composite damages using OTDR [58].

There are also some field applications of OFS applied to composite structures, in addition to FBG-based ones [52], such as monitoring an aircraft structure [59] or monitoring competition yachts [60] using BOTDR. However, due to the heterogeneity of FRPs, damage in structures often initiates at the material level or relatively local geometric level, thus small-gauge length sensing is a common requirement for these material. This is one of the reasons why FBGs have become a reliable monitoring tool among OFSs for composite materials both during manufacturing process and once the structure has been finished. Based on all these considerations, an important part of the research work carried out during this thesis is devoted to sensing elements for composite materials.

### **2.1.2.1. Composites monitoring using FBGs**

There are still some drawbacks limiting the application of composite materials, where the greatest problem lies in the instability of the product quality from the diverse curing processes. To improve the performance of composite materials, the quality control of the curing process becomes indispensable. Composite materials undergo a large number of physical and chemical changes during this process. Factors such as temperature, resin viscosity and internal stress could have a tremendous impact on the performance of composite materials during the curing process. The elevated temperatures applied during the curing provide the heat required for initiating and maintaining the chemical reactions in the resin, what causes the desired changes in the molecular structure. The applied pressure provides the force needed to squeeze the excess of resin out of the material and to establish the compaction of the produced structure. The curing process monitoring and intelligent curing control of composite materials have become a research hotspot during the last years.

Although other OFS techniques have been applied to monitor the curing process, FBGs have shown a remarkable performance in this task by being embedded into the manufactured material [61]. This technique can achieve,

not only single-point and multi-point cure monitoring, but also real-time online cure monitoring. Despite the complexity of the FRP curing process, it can be tracked by analyzing its temperature and strain during the vitrification. Consequently, by embedding FBGs into the laminate, these parameters can be measured [55, 62].

The analysis of the curing process provides information about the chemical properties of the manufactured structure. However, to determine the physical properties of the structure, some additional mechanical characterization is required. The first attempts were directly linked to the cure monitoring, where, by employing the same embedded FBGs, the residual stress provoked during the cure can be measured [62–65]. The same FBGs embedded into the structure can be also employed to obtain the deformation along the material when a load is applied [62, 66] or even to measure more complex parameters such as the dynamic strain response or modal frequencies [66].

Having into account that composite materials are usually non-uniform structures formed by very different materials (i.e. polymer matrix and reinforcement fibers), complex artifacts can affect the mechanical properties of the material. However, with embedded FBGs, several of these artifact can be detected and evaluated. There are examples such as quantifying crack propagation by analyzing FBGs spectra [67, 68] or studying the delamination growing by different FBG responses [69–71] and even to measure debonding processes [72].

These kinds of mechanical defects are usually provoked by wrong operation conditions or by some external causes that, sometimes, have a known mechanical response on the structure. One example of a known cause are impacts, that can be detected by embedded FBGs [73] and even located, as well as their associated damages [58, 74, 75]. Another typical wrong operation condition when working with composite materials is the repairing of a damaged structure, where usually an extra composite patch is attached to the damaged area. This kind of reparation introduce a difference in the mechanical response that can be also monitored using FBGs [76, 77].

All of the described sensing techniques have been applied under controlled conditions; however, most of them can be employed to improve composite structures when operating under real conditions, exhibiting the benefits of

having a sensor system perfectly integrated into the host structure.

### 2.1.2.2. Structures instrumented with FBGs

With the acceleration on the development of advanced composite materials, their combination with OFS techniques become more attractive to different fields. Classical civil engineering applications where composite materials have been introduced, take advance of OFS techniques to study their field response. Examples such as the employment of FBGs for real-time strain monitoring of composites bridges [24, 53, 78–80] or even particular composite parts and reinforcements that avoid the corrosion [81], are the proof of the benefits of employing OFS techniques for civil engineering monitoring.

Although civil engineering applications are the most intuitive examples of SHM, the combination of composite materials and OFS techniques has attracted a considerable attention in other research fields such as aviation and aerospace structures [82]. Particularly Carbon Fiber Reinforced Plastics (CFRPs) in combination with FBGs have been widely employed for many different purposes. Compared to metallic materials, CFRP exhibits lighter weight, higher resistance to fatigue and corrosion and higher strength and stiffness ratio.

In order to achieve a better understanding of these new materials applied to high performance applications, many examples of embedding OFSs have been found in the literature. Particularly, FBGs have been embedded into CFRP during fabrication to monitor real-time health and performance during the operation of aircrafts [33]. The study of the dynamic response of wing designs [83]; the modal analysis of aircraft parts [84] and even structural condition and fire detection monitoring [85] have been performed by means of embedded FBGs into real structures. Besides studying the structural status of aircrafts, FBGs have been also employed to detect damages of critical parts such as wings [86] or repaired panels [87].

Another widespread application scenario for composite materials is marine structures, where corrosion is a critical factor. Nowadays, an increasing number of CFRPs have been introduced in the design of offshore structures and ships, greatly reducing the weight and improving the cost-effectiveness and reliability of these marine structures.

Several attempts to study the performance of new designs based on composite materials have been carried out employing OFSs to analyze and improve the structural design of several high-performance vessels, embedding FBGs into CFRP hulls [34, 88, 89]; measuring the mast load [33] or even evaluating the quality of ship joints [80, 90, 91].

A large number of engineering application examples have verified the validity of FBG sensors for composite SHM. FBG sensors offer important advantages over traditional instrumentation in many cases, and due to their reliability and cost-effectiveness are the most employed OFS technique to monitor composite materials. Although FBG sensors have been of considerable interest for monitoring composite structures during the last few years, many challenges associated with applying FBG sensors in real-world applications have not yet been addressed.

### **2.1.3. Cost reduction on Optical Fiber Sensors**

During the last years, the reduction on the cost associated with OFS techniques has helped their introduction in different areas. However, there are still several scenarios where their relative “high” cost makes their application impossible. Typically, high performance OFSs are based on a wavelength window from 1530 to 1565 nm because of the availability of commercial equipments and the low transmission losses of silica fibers. However, although the price of these devices has recently decreased, for many application scenarios can be excessive.

On the other hand, OFS based on other light sources and detectors can reduce the final price, achieving very high competitive prices and keeping most of the OFS advantages. Under these conditions, Polymer Optical Fibers (POF) have been proved to be a reliable technology with several advantages in terms of manageability in comparison to silica optical fibers [92]. Despite their higher transmission losses, POFs provide a significantly lower cost alternative to silica optical fibers because of their manageability (higher core diameters and higher NA), having additional advantages including high elastic strain limits (up to 40%, [93]), high flexibility in bending and high strain sensitivity. When the final sensor performance is not a limiting factor, the final sensor price can be dropped just by choosing the right light source, particularly when work-

ing with multimode fibers (intensity-based or interferometric). By employing visible-range light sources and detectors (such as silicon CCDs), low cost OFS sensor systems can be achieved keeping enough sensitivity for the required application

In addition to low-cost implementations and based on POF technologies, lots of high performance systems have been also reported such as: OTDR systems capable of obtaining measurements using large diameter fibers (1mm) [94] and even measuring the maximum achieved strain due to POF's "memory effect" [95]; Time-of-flight based systems to monitor aircraft wing deformations [96, 97]; POF-Fiber Bragg gratings inscribed into monomode fiber [98, 99] and into micro-structured (mPOF) [100] and even non-linear distributed sensing [101]. However, all these techniques have been originated in silica based fibers and afterwards applied to POFs, what implies too many drawbacks to perform almost the same tasks as silica fibers do, against very poor benefits.

However, there are several application examples that take advantage of the simplicity of some POF techniques, particularly, by embedding POFs into textile materials, large strain values have been measured using an intensity based sensing system [93, 102] or the appearance of cracking into concrete structures has been also detected by measuring the optical power [103]. These practical solutions have been also applied to composite materials where, by embedding POF, the applied strain [104–106] and even crack detection [104] has been measured analyzing the optical losses of the embedded fiber.

Despite the fact that intensity-based POF sensors have been widely applied in very different scenarios with a good cost-performance ratio, there are also application scenarios where some improvements are required. Interferometric sensors have been employed in many different application as a high precision sensing method based on measuring the phase-shift of the propagated light in the test fiber (under perturbation) relative to a reference fiber (without perturbation). Several POF-based Mach-Zehnder interferometric systems have been reported [107, 108] based on single mode POFs and even using larger fibers (1 mm) [109], what reduces the final sensor cost. Another promising low-cost technique for SHM purposes is speckle interferometry based on multimode fibers. Although speckle has been widely employed in imaging applications [110], this kind of mutual interference can be also found inside multimode

fibers. Known as Fiber Specklegram Sensors (FSS), this kind of fiber sensors has been successfully applied to measure vibration [111], displacement [112, 113] or temperature [114], keeping the possibility of employing a low cost implementation without limiting their final performance.

One drawback of the interferometric approaches is their limitation in terms of the dynamic range. Several efforts have been reported to overcome these limits such as phase-displacement response studies of POFs [115] to be applied in Mach-Zehnder interferometry or to employ photorefractive materials to stabilize FSSs [116]. However, these limitations can be overcome using new processing schemes, enabling low-cost POF based sensors for SHM applications.

## 2.2. Remote Optical Fiber Sensors

The previous sections have been mainly focused on determining which is the status of the structure itself. However, Smart Structures must react to certain environmental conditions, what implies that some data about the status of the surrounding environment are usually required. Beyond the closer environment, what can be understood as part of the hosting structure, several environmental parameters far from the structure location may be required in particular scenarios.

There are a lot of available OFS technologies that deal with long distance sensing like distributed techniques such as Brillouin in combination with Raman amplification [117, 118] that can reach hundreds of kilometers of sensing area. Although distributed measurements can provide a lot of intermediate values, in particular applications it may be necessary to monitor a small area with a very high resolution. Under these requirements, FBG Laser Sensors (FBGLS) exhibit a remarkable performance, where one or several wavelength matched FBGs create an in-fiber cavity whose output is a laser signal. There are a lot of applications for FBG based lasers but, when configured as sensing elements, changes in the environmental conditions (that affect the laser cavity, FBGs or both) can be detected by monitoring the laser output.

Laser sensors can be implemented in very different ways such as using very long fiber Raman lasers employing FBGs as sensing heads and the standard

optical fiber as active medium [119–121] or combining local generated laser signals (using short cavities) to be propagated without attenuation by combining Raman amplification and erbium-doped fiber amplification [122, 123]. Based on the idea of local laser generation, several attempts have been also reported to improve the cavity implementation achieving a laser that responds identically to its reflectors (usually FBGs) [124, 125] and even reaching Single Longitudinal Mode operation [126, 127] or employing both orthogonal modes to obtain a polarimetric laser sensor [128].

Combining these two techniques: Raman amplification and locally generated lasers, very long distance sensor systems can keep enough resolution for many specific applications. These capabilities (long distance and high resolution) can help Smart Structures by providing data from critical and distant points to prevent possible unexpected situations.

## 2.3. Data managing

The huge amount of data provided by the new generation of sensing technologies can lead to a better understanding of smart materials and structures. However, as the amount of raw data increases, extracting the useful information becomes a very challenging problem, being even more complex under dynamic situations.

In Information and Communication Technologies (ICTs), there are a lot of reported field applications of information retrieval using almost an infinity of algorithms and techniques [129]. However, adapting all these methods for particular purposes (i.e. SHM) requires some extra studies having into account the available data, the final application, its implementation. . . Although several algorithms have been employed in SHM scenarios such as statistical methods applied to aircraft wings [130] or concrete bridges [131] diagnosis, there are still many challenges to obtain a truly Smart Structure.

A Smart Structure must be able to respond to changes in the environment or in its own condition. This reaction process implies several steps starting from data acquisition and conditioning, an evaluation of the current status (of the structure and its environment) is followed before reaching the decision making about the response and its further execution (actuation).

Data acquisition and conditioning for SHM purposes have been widely described in previous sections (mainly focused on OFS techniques). However, after having the data conditioned (e.g. retrieving FBG peak displacements from a distorted spectrum using machine learning approaches [132]), the evaluation of the current structure status follows. This analysis begins with the identification of failure modes (such as delamination in a composite material or structural overloads) and the random variables that contribute to these failure models (such as projectile impact velocity, ply orientation angles or material density). During the last years, several models have been developed to summarize all the collected data into a single status. Particularly, OFS techniques have been employed in combination with mechanical models to determine the inner damage of a structure [133] or to calculate the failure probability of certain components based on reliability analysis [134].

After the determination of the structure status, a decision must be taken to adapt the structure status to the subsequent reaction. Although several attempts have been reported using model-based decision making systems [134], due to the usual model complexity, machine learning approaches have attracted a lot of interest during the last years. Examples such as employing Artificial Neural Networks for predicting fatigue damages of aircraft cracked joints [135] or applying Genetic Algorithm to monitor external loading damages [136] reflect the interest in these techniques.

Finally, once the decision has been made, some kind of reaction is expected from a Smart Structure. Several attempts of structures that react to specific perturbations have been reported. Based on a FBG sensor network that feeds control loops, different actuators have been employed to reduce vibration [137, 138] or to stabilize an actuator [139]. Although the reported application examples employ simple models and decision making schemes (feedback loops), some efforts to model more complex applications have been also reported using machine learning approaches such as employing ANN's output to handle (offline) the actuator of an adaptive wing [140].

## 2.4. Challenges of Optical Fiber Sensors in Smart Structures

OFS techniques have been successfully applied to measure many different parameters inside and outside laboratories. Their ultimate goal (from a SHM perspective) is being able to monitor structures under operation, but this application requires a perfect integration of the sensing heads into the hosting material, not affecting the mechanical structure response, but also protecting the optical fiber sensor.

Several works have been reported improving the package of OFS sensing heads taking into account their final application. However, this remains as one of the greatest challenges on Smart Structures, being even more important for composite structures. These final applications can be extremely different, thus, to obtain a technology able to work under harsh environments or to reduce the final system cost, can be sometimes very difficult tasks to accomplish simultaneously.

Related to the structural integration, OFS techniques require, in most cases, some kind of optoelectronic (OE) unit to convert the light modulated by the perturbation to the electronics/informatics domain. Usually, this OE unit can be placed in non-critical structural locations (or even far from the structure), but the development of OE units capable of working in real scenarios is, currently, another limitation for OFS technologies. Having a reliable on-line diagnosis tool will speed up the SHM evolution, providing data during structure operation.

With the growing of available data due to the OFS widespread, the extraction of useful information from all the raw data becomes a real challenge. On a Smart Structure, these data must be employed to decide which is the right action. The algorithms employed to decide must be able to reflect the structural model complexity, what implies that new algorithmic solutions are also required as a consequence of the amount of available data.

Another existing problem in OFS is the cross sensitivity to several parameters or multi-axial discrimination. Particularly, this is a problem widely addressed regarding FBGs, where the temperature-strain discrimination has been generally discussed. However, both parameters are fundamental for

Smart Structures and it is still an open problem without a definitive solution, because it strongly depends on the final installation of the sensing head. As structures become more complex, new features are required to evaluate their current status (besides strain and/or temperature). Obtaining the complete status of a complex Smart Structure may require some particular data to model specific materials and/or designs. Starting from a better understanding of their base materials, new sensing heads capable of measuring other parameters such as bending, torsion or inner material properties will also improve existing SHM models. In addition, these higher level structural parameters can provide enough information to reach sensing heads and networks with self-diagnosis capabilities, removing some actual measuring uncertainties.

OFS techniques have been applied during several decades, however, their evolution has been very different depending on the final application. Having into account their expected introduction into many different sectors, some kind of standardization is required to ensure the final performance. Creating a standard for new and different techniques can be a huge challenge, but its consequence can improve Smart Structures by reducing costs and ensuring their performance.

## **2.5. Conclusions**

Smart Structures are a truly multi-disciplinary research field where sensing, processing and actuation skills are required. Particularly, the combination of composite materials (e.g. Fiber Reinforced Plastics) and Optical Fiber Sensors allows the construction of new smart structures to solve specific challenges in many different scenarios.

Composite materials and OFSs have evolved simultaneously and started their link during the composite materials development, where OFSs have been employed to have a better understanding of these new materials. After both technologies merged, OFSs have been widely employed to monitor composite structures exhibiting the advantages of combining sensing methods with new materials.

Centered on this combination, some challenges regarding Smart Structures and OFSs have been identified during the revision of the state of the art. The

most remarkable research challenges can be summarized as follows:

- Based on the increase of computing resources, new approaches must be studied to extract new features from existing transducers, such as resolution and dynamic response improvement.
- Although there are lots of successful field applications of OFS, specific packages must be developed to endure the manufacturing process of new materials (i.e. composites), without affecting the mechanical response of the host material.
- With the rise on SHM complexity, different sensing heads sensitive to other measurands (usually related to specific materials or designs) are required to complete these models, that are the basis of complex smart structures.
- The development of low cost sensor systems with enough performance to fit particular requirements is a key factor to reach wider application scenarios.
- Since a smart structure has to react to its environment, adding high resolution data from distant points (remote sensors) can be useful to anticipate the reaction of the structure.
- With the development of sensing technologies, to extract useful information from huge amounts of available raw data becomes a complex problem, requiring new solutions to analyze the monitored structure.
- Beyond the development of sensing networks, several actuation capabilities and their interaction with new materials must be addressed to achieve dynamic materials and structures with reaction capabilities.

Trying to overcome some of the identified needs, different works have been carried out during the current thesis.



# Chapter 3

---

## Objectives

---

This work does not try to explain the basis of Optical Fiber Sensors but, to apply them in addition to other techniques to obtain operative Smart Structures. OFS techniques must be adapted to these purposes, and also be combined with decision and action systems, to achieve a structure with reaction capabilities. By adapting OFS techniques to new available materials, different structural parameters can be measured, completing the available structural information. These sensing methods provide raw data that must be processed to evaluate the status of the hosting structure. Finally, after the evaluation, some structural parts can be adapted as a reaction of the current structural status.

The main objectives of this work have been derived from some key aspects identified in the previous state-of-the art that need further research efforts. These objectives can be grouped into three big sets regarding: sensing, decision making and actuation, and can be summarized as follows:

1. **To improve the present FBG-technology platform and to develop new sensing heads:** Based on FBG technology, several transducers will be developed to measure basic structural parameters. The obtaining of new features such as achieving intra-grating strain resolu-

tion will be performed over already existing sensing heads. Trying to deal with new materials and structures, particular parameters of composite materials will be also measured using especially designed FBG transducers. Existing problems such as strain-temperature discrimination will be also addressed by combining FBGs with different composite plates. Several application scenarios where, the integration of the optical fiber is critical, will also be studied to be instrumented with FBG strain gauges.

2. **To achieve more suitable OFSs for low cost applications:** Although high performance OFSs are widely applied, there are still specific application scenarios where cost is a limiting factor. By employing POF sensing heads in combination with speckle interferometry, new sensing approaches will be studied. Several mechanical parameters such as strain or vibration should affect the speckle pattern of a multimode optical fiber. This technique will be evaluated in terms of sensor performance, viability and cost for different application examples.
3. **To obtain high precision remote measurements for environmental monitoring:** A truly Smart Structure must also be aware of its surrounding environment, thus, it is required to obtain high precision measurements beyond the structure itself is required. Dealing with this problem, different remote sensing techniques will be studied to achieve high resolution remote sensors and to help in their designing stage. By combining FBGs with active optical fibers, laser cavities can be formed and employed as sensing heads. Particularly, DBR lasers will be studied as long-distance sensing heads and new filtering techniques will be evaluated to improve the laser performance.
4. **To combine OFSs techniques with actuation systems:** Using FBGs with Shape Memory Alloys (SMA), both sensing and action capabilities can be combined to obtain new active structures. The integration of this kind of materials (that recover their original shape when heated) will be studied to design new sensing methods. The integration of both technologies into a smart material will be also addressed, trying to characterize its response under typical structural scenarios in order to reach a truly Smart Structure.

- 
5. **To employ different algorithms to process OFS data:** Data managing is a current problem for large OFS systems: there are too many sensors and a very short time to make a decision. Different machine learning approaches (both classical and new) will be applied to real OFS data to take decisions regarding the structure status. Decision making is currently a very interesting challenge for Smart Structures and employing these algorithms, several conclusions will be obtained regarding sensors location or about the algorithm complexity.

A work plan has been followed to achieve the outlined objectives. The main results have been included in the following chapters. Chapter four is devoted to sensors and techniques based on FBG technology. Chapter five includes the contributions on the cost reduction in OFS by developing speckle based fiber sensors. Chapter six is centered on remote sensing using Fiber Laser Sensors. Chapter seven is dedicated to the combination of FBGs with new materials (SMA) to create new sensing and actuation devices. Chapter eight deals with the data managing problem for sensing applications. The third part is devoted to the conclusions and future lines. Finally, the fourth part includes a summary of the references employed during the research part of this PhD and the papers that have been published and submitted for publication in the framework of this thesis work.



# Part II.

## Contributions

In this part, several contributions to the development of Optical Fiber Sensors for Smart Structures are detailed. First of all, different FBG-based approaches and techniques are proposed to improve different features of existing sensors such as performance or their integration into different structures. Secondly, several POF sensors based on speckle interferometry are explored to be employed as a low cost sensing solution for Smart Structures. Later, Fiber Laser Sensors are proposed and studied for remote sensing applications. Finally, two inherent Smart Structures factors are addressed (action and decision): starting from acting-sensing structures based on the combination of FBG and SMA and finishing by evaluating Machine Learning approaches to deal with raw data. The chapters included in this section are:

- Chapter 4: Sensors based on FBG technology
- Chapter 5: Speckle based sensors using POF
- Chapter 6: Fiber laser sensors
- Chapter 7: Hybrid FBG-SMA techniques
- Chapter 8: Data managing and decision making



# Chapter 4

---

## Sensors based on Fiber Bragg Grating technology

---

Fiber Bragg Gratings (FBGs) have been widely employed in Smart Structures, however, additional knowledge and techniques are required to improve their application to real scenarios. By improving the existing methods and adding new sensing capabilities, FBGs can be extremely useful for Smart Structures and, particularly, for those based on composite materials.

Based on FBGs, different contributions have been developed during this thesis work, and they can be grouped into three sections. The first one tries to improve the final performance of existing sensing heads by retrieving their inner strain profile (Section 4.1, *Intragrating distributed technique*). The next contribution deals with the widely studied problem of strain-temperature discrimination of FBG based transducers. In Section 4.2 (*Designs for temperature-strain discrimination*), different sensing heads designs are evaluated to obtain both measurands employing one or two FBGs. Finally, different transducers are designed to evaluate specific composite materials parameters such as bonding quality or compaction pressure. These new designs and different field applications have been grouped into Section 4.3 (*Embedded transducers for laminated composites*).

## 4.1. Intragrating distributed technique

Nowadays, Fiber Bragg Gratings [1] are a mature technology widely used in a large set of devices for different scenarios such as sensing [2] and optical communications [3], but the majority of their applications assume that no deformation or homogeneous deformations are applied to the FBG length and, consequently, its spectral shape is maintained. However, under many real circumstances, the FBG is under a non-uniform strain distribution, modifying its spectral shape and complicating the extraction of clear measurements.

There are several approaches that try to determine the non-uniform strain profile applied to a single FBG. In the first work based on the FBG reflection spectrum [4], the strain profile is obtained from its amplitude value, but just for monotonic strain distributions when the slope is known. Trying to reduce the a priori knowledge about the applied strain, other approach based on the Fourier Transform was proposed [5], where, using the intensity and phase of the reflection spectrum, an arbitrary strain profile was obtained. This method was very sensitive to noise and it required a low FBG reflectivity (lower than 30%). A time-frequency signal analysis technique that used the reflection spectrum intensity and phase to get the deformation profile was also proposed [6]. These works show the possibility of reconstructing any arbitrary strain profile, but the suggested technique is difficult to be implemented with short FBG lengths. Employment of the phase measurements to get the deformation profile has also been reported [7]. This approach based on low coherence interferometry obtains any arbitrary strain profile from just two phase measurements of the FBG spectrum.

Optimization techniques have also been considered as a mean to obtain non-uniform strain distributions of a FBG. In [8], an optimization technique is applied by analyzing the intensity of a FBG reflection spectrum using a genetic algorithm. This method adjusts the coefficients of a polynomial formula that fits the deformation profile, requiring a priori knowledge of the applied deformation. In [9], an optimization algorithm is proposed to estimate some parameters of a chirped FBG under a predefined strain profile from the FBG spectrum. Genetic algorithms [10] and Particle Swarm Optimization (PSO) [11] have also been proposed to obtain the transverse strain applied to a FBG,

demonstrating the capabilities of these algorithms for spectral synthesis.

Different spectral synthesis algorithms based on Particle Swarm Optimization [12] have been employed to obtain the longitudinal deformation profile of FBGs, just employing their reflection spectrum intensity. Based on Sampled FBGs, and employing a simple error function, the algorithm convergence can be fast but with a limited spatial resolution. On the other hand, using uniform FBGs, an improvement on the spatial resolution can be reached, at the expense of a higher computational cost. These techniques can be applied to quasidistributed sensing with intragrating resolution, by processing each FBG spectrum individually.

### **4.1.1. Sampled FBGs**

This technique employs the spatial modulation of Sampled FBGs to retrieve the deformation of each individual section. Based on the PSO technique, different synthetic spectra are generated using different deformations for each SFBG section. These synthetic spectra are compared to the measured ones and, when both spectra match, the algorithm returns the strain profile used for the synthetic spectrum.

The proposed algorithm combines a custom defined error metric to compare the measured and the synthetic spectra and the Particle Swarm Optimization technique to get the deformation profile. Although the achieved spatial resolution is fixed by the chosen Sampled FBG, this limitation speeds up the algorithm convergence.

Several controlled axial deformation profiles are employed to verify both theoretically and experimentally the proposed technique, where the individual deformation of each SFBG section ( $<1\text{mm}$ ) is obtained without deformation restrictions. Simulations and experiments show a rather correct deformation determination of each SFBG section under complex situations despite the model inaccuracy and fabrication imbalances.

#### **4.1.1.1. Teoretical Model**

A sampled FBG can be understood as an in-fiber grating whose axial index variation profile is modulated by a periodic sampling function of period  $P$  (Fig. 4.1) according to the expression [13]:

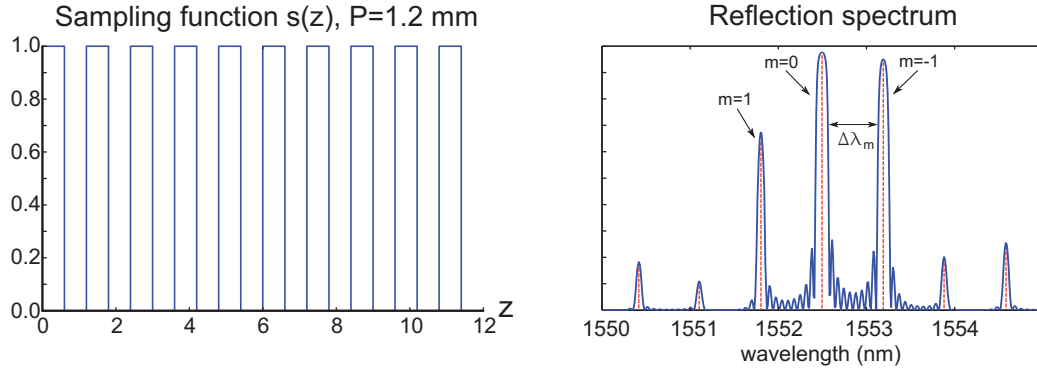


**Fig. 4.1.:** Non apodized ( $a(z) = 1$ ) Sampled FBG illustration with  $N = 20$  sections. A periodic sampling function ( $s(z)$ ) is applied to the FBG structure creating extra reflection peaks in the reflection spectrum.

$$\Delta n(z) = s(z)a(z) \cdot A(z) \cdot e^{j\frac{2\pi}{\Lambda}z + j\phi(z)} + c.c., \quad (4.1)$$

where  $\mathbf{s}(z)$  and  $\mathbf{a}(z)$  are the sampling and the apodization functions respectively,  $\mathbf{A}(z)$  is the grating apodization profile,  $\Lambda$  is the FBG period and  $\phi(z)$  is the phase. The period ( $P$ ) of the sampling function is much larger than the period of the grating ( $\Lambda$ ), causing a double modulation in the structure: a rapidly varying component with a period  $\Lambda$  and a slowly varying sampled envelope with a period  $P$ . Based on Fourier theory, the periodic sampling function of period  $P$  can be expressed as a comb function modulated by complex coefficients  $F_m$ :

$$s(z) = \sum_m F_m \cdot e^{j\frac{2m\pi}{P}z}, \quad (4.2)$$

being  $m$  the Fourier order. For each comb ( $m$ ) of the Fourier equivalent function, a *ghost* grating appears on the resulting spectrum. The spectral separation between two *ghost* gratings is inversely proportional to the sampling period:  $\Delta\lambda_m \propto \frac{1}{P}$

Due to its slow varying periodic structure ( $P \propto 1mm$ ), a clear spatial division is created on the grating structure and more information (in comparison to an uniform FBG) can be obtained by analyzing the SFBG spectral response with the same span. Besides the main spectral contribution of the  $m=0$  order, some *ghost* gratings can be also analyzed giving extra points of view of the fiber deformation structure.

The main aim of this work is to obtain the individual deformation of each

of the sampled sections of the SFBG by, properly, comparing the measured spectrum to a synthetic one. The later is generated by the proposed theoretical model from a strain profile for a given SFBG. The optimization algorithm is used to adjust the deformation of each section until the synthetic spectrum matches the measured one. This challenge leads to two main goals: the assignation of a metric that compares two spectra and the optimization of a N-dimensional blind problem (being N the number of sections of the SFBG).

In order to determine the deformation profile (with the sampling period resolution), each sampled section is deformed within a fixed range. For each deformation case, the SFBG response is calculated (synthetic spectrum) and compared to the measured (desired) spectrum. For this reason, the metric to evaluate the error between the synthetic and the desired spectra, and the optimization technique used to calculate the deformation of each section are both very critical.

### Metrics for spectral comparison

The whole synthetic spectrum challenge relies on a correct error metric for spectral comparison. Using an incorrect metric can lead the optimization algorithm to a wrong solution by assigning a lower error to a worse deformation profile. The employed error metric may also be able to manage the noise and acquisition differences of the measured spectra and the synthetic ones because the synthetic algorithm must work with real spectra. Thus, the error metric may have enough sensitivity to distinguish between two similar deformation cases, but it may also deal with noise in real data. In order to meet both requirements, some parameters of each spectrum are evaluated providing extra points of view:

- **Spectral correlation:** The correlation between the two central wavelengths of both spectra is calculated. This metric should be enough if there is no noise and measurement errors in the spectra; consequently, this value should be complemented with other parameters in a real situation.
- **Peak position:** The difference between the wavelength of the most relevant peaks of the synthetic and measured spectra is calculated. This

value can indicate an offset deformation between the two compared spectra.

- **Peak value:** The difference between the reflection value of the most relevant peaks of the synthetic and measured spectra is calculated. When a different strain profile is applied to a SFBG, the peak reflection values also change depending on the grating deformed length matching each grating period (wavelengths).
- **Peak width:** The width (measured in nm) of the most relevant peaks of the synthetic and measured spectra is calculated. This error value will penalize when the most reflective peaks are not the same in different spectra.
- **Peak ratio:** The ratio between the two most relevant peaks is calculated. The peak ratio should remain unaltered despite the noise intensity.
- **Number of peaks:** The number of peaks exceeding a specific threshold of both spectra are also subtracted. As this parameter increases, it indicates that both spectra are in very different deformation cases.
- **Peak Kurtosis:** The Kurtosis of each of the most relevant peaks is computed in a prefixed lambda span. This value indicates the *sharpness* of a peak but it is also very noise sensitive.

All these parameters are scaled and added to get a single error metric. Depending on the measurement equipment and the noise present in the obtained data, some scale weights have to be trimmed. Getting a proper adjustment of the scale weights would offer more accurate results, but setting the weights to a very accurate target requires many controlled experiments. For the same experimental setup, these weights should be constant to evaluate all the obtained data in the same conditions.

In Fig. 4.2, a comparison between two spectra is shown. The most remarkable parameters are detailed considering just the main peak of both spectra (for drawing clarity). Besides the correlation between the central section of the desired spectrum and the synthetic one, the main peak position, peak value and peak width are computed as individual contributions to the final

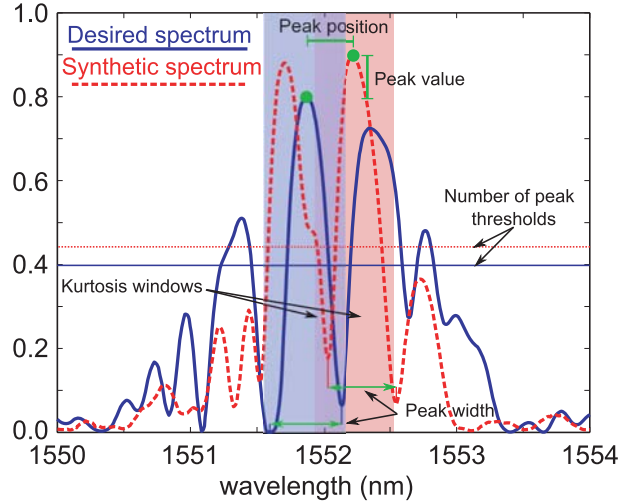


**Fig. 4.2.:** Some parameters of the employed error metric are applied to two different spectra. The main peak from both spectra are just considered for drawing clarity.

error value. The employed thresholds (half value of the higher peak) to get the number of peaks of each spectra are also shown, obtaining four peaks for the desired spectrum and two for the synthetic one. The windows where the kurtosis of the most relevant peak of each spectrum is evaluated are also shown. Most of the employed metrics can be applied to a higher number of peaks, increasing the final error value with unmatched spectra.

### Optimization method: Particle Swarm Optimization

Once the error function between the synthetic and measured spectrum has been defined, an optimization strategy can be followed to minimize it. The target is to obtain a synthetic spectrum from a simulated deformed case that matches the measured spectrum, obtaining the equivalent deformation profile of the measured SFBG. To obtain the equivalent deformation profile, each SFBG section is individually deformed by the optimization algorithm.

A blind optimization operation has to be performed into a N-dimensional space to get the equivalent deformation profile, where N is the number of sections of the SFBG. After some initial studies, Particle Swarm Optimization (PSO) [12] was chosen as a suitable technique to be applied in this field, given its simplicity and widespread use in several scenarios.

In a simplified way, PSO is a blind optimization algorithm that moves a population of candidate solutions (particles) within a search-space according

to a prefixed rule. Each particle's best position and the swarm (collection of particles) best position are taken into account for the particle movement as well as each particle's current position and velocity. Two random values are also employed for the particle's movement, helping the algorithm to explore the search-space while the swarm is being guided to the best calculated position. The original PSO algorithm can be summarized as follows:

1. Initialize a population array of particles (SFBG strain vector) with random positions and velocities in the search space of N dimensions (number of SFBG sections).
2. Evaluate the error function for each particle (comparing the synthetic spectrum of each particle with the desired one as explained in Section 4.1.1.1).
3. Compare the latest error evaluation of the current particle with its "previous best" error value:  $p_{best}$ . If the current error value is better, then  $p_{best}$  will be updated, and  $p_i$  (previous best position) will be updated to the current location  $x_i$ .
4. Determine the particle within the swarm with the best error value ( $g_{best}$ ) and assign its location to  $p_g$ .
5. Change velocity and position of each particle within the swarm according to the following expression:

$$\begin{cases} v_{id}(t+1) = w \cdot v_{id}(t) + c_1 \cdot r_1 \cdot (p_{id}(t) - x_{id}(t)) + c_2 \cdot r_2 \cdot (p_{gd}(t) - x_{id}(t)), \\ x_{id}(t+1) = x_{id}(t) + v_{id}(t+1) \end{cases} \quad (4.3)$$

where  $w$  is the inertia weight,  $c_1$  and  $c_2$  are positive constants, typically defined as learning rates, and  $r_1$  and  $r_2$  are random functions in the range  $[0,1]$ .

6. If the stopping condition is met then exit with the best result so far; otherwise repeat from point 2.

Each particle within the swarm is defined by its position  $X_i$  and velocity  $V_i$  within the  $N$ -dimensional search space, where:

$$\begin{cases} X_i = (x_{i1}, x_{i2}, \dots, x_{iN}) \\ V_i = (v_{i1}, v_{i2}, \dots, v_{iN}) \end{cases} \quad (4.4)$$

The position of each particle ( $X_i$ ) represents a possible strain vector applied to the SFBG model and the velocity ( $V_i$ ) is a vector that represents how the particle evolves within the search space. With the proposed error metric, the optimization goal is to find the deformation profile that causes the desired spectrum so, the best particle position found during the PSO run should match the physical strain profile of the SFBG. Due to the stochastic nature of the PSO, the obtained strain vector ( $X_p$ ), corresponding with the best error value found in the swarm ( $g_{best}$ ), may also be a local minimum of the error function. Using a high ( $> 100$ ) number of starting particles should be enough to reduce the local minimum convergence. However, wrong solutions caused by a local minimum can be detected just by comparing the obtained best error value ( $g_{best}$ ) to a specific threshold. If a wrong solution is detected, the PSO algorithm should be run again with a higher number of starting particles.

The PSO algorithm with the defined error metric has been tested with different deformation cases using both simulated and experimental spectra. All the performed tests are based on a  $N = 5$  section SFBG with a total length of  $L = 4 \text{ mm}$  and with a linear decreasing apodization profile with a decreasing factor  $M = 0.25$ . For each strain vector, the synthetic spectrum is calculated using the Transfer Matrix method (with  $N = 5$  sections) and compared to the desired one with the defined error function. The spatial resolution of the employed structure is  $P/2 = 0.8 \text{ mm}$ . In the following section, the response of the algorithm to simulated spectra is analyzed under ideal and realistic situations.

#### 4.1.1.2. Simulations

Some simulations have been performed by feeding artificial SFBG spectra to the PSO algorithm. These artificial spectra were simulated by applying different strain profiles to the SFBG structure. Artificial spectrum runs have been used to check the whole optimization algorithm and to adjust the error function scale factors.

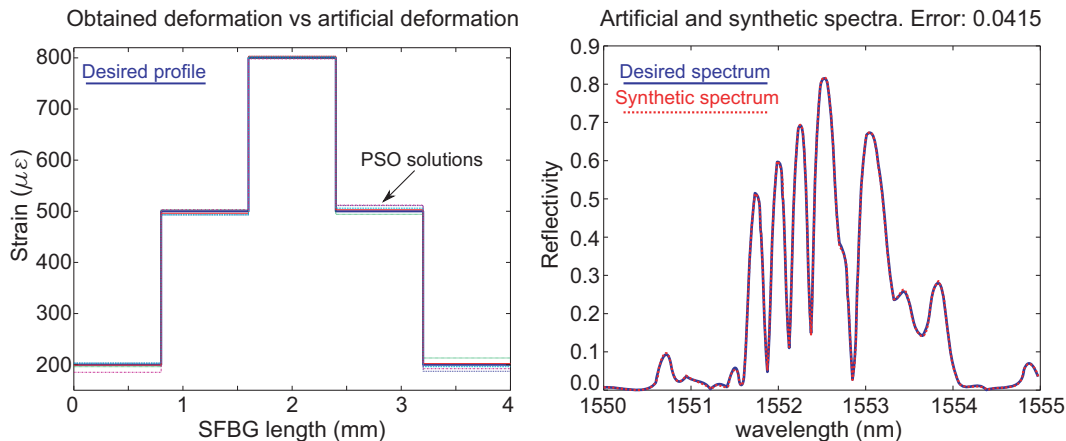


**Fig. 4.3.:** Five solutions obtained by the proposed optimization algorithm compared to the reference deformation values used to generate the artificial spectrum (left) and a synthetic spectrum generated with the PSO solution compared to the artificial (desired) one (right).

In the first tests, each section of the SFBG is uniformly deformed using different strain values for each section. This case reproduces an ideal situation where the deformation profile exactly matches the spatial resolution of the structure ( $P/2 = 0.8 \text{ mm}$ ). In other simulated cases, the deformation value applied to each section is non-uniform, trying to reproduce a continuum strain profile. All the artificial spectra are generated using the Transfer Matrix method [14]. For the uniform deformation scenarios, the number of employed sections to compute the artificial spectrum is set to  $N = 5$ , matching the SFBG structure. For the non-uniform deformation cases, the number of employed sections was set to  $N = 50$ , having  $N_s = 10$  different deformation values within each sampling section.

All the performed tests were simulated using a wavelength span of 5 nm with a resolution of 5 pm. Due to the reduced wavelength span, and also to allow an in-range convergence, the SFBG sections with null envelope ( $A(z) = 0$ ) are initialized to a random number within the deformation values of their neighboring sections. Detecting an out-of-range deformation of the null enveloped sections could be impossible dealing with a limited wavelength span. This assumption also recreates a real situation where a particular section deformation is related to the deformation applied to its neighbors.

In Fig. 4.3 (left), five strain profiles obtained with the proposed algorithm

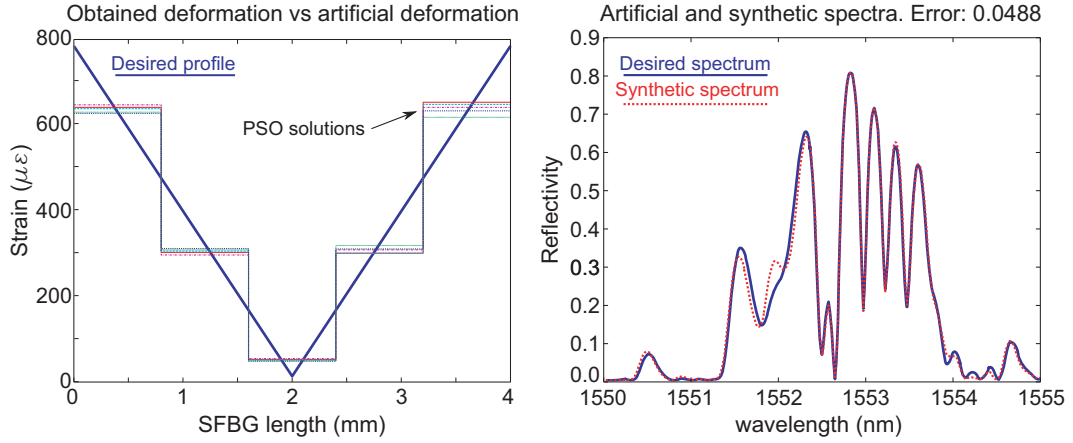


**Fig. 4.4.:** Continuous strain profile used to compute the artificial spectrum compared to five PSO solutions (left) and a synthetic spectrum compared to the artificial one (right).

are shown against the deformation profile of the artificial spectrum. The PSO output converges to the correct strain profile employed to compute the artificial spectra. Due to the continuum range value of the algorithm outputs and to the stochastic convergence of the PSO technique, solutions considered as “correct” are distributed within a range. For this test, the achieved range that contains the correct solution is  $\Delta\epsilon = \pm 15\mu\epsilon$ . On the right side (Fig. 4.3), the synthetic spectrum of the best achieved solution is compared to its artificial (desired) spectrum. Both spectra match each other almost perfectly, giving rise to an error value lower than 0.25 that has been considered the error stop condition. Although these tests recreate situations where the spatial deformation variations perfectly match the proposed sensing structure ( $P/2 = 0.8\text{ mm}$ ), they are helpful to validate the algorithm resolution and repeatability.

A more realistic scenario is also proposed: the deformation of each sensing section is not uniform along the section length ( $P/2 = 0.8\text{ mm}$ ). A two-stages linear varying deformation profile is used to generate the artificial spectrum. In Fig. 4.4 (left), five obtained strain profiles are compared to the strain profile used to generate the artificial spectrum. As the resolution of the sensing principle is limited to the section length, the obtained strain for each section is the averaged deformation of the correspondent length. The resulting strain profiles qualitatively follow the deformation profile applied to get the artificial spectrum. In these tests, the achieved range containing the correct solution

is  $\Delta\epsilon = \pm 30\mu\epsilon$ . This range is worse than the already commented, but it still is sufficiently small to be considered as highly accurate. In Fig. 4.4 (right), the synthetic spectrum of the best obtained solution is compared to the artificial one. The two depicted spectra are in good agreement, having a small error value (lower than the established threshold of 0.25 for simulated scenarios). The synthetic spectrum exhibits the same characteristic shape as the artificial one: two smooth peaks at lower wavelengths followed by four sharper peaks at higher wavelengths. There are slight mismatches due to the higher order spectral components of the simulated spectra. These components are more sensitive to the slight mechanical deformations introduced, in this scenario, by the spatial resolution of the employed model. This second case is more realistic, thus demonstrating the good algorithm response even under non-ideal conditions.

#### 4.1.1.3. Experimental tests

Some experimental tests were also performed using controlled SFBG deformations to validate the proposed sensing principle. A controlled strain profile was applied to a short SFBG (a few millimeters) to analyze the algorithm performance. The SFBG was embedded into a plastic block with a predesigned shape that deforms the optical fiber following a preset profile, obtaining non-uniform deformation values within the SFBG length. The short SFBG was manufactured with the same characteristics of the simulated model:  $N = 5$  sections of  $P/2 = 0.8 \text{ mm}$  linearly apodized with a decreasing factor of  $M = 0.25$  as shown in Fig. 4.5. This SFBG was embedded into an epoxy resin block with a specific shape to cause a non-uniform strain profile in the SFBG. The resin block has been also mechanically simulated using Finite Element Analysis to qualitatively obtain the applied deformation profile.

The SFBG was written into a standard telecommunications optical fiber using the phase mask technique with a continuous laser emitting at 244 nm. The sampling effect was generated by opening and closing the laser shutter at preset locations. The apodization effect was generated by changing the recording speed during the laser scanning process: the higher the envelope, the lower the speed. To build the resin block, the FBG was aligned with a nonstick mold with the desired shape. Once the SFBG was placed into the mold, a low

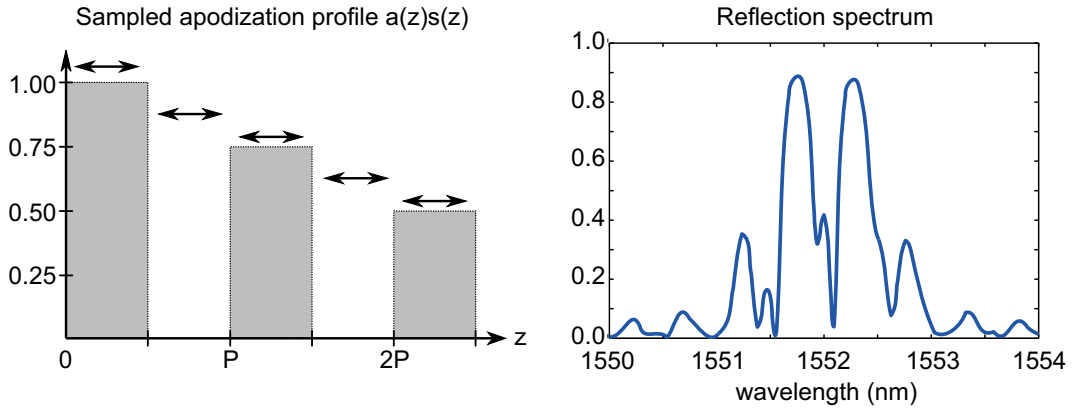


**Fig. 4.5.:** Illustration of the sampled apodized SFBG profile (left) and its characteristic spectrum (right) used in the experimental demonstration.

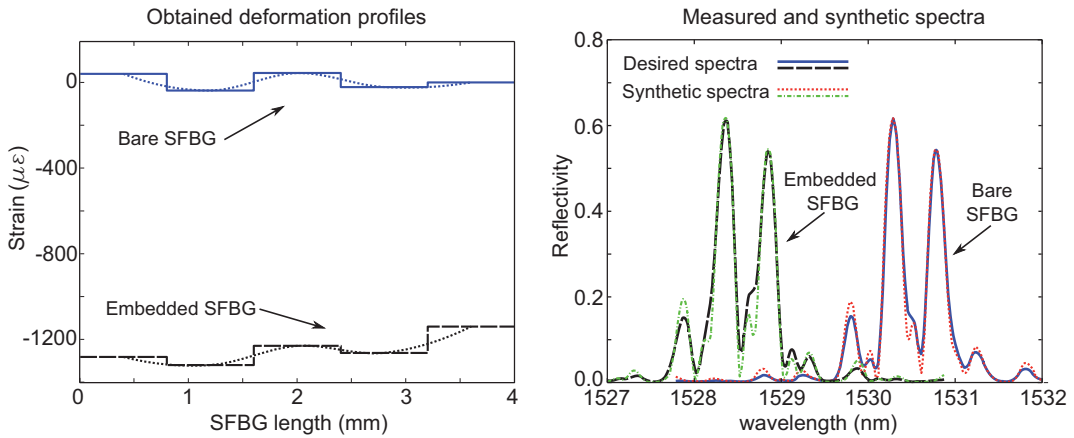


**Fig. 4.6.:** Right: spectrum of the written SFBG before being embedded into the resin block (solid line) and after the embodiment (dashed line) against their synthetic spectra (thin lines). On the left: the obtained deformation profile of the residual strain and its interpolation (dotted line).

viscosity epoxy resin was poured into it. To build the nonstick mold, a male mold was mechanized with the desired shape in PMMA using a Computer Numerical Control (CNC) cutting machine. This male mold was covered with nonstick silicone, creating the holding mold for the epoxy resin. After the resin was poured, a vacuum stage following to guarantee the homogeneity of the final block by removing the air bubbles. The epoxy resin was thermally cured for a few hours to obtain the final block.

The curing process of epoxy resin introduces a residual strain to the SFBG, slightly changing its spectral shape. The small changes in the reflection spectra (Fig. 4.6, right) suggest a non-uniform residual strain, so a new deformation

profile has to be set as a reference. The proposed algorithm is applied to both spectra to get the residual strain profile (Fig. 4.6, left). The obtained deformation profile indicates that the residual strain of the final sections of the SFBG is slightly higher ( $\approx 200 \mu\epsilon$ ) than the first ones, so further deformation profiles have to be compensated using the obtained residual strain profile as a reference. This compensation step is required since the entire block is stretched, not just the written SFBG, so the reference deformation profile is the packaged one. To obtain the strain profile transferred to the SFBG by the resin block, a Finite Element Analysis (FEA) has been carried out and it is detailed in the following.

### Strain profile simulation: Finite element analysis

A simplified resin block model is developed by using the stress analysis suite of Autodesk Inventor (Autodesk Inc). Developing highly reliable FEA models of heterogeneous pieces with absolute results can be a very complicated issue, but the generation of a qualitative deformation profile can be usually accomplished by means of a simplified model. Within this scenario, the acquisition of this qualitative profile allows to study the deformation caused to the SFBG when a load is applied.

The pierced central part of the resin block exhibits a higher sensitivity to longitudinal axis deformations, as shown in Fig. 4.7. The model is based on a constant thickness ( $h = 0.8 \text{ mm}$ ) resin block where an optical fiber is embedded into the longitudinal axis. The Young's modulus is set to 3.5 GPa for epoxy resin and 74 GPa for optical fiber silica. The employed SFBG of  $L = 4 \text{ mm}$  length is longitudinally centered within the resin block as shown in Fig. 4.7 with a tolerance of  $\pm 0.1 \text{ mm}$ .

In Fig. 4.7, the deformation profile applied to the optical fiber is qualitatively modeled using FEA. The pierced part of the block is more deformed than its sides when an uniform load is applied, creating a non-uniform deformation profile in the SFBG. The resin block is mounted in a mechanical setup to create the desired deformation with a controlled environment to perform the experiments discussed in the next section.

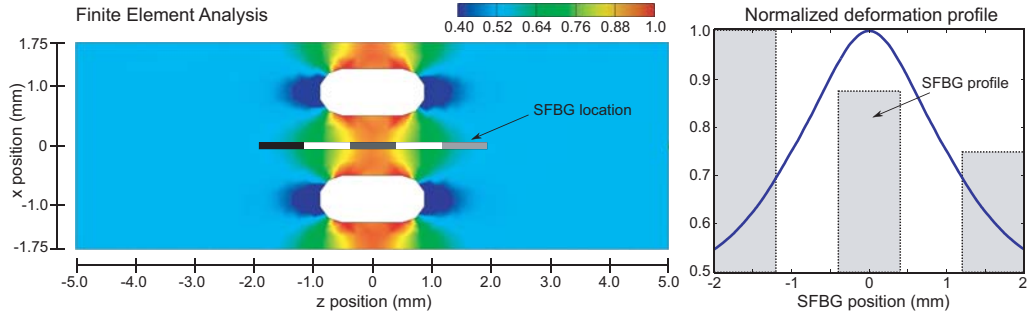


**Fig. 4.7.:** Resin block dimensions and SFBG location (left). Simulated deformation profile applied to the SFBG (right).

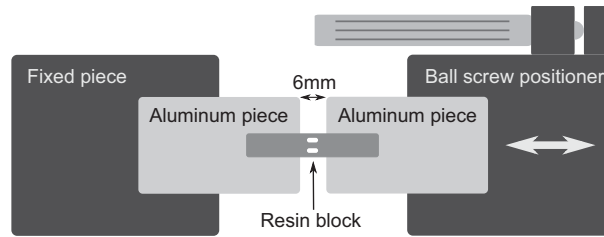


**Fig. 4.8.:** Experimental setup employed for loading the resin block. The block is glued to two aluminum pieces that are slightly separated using a ball screw positioner.

## Experimental measurements

The manufactured resin block is glued to two aluminum pieces separated 6 mm using cyanocrylate adhesive. The central section of the resin block is centered on the gap between the metallic pieces, leaving unglued the central block section of 6 mm. Both pieces are attached to linear micropositioners to stretch the central section of the resin block (Fig. 4.8). The alignment process of the aluminum pieces where the block is glued is a critical point to get an uniform load on the block. Slight misalignments can provoke an asymmetrical load to the central block section rendering useless the mechanical model. The SFBG is connected to an optical spectrum analyzer (HP86140A) and to a white light source (HP83437A) through a 50/50 coupler.

Once the holding pieces are perfectly aligned, the distance between the two aluminum pieces is progressively increased using the micropositioner. Reflecting spectra of the SFBG are captured for different loads (positions). These spectra are fed into the proposed algorithm to get their deformation profiles, performing  $N_i = 20$  runs for each of the five captured spectra to delimit the algorithm convergence range. The stop condition for the maximum allowable

error has been set to 0.75 based on previous runs. If a particular PSO run obtains a final error higher than the threshold value (less than 10% of total runs), the algorithm is executed again with a higher number of starting particles. The achieved convergence range for real spectra was  $\pm 50 \mu\epsilon$ . The spectrum captured with the higher strain value is detailed in Fig. 4.9, where the obtained results for the resin block subjected to a high load are shown. On the right side, measured and synthetic spectra of the highest deformation case are presented (an increase of  $\Delta L \approx 25 \mu m$  over  $L = 6 mm$ ). Both spectra show a very good agreement (the depicted synthetic spectrum has an error metric of 0.667) exhibiting the same characteristic shape as the measured one (four sharp peaks at lower wavelengths followed by two smoother ones at higher wavelengths). However there are still small differences mainly caused by the higher order spectral components of both spectra such as the incorrect location and width of the last lobe or the value of the less reflective lobes. These mismatches are created by small contributions of several factors that will be discussed in the next section. Also in Fig. 4.9, the deformation profile of the synthetic spectrum is compared to the normalized deformation profile simulated with FEA. The obtained profile is also compensated for the residual strain caused during the resin block. Both profiles are also interpolated for viewing purposes. The compensated profile remarkably agrees with the simulated one, thus demonstrating the correct response of the proposed algorithm.

##### 4.1.1.4. Specific remarks

Both simulations and experimental results exhibit a very good agreement with the applied deformations (under different conditions). For achieving this remarkable agreement, the proposed algorithm has to be trimmed to better fit any particular application, so simulated tests are required to make an initial adjustment of several parameters of both error metrics and PSO algorithm. Once the algorithm parameters are set, an experimental stage follows to evaluate the whole process performance under real conditions.

The optimization algorithm is applied to two different simulated scenarios where an ideal deformation case and a more realistic one are presented. In the first deformation profile, uniform but different deformation values are applied

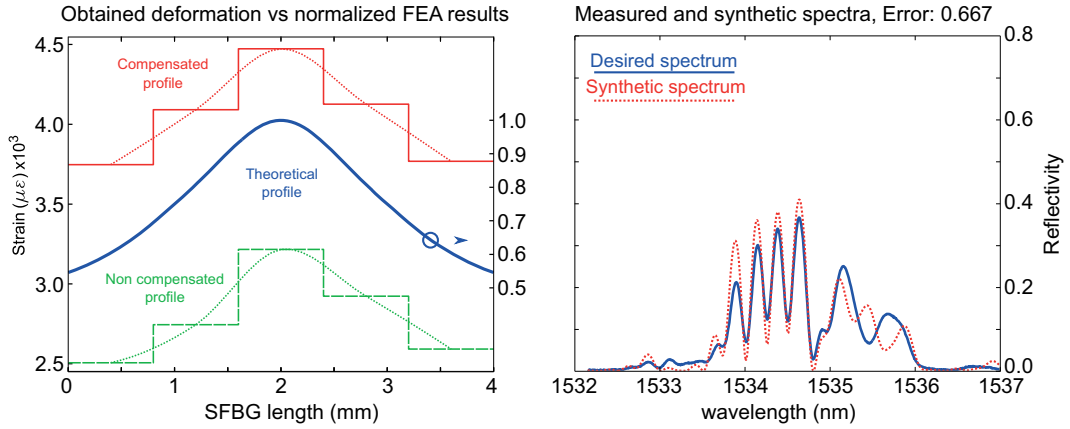


**Fig. 4.9.:** Deformation profile of the measured spectrum (with and without compensation) against the simulated normalized deformation (left). Measured spectrum of the SFBG under load condition compared with its synthetic one (right).

to each of the  $N = 5$  SFBG sections. Results show a perfect match between the desired and synthetic spectra with a great repeatability under this ideal environment. Once the error metric and the PSO algorithm are validated, a more realistic deformation profile where each SFBG section is deformed with a non-uniform strain profile is tested. The achieved results match almost perfectly the applied deformation profile proving the ability of the algorithm to work with non-uniform deformation cases.

For the experimental validation a SFBG of  $L = 4 \text{ mm}$  was embedded into a resin block designed to apply a non-uniform deformation profile to the SFBG when it is stretched. The obtained deformation profiles are compared with the theoretical deformation profile obtained using FEA, which is applied to the SFBG. Due to the fabrication process, a residual strain profile is created into the SFBG prior to stretching the block, so the obtained deformation profiles have to be compensated with the residual strain profile. Even after the compensation, the obtained deformation profile remarkably matches the FEA simulations, having also a very good agreement between measured and synthetic spectra. Under experimental conditions the algorithm exhibits an excellent performance, but it also shows some disadvantages.

Due to the problem complexity (non-linear spectrum synthesis) and the stochastic nature of the optimization scheme (PSO), the achieved results fall within a convergence range ( $\pm 50 \mu\epsilon$  for the experimental case). This convergence process has to be controlled by evaluating the obtained error and

re-running the algorithm when it is required. In addition to the intrinsic algorithm nature, some additional factors reduce its final performance when it deals with real spectra: the simplified optical model selected to reduce the computation time does not perfectly replicate a real SFBG structure (slight misalignments during the SFBG fabrication or the apodization effect due to the laser spot width). The interpolation technique and the resolution of the Optical Spectrum Analyzer (60 pm) reduces the correlation with the synthetic spectrum (not interpolated). The limitation of the optical model, in addition to the difficulty of accurately stretching small pieces, even an incorrect gluing process may lead to less accurate results.

To deal with all these error sources, the error metric has to be carefully defined, being enough discriminant to reach the correct synthetic algorithm, but also enough permissible to deal with the optical model and mechanical errors. In order to obtain a higher accuracy in the experimental runs, the error metric was re-adjusted by slightly changing its weights, demonstrating the importance of the error metric in the whole process.

All the obtained results are based on the same SFBG structure of  $N = 5$  sections of  $P/2 = 0.8 \text{ mm}$  with a linear apodization, but the algorithm is applicable to any SFBG structure. By increasing the number of sections ( $N$ ), the computation time is also increased. All the performed tests were run in a custom implementation made in Matlab (The MathWorks, Inc.) and each run of the whole algorithm takes a few minutes. By using a more efficient implementation, this computation time can be reduced to a few seconds for each spectrum, allowing the proposed algorithm to work in quasi-on-line applications.

### 4.1.2. Uniform FBGs

In the previous section, the FBG structure complexity has been limited to make the comparison task between two spectra easier by ensuring some spectral artifacts that can be evaluated (e.g. several peaks for the Sampled FBGs) and to speed up the PSO convergence. However, based on a similar approach (error function and PSO), the spatial resolution can be improved by employing uniform FBGs.

The FBG length is divided into  $N$  sections, whose strain values are modi-

fied (PSO candidates) until measured and synthetic spectra match. Since a FBG under a non-uniform strain profile can generate very different spectra, the error function employed as minimization target must deal with these spectral variations. A high level error metric (Geometrical processing) has been implemented as an error function to cover both requirements.

The whole technique (geometric processing and PSO) has been applied to different simulated scenarios to analyze its performance. In addition, a uniform FBG of  $L = 5 \text{ mm}$  has been subjected to an asymmetric thermal perturbation and its reflection spectrum has been analyzed with the proposed technique. The achieved results exhibit a good spatial resolution ( $\Delta L = 0.5 \text{ mm}$ ), being mainly limited by the computation time.

#### 4.1.2.1. Geometrical processing

The main problem when there is a lack of a-priori knowledge about the strain distribution applied to a FBG is the wide divergence of the response spectra. The large amount of possible spectral shapes makes it difficult to compare between them in an efficient way. The geometrical processing scheme must have enough sensitivity to distinguish between two close spectra and also enough goodness to assign a low error to a synthetic spectrum generated from a strain profile with less spatial resolution than the desired one (usually a continuous profile). To achieve these two goals the proposed metric analyzes several parameters related to the general “shape” of each spectrum. Each peak of the spectrum is associated with its 2-D coordinates (wavelength and reflectivity value) and the most relevant ones are assigned to their corresponding of the other spectra when their error distances are low. An example of the geometrical processing is depicted in Fig. 4.10.

After matching the most relevant peaks, three key values are weighted to obtain the final error value: the ratio of unmatched peaks, the Euclidean distance between the matched peaks (for lambda and reflectivity axes) and the overlapped area between the two spectra. When the target (desired) spectrum has enough peaks to evaluate, the two first values are usually dominant in the error. However, for smoother spectra (e.g. a uniform strain profile applied to a uniform FBG has a single peak) the fine error value is given by the overlapped area under both curves, offering the required adaptability.

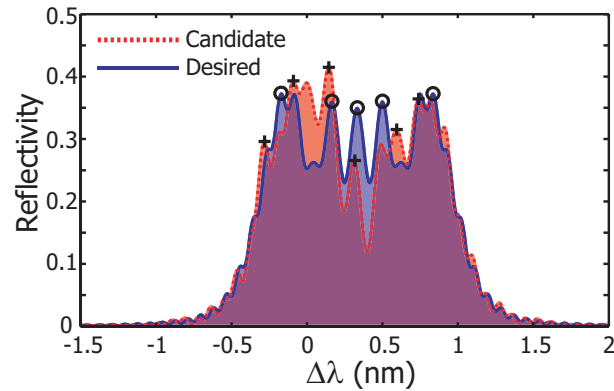


**Fig. 4.10.:** The spectrum of a uniform FBG under the desired perturbation (solid line) is compared to the corresponding spectrum of a PSO candidate vector (dotted line). The error is computed using the main peaks of both spectra (crosses and circles) and the overlap under both curves.

The described error metric has been employed as the quality measurement for the PSO algorithm. In order to improve the convergence, a smoothing process is applied to each of the PSO strain profile candidates, where each strain value is averaged with its two neighbors of the strain profile (80% itself and 10% each neighbor). This step speeds the convergence up because the strain profiles to be reconstructed are usually continuous, thus each strain value is related to its neighbors (as happens in real measurements).

#### 4.1.2.2. Simulations

Several artificial spectra have been generated by applying non-uniform strain profiles to a uniform FBG of 10 mm length. These spectra have been employed to evaluate the synthetic algorithm performance.

A simulated spectrum obtained by applying a non homogeneous strain distribution to a uniform FBG has been analyzed. Two different spatial resolutions have been employed: 10 and 12 sections over 10 mm length. The results are depicted in Fig. 4.11 (top). The averaged values of five algorithm outputs for both resolutions (dashed line for  $N=10$  and dotted line for  $N=12$ ) are compared to the original strain distribution (solid line). Five individual outputs of the algorithm for the  $N=12$  case are also detailed in Fig. 4.11 (top). The desired spectrum (solid line) is also compared to the best achieved solutions for both spatial resolutions in Fig. 4.11 (bottom) (dashed line for  $N=10$  and

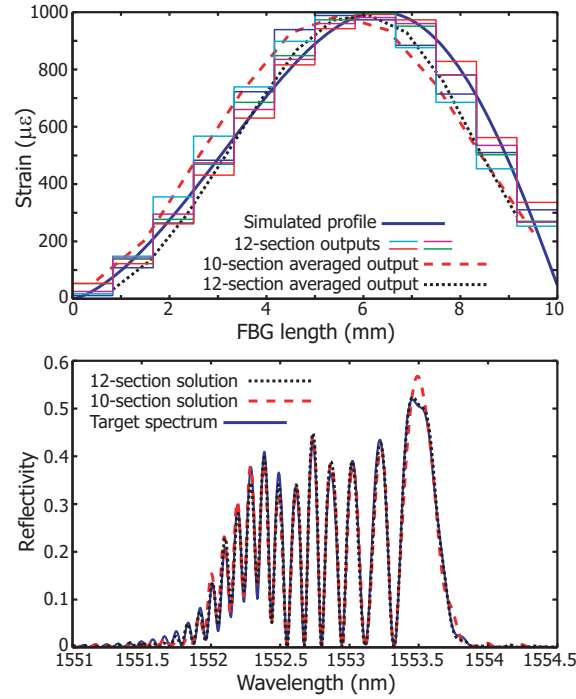


**Fig. 4.11.:** *The original strain profile is compared to PSO outputs for two different spatial resolutions (top). Best spectra for both resolutions are compared to the desired spectrum (bottom).*

dotted line for  $N=12$ ). As the spatial resolution is increased (by increasing the number of sections,  $N$ ), the achieved results are more accurate (mean strain error of  $74.3 \mu\epsilon$  for  $N=10$  and of  $25.8 \mu\epsilon$  for  $N=12$ ), what can be noticed by analyzing the output spectra. Although the error in the recovered strain profiles is higher than the synthetic spectra error, the achieved strain resolution should be enough for mechanical sensing applications.

Due to the symmetry of uniform FBGs, there is an uncertainty about the direction of the perturbation: the spectra corresponding to an axial perturbation applied forward and backwards are the same. This problem can be avoided by applying some apodizing function to the FBG structure instead of employing a uniform envelope. Otherwise, some a-priori knowledge about the perturbation is required to solve this uncertainty.

### 4.1.2.3. Experiments

The geometrical processing scheme has also been tested using real data: a uniform FBG of 5 mm length has been written into standard optical fiber and

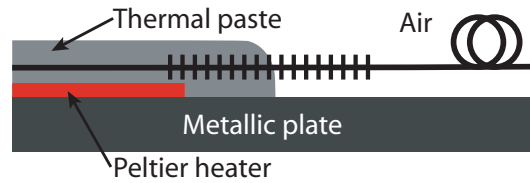


**Fig. 4.12.:** A part of the FBG is immersed into thermal paste while the rest is exposed to the air. The temperature increase is provoked by a Peltier heater.

it has been stressed using an asymmetric thermal perturbation. The setup is depicted in Fig. 4.12 and it is based on a Peltier heater. Part of the FBG is exposed to the air temperature while the other part is immersed into a thermal paste that is in direct contact to the Peltier heater. The heat transfer is more efficient within the thermal paste than through the air, creating an axial thermal difference in the FBG.

The Peltier temperature has been risen up to  $70^{\circ}\text{C}$  while the room temperature was  $25^{\circ}\text{C}$ , creating a non-uniform axial thermal distribution along the fiber, and consequently changing the spectral response of the FBG. The FBG spectrum has been captured using an Optical Spectrum Analyzer (HP86140A) and a broadband light source (HP83437A) connected through a circulator. A synthetic spectrum (dashed line) based on a  $N=10$  sections approach is compared to the measured (solid line) in Fig. 4.13 (top). Considering a FBG thermal sensitivity of  $11 \text{ pm}/^{\circ}\text{C}$ , the PSO outputs have been scaled to obtain the thermal perturbation along the FBG. The achieved results are detailed in Fig. 4.13 (bottom).

In Fig. 4.13, ten of the PSO outputs are depicted (solid lines). These outputs have been averaged obtaining the axial thermal distribution along the FBG (dotted line). Analyzing the achieved results, the five initial sections exhibit a higher temperature because they are immersed into the thermal paste and, besides, the first section exhibits a higher temperature, being the closest to the Peltier heater. The last five sections show a decreasing temperature associated with the cooling process of the air-surrounded fiber. For the measured spectrum, several runs have been performed obtaining an averaged standard deviation of less than  $0.9^{\circ}\text{C}$  with a maximum drift of  $9^{\circ}\text{C}$ .

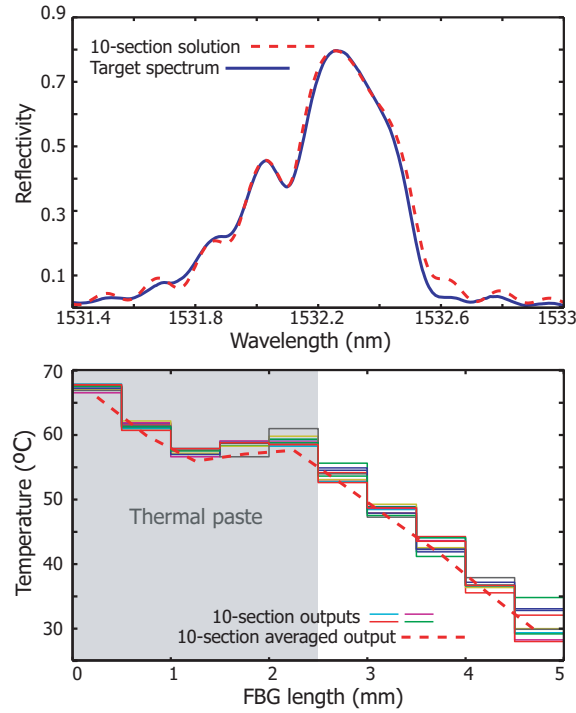


**Fig. 4.13.:** Measured and a synthetic spectra obtained from a PSO output (top). Different PSO outputs and their averaged value (bottom).

#### 4.1.2.4. Specific remarks

Based on the simulated results and comparing the measured spectrum to the synthetic, it can be seen that the geometrical processing is working properly as error metric by driving the PSO algorithm to the right solution. Despite typical problems of comparing measured to simulated spectra, slight differences between the simulated and the manufactured FBG structure, or lack of resolution of the measuring equipments (60 pm of the employed OSA), the achieved PSO outputs produce spectra very similar to the measured one, exhibiting a very good agreement with the employed setup.

Due to the iterative operation of PSO, obtaining the optimal solution can not be ensured because it may fall into a local minimum. However, the convergence process can be evaluated with the error metric, guaranteeing a convergence range where the solution must fall within. When the final error value is higher than a threshold, PSO must be re-run with a higher number of swarm particles. If the sensitivity must be increased, several PSO outputs can be averaged to improve the results; however, this gain requires more PSO

runs thus the overall computation time increases. Another advantage of the proposed technique lies in the fact that the resolution is not limited by the measured data but by the computation time. The PSO algorithm performs a blind optimization over a N-dimensional problem, being N the number of sections, thus the computation complexity increases exponentially with the number of sections.

### 4.1.3. Summary

In summary, different processing schemes have been proposed to retrieve the longitudinal axis deformation of FBGs just from the intensity of their reflection spectra. The proposed algorithms combine a custom defined error metric for spectral comparison and a Particle Swarm Optimization technique to get the deformation values of different FBG sections. The first approach is based on Sampled FBGs, where the sampling period limits the final spatial resolution but also simplifies the convergence, resulting in a faster algorithm. The resulting algorithm has been adapted to work with uniform FBGs, without spatial resolution limitations, by dividing the FBG length into N sections. Due to the wide divergence of uniform FBG spectra under arbitrary strain profiles, the metric for spectral comparison must be adapted to have enough sensitivity to distinguish between two close spectra and also enough goodness to deal with noise (geometrical processing).

Both approaches have been simulated and experimentally tested achieving good accuracy and repetitiveness of the proposed algorithms. Particularly, SFBG synthesis has been able to recover a strain profile with a spatial resolution under 1 *mm* from a measured reflection spectrum. Employing the geometrical processing with the modified PSO technique, an arbitrary perturbation has been successfully recovered from the reflection spectrum of a uniform FBG with a spatial resolution under  $\Delta \approx 0.5$  *mm*, being mainly limited by the computation time. Both techniques can be very useful for quasi-distributed sensing applications based on FBG technology by retrieving individual intra-grating strain distribution of several FBGs.

## 4.2. Designs for temperature-strain discrimination

Composite materials technology has been widely applied to design and manufacture in a lot of new different scenarios. A wide set of applications from civil engineering to aerospace industry have adapted this technology to overcome their limitations. This growing technology is a perfect scenario to add sensing capabilities to study their properties during the material development. Particularly, optical fiber sensors [2] have been proved as a highly compatible technology to be embedded into these composite materials, making it possible to obtain real time measurements during the manufacture process and even under operation, when the final structure has been completed.

Within optical fiber sensors, Fiber Bragg Gratings have also been reported as very suitable sensing solutions to be embedded into composite materials [15]. They have been applied to monitor composite curing processes [16], to evaluate patch repairs of composite structures [17, 18] or even to detect composite damage [19], but one common problem is the thermal dependence of this kind of sensor. The measured reflection peak of a FBG depends both on deformation and on temperature thus, when strain measurements have to be performed in environments without temperature control, the employed FBG sensors require thermal compensation.

There are several works dealing with the simultaneous measurement of strain and temperature such as: different types of FBGs [20], superstructure gratings [21], reversed index gratings [22] or even FBGs printed in special optical fibers like Bowtie [23] or microstructured [24]. However, most of the described solutions are non-suitable for Structural Health Monitoring (SHM) purposes [25], where reliability and cost requirements are highly relevant.

By embedding FBGs into composite materials, different solutions have also been reported to deal with the temperature compensation task. These reported solutions create different responses when strain and/or temperature are applied to a pair of embedded FBGs just by employing a different number of layers [26] or changing composite material within the FBG pair [27]. Although these reported solutions can be more suitable for SHM purposes (they are based on a reliable and mature technology), their manufacture process can be simplified by employing the same host material.

Two main principles have been verified in this section. Based on a pair of FBGs and on a single FBG, different transducers have been proposed to discriminate between strain and temperature. By drilling different holes at preset locations or by varying their external shape, different sensitivity areas are created within each sensing head. The proposed designs are based on embedding FBGs into a constant thickness Carbon Fiber Reinforced Plastic (CFRP) plate whose shape has been designed to provoke different strain sensitivities along their central axis. All the proposed designs have been simulated using the Abaqus Finite Element Analysis (FEA) software (Dassault Systèmes Inc.) to study their mechanical response before their manufacture and experimental test. Optical spectra, simulated using the T-matrix method implemented in Matlab, remarkably agree with the loading test results. The achieved results also enable this new sensing head design to perform temperature-independent strain measurements just by employing a single long FBG.

### **4.2.1. Strain and temperature sensors**

The main goal of this work is to develop Fiber Bragg Grating (FBG) sensors based on CFRP plates capable of measuring both strain and temperature simultaneously. The designed sensors must be easy to manufacture thus, maintaining a constant thickness, the shape of the CFRP plates are modified to provoke different strain responses to each FBG of an embedded pair. Since the hosting material is the same, the thermal sensitivity of both FBGs must be similar so, by increasing the strain sensitivity difference, a better strain-temperature discrimination must be obtained [28]. By embedding a pair of FBGs into four layers of unidirectional CFRP, a new holed design has been manufactured and experimentally tested. This design has been also compared to three reference plates of different properties. In addition, the new sensor design based on drilling the plate at preset locations has been evaluated to obtain temperature-independent strain measurements using a single (but long) FBG.

#### **4.2.1.1. Holed design**

Starting from a rectangular plate of 150 mm by 30 mm, two holes of the same diameter are drilled in one side of the plate to increase its strain sensi-

tivity. These holes are symmetrically located with respect to the central axis of the plate, where the optical fiber is embedded. As the drilling diameter is increased, the strain sensitivity within the surrounding area also increases. For a given distance between holes, there is an optimum diameter that creates a practically flat deformation in the central area. However, the strain sensitivity can still be increased by enlarging the drilling diameter, but the strain profile within the FBG length may not be so flat and may deform the FBG spectral response.

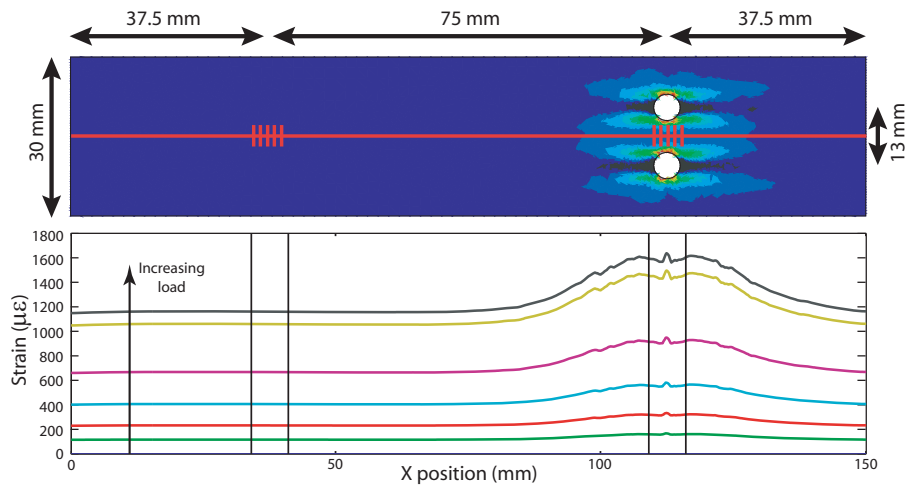


**Fig. 4.14.:** Simulated deformation of the holed design (top). Strain profile along the central axis of the piece for different loads (bottom).

In Fig. 4.14, the simulated strain profile of a holed plate with two holes of  $d = 6 \text{ mm}$  diameter separated  $D = 13 \text{ mm}$  is depicted. For the chosen hole diameter ( $d = 6 \text{ mm}$ ), the best drilling distance must be  $D \approx 13 \text{ mm}$  to obtain a flatter deformation. If the drilling distance is lower, the deformation in the central axis is driven by the section reduction caused by the holes thus, the central area is more deformed than the side areas. This effect can be observed in Fig. 4.14 (down) with the appearance of a small peak within the central area. Otherwise, when the drilling distance is higher, the strain in the central axis is driven by the combination of side effects due to stress redistribution of both holes, causing a lower strain in the central area than in the side areas.

When a flat section is required, there is a trade-off between the hole diameter and the center-to-center distance to obtain a central section deformation equal to the side deformation (driven by stress redistribution). However, if a wide

flat section is not required (e.g. by employing a short FBG), the hole diameter can be increased to achieve a greater deformation, but a deformation peak will appear at the central section. This effect can be avoided by placing the FBG slightly misaligned with respect to the holes central axis, leaving the deformation peak out of the FBG.

#### 4.2.1.2. Triangular design

In this design, the plate width is linearly decreased from one edge to the other: as the plate width decreases, its strain increases. Depending on the material properties, there is a maximum width gradient (width reduction slope) to take advantage of, given that, when the gradient is too high, the stress is not redistributed over the whole new width, so the width variation is rendered useless. Maintaining a plate length of 150 mm, a decreasing width variation from  $d_1 = 30$  mm to  $d_2 = 10$  mm has been simulated.

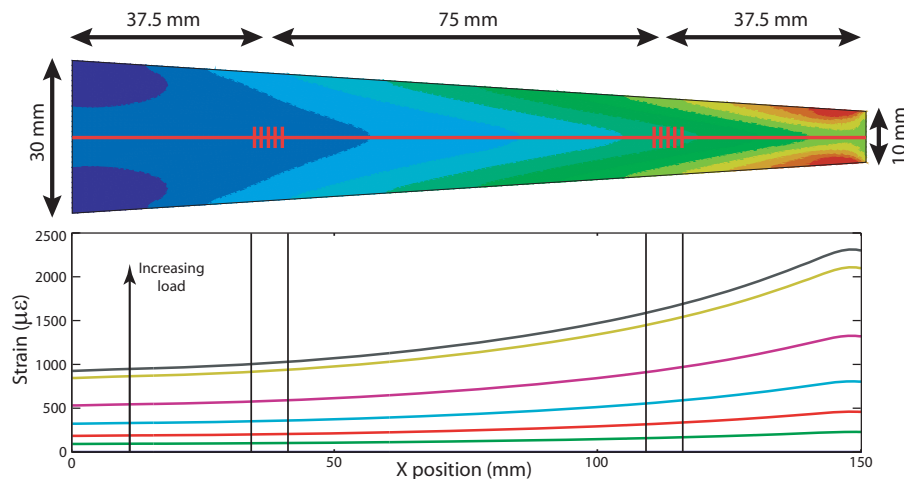


**Fig. 4.15.:** Simulated deformation of the triangular plate (top). Strain profile along the central axis of the piece for different loads (bottom).

The simulated strain distribution of the triangular plate is depicted in Fig. 4.15. When the cross section is not uniform, the applied stress has to be redistributed over the new available section, but, depending on the material properties, the stress redistribution may not follow the cross section variation, and the stress is distributed over a smaller section. In the depicted situation, the stress redistribution seems to work properly, being faster at narrower

sections and softer when the cross section increases.

The achieved strain sensitivity difference between areas (where FBGs are supposed to be located) is enough for the designing purposes ( $\Delta\epsilon \approx 40\%$  for the depicted plate), and this difference depends directly on the width difference (provided that stress redistribution works properly). However, the strain profile applied to a FBG placed in the narrow section (more deformed) is not flat, thus, when a high deformation is applied, the FBG spectrum may be deformed.

#### 4.2.1.3. Different widths (step)

The plate is divided into two sections of different widths to provoke a strain difference. The strain sensitivity variation is driven by two factors: the difference between widths and stress redistribution from the narrower section to the wider. A narrower section entails an increase in strain sensitivity; however, the stress redistribution to a wider section may result less efficient. Depending on the chosen material, the trade-off between length and width has to be trimmed to enhance the strain sensitivity difference.

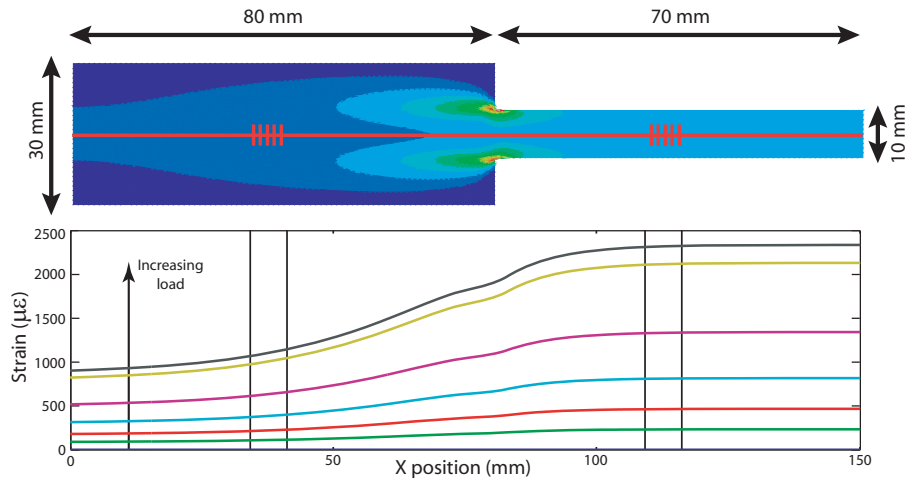


**Fig. 4.16.:** Simulated deformation of the plate with different widths (top). Strain profile along the central axis of the piece for different loads (bottom).

In Fig. 4.16, FEA simulations of a 150 mm length plate with a width reduction from  $d_1 = 30$  mm to  $d_2 = 10$  mm are depicted. Due to the constant width of the narrower section, the strain profile of this area becomes flat,

making it possible to measure higher deformations without distorting the FBG spectrum. As happens with the triangular plate, this design is also limited by the capability of the hosting material to redistributing the stress. However, since the sections of the same width are larger, the achieved strain difference becomes greater ( $\Delta\epsilon \approx 50\%$  for simulated plate). The main drawback of this design is the transition section where corners create weak points where stress becomes higher.

#### 4.2.1.4. Different widths (chamfered)

The previous design has been improved to overcome the punctual stress locations due to corners. A chamfered section has been introduced to smooth the stress redistribution, decreasing punctual stresses. This design exhibits the same benefits of the previous one: a flatter strain distribution in the narrow section and a great strain sensitivity difference (above  $\Delta\epsilon \geq 50\%$ ). A width reduction from  $d_1 = 30 \text{ mm}$  to  $d_2 = 10 \text{ mm}$  has been performed over a total length of  $L = 150 \text{ mm}$  using a chamfered section of  $L_c = 10 \text{ mm}$  length.

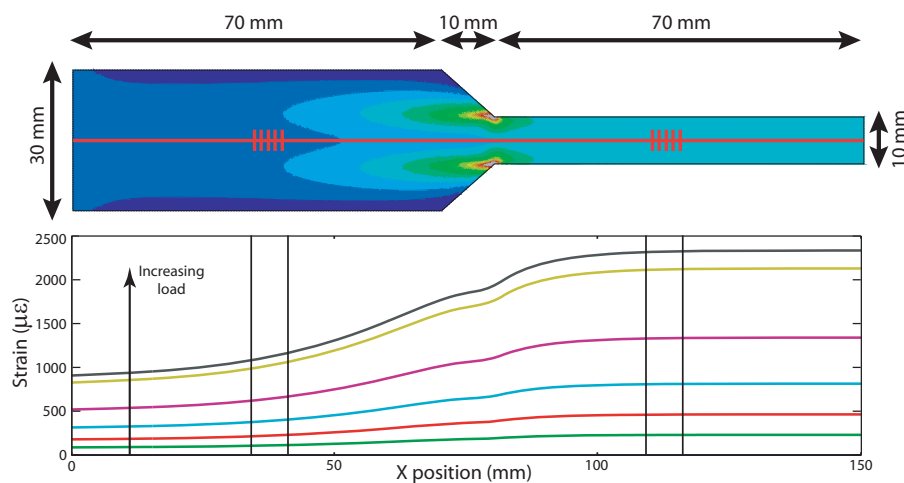


**Fig. 4.17.:** Simulated deformation of the chamfered plate (top). Strain profile along the central axis of the piece for different loads (bottom).

The results achieved for a chamfered plate are depicted in Fig. 4.17. It can be observed that the strain is spread better across the new section than in the previous design, achieving a higher strain sensitivity difference. Although there still are some punctual stress concentrations due to corners, the

absolute value is lower than in the non-chamfered design. This effect can be minimized by employing curved chamfers, but the sensitivity difference may also change. Some slight sensitivity improvement can be achieved by enlarging the chamfered section (e.g. with a length of  $L_c = 20 \text{ mm}$ , the strain sensitivity difference should be  $\Delta\epsilon \approx 53\%$ ).

All the proposed designs are based on a pair of embedded FBGs to obtain both measurands (strain and temperature) simultaneously. However, just obtaining one measurand without having cross-sensitivity error (e.g. thermal error for FBGs) may be enough. Based on the holed design, another approach using a longer FBG has also been tested to obtain strain measurements without temperature dependence by forcing two different strain sensitivities within the FBG length.

#### 4.2.2. Temperature-independent strain sensor

A single FBG of  $L = 30 \text{ mm}$  is embedded into the middle of a rectangular CFRP plate of constant thickness ( $0.5 \text{ mm}$ ). To obtain temperature-independent strain measurements, the main goal is to create two areas within the FBG length whose strain sensitivities were different (Fig. 4.18). Steeper deformation profiles can be achieved by drilling holes closer to the fiber, so two small holes are placed close to one edge of the embedded FBG, creating two flat deformation areas: one close to the hole and the other on the opposite FBG edge. This strain sensitivity difference may split the single FBG spectral peak into two. The distance between these two peaks may be proportional to the applied deformation, but not to the applied temperature.

Based on a rectangular CFRP plate of  $150 \text{ mm}$  by  $30 \text{ mm}$  of constant thickness, two small holes (of  $D = 3 \text{ mm}$ ) are performed close to a FBG edge. The area between holes exhibit a higher strain sensitivity, and, if the distance between holes and the central axis is related to their diameter, the achieved deformation profile must be flat. Since holes are closer to the fiber axis, the gradient of the strain sensitivity is greater and, consequently, the strain profile quickly evolves from higher to lower sensitivity areas. This steeper deformation profile allows the creation of two flat deformation areas at both FBG edges.

In Fig. 4.18, FEA simulations of the proposed design are depicted. Two holes of  $D = 3 \text{ mm}$  diameter separated  $d = 6.4 \text{ mm}$  and at  $dL = 5 \text{ mm}$

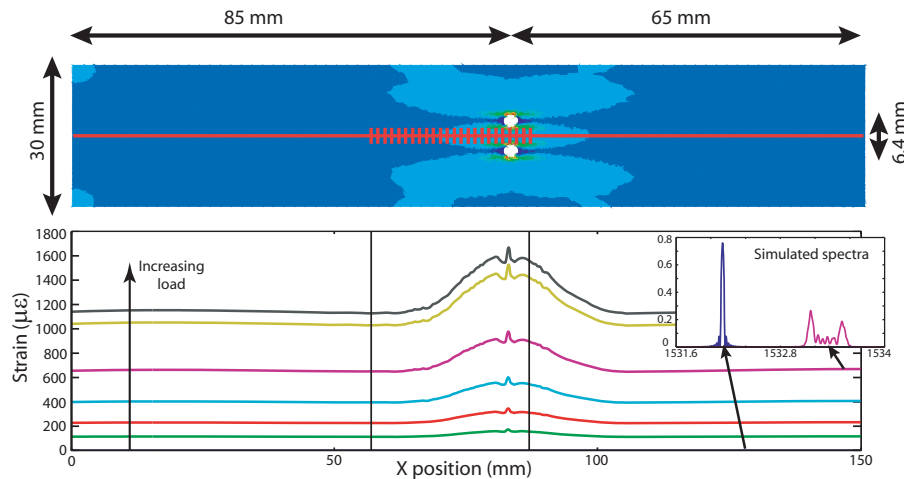


**Fig. 4.18.:** Simulated deformation of the temperature-independent strain sensor (top). Strain profile along the central axis of the piece for different loads (bottom) and their simulated FBG spectra.

distance from one FBG edge have been simulated. The strain profile applied to the FBG consists in two flat areas separated by a transition area where the strain varies quickly. The two flat areas will split the FBG spectrum into two peaks, each one proportional to each flat deformation area.

After manufacturing the plate using the same procedure explained before, two holes of 3 mm diameter have been drilled to the CFRP plate following the proposed design.

### 4.2.3. Plates manufacture

All the designed plates have been manufactured using 4 layers of HS160REM prepreg with unidirectional orientation (0-0-0-0). Optical fiber sensors have been embedded into the middle of the CFRP along the longitudinal axis of all plates. Each FBG pair consisted of two Fiber Bragg Gratings of  $L = 6 \text{ mm}$  length with a reflectivity of 70%, and have been written in a standard optical fiber separated  $D_{FBG} = 75 \text{ mm}$  using two different Bragg wavelengths. For the single FBG design, a long FBG of  $L = 30 \text{ mm}$  also written in standard optical fiber and with a reflectivity of 60% has been employed.

After cutting four layers for each desired shape, two layers of each design are placed over the curing table before embedding the FBGs. Once aligned, the optical fiber is glued to the carbon prepreg far from the FBGs to maintain

their position, having no influence on the strain distribution. Two polyimide tubes have been placed at both fiber sides to protect them at their exits from the carbon plate. The two remaining carbon layers were added before starting the curing process. Once ready, the four plates were placed in an autoclave during 60 *min* at a temperature of 130 °C with a pressure of 2 *bar*, being the vacuum bag at  $-0.5$  *bar*.

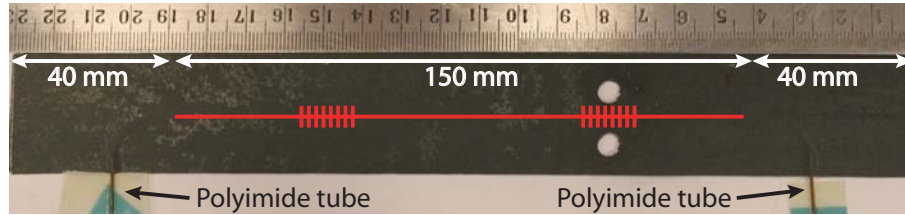


**Fig. 4.19.:** Detailed photo of the holed plate after drilling the holes. Two polyimide tubes have been added to the fiber to protect it from exiting the composite.

All the plates have been enlarged  $\delta L = 40$  *mm* on both sides to clamp the plates at the loading machine, having a total length of  $L_T = 230$  *mm*. All the plates have been manufactured with their final shape with the exception of the holed plate (Fig. 4.19), where, starting from a rectangular plate, two holes of 6 *mm* diameter have been drilled at preset locations. Strain and temperature responses of the resulting plates have been obtained and are described below.

#### 4.2.4. Experimental response

Using a commercial FBG interrogating system (Fibersensing FS2200) with an accuracy of 2 *pm*, both strain and temperature characterizations have been performed for each manufactured plate. To obtain strain sensitivities, a loading test machine (Instron mod. 5869) has been employed to apply different loading cycles keeping the plate temperature constant ( $T^\circ = 25$  °C). To obtain the thermal sensitivity, a temperature sweep from 30 °C to 70 °C has been performed without applying any load to the plates.

##### 4.2.4.1. Strain response

Five cycles reaching the same peak load have been performed for each plate. Initial cycles were performed to overcome the accommodation effect of FBG

sensors to the host material [29]. The peak load has been trimmed for each plate (from 1kN up to 3kN), maintaining the maximum deformation under  $\Delta s \leq 3000 \mu\epsilon$ , and taking into account the available clamping area of each plate. All the applied cycles have rising and falling times of  $t = 30 s$ .

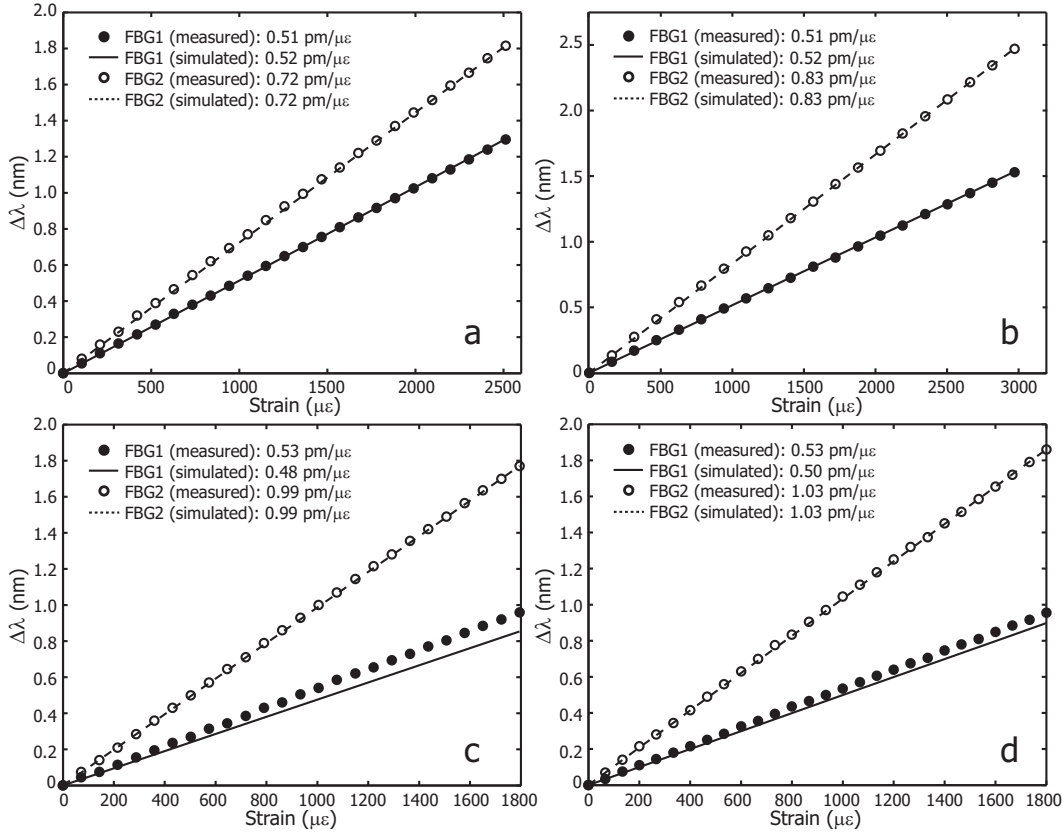


**Fig. 4.20.:** Achieved strain response of each plate is compared to simulated ones (dashed lines) of holed plate (a), triangular (b), different widths (step) (c) and different widths (chamfered) (d).

In Fig. 4.20, the achieved strain response of each plate is compared to FEA simulations. All the achieved results agree remarkably well with their simulated response, having a sensitivity around  $\kappa_\epsilon \approx 0.5 pm/\mu\epsilon$  for wider sections, what corresponds to less sensitive FBGs. Due to the drilling process, a slight imbalance has been produced in the holed plate (both holes are displaced 0.5 mm off-axis, but their relative distance has been maintained). This imbalance has been added to the FEA model to perform the simulation depicted in Fig. 4.20 (a).

Due to the clamping system of the testing machine, a lower plate area has

been clamped (25 mm of the total width of 30 mm), having no influence to the strain response of the holed and triangular designs, although it may introduce some errors in plates based on different widths. In addition to other factors, designs based on different widths have some punctual stress concentrations due to the width reduction that may damage the plate under load. This damage is more critical for these designs because strain redistribution is highly dependent on passing through high stress transition areas.

The temperature-independent strain sensor based on a single FBG has been tested using the same procedure. Once drilled, the plate has been clamped to the testing machine (Instron mod. 5869) to perform 5 loading cycles (with rising and falling times of  $t = 30$  s), reaching a peak load of 3 kN. During the loading test, the FBG has been interrogated using a commercial system (Fibersensing FS2200), recording the FBG spectra. In Fig. 4.21, the FBG spectra measured for 4 different loads are depicted.

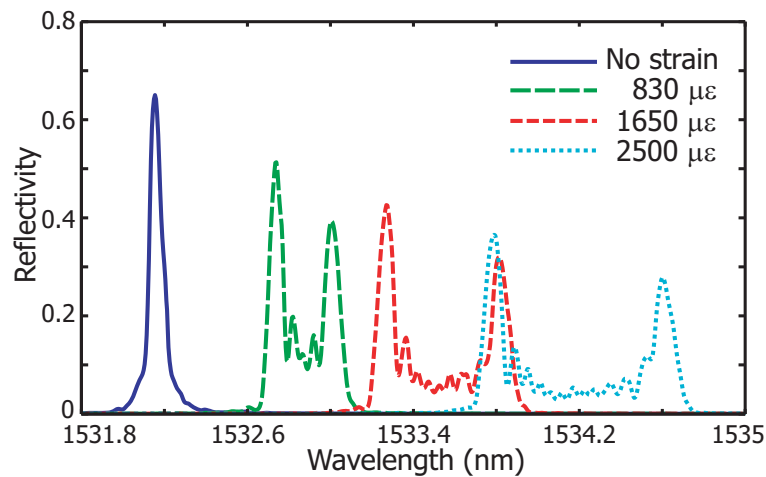


**Fig. 4.21.:** Measured FBG spectra of the manufactured plate under four different loads. Peak distance is proportional to the applied load.

When no load is applied to the plate, the FBG spectrum keeps its original shape (single peak), but, when the load is increased, the single FBG peak splits into two, each one corresponding to both flat deformation areas. The lower peak is more defined because its corresponding area (far from holes) is flatter than the area close to the holes (that provoke the other peak). The distance between the two spectral peaks is proportional to the applied strain. This structure can be understood as two FBGs with different strain sensitivities

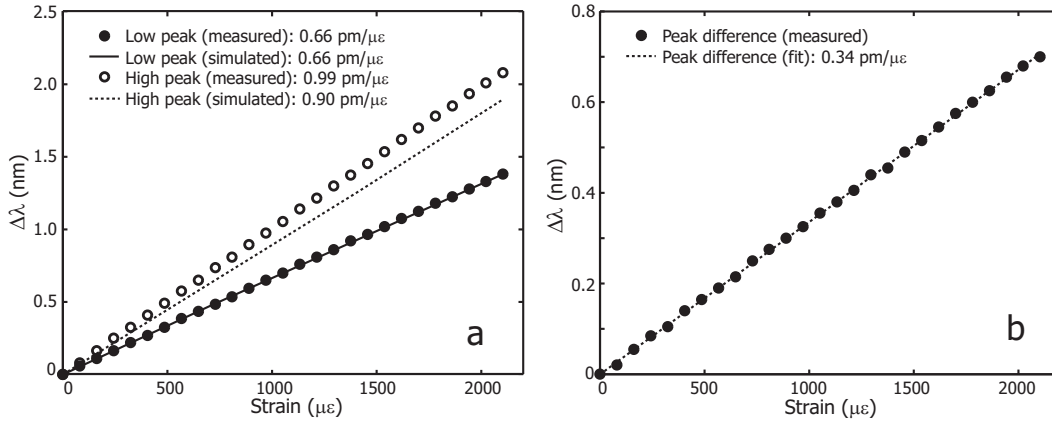


**Fig. 4.22.:** Measured (dots) and simulated (line) peak wavelength drift (a) and their relative distance (b).

sharing the same Bragg wavelength thus, their peak distance is proportional to their strain sensitivity difference.

From simulated deformation profiles, FBG spectra are computed using the T-matrix method for each different load. The peak distance of both measured and simulated spectra are detected and their distance is compared in Fig. 4.22. The simulated results have been scaled to the lower peak sensitivity. The experimental results exhibit a higher strain difference than the simulated model ( $\Delta\kappa_{\epsilon_m} \approx 0.34 \text{ pm}/\mu\epsilon$  against  $\Delta\kappa_{\epsilon_s} \approx 0.24 \text{ pm}/\mu\epsilon$ ). However, the expected peak splitting is reproduced. This plate has been manufactured using a non re-coated FBG so, the surrounding carbon sheets are closer to the optical fiber, having a smaller gap to be filled with epoxy resin. A lower epoxy resin concentration surrounding the optical fiber allows a better deformation transference from the carbon sheets and, consequently, steeper deformation profiles are achieved.

#### 4.2.4.2. Temperature response

After obtaining the strain sensitivity of all plates, their thermal response have been characterized by applying a temperature sweep (35 °C to 70 °C) to each plate without applying any load. During the sweep, spectra of both FBGs of each plate have been analyzed using the Fibersensing unit. The achieved

wavelength drifts are depicted below.

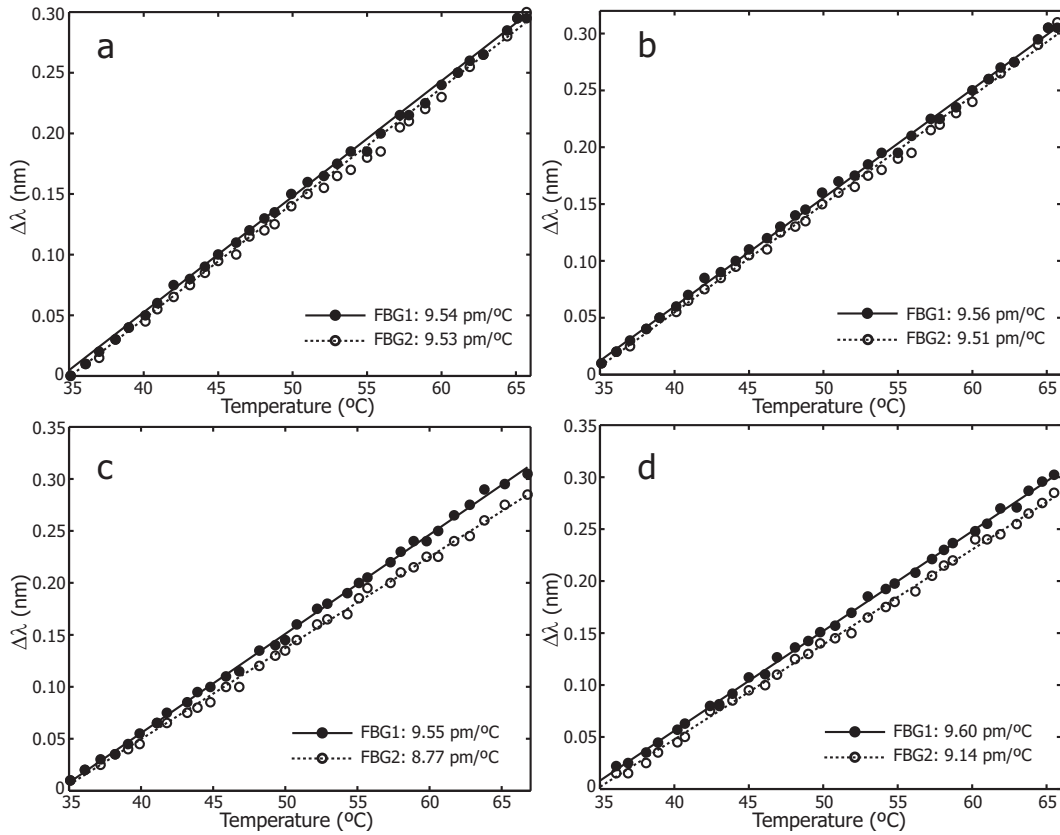


**Fig. 4.23.:** The achieved temperature response of each plate is depicted against its linear fit (dashed lines) of holed plate (a), triangular (b), different widths (c) and chamfered (d).

The achieved thermal response is shown in Fig. 4.23. Since all the plates have been manufactured using the same host material, their thermal sensitivities are practically equal ( $\kappa_T \approx 9.5 \text{ pm}/^\circ\text{C}$ ). There are some slight differences due to the manufacture process such as FBG re-coating acrylate or slight fiber misalignment with the Uni-Directional (UD) carbon fiber. However, FBGs placed on narrower sections of plates of different widths (with higher strain sensitivity) exhibit a lower thermal sensitivity because the surrounding CFRP has a lower epoxy resin ratio. This lack of resin is mainly caused by a width reduction in the carbon plate, what makes it easier for the resin to leak during the curing process (a re-coated FBG of  $250 \mu\text{m}$  is embedded into a  $500 \mu\text{m}$  thickness composite of  $10 \text{ mm}$  width).

The thermal response of the single FBG sensor has been obtained using

the same procedure. The plate has been subjected to a temperature sweep (35 °C to 70 °C) to obtain its thermal sensitivity. As shown in Fig. 4.23, the plates manufactured with a homogeneous shape, where the mechanizing process has been performed after curing the composite (e.g. holed design), exhibit a uniform thermal sensitivity (the ratio between carbon fiber and epoxy resin is maintained). The achieved temperature sensitivity ( $\kappa_T = 8.84 \text{ pm}/^\circ\text{C}$ ) seems to be lower than the obtained with re-coated FBGs ( $\kappa_{T_R} \approx 9.50 \text{ pm}/^\circ\text{C}$ ), that suggests a lower epoxy resin concentration surrounding the optical fiber.

#### 4.2.5. Error analysis

The proposed design based on a FBG pair exhibits different sensitivities to strain. In this regard, it is possible to obtain both measurands simultaneously from the wavelengths of each FBG pair [27]. Knowing the strain and temperature variations and having the sensitivities of both parameters, the Bragg wavelength of each FBG is given by:

$$\begin{bmatrix} \Delta\lambda_1 \\ \Delta\lambda_2 \end{bmatrix} = \begin{bmatrix} \kappa_{T_1} & \kappa_{\epsilon_1} \\ \kappa_{T_2} & \kappa_{\epsilon_2} \end{bmatrix} \begin{bmatrix} \Delta T \\ \Delta\epsilon \end{bmatrix} \quad (4.5)$$

being  $\kappa_\epsilon$  and  $\kappa_T$ , the strain and temperature sensitivities of each FBG of a pair, thus, by obtaining the inverse matrix of the relation, both measurands can be obtained from the Bragg wavelengths (Eq.4.6):

$$\begin{bmatrix} \Delta T \\ \Delta\epsilon \end{bmatrix} = \frac{1}{D} \begin{bmatrix} \kappa_{\epsilon_2} & -\kappa_{\epsilon_1} \\ -\kappa_{T_2} & \kappa_{T_1} \end{bmatrix} \begin{bmatrix} \Delta\lambda_1 \\ \Delta\lambda_2 \end{bmatrix} \quad (4.6)$$

where  $D = \kappa_{\epsilon_2}\kappa_{T_1} - \kappa_{\epsilon_1}\kappa_{T_2}$  is the matrix determinant. The stability of this method can be evaluated employing this determinant [28]: the higher its value, the more accurate are the results. Since the strain sensitivities of each FBG pair are different, the determinant of each FBG pair must be non-zero, and the achieved errors depend on the difference of the strain sensitivities.

In Fig. 4.24, the achieved resolution of all the plates is depicted. Each graph is obtained by varying one measurand while the other was fixed. For each plate, the applied sweeps (strain and temperature) are depicted (solid lines) against the computed variations using wavelength drifts (dots). As the

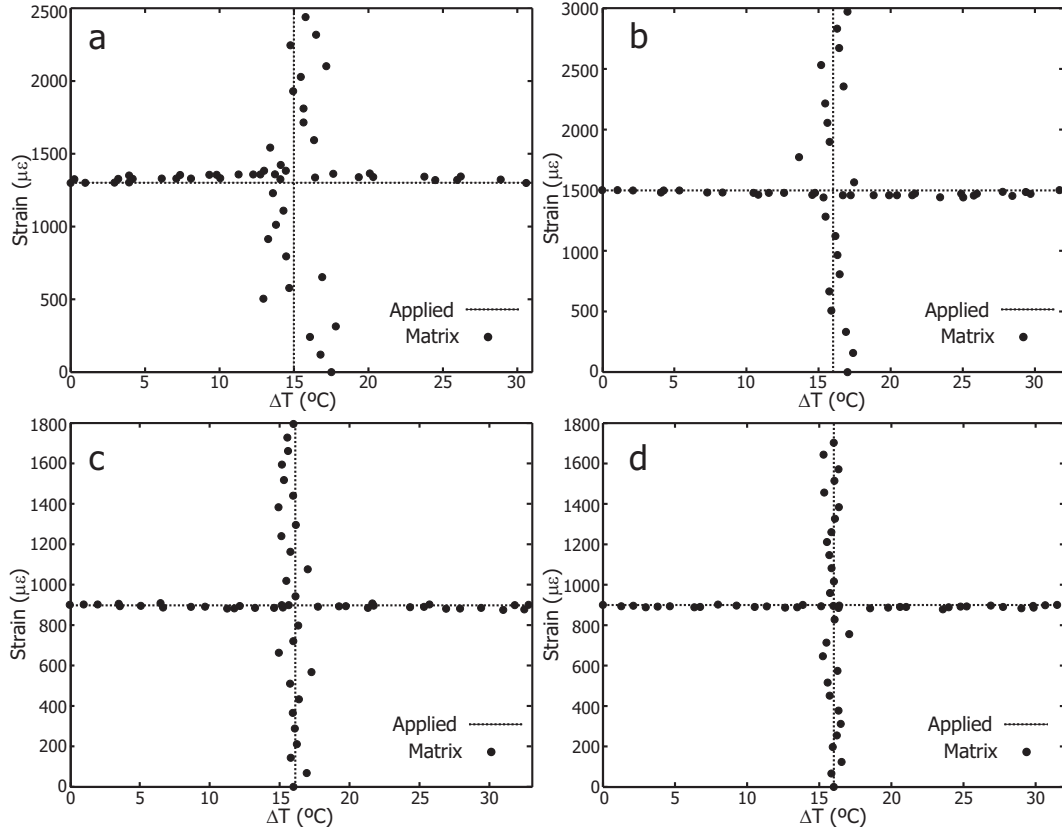


**Fig. 4.24.:** Resolution of the four designs: holed plate (a), triangular (b), different widths (step) (c) and different widths (chamfered) (d) under a strain ramp at constant temperature and under a temperature sweep at constant load.

strain sensitivity of each FBG pair increases, the computed results improve. A table summarizing the obtained parameters is shown below:

The error of the single FBG approach has been also analyzed. Since both peaks have the same thermal sensitivity ( $\kappa_T = 8.84 \text{ pm}/^\circ\text{C}$ ) and the strain is proportional to their distance ( $\Delta\kappa_{\epsilon_P} \approx 0.34 \text{ pm}/\mu\epsilon$ ); the Matrix equation detailed in Eq.4.6 (considering each peak as an independent FBG) can be simplified for the strain value as:

$$\Delta\epsilon = \frac{1}{\kappa_T \cdot (\kappa_{\epsilon_{P2}} - \kappa_{\epsilon_{P1}})} \cdot \kappa_T \cdot [\Delta\lambda_{P2} - \Delta\lambda_{P1}] = \frac{1}{\Delta\kappa_{\epsilon_P}} \cdot \Delta\lambda_P, \quad (4.7)$$

where  $\Delta\lambda_P$  is the peak distance and  $\Delta\kappa_{\epsilon_P}$  the difference of strain sensitivities.

In Fig. 4.25 (a), the temperature values calculated using the matrix equation are compared to the applied temperature while a deformation sweep was

	Holed	Triangular	Step	Chamfered
Strain $FBG_1$ ( $\kappa_{\epsilon_1}$ ) ( $pm/\mu\epsilon$ )	0.51	0.51	0.53	0.53
Strain $FBG_2$ ( $\kappa_{\epsilon_2}$ ) ( $pm/\mu\epsilon$ )	0.72	0.83	0.99	1.03
Temp. $FBG_1$ ( $\kappa_{T_1}$ ) ( $pm/^\circ C$ )	9.54	9.56	9.55	9.60
Temp. $FBG_2$ ( $\kappa_{T_2}$ ) ( $pm/^\circ C$ )	9.53	9.51	8.77	9.14
Mean strain error ( $\mu\epsilon$ )	38.0	26.5	9.3	8.0
Mean temp. error ( $^\circ C$ )	2.19	0.97	0.49	0.32

**Table 4.1.:** Experimental sensitivities and errors of the tested designs.

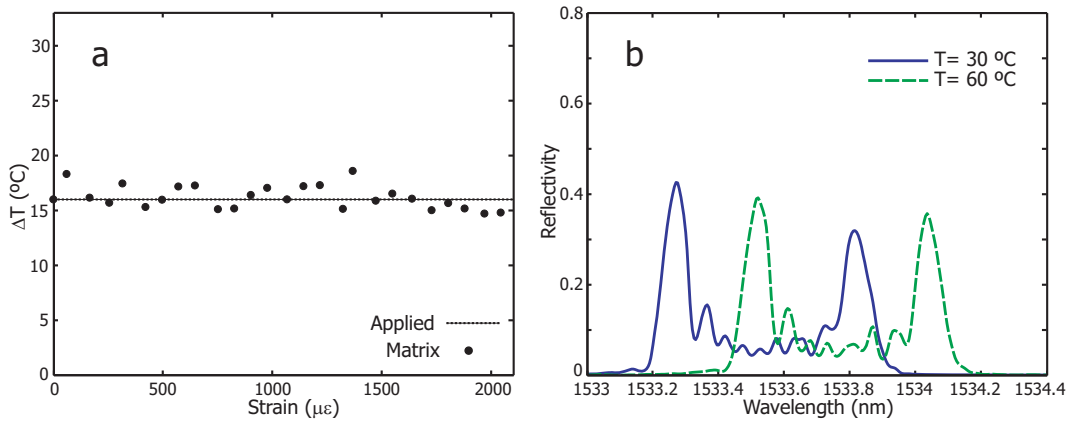


**Fig. 4.25.:** Calculated values (dots) are compared to the temperature during the strain sweep (a). Two FBG spectra under same load ( $\Delta s \approx 1600 \mu\epsilon$ ) but at different temperature (b).

performed. The mean temperature error is  $\overline{\Delta T} \approx 0.81 \text{ }^\circ C$ , with a maximum drift of  $\Delta T \approx 2.60 \text{ }^\circ C$  under a strain sweep of up to  $\Delta s \approx 2200 \mu\epsilon$ . In Fig. 4.25 (b) two measured FBG spectra corresponding to two different temperatures ( $T_1 = 30 \text{ }^\circ C$  and  $T_2 = 60 \text{ }^\circ C$ ) under the same loading condition ( $\Delta s \approx 1600 \mu\epsilon$ ) are depicted. The peak distance is proportional to the applied deformation but their offset position is modified by the temperature, so just the temperature values are affected by the error, not exhibiting error in the strain discrimination.

All the tested plates have been designed to be easy to manufacture so, based on the same composite material (CFRP) and using the same thickness ( $0.5 \text{ mm}$ ), their 2-dimensional shapes have been modified to achieve different strain sensitivities on their embedded FBGs. The achieved results show the capability to obtain both measurands (strain and temperature) using the

wavelength drift of each FBG pair, although the measured error of the tested plates is different. The best results have been obtained employing two sections of different widths, where both FBGs have been embedded, but this approach requires the narrowing of one side of the sensing head, making its installation more difficult. The holed design has a lower sensitivity difference to strain (and a higher error); however, the structure is symmetrical what makes its installation process easier. In addition, this design can be improved by enlarging the holes and displacing them from the FBG center (avoiding the middle strain peak).

All the proposed designs agree remarkably well with the simulated models. Although the holed design shows a lower strain sensitivity difference than the other tested plates, it exhibits some advantages in the temperature response. All the tested designs are based on the same manufacturing process, same material and thickness, but there are still some differences that makes the holed design able to obtain temperature-independent strain measurements.

In order to simplify the manufacturing process, reference designs (triangular and with different widths) have been cut before curing. On the contrary, for holed plates, it is easier to drill the holes after curing. Although the curing process has been performed under the same pressure and temperature conditions, the resulting amount of epoxy resin surrounding the optical fiber was not the same. For designs where a narrower section is required (e.g. different widths), the resin leak is more relevant due to the chosen dimensions and materials; leaving less resin surrounding the optical fiber. This situation is noticed by a lower thermal sensitivity at narrower sections and it complicates the temperature-independent strain measurements. On the other hand, the holes have been drilled after the curing process so, the surrounding epoxy resin was maintained, achieving the same thermal sensitivity along the plate. Although the achieved difference of strain sensitivity for the holed plate is lower in comparison to reference designs, its uniform thermal sensitivity partially compensates the lack of strain sensitivity, achieving a relatively good strain discrimination. However, a higher difference between temperature sensitivities is required to improve the temperature discrimination.

In addition, a uniform temperature sensitivity makes it possible to perform temperature independent strain measurements by embedding a single FBG

into a carbon plate. Two small holes are drilled in the plate to force the FBG spectrum to split into two peaks, whose difference is proportional to deformation. This configuration exhibited an error-free strain discrimination without temperature cross-sensitivity.

#### **4.2.6. Summary**

Using CFRP as host material, several sensing heads for strain-temperature discrimination based on embedding Fiber Bragg Gratings into composite plates have been designed and experimentally tested. The most interesting design relies on drilling two symmetrical holes to provoke different strain sensitivities to embedded FBGs, and it has been compared to three reference composite designs. The achieved results agree remarkably well with their simulated response, making it possible to obtain both measurands (strain and temperature) simultaneously. Besides, due to the uniform temperature sensitivity of the proposed design, a temperature-independent strain sensor has been also manufactured and tested. By creating a non-uniform strain profile on an embedded long FBG, its spectral peak has been split into two, being its distance proportional to plate deformation. Since the characteristics of the proposed designs are given by their shape, the employed hosting material can be changed to fit the desired application.

### **4.3. Embedded transducers for laminated composites**

Although FBGs have been widely employed in structural monitoring, with the growing of composite materials new features can be studied using OFS techniques. Composite structures have a complex behavior that can be evaluated from their initial manufacture steps [16, 30] to their final application [31]. However, with the widespread use of these technologies, new monitoring requirements have appeared. More complex artifacts such as evaluating crack growing [32–34] or to monitor debonding processes [35] are examples of how OFSs (and particularly FBGs) can guide these new materials and structures to a better performance.

Because all these sensing solutions are usually originated in laboratory environments [36], sometimes their final application scenario can be slightly neglected [25]. This is why the integration of OFSs into composites becomes such an important issue: having a perfectly integrated sensing system into the host structure without structural influence improves both performances. The sensor system is protected and can operate under harsh environments showing no influence to the host structure and it provides very valuable information that can be employed to improve the structure [37–39].

Both aspects related to new composite materials are addressed in this section: sensing of new features and field implementations of FBG based sensors. First of all, a new bonding sensor for composite material manufacturing based on a single uniform Fiber Bragg Grating (FBG) is proposed and demonstrated. The sensor design includes two edge sections attached to the bonded parts and a central strain free region, all made of an epoxy resin block of constant thickness, where the FBG is embedded. The quality of this bond is quantified by measuring the FBG spectral evolution.

Regarding the curing process of composite materials, an optical fiber sensor for monitoring the compaction pressure of a composite material during the molding process is described next. The sensor is based on a Fiber Bragg Grating embedded into a composite material, and it is able to measure the compaction pressure during the manufacturing process and the strain information while the structure is in operation. Although this sensor is embedded into a composite material and it is able to obtain strain measurements after the embodiment, another specific strain sensor has also been developed during this work.

Based on a single FBG, a resin block is built surrounding the optical fiber, protecting it from external damages. This block comprises two reinforcements that limit the transverse axis pressure that can damage and even break the optical fiber. The proposed sensor is oriented to be embedded into large composite structures such as wind turbine blades or vessels hulls, where high compaction pressure is employed to obtain high performance materials.

Finally, two application examples of FBG based transducers are described. The first one is related to pre-stressed concrete beams where a quasi-distributed transducer has been embedded during the concrete curing to evaluate how the

beam relaxation evolves after its release. The second example is devoted to a wind turbine blade instrumentation using surface glued FBG patches to monitor its deformation during different loading tests.

### **4.3.1. Bonding transducer**

The manufacture process of complex structures implies bonding stages in several industries. In particular for composite materials, the bonding stages are widely used to assemble different parts to get the whole structure or to attach some external elements such as metallic fixing points. These joints are usually built blindly, e.g. having no means to check the quality during the process. However, in the growing industry of composite materials, optical fiber sensors have been widely reported to evaluate the status of a structure even during its manufacturing process [15, 17]. In particular, FBGs have been applied to detect delamination growth and the direction of the growing process with chirped FBGs [34], or to quantify the damage induced into a composite structure with a full-spectrum interrogation technique [19]. Repaired composite pieces have also been monitored with FBGs to analyze the quality of the process by measuring the FBG spectral shape [18] under load conditions. Some external non-destructive evaluation techniques have been reported to be able to check the bonding quality such as ultrasonics or thermography [40]. Composite joints have also been monitored with chirped FBGs embedded into the bonding area to quantify the disbond status and direction by measuring the spectral width reduction of the chirped FBG [41]. However, this approach requires a large spectral bandwidth (around 20 nm) and, therefore, it limits the possibility of sensor multiplexing. Another work also gets the deformation profile from the reflected spectrum of a uniform FBG using complex algorithms. In [8], a Genetic algorithm is employed to obtain the polynomial coefficients of a modeled chirp effect that reproduces the FBG deformation. This is a very good approach when the obtained deformation can be previously modeled, but it works worse with unexpected deformations.

Based on a single uniform FBG, a new sensing head to evaluate the quality of a joint has been built and tested during this work. The transducer has been designed to be placed during the bonding process in contact with the two parts, causing a heterogeneous deformation in the FBG. Some scenarios

have been studied to detect a different deformation of each bonded piece and the relative displacement between the pieces. The FBG response has been simulated with the Transfer matrix method in order to determine the main characteristics of the reflecting spectrum under these different situations.

#### 4.3.1.1. Sensor design

The sensing head has been conceived to be embedded in a bonding joint: one side attached to one of the bonded parts and the other side to the opposite one. The central section of the sensor is not bonded to any surface, trying to get the relative displacement between the bonded parts. The sensor is based on a uniform FBG embedded into an epoxy resin block of constant thickness. The “quality” of the joint can be determined from the strain in the longitudinal axis of the sensor and, consequently, from the FBG spectrum. The sensor should exhibit a minimum intrusion and its size and thickness are critical to prevent a joint malfunction. As shown in Fig. 4.26, the central part of the sensor is modified by performing two symmetrical holes near the optical fiber axis to get a higher deformation in this area for the same load.

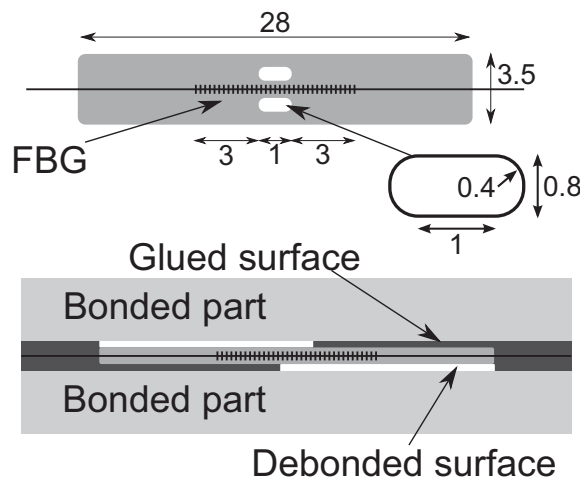


**Fig. 4.26.:** Sensor illustration (top) and installation scheme (bottom). Dimensions are in millimeters

With the proposed scheme, three sections are defined in the FBG: one central section to measure the relative slide between the two bonded parts and two side sections bonded to the different parts to get their deformation. When

the joint is working properly, the longitudinal axis deformation of the sensor is homogeneous along the three FBG sections, thus obtaining a clear FBG response. On the contrary, when one of the bonded parts has a higher or lower deformation or a slide between them takes place, the spectral evolution of the FBG varies. The central shape is modified to increase the sensitivity of the sensor to slides between the two bonded parts. An installation scheme is shown in Fig. 4.26, where different sides of the sensor are glued to different bonded parts, leaving the central section unbounded.

#### 4.3.1.2. Simulations

The mechanical deformation studies have been performed with Finite Element Analysis (FEA) [42]. The goal is to get the relation between the sensor deformation over the longitudinal axis at the different working situations. The obtained deformation profile evaluated at the FBG inner position is also optically simulated with the Transfer Matrix (T-Matrix) method in an attempt to simplify the optical simulation model into three constant deformation sections (one central and two sides) obtaining an easier-to-use sensor model.

#### Mechanical response: Finite Elements Analysis

A simplified sensor model is developed by using the stress analysis suite of Autodesk Inventor (Autodesk Inc). Making highly reliable FEA models of heterogeneous pieces with absolute results can be a very complicated issue, but the generation of a qualitative deformation profile can be usually done by means of a simplified model. Within this scenario, the obtaining of this qualitative profile allows to reduce the complexity of the optical model.

The first step is to study the isolated sensor behavior to validate the initial hypotheses. The pierced central part of the sensor exhibits a higher sensitivity against longitudinal axis deformations, as shown in Fig. 4.27. The model is based on a constant thickness (0.8 mm) resin block where an optical fiber is embedded into the longitudinal axis. The employed FBG is 7 mm length, so the total length of the modeled block is reduced to 10 mm to improve the computation time. The remaining dimensions are shown in Fig. 4.26.

By examining the obtained deformation profile over the longitudinal axis, it can be observed that the central section is more sensitive to strain, but

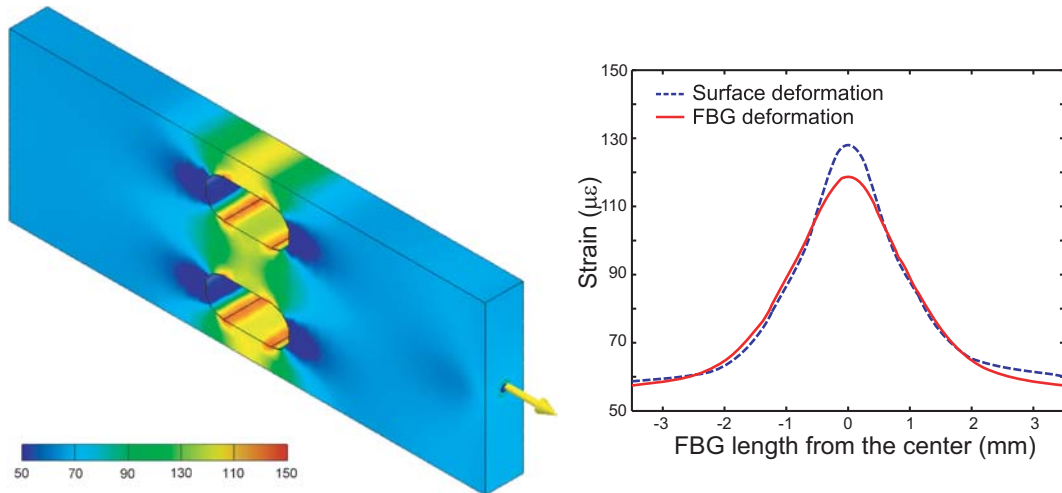


**Fig. 4.27.:** Graphic illustration of the simulated sensor (right) and its longitudinal axis deformation (left).

the transition to the other sections is very smooth. The relation between the inner and outer deformation is very linear despite the different mechanical properties of epoxy resin and silica (Young's modulus was set to 3.5 GPa for epoxy resin and 73 GPa for optical fiber silica). This model does not replicate a real working situation because the simulated sensor is deformed just having into account its own shape. Under real conditions, the deformation along the longitudinal axis of the sensor is mainly driven by the glued sections, so the transition between different sections should be more abrupt. A more realistic situation is presented below: the sensor is just fixed by one side to each part of the joint (as shown in Fig. 4.26) leaving the central section unbounded. The simulation replicates the stretching of one of the “bonded” parts while the other is compressed.

In the proposed case, the bonding interfaces cause a very abrupt deformation on the sensor surface, being smoother in the inner optical fiber. Viewing the longitudinal axis deformation profile, the central section can be established between the two abrupt peaks to get a simpler optical model to fit the problem. There is no clear limit to establish the central section length (it may depend on the deformation situation), but it must always lie within the central holes length: 1.8 mm. These holes have a central area of 1 mm with a constant width of 0.8 mm so, for the simplified model, the central section length is set to 1 mm. With this assumption the final model has three sections: a central

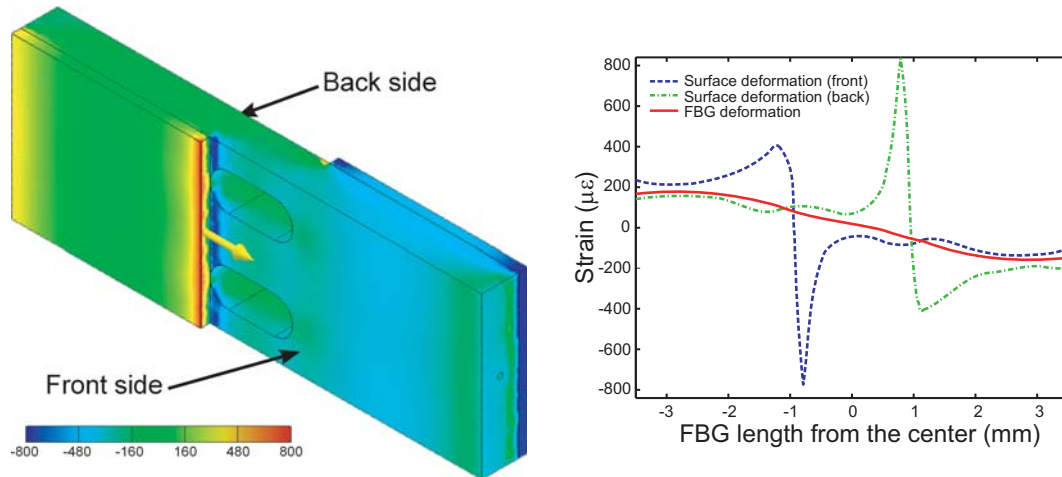


**Fig. 4.28.:** Graphic illustration of the simulated sensor (right) and its longitudinal axis deformation (left)

one of 1 mm length and two side sections of 3 mm length.

### Optical response: Transfer Matrix Method

With the proposed sensor, three main deformation cases are considered: a homogeneous longitudinal axial deformation of the whole sensor (a correct working joint), asymmetrical deformation of the different bonded parts (the side sections of the sensor with different deformations) and the relative slide of the two bonded parts (the central section of the sensor with a different deformation).

The optical simulations are performed with the Transfer Matrix method [43]. In this method, the FBG length ( $L$ ) is divided into  $N$  sections ( $L = \sum_{j=1}^N \delta l_j$ ). The output fields of a section ( $\delta l$ ) are calculated assuming the section as homogeneous. The FBG may be considered as a four-port device, where the transfer matrix  $T$  represents the grating amplitude and the phase response, so the reflected amplitude ( $\rho$ ) is given by:

$$\rho = \frac{T_{21}}{T_{11}}, \text{ being } T = \prod_{j=1}^N [T^j].$$

The lower limit of the number of sections ( $N$ ) is determined by the required accuracy. For uniform gratings the number of sections can be set to  $N = 1$ , but in heterogeneous situations the number of sections has to be increased to fit the chirp, apodization or deformation patterns. The upper limit of the

number of sections is determined by the section length ( $\delta l \ll \Lambda$ ) because the employed coupled-mode-theory approximations are not valid when the section length is only a few grating periods long [44]. For most cases, setting the number of sections  $N \approx 100$  is enough to get accurate results.

The T-Matrix method is employed to evaluate the mechanical approximation made with FEA simulations. The aim is to reduce the number of sections from  $N \approx 100$  sections to  $N = 3$  to analyze the sensor behavior in the most relevant situations: different deformation of each bonded part and relative slide between the bonded parts. Taking the second modeled case, the longitudinal axis deformation is rounded to  $N = 100$  quasi-uniform FBG sections of  $\delta l \approx 70\mu m$ , thus obtaining an integer number of grating periods ( $\delta l_j = 132 \times \Lambda$ ) to have a transition between sections without phase changes. The discretized deformation profile of  $N = 100$  sections is applied to the T-Matrix simulation and compared to the  $N = 3$  sections approximated profile with a central section of  $\delta l_c = 1mm$ .

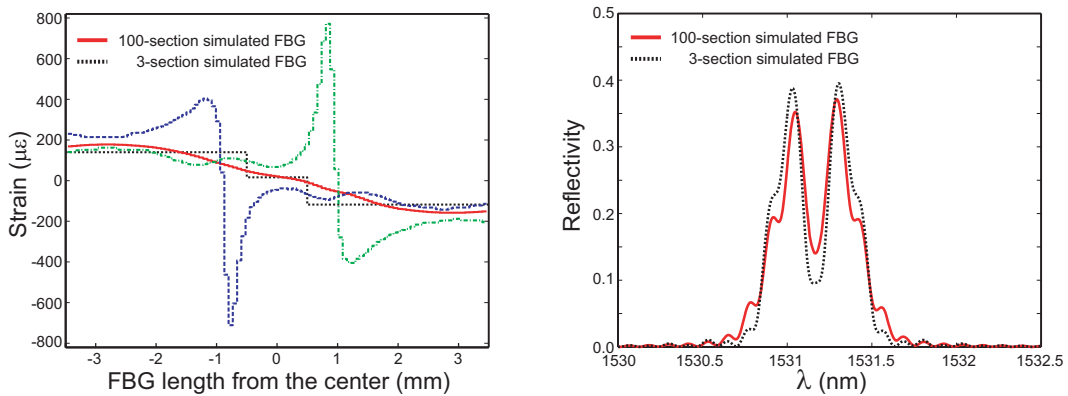


**Fig. 4.29.:** *Approximated longitudinal axis deformation on the front (dashed line) and back (dot-dashed line) surfaces and in the optical fiber (solid line) against the 3-section approximated deformation (dotted line) (left). Spectrum obtained with the 100-sections model (solid line) against the 3-section model (dotted line) (right).*

In Fig. 4.29, the 100-section approximated deformation profile of the inner optical fiber is approximated by a 3-section model with a central section of  $\delta l_c = 1mm$  and two side sections of  $\delta l_s = 3mm$ . For this case, one of the bonded parts is stretched and the other bonded part is compressed leaving the central section almost undeformed (replicating a case where there is no relative displacement between the bonded parts). This difference between the

two bonded parts deformation causes a splitting of the main FBG peak into two separated peaks, as shown in Fig. 4.29. Despite this difference between the 3 and 100 sections models, the main expected spectral effect (peak splitting) is reproduced in a similar way, thus validating the proposed approach.

Once the simplified model has been established (central section of 1 mm and two sides sections of 3 mm), a few longitudinal axis deformation profiles are studied replicating the most typical situations: equal and different deformations of the two bonded parts and/or a slide between the bonded parts.

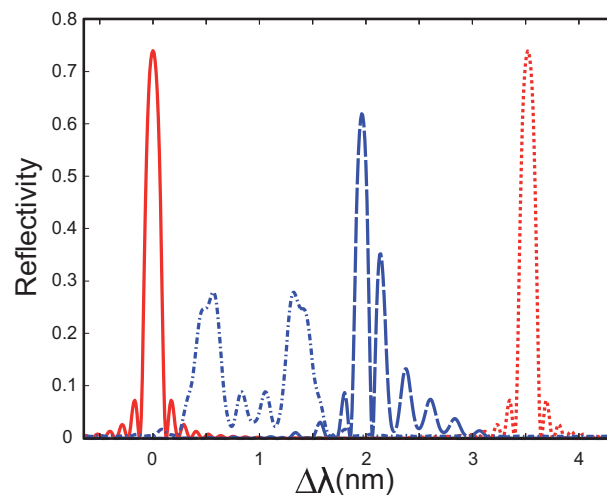


**Fig. 4.30.:** Simulations of the three typical cases: No deformation (solid line); higher deformation in one side with relative slide between them (dash-dotted line); relative slide between the two parts (dashed line); homogeneous deformation (dotted line).

In Fig. 4.30, the main spectral deformations associated with the typical cases are shown. When the joint is working properly, the two bonded parts have the same deformation and their relative position is fixed. This situation causes a constant deformation along the the FBG, maintaining its spectral shape. When one of the bonding parts is more deformed than the other, one of the side sections ( $\delta l_s = 3mm$ ) is also more deformed than the other, causing a peak splitting in the FBG response. If the relative slide has the mean deformation value of both parts, the two split peaks will show the same reflectivity but, if the relative slide is closer to one side deformation, the corresponding peak will be higher than the other. Finally, the relative slide mainly causes a central section deformation ( $\delta l_c = 1mm$ ), provoking a chirping effect over the uniform FBG. The resulting spectrum exhibits more secondary lobes due

to the chirp effect and a wide and low offset response corresponding to the central section deformation.

With the simplified spectral repercussion of the proposed cases (asymmetrical deformation and relative slide of different bonded parts), more complex situations with a combination of both cases can be detected with a simple spectral shape analysis, at least in a qualitative way.

#### **4.3.1.3. Experiments**

A proof-of-concept sensor has been manufactured and installed in a flexible setup that recreates a bonded joint. Different deformation profiles have been applied to the sensor in an attempt to evaluate its spectral response.

##### **Sensor manufacture**

The sensor is based on a uniform epoxy resin block of 0.8 mm constant thickness with a 7 mm length FBG embedded. The FBG is written in a standard telecommunication optical fiber using the phase mask technique with a continuous laser emitting at 244 nm. To build the resin block, the FBG is aligned with a nonstick mold with the desired shape. Once the FBG is placed into the mold, a low viscosity epoxy resin is poured into it. To build the nonstick mold, a male mold is mechanized with the desired shape in PMMA using a Computer Numerical Control (CNC) cutting machine. This male mold is covered with nonstick silicone, creating the holding mold for the epoxy resin. After the resin is poured, a vacuum stage follows to guarantee the homogeneity of the final block by removing the air bubbles. The epoxy resin is thermally cured for a few hours to obtain the final sensor.

When the sensor is cured, demoulding products are applied to the sensor surface to prevent the bonding of unwanted areas during installation. In this case, polyvinyl alcohol is applied to the opposite half sides of the sensor and to the holes in the middle of the sensor to determine the surface to be glued.

##### **Sensor testing**

The sensor of the Fig.4.31 is installed in a mechanical setup which replicates the behavior of a bonding joint. One side of the sensor is glued to a plastic piece (PMMA) and the other side to another one. These pieces work as the different



**Fig. 4.31.:** *Manufactured sensor previous to its installation. The left side of the sensor is covered with polyvinyl alcohol to prevent bonding of the section.*

bonded parts in a real joint. The central section of the sensor remains unglued to get the relative displacement between the two plastic pieces (bonded parts).

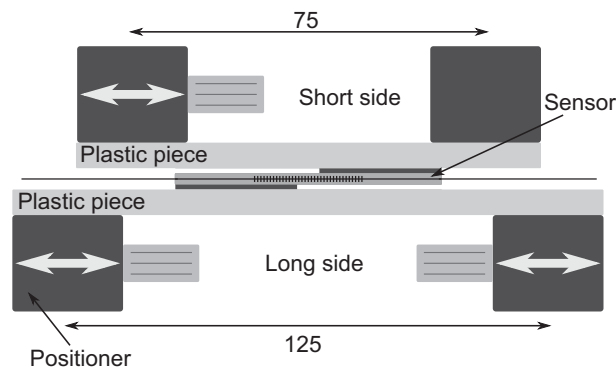


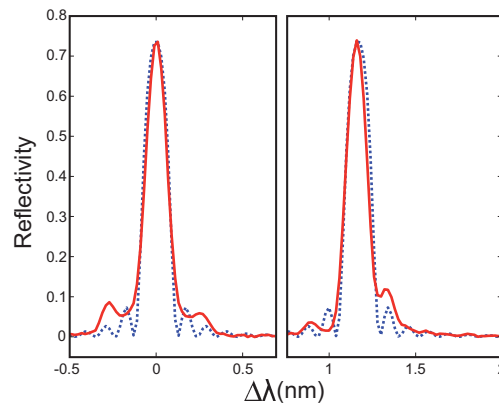
**Fig. 4.32.:** *Experimental setup used for replicating the joint working conditions. The sensor is bonded to two plastic pieces fixed to three positioners. Dimensions are in millimeters.*

The two plastic pieces with the glued sensor are fixed to three positioners as shown in Fig. 4.32. One side of the *short* plastic piece (75 mm) is fixed to a static holder and the other to a positioner. The two sides of the *long* plastic piece (125 mm) are fixed to both positioners. With the three positioners of the setup, each plastic piece can be individually deformed, provoking a different deformation of each section. Besides, the *long* plastic piece (moving side) can be displaced with respect to the *short* one (static side), provoking a controllable deformation of the sensor's central section (relative slide). The deformation of each section is estimated from the micro-metric screws of the three positioners.

The sensor is connected to an optical spectrum analyzer (HP86140A) and to a white light source (HP83437A) through a 50/50 coupler. By trimming the positioners, the sensor is subjected to different deformation cases that replicate the most typical real situations.

#### 4.3.1.4. Results

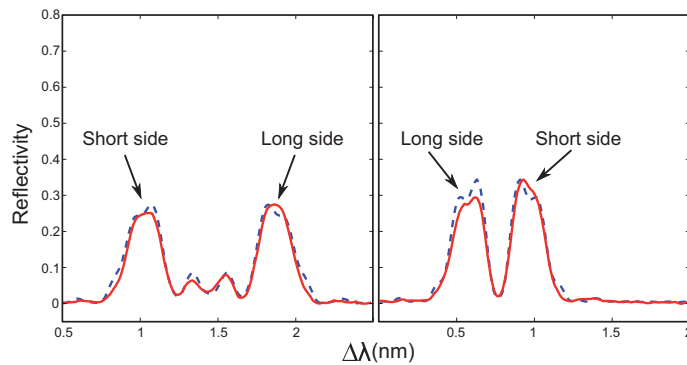
Starting from a spectrum of an unloaded sensor, the most common situations of a bonding joint are replicated in the presented setup: uniform deformation of the sensor, deformation of one holding piece more intense than the other and performing of a relative displacement between the two holding pieces (bonded parts).



**Fig. 4.33.:** Measured (solid line) and simulated (dashed line) spectra of a correct joint during uniform load condition.

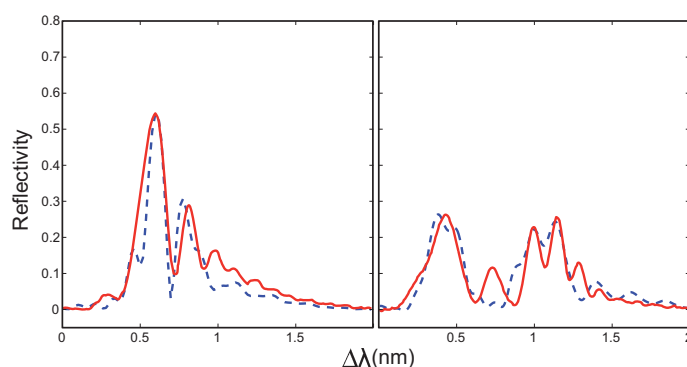
In a correct joint, the deformation is constant along the FBG, so the original spectral shape remains unchanged. In Fig. 4.33, the spectra of a joint with and without load conditions are shown. The FBG spectrum peak is almost the same under different loads, thus matching rather correctly the simulated sensor response. The difference between the two peaks indicates a strain load about  $1150 \mu\epsilon$ . The estimated deformation obtained from the micrometric screws is  $1300$  and  $1200 \mu\epsilon$  for the *short* and *long* pieces respectively ( $0.1$  mm in  $75$  mm and  $0.15$  mm in  $125$  mm)

Fig. 4.34 shows a sensor spectrum in a bonding joint that is not working properly, being one side more deformed than the other. The single FBG peak splits into two that follow each holding piece (bonded part). Two asymmetrical



**Fig. 4.34.:** Measured (solid line) and simulated (dashed line) spectra of different deformation cases. Long side is more stretched than the short one (left) and the long side is compressed with respect to the short one (right).

deformation cases are shown in the figure. In the left case, the *long* side of the FBG is stretched about  $600 \mu\epsilon$  more than the *short* one (0.2 mm in 125 mm (*long*) and 0.08 mm in 75 mm (*short*)). The relative slide between the plastic pieces (bonded parts) is set to the mean deformation of each holding piece to get a symmetrical spectrum. The central lobes of the studied case are due to the chirp effect introduced by the asymmetrical deformation of the central section and it is visible because the other peaks are enough spectrally separated. In Fig. 4.34 (right), the *long* side of the FBG is less stretched ( $700\mu\epsilon$ ) than the *short* side ( $1000\mu\epsilon$ ). The observed peak height difference is due to the central section deformation, which is closer to the *short* side deformation



**Fig. 4.35.:** Measured (solid line) and simulated (dashed line) spectra of relative slide cases. On the left side, relative slide is more significant than the asymmetrical deformation. On the right side, both relative slide and asymmetrical deformation are significant.

The other main case of a joint working incorrectly is the relative slide between the two bonded parts. In Fig. 4.35 this situation is illustrated by increasing the relative slide over the asymmetrical deformation (right) and with a comparable contribution of both studied effects (left). With a higher relative slide, the central section of the FBG shows an equivalent chirp that increases the higher wavelength lobes of the FBG spectrum. In Fig. 4.35 (left) a relative slide of  $500 \mu\epsilon$  is forced in the central section of the sensor in comparison to the more subtle asymmetrical deformation of  $100\mu\epsilon$ . In the most complex case (Fig. 4.35, right), there is a peak splitting and the side lobes increase. The peak splitting indicates an asymmetrical deformation and the increase of the side lobes suggests a relative slide. These side lobes appear at higher wavelengths, thus indicating a relative slide higher than the asymmetrical deformation. In this example, an asymmetrical deformation of  $400 \mu\epsilon$  and a relative slide of  $800 \mu\epsilon$  are applied to the sensor.

For more complex situations, the simulated spectra with the simplified employed model poorly fit the experimental data, but the two main considered effects (relative slide and asymmetrical deformation) can be still correctly identified. The obtained mismatch is mainly caused by the complex deformation profiles obtained under these situations where the approximated model does not accurately fit the real deformations, but the matching between the simulation and measured examples is still remarkable.

The proposed sensor is able to qualitatively evaluate how a bonding joint is working. Two malfunction cases are differentiated: an asymmetrical deformation of the bonded parts and a relative slide between them. In a simple way, each case gives rise to a characteristic response: the asymmetrical deformation of the bonded parts splits the main FBG peak into two with a separation between them proportional to their deformation difference. The relative slide between the bonded parts causes a different central section deformation of the sensor entailing a chirp effect. This chirp effect increases the side lobes of the FBG spectrum and their position can help to estimate, in a qualitative way, the central section deformation.

One of the main drawbacks exhibited by the proposed simplified model is its mismatch in situations with complex deformations. In these scenarios the 3-section model does not “perfectly” fit the measured spectra because the real

deformation of each section can not be assumed to be constant. However, it is enough to distinguish between the two main studied cases. In order to get a more realistic model of the proposed sensor, a more accurate finite element model has to be developed to obtain the longitudinal axis deformation profile of the FBG. Based on the obtained deformation profile, a new approximation with a higher number of sections has to be established. Another option would be to directly apply the deformation profile to the FBG. This model should better fit the spectral response under complex cases, but it would also be less intuitive and computationally more expensive even employing advanced optimization algorithms to replicate the deformation profile. The obtaining of this high-precision spectral response would be interesting from the analysis point of view, but the qualitative evaluation of a bonding joint could be too difficult to be used.

#### **4.3.1.5. Specific remarks**

A FBG-based bonding sensor has been designed, built and demonstrated. The sensor has been mechanically simulated using the Finite Element Analysis to study the longitudinal axis deformation profile where the FBG is fixed under different conditions. The heterogeneous shape of the proposed device and the installation procedure force different sections on the FBG which are assumed as uniformly deformed. A simplified model of three sections is proposed and optically simulated using the Transfer Matrix method. The spectral response of the sensor is given by the individual contributions of each section so, by analyzing the spectral evolution of the FBG, the status of the bonding joint can be estimated. The dependence of the FBG spectrum to different artifacts adds self-diagnosis capabilities to this kind of sensors. Five different cases were experimentally reproduced under controlled conditions and the same situations were replicated in the simulation environment. The test results show a very good agreement between the expected and real sensor behavior despite the use of a simplified model and the fabrication limitations.

#### **4.3.2. Compaction pressure transducer**

Ensuring the final performance of a composite structure implies a perfect control of the manufacturing process. Some manufacturing parameters such

as the curing temperature or the compaction pressure need to be accurately set to achieve the material optimal performance. This is significantly relevant in Vacuum-assisted Resin Infusion (VaRI) or in Vacuum-assisted Resin Transfer Molding (VaRTM)[45], where the structure is molded using a rigid mold and a thin flexible membrane over the fiber that compresses it against the mold surface due to the outer atmospheric pressure. Regarding this process, the strict control of the compaction pressure is a critical point. As shown in [46], a pressure variation during the VaRTM may lead to a different thickness within the structure, so the monitoring of this parameter will ensure a better behavior of the structure. This strict control becomes more important for larger structures where thicker composites are required (reaching several centimeters) such as vessels or wind turbine blades.

There are lots of reported applications where different manufacturing parameters have been monitored. Examples such as the monitoring of the resin flow with artificial vision [47] or with electrical arrays [48] or measuring the inner strains or temperatures by optical means [49] have been successfully tested. Optical fiber sensors [2] and particularly Fiber Bragg Gratings (FBGs) [44] have been proved as a highly compatible technology with composite materials [25]. Their light weight, small size and electromagnetic immunity, make optical fibers highly compatible with composite materials to be embedded into the structure. This kind of sensors have been successfully employed to characterize the manufacturing process by analyzing the curing reactions using fluorescence [50] or by recording the inner strain and temperature during the curing process [51]. However, by embedding optical fiber sensors during the manufacturing process [52], it is also possible to obtain a sensor network capable of providing information during the structure operation. There are many examples where strain and temperature measurements are obtained with embedded optical fiber sensors [15, 53] but, by combining these data with processing schemes, more complex artifacts can be detected such as cracks or damages [54], thus preventing a structure malfunction.

In this section, an optical fiber sensor to measure the compaction pressure during the manufacturing process is designed and tested. The proposed sensor is embedded into the composite material during the manufacturing process, recording the pressure during the molding. This process can be critical

for large composite structures where thickness of several centimeters must be achieved. Once it has been embedded, the sensor is also able to obtain strain or temperature measurements of the hosting structure under working conditions without degrading its mechanical behavior. Several characterization steps have also been performed to obtain the sensor response to pressure, strain and temperature, exhibiting a great sensitivity and repeatability.

#### 4.3.2.1. Transducer structure

The transducer is based on a plastic block with an embedded Fiber Bragg Grating. The central section, where the FBG is embedded, is arc-shaped to be compressed when a transversal load is applied (Fig. 4.36). Surrounding the arc-shaped section, two straight glass fiber filaments were included to limit the central section compression after being installed. The proposed design is oriented to be embedded into a composite structure during its manufacturing process, so it has to be small enough to avoid the modification of the structural mechanical response, but solid enough to withstand the fabrication process.

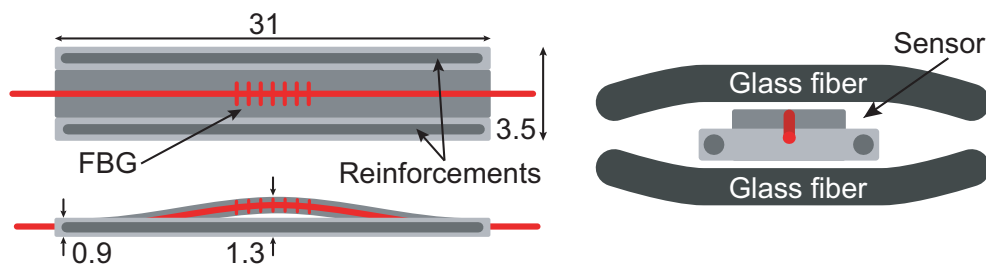


**Fig. 4.36.:** Sensor structure (left) and embodiment scheme (right). The arc-shaped section is compressed while a transversal load is applied. Dimensions are in millimeters.

Once the sensor is embedded into the composite material, the central section is compressed as the transversal pressure increases. The compression can be measured using the wavelength shift of the embedded FBG, while the dimensions of the central arc determine the sensitivity of the sensor to the pressure. However, the arc can be not excessively abrupt, enhancing the pressure sensitivity, because it will create a non-uniform deformation along the FBG, what would deform its spectral shape complicating the peak determination. A correct behavior of a FBG relies on a uniform deformation of its periodic variation and, consequently, any odd artifact close to the FBG can

limit its final performance.

The arc shape of the central section is maintained by two surrounding glass fiber reinforcements that also help to limit the sensor compression by establishing a minimum thickness. Once the composite structure has been manufactured, the sensor remains compressed inside the material maintaining the FBG orientation parallel to both sensor surfaces, so further strain measurements can also be performed employing the same sensor. A simplified version of the proposed design has been simulated using the Abaqus Finite Element Analysis (FEA) software (Dassault Systemes Inc.). The simulated model just reproduces the central section using the proposed arc dimensions, and it has been employed to obtain the qualitative sensor response, validating the chosen dimensions. The central block has been considered as a homogeneous resin block under distributed pressure over its surface. Although the surrounding glass fiber reinforcements have not been included in the model, the expected sensor response must be similar.

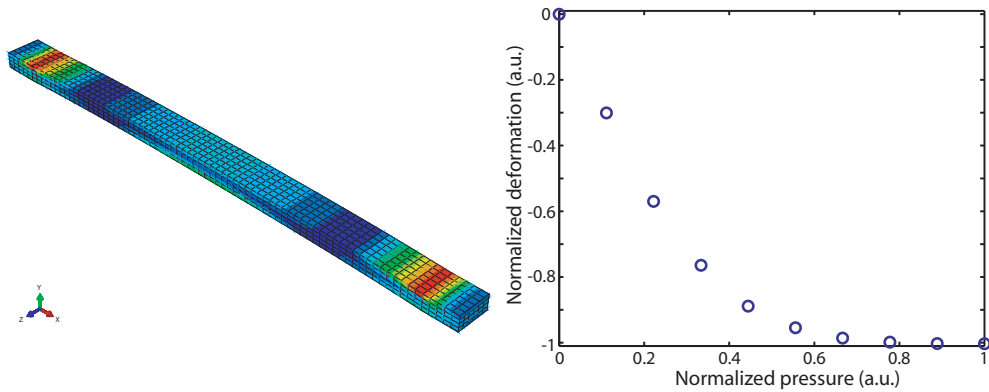


**Fig. 4.37.:** *Simplified model of the proposed design (left) and simulated strain applied to the FBG as the pressure increases (right).*

The simulated mechanical response and the FEA model are depicted in Fig. 4.37. At lower pressure, the arc is easily deformed and, consequently, the achieved sensitivity at lower pressures is better than at higher pressures. However, after the sensor has been compressed, its sensitivity becomes very low following a logarithmic trend as can be noticed in Fig. 4.37 (right).

#### 4.3.2.2. Manufacture and embodiment process

The sensor is built in epoxy resin using two glass fiber filaments of 0.6 mm of diameter as reinforcements. To obtain the desired shape, a mold is manufactured using non-stick silicone from a plastic (PMMA) CNC processed male. Some alignment points are included in the sensor design to accurately place the FBG and the glass fiber reinforcements. After finishing the mold, the glass fiber reinforcements are placed on both sides. After that, the FBG is placed into the central section of the mold, following its arc shape. For this application, a FBG of 4 mm length has been employed. Its length is a trade-off between its final resolution and its short length to avoid heterogeneities. When the optical fiber and the reinforcement filaments are located, a low viscosity epoxy resin is poured into the mold. After the pouring, a vacuum stage follows to guarantee the homogeneity of the final block by removing the air bubbles. The epoxy resin was thermally cured for a few hours to obtain the final block. A photo of the obtained sensor is shown in Fig. 4.38.

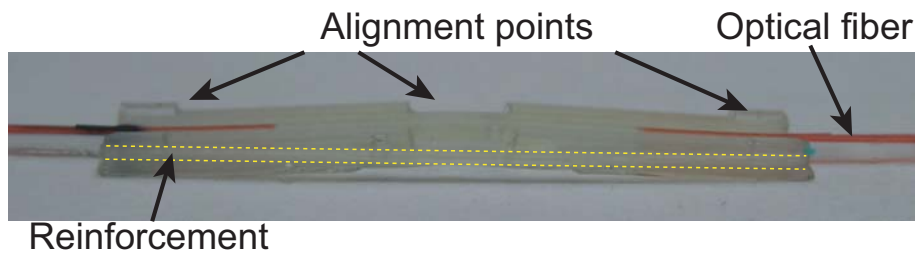


**Fig. 4.38.:** *Manufactured sensor. Some alignment points can be observed on top of the arc-shaped section.*

The two key characteristics of the proposed sensor can be observed in Fig. 4.38: two straight sections with reinforcement filaments and a central arc-shaped section with the embedded FBG. The observed holes around the central area as well as the four brackets of both edges are alignment means included to help during the molding process. Once finished, the sensitivity of the sensor is characterized for different compaction pressures. After the compaction characterization, the sensor is embedded into two sheets of bidirectional weaves to obtain its sensitivity to strain and temperature.

### 4.3.2.3. Experiments and Results

Several tests have been performed to obtain the sensor response to different parameters. The goal is to quantify the compaction pressure of a composite structure during its manufacturing process and, once it has been finished, to measure strain or temperature of the hosting structure in operation.

#### Compaction pressure

An equivalent VaRTM setup is proposed to obtain the sensitivity of the proposed design to the compaction pressure. The sensor is placed between two bidirectional glass fiber weaves of  $300 \text{ gr}/\text{m}^2$  and covered with a plastic vacuum bag. The bag is sealed and a controlled vacuum pressure is applied to the setup while the wavelength deviation of the FBG is measured.

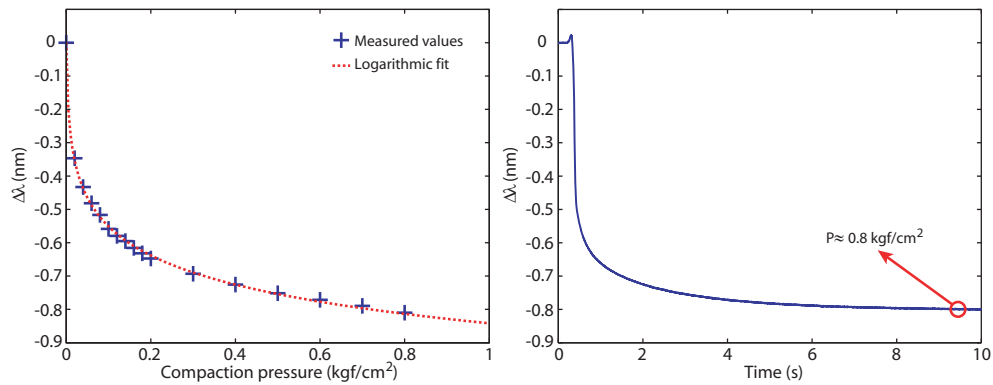


**Fig. 4.39.:** Wavelength shift of the FBG against the compaction pressure (left). A single sweep reaching a compaction pressure of  $0.8 \text{ kgf}/\text{cm}^2$  (right).

After five initial pressure cycles performed to allow the accommodation of the FBG to the sensor material, the sensor has been subjected to several compaction pressure sweeps from 0 to  $0.8 \text{ kgf}/\text{cm}^2$ . The obtained wavelength displacement has been averaged maintaining the compaction pressure. The obtained results are depicted in Fig. 4.39 against their logarithmic fit ( $R^2 \approx 0.9992$ ). The maximum divergence in the wavelength shift was  $\Delta\lambda_\epsilon \approx 0.02 \text{ nm}$  at lower pressures (under  $0.2 \text{ kgf}/\text{cm}^2$ ) and  $\Delta\lambda_\epsilon \approx 0.01 \text{ nm}$  at higher ones. As the pressure increases, the compression of the FBG also increases, what gives rise to a decrease of its peak wavelength. The sensor response remarkably matches a logarithmic response: the arc-section is easily compressed at lower

pressures but, as the pressure increases, the deformation range is limited by the lateral reinforcements, also limiting the FBG compression. This experimental results can be compared with the simulated response depicted in Fig. 4.37.

### Spectral behavior

Due to inhomogeneities within the sensor block, the FBG can be asymmetrically compressed, deforming its spectral shape and making it useless for further measurements. During the compaction pressure characterization, the spectral FBG response has also been analyzed.

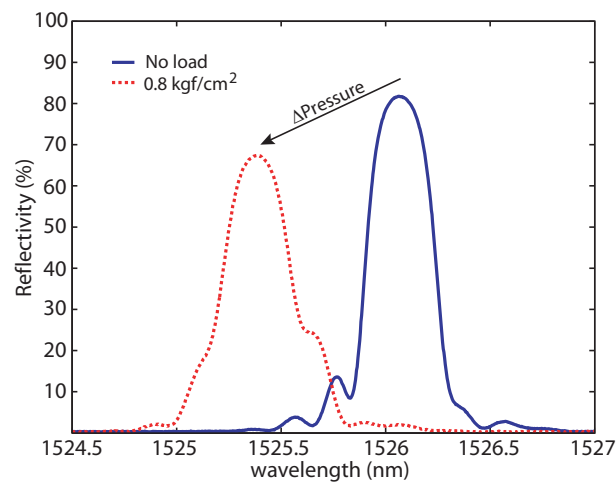


**Fig. 4.40.:** *FBG spectra under a compaction pressure of  $0.8 \text{ kgf/cm}^2$  (dotted line) and without load (solid line). Both FBG spectra peaks are clearly identifiable.*

As shown in Fig. 4.40, the FBG spectrum is slightly modified due to manufacturing inhomogeneities that create a non-uniform compression on the FBG. However, the main FBG spectral shape is still maintained, being its peak clearly identifiable and allowing further measurements. Besides, when a high load is applied, there is little drop in the received optical power due to the micro-bending losses of the optical fiber, but it still remains high enough for sensing applications.

### Strain response

Once the compaction pressure characterization was performed, the sensor was embedded into a composite material of two bidirectional glass fiber weaves

of  $300 \text{ gr}/\text{m}^2$  using the wet lay up technique. An extra weight was added to set the compaction pressure up to  $P \approx 0.9 \text{ kgf}/\text{cm}^2$ . This value was checked using the proposed sensor and obtaining a wavelength displacement of  $\Delta\lambda = -0.82 \text{ nm}$ . After the material curing process, the resulting beam was 450 mm by 40 mm with a constant thickness of 1.5 mm. In addition to the proposed sensor, an extra bare FBG was embedded into the two glass fiber weaves as a reference.

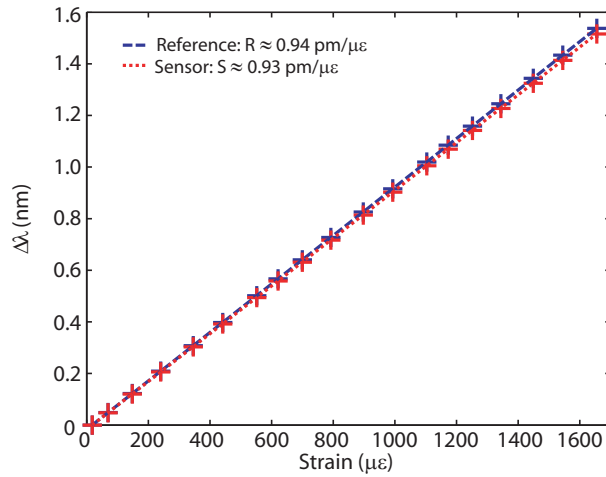


**Fig. 4.41.:** Reference FBG (dashed line) and the proposed sensor strain response (dotted line) and their associated linear fits.

In the initial stage, five loading cycles (with a peak deformation of  $\Delta\epsilon \approx 500 \mu\epsilon$ ) were applied to the beam to overcome the accommodation effect of both sensors (pressure and reference) to the host material [29]. Following, a stretching ramp was applied to the resulting beam and the FBG response is depicted in Fig. 4.41. Both FBGs exhibit a great linear gauge factor to the applied strain. The gauge factor of the proposed sensor is somewhat lower due to the amount of resin located between the glass fiber weaves and the optical fiber caused by the sensor package. The reference FBG is closer to the glass fiber weaves, so its sensitivity is a little higher, but a bare FBG can be damaged during a composite manufacturing process. However, a small error is also caused by slight misalignments during the stretching process. A cross section photo of the embedded sensor is shown in Fig. 4.42. The two glass fiber reinforcements and the optical fiber can be appreciated while the whole sensor is perfectly integrated into the composite material.

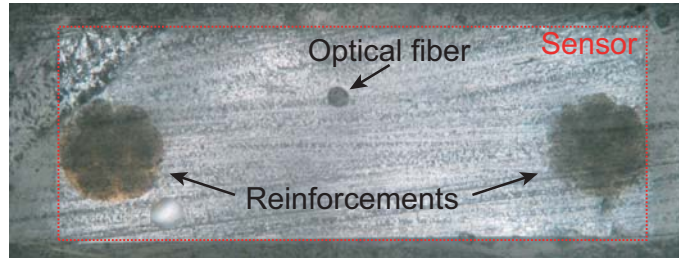


**Fig. 4.42.:** Cross section photo of the embedded sensor. The resin block of the sensor is hard to be distinguished from the surrounding material.

### Temperature response

Most FBG sensors are temperature sensitive, so further measurements must be compensated to remove the thermal error. In order to quantify the thermal response, the instrumented composite beam is subjected to a temperature sweep from  $10^{\circ}C$  to  $40^{\circ}C$ , thus obtaining its behavior. The obtained results are depicted in Fig. 4.43. The response of the sensor to the temperature is slightly higher than the reference FBG because the thermal expansion coefficient of the epoxy resin without reinforcements is higher than with them. When some extra epoxy resin is placed between the composite material and the FBG, this is partially isolated from the response of the whole material. However, this effect can be minimized by introducing the proposed sensor in a composite material strong enough (with a higher thickness) to stretch the inner sensor despite the extra epoxy resin.

The depicted response was obtained once the sensor was embedded into a hosting material; consequently this sensor can be also employed to measure the temperature (or strain) of the hosting structure during its operation with a sensitivity of  $C_T \approx 34pm/^{\circ}C$ . However, the deviation of the FBG wavelength due to the thermal expansion may introduce some errors during the infusion step of the VaRTM process, because the resin temperature can be different (typically higher to decrease its viscosity). Extra temperature measurements are required to compensate this error to maintain the monitoring of the compaction pressure during the infusion. The thermal response of the bare sensor (without being embedded) was also characterized and, it matches the response of the employed epoxy resin ( $C_T \approx 55pm/^{\circ}C$ ) and can be used to compensate the pressure measurements during the infusion step.

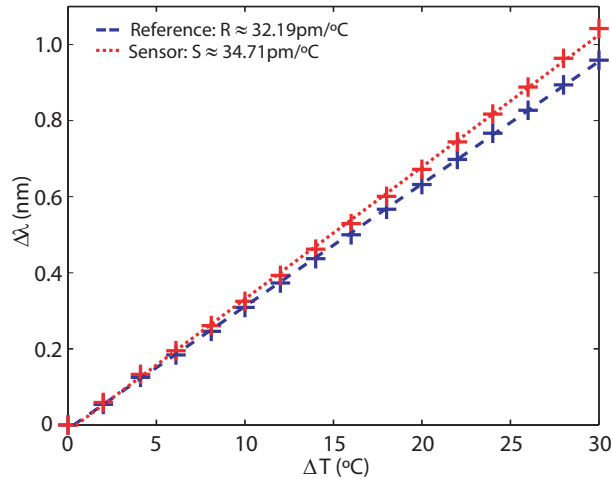


**Fig. 4.43.:** Temperature response of the proposed sensor (dotted line) against the reference FBG (dashed line) with their associated linear fit.

#### 4.3.2.4. Specific remarks

A FBG based sensor for monitoring the compaction pressure of a composite material during its manufacturing process has been proposed and experimentally demonstrated. The achieved sensor can be employed to monitor the manufacturing process of thick composite structures (several centimeters). The same sensor can be used to measure strain or temperature once the hosting composite material has been manufactured. Several experiments have been performed to obtain the sensor response to the three parameters that can be measured: compaction pressure, strain and temperature. The obtained results show a very good agreement with the expected behavior of the different parameters, exhibiting a logarithmic response for pressure and a linear one for both strain and temperature. The obtained sensor can provide information during a composite structure manufacturing process and, once it has been finished, give useful measurements for structural health monitoring applications.

### 4.3.3. Embedded strain transducer

Fiber Bragg Gratings have been widely applied to monitor in field structures during the last years. Applications such as civil engineering structures [55, 56], aircraft wings [31] or marine structures [57] are examples of the challenge of monitoring in-field structures. Most of these applications have been mainly

developed within a laboratory and, after particular adjustments [36], have been employed to monitor some structures. These initial tests are extremely useful to retrieve information for both developments: sensing systems and structures.

However, after these initial field tests, an extra effort is required to achieve a truly reliable sensing system to be merged with a working structure. This is a complicated challenge, because each final application has a lot of small details to have into account when both sensing and structure technologies are pushed to the edge, what reduces the available technologies to those already well-known. Particularly, FBGs are a mature technology, which several sensing companies have relied to develop their sensing solutions in. With their application to composite structures, new kinds of commercial sensors have been developed, but most of them have been conceived to be installed after the structure manufacture.

In this section, a specific FBG based transducer is developed to be embedded into large composite structures, being able to survive the manufacture process. Based on a resin block, the FBG is protected against the transverse pressure required to compact the final composite material. Their shape and dimensions have been chosen for a large structure standard, so the final mechanical response of the structure is not influenced by the sensing system. Several individual transducers can be combined to obtain quasi-distributed measurements of critical structure points.

##### **4.3.3.1. Transducer structure**

The proposed scheme must be only sensitive to the longitudinal axis strain, remaining insensitive to transverse axis deformations. Besides, the transducer is going to be embedded into a composite material during its manufacturing process, thus the optical fiber requires extra protection, being especially remarkable at the FBG location. This might not be a critical issue in the manufacturing of high precision composite structures [26, 27], but, when larger structures of several meters are manufactured, some extra transducer toughness is required.

Particularly, the proposed transducer should support very high transverse loads during the compaction of the composite material, but be also capa-

ble of measuring longitudinal deformations. From the structure point of view, transducers must not affect the mechanical response of the host material, what limits both the dimensions and materials to be employed. A scheme of the transducer is depicted in Fig. 4.44. A FBG is embedded into a resin block where two parallel fiber reinforcements have been included. These reinforcements have a greater diameter than the optical fiber, and limit the transverse compression of the resin block.

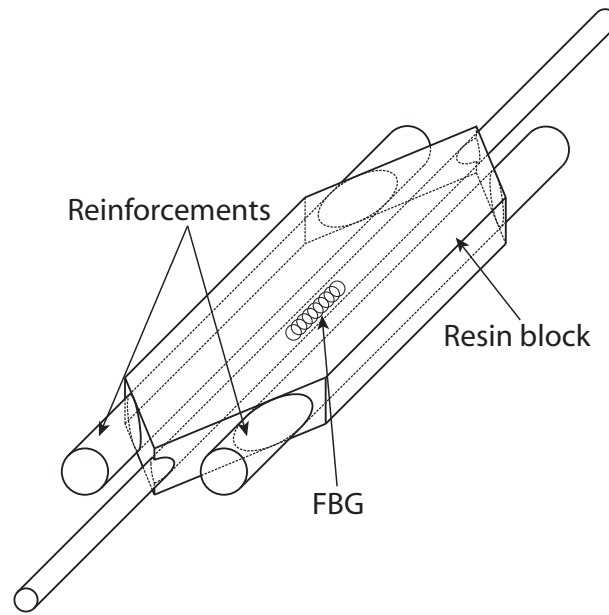


**Fig. 4.44.:** *Sensor design: two surrounding reinforcements limit the transverse pressure to the embedded FBG.*

Trying to reduce the mechanical influence of the proposed design, the same materials of the hosting structure should be employed in the transducer manufacture. In addition to the improvement of the transducer robustness and the low sensitivity to transverse deformation, this design helps its alignment, making its installation into the host structure easy. In the following section, its manufacturing process and final dimensions are adapted to be embedded into Glass Fiber Reinforced Plastics (GFRPs).

#### 4.3.3.2. Manufacturing process

A practical implementation of the proposed design has been manufactured. With a total thickness of  $h \approx 0.7 \text{ mm}$ , its final final design is detailed in Fig.

4.45 (top). Due to mechanizing limitations, its edges have been simplified from the original design, but the main block distribution and reinforcements have been maintained. Using a Computer Numerical Control (CNC) cutting machine, a male mold has been mechanized following the proposed design. This mold has been employed to build also a female mold using nonstick silicone.

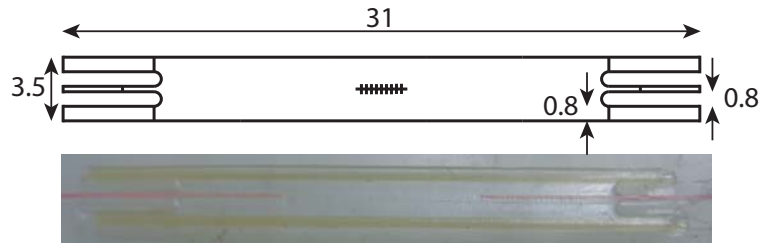


**Fig. 4.45.:** Final block dimensions in millimeters (top). Photo of the final transducer (bottom).

After locating two glass fiber rovings at both mold sides, a  $L = 4 \text{ mm}$  length FBG, written into a standard telecommunication optical fiber using the phase mask technique, is aligned with the middle axis. Then, a low viscosity epoxy resin is poured into the mold and a vacuum stage follows to guarantee the homogeneity of the final block by removing the air bubbles. The epoxy resin is thermally cured for a few hours to obtain the final sensor. A photo of the manufactured strain transducer is depicted in Fig.4.45 (bottom).

In order to verify the suitability of the whole process, a total of 60 transducers have been manufactured with slightly variations regarding the procedure. Finally, 48 transducers have been manufactured maintaining the same procedure, each of them has been tested using the same transverse pressure employed for the compaction of real GFRP structures. A total of 46 transducers have passed these tests where an equivalent VaRTM setup has been proposed to apply a controlled compaction pressure. Each transducer has been placed between two bidirectional glass fiber weaves of  $300 \text{ gr/m}^2$  and covered with a plastic vacuum bag. The bag was sealed and a controlled vacuum pressure was applied to the setup while the FBG spectrum was monitored to determine if the tested transducer was valid.

### 4.3.3.3. Experiments

Although the ultimate goal of the proposed transducers was the measurement of the longitudinal axis deformation, their main challenge is to support high transverse pressures. However, several strain tests have been performed both embedding and gluing different transducers to a GFRP beam. Their achieved response was linear, as expected and their sensitivity depends on the installation procedure. Regarding the transverse pressure, and besides the preliminary quality tests, some extra experiments have been performed.

### Transverse Pressure

The main problem when an Optical Fiber Sensor has to be embedded into a large composite structure is to survive to the manufacturing process, because high compaction pressures are employed. This step puts pressure on the glass fiber weaves to the optical fiber, provoking a non-uniform deformation along the FBG. Trying to evaluate this influence, a bare FBG and the designed transducer have been pressed through a glass fiber weave while their spectra were measured.

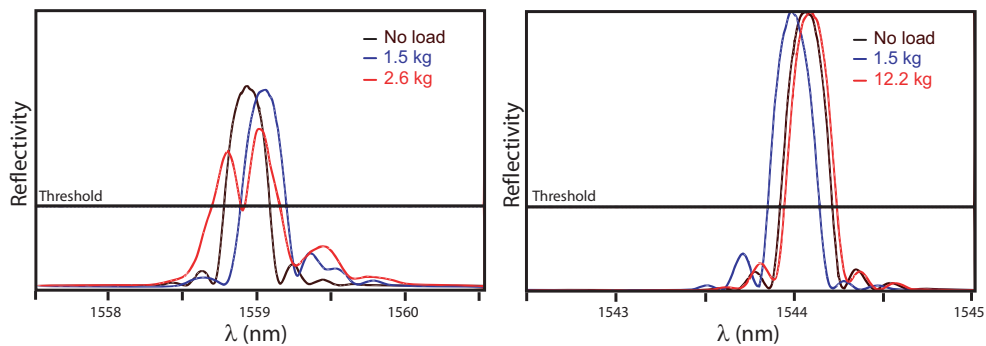


**Fig. 4.46.:** Bare FBG spectra under different loads (left). Spectra of the proposed transducer under different loads (right).

In Fig. 4.46, the spectra of a bare FBG and the proposed transducer are depicted for different loading conditions. The resin block of the transducer helps to redistribute the transverse pressure and the surrounding reinforcements limit their cross deformation. On the other hand, when a bare optical fiber is pressed against an irregular surface, these irregularities are transferred to the FBG structure, deforming its final spectrum.

## Temperature response

The thermal response of a FBG embedded into composites is mainly driven by the amount and type of the surrounding resin. However, when a transducer is embedded into a host composite material, its final thermal sensitivity is given by the hosting material properties. The thermal response of the proposed transducer has been obtained by applying a temperature sweep to both free and embedded transducers. The achieved results are depicted in Fig. 4.47.

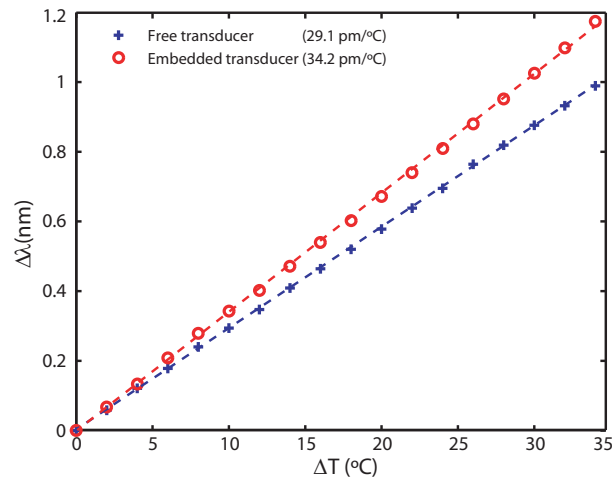


**Fig. 4.47.:** Temperature response of a free (crosses) and embedded (circles) transducer against their linear fit.

The thermal response of a free transducer is determined by its geometry and ratio of fiber reinforcements and resin. However, when it is embedded into a bigger composite block, the ratio between reinforcement fibers and resin changes. In this case, the amount of resin that surrounds the FBG is higher when the transducer is embedded, thus its thermal sensitivity increases. Despite this variation, when different transducers have been included into the same composite material, they offered the same thermal sensitivity. This kind of embedded sensors must be thermally characterized after their embodiment into the final material.

### 4.3.3.4. Specific remarks

A different implementation of a classical FBG strain gauge has been developed for its embodiment into large composite structures. An easy-to-

manufacture transducer based on a resin block with two surrounding reinforcements has been designed to support the high transverse pressures applied during the manufacture of composite materials. The achieved results exhibit a low transverse pressure sensitivity even with fabrication imbalances (such as the appearance of air bubbles close to the FBG). Several transducers have been manufactured using the same process exhibiting a great repeatability and tolerance, enabling both design and process for industrial applications.

#### **4.3.4. Field demonstrations**

All the proposed transducers have been experimentally verified under laboratory conditions, being useful to generate new knowledge and techniques to improve the present technology platform. However, all the proposed devices and techniques must also be tested under real conditions to be successfully applied in real scenarios.

Two field implementations of FBG based transducers have been applied to real scenarios. Starting from the characterization of civil engineering materials by embedding FBG based transducers into a pre-stressed concrete beam and following by adding a strain sensing system to a wind turbine blade of 37 meters length, both examples are useful to improve their further applicability.

In both applications, different FBG transducers have been adapted to be able to work under field conditions. Many implementation problems have to be solved before installing each transducer such as: the alignment of the sensors during the installation, the optical fiber protection to reach the structure, the protection of the interrogation equipment and so on. However, each of these challenges gives rise to the development of more robust OFS sensor systems capable of working under real environments.

##### **4.3.4.1. Pre-stressed concrete beam monitoring**

In the construction of some precast concrete structures, the armor is pre-stressed before the concreting process. After the concrete is hardened and has gained the right strength, the armor is slacked. During the slacking period, the pre-stressing force initially applied to the armor is transferred by adhesion to the concrete. This inner process has not been properly modeled yet, because

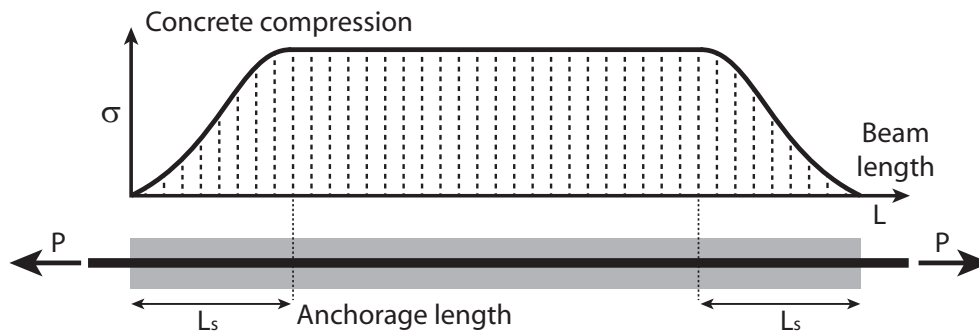


**Fig. 4.48.:** Expected compression force distribution after the unstressing step during the fabrication process.

the employed techniques were low reliable and with low precision for these requirements, thus limiting the existing models of armor response.

The adherent nature of a pre-stressed reinforcement is defined through the conventional anchorage length ( $L_s$ ) after the unstressing process. As illustrated in Fig. 4.48, the anchorage length ( $L_s$ ) can be defined as the length of the coating required to ensure the transmission of the maximum pre-stressing force (from the armor to the concrete). This transmission can be noticed in concrete structures by releasing the reinforcement ends, initially stressed to the 80% of their nominal breaking load.

The standard UNE 7-436-82 “*Bond test of steels wires for pre-stressed concrete*” [58] defines the procedure to determine this parameter and its confidence criterion. This method is based on measuring the penetration length of both reinforcements edges after releasing the armor stress. This measurements should be repeated after 1, 6, 24 and 168 hours to monitor the whole slacking process.

However, these measurements are usually performed by very traditional procedures: several points are marked on the beam surface and the distance between them is measured during the slacking period. This commonly used method is unable to get real measurements of the inner part of the beam and some measurement errors are easily committed, reducing its final performance. Based on FBGs, a quasi-distributed sensor system able to measure both temperature and strain/elongation along the longitudinal axis (inside the beam) has been employed to measure the anchorage length of pre-stressed concrete beams.

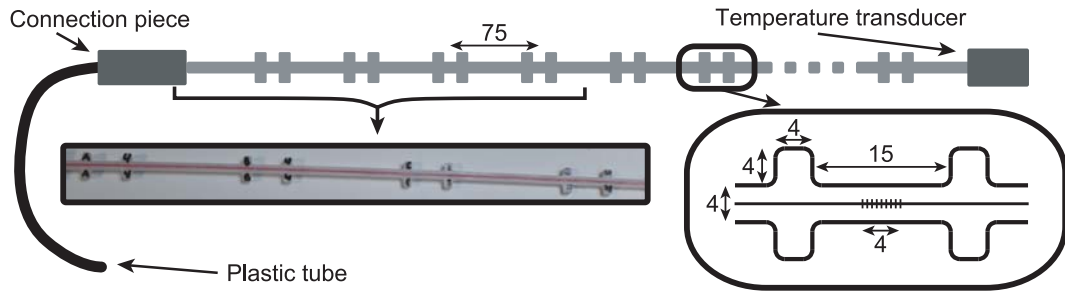


**Fig. 4.49.:** Design details and a photo of the manufactured transducer. Dimensions are in millimeters.

### Transducer design and manufacture

The compression at different beam positions has to be measured to determine the anchorage length. A plastic (PMMA) holder of 3 mm thickness has been especially designed to house 16 FBGs at preset locations. Two fixing areas surround each sensing point to force a better joint with the concrete, causing a homogeneous deformation on the central part of each sensing point. An extra FBG has also been included at the transducer edge to obtain the inner beam temperature. The holder is detailed in Fig. 4.49.

A groove has been mechanized into the central axis of the holder to accommodate 4 optical fibers, each one with 4 FBGs to measure the compression at each sensing point. Each FBG is glued (using cyanoacrylate) to the bottom surface of a central groove made in the holding piece before sealing the groove using thermofusible adhesive. This groove is also used to guide the optical fibers along the transducer, protecting them from possible hits or cracks during the installation. The extra FBG has been embedded into an epoxy resin block to enhance its thermal sensitivity and it has been placed loosely, isolated from the transducer deformation. The four optical input-output fibers were protected with a plastic tube to reach the outer edge of the beam.

### Transducer Installation

The manufactured transducer has been embedded into the central axis of a prismatic concrete beam of rectangular section ( $0.2$  by  $0.15$   $m^2$ ) of  $3.55$   $m$  length. The beam has been built using a concrete with a minimum value of resistance of  $65$  MPa at 28 days. During the concreting process, three cylindrical test control samples were prepared ( $h = 300$   $mm$  and  $\phi = 150$   $mm$ )

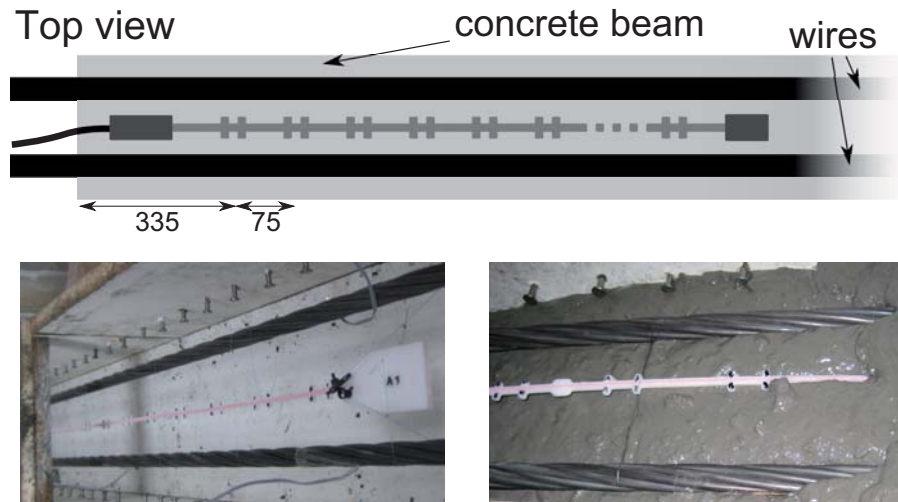


**Fig. 4.50.:** *Installation scheme and photos during the embodiment. Dimensions are in millimeters.*

to determine the concrete compressive strength. Two surrounding steel reinforcements have been pre-stressed before the concrete curing. An electric strain gauge has been glued to each reinforcement wire to verify the steel stress during the clamping process.

The loading process of the reinforcements has been performed in several steps (with a minimum of three), recording the applied load and deformation of both wires. These values are compared to the typical stress-strain diagram of the tested steel, in order to avoid errors in the initial clamping force. After the applied load is stable, a period of 24 hours is required before concreting the beam.

Given that the adhesion properties of the pre-stressing reinforcement have to be measured, the transducer is placed near one edge of the concrete beam to analyze its compression evolution. It is fixed in the middle of the two steel reinforcements using nylon wires before the beam concreting. The first sensing point is placed at 335 mm from the edge of the beam and the last at 1460 mm. The distance between two consecutive sensing points is 75 mm. Installation details are depicted in Fig. 4.50.

When the concrete had acquired the right strength (5 days after), the stored samples were broken to measure the achieved resistance. The mean resistance value of the three samples was 38.5 MPa, which is higher than the standard test requirement of 24.5 MPa. After the resistance test, the formwork has

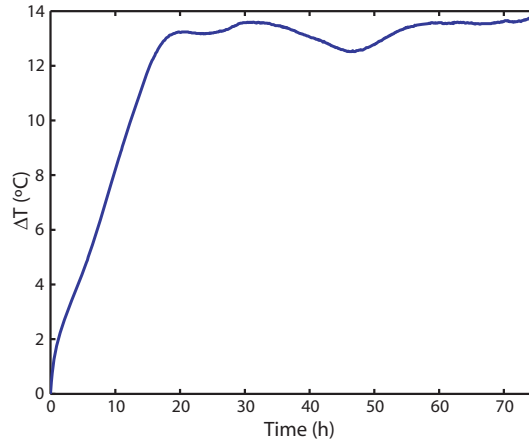


**Fig. 4.51.:** *Temperature evolution during the concrete curing process.*

been carefully removed before placing two comparators at both beam sides that recorded the initial penetration values before the releasing process of the reinforcement wires.

## Results

The whole process has been monitored since the pouring process. The stress of the reinforcement wires has been maintained during the concrete curing. After the beam curing, both reinforcement wires have been released while the beam deformation was measured during 220 hours. The first remarkable result is the temperature evolution during the concrete curing. As shown in Fig. 4.51, the temperature stabilizes after 20 hours with a final rise of  $\Delta T \approx 13^\circ C$ .

After the concrete curing, the stress of the reinforcement wires is removed. For this process, each wire is stressed to release the fixing means and afterwards the load is reduced gradually. The process is repeated for each wire. The greater compression is obtained during the starting minutes but the beam continues comprising with time. The compression measured during the releasing of both wires is depicted in Fig. 4.52 (left). Several time references have been taken to get the spatial evolution of the beam deformation (1, 6, 24, 168 and 220 hours after the releasing) and the deformation for these references is depicted against the beam length (Fig. 4.52, right).

The achieved results have been fit by two lines whose intersection sets the measured anchorage length at  $L_s \approx 1085 \text{ mm}$  (Fig. 4.52, right). This value has also been calculated according to the analyzed standard, employing the

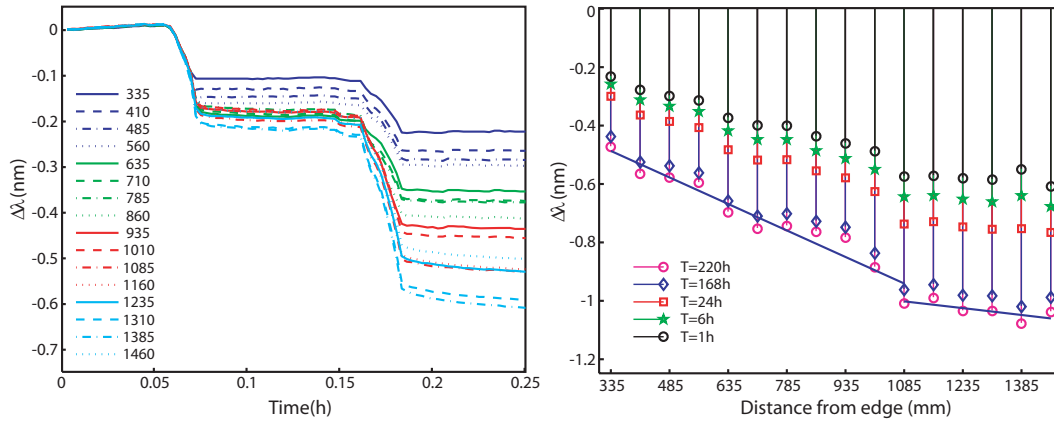


**Fig. 4.52.:** Initial compression during the releasing process (left). Deformation along the beam at different times: 1, 6, 24, 168 and 220 hours after releasing (right).

averaged value of penetrations in both reinforcements ( $\delta_m$ ). The standard defines the anchorage length as (Eq. 4.8):

$$L_s = 3.5 \frac{E_s \cdot A_{pm}}{f_{pm,G}} \delta_m, \quad (4.8)$$

where  $E_s$  is elastic modulus of the active reinforcements (steel,  $E_s \approx 200 \text{ GPa}$ );  $A_{pm}$  is the cross-section area of the active reinforcement ( $A_{pm} \approx 140 \text{ mm}^2$ );  $f_{pm,G}$  is the guaranteed breaking load of the active reinforcements ( $f_{pm,G} = A_{pm} \cdot f_{max,k} \approx 140 \text{ mm}^2 \cdot 1860 \text{ MPa}$ ); and  $\delta_m$  is the averaged value of penetrations for the three samples after 7 days (168 hours). According to the standard, the anchorage length of the passive side is  $L_{s,p} \approx 1095 \text{ mm}$  and the averaged anchorage length is  $L_{s,m} \approx 1054 \text{ mm}$ .

The results achieved with the proposed method match those calculated using the formulation proposed by the reference standard. The difference between the classical approach and the proposed transducer is  $\epsilon \approx 10 \text{ mm}$ , mainly given by the spatial resolution of the proposed technique. However, the achieved values are under a 1% error with a 10% tolerance level in the standard when using alternative methods for determining the anchorage length.

### Specific remarks

The determination of the anchorage length of an active reinforcement of a concrete structure is given by the UNE standard. This process is based on measuring the penetration depth of the reinforcements using traditional (with

low precision) methods. A quasi-distributed transducer based on several FBGs has been developed and tested to measure this parameter. The proposed transducer enables a high precision monitoring of the elongation and temperature into the beam core-axis at different locations.

After the seven days proposed by the standard (UNE 7-436-82) for measuring the penetration, it has been observed that the deformations are not stable and the beam shortening process continues, thus contradicting the standard assumption. This OFS technology will be proposed to be admitted into the standard to monitor these parameters.

#### **4.3.4.2. Wind turbine blade monitoring**

Employing FBG based transducers, a full-scale wind turbine blade (AB37-II) manufactured by the company Aeroblade Inc. has been monitored. Starting from a high precision strain transducer, a strain patch has been designed to be installed on the structure surface (as in commercial systems). Employing a total of 15 strain patches, a sensor system capable of retrieving the strain distribution of a loaded structure has been experimentally verified during 4 loading tests. All sensing patches have been distributed into three critical areas to evaluate the wind turbine blade response. The final tests exhibit a great linearity and repeatability proving the feasibility of applying FBG-based sensing technology in this field of application.

#### **Transducer design and manufacture**

The whole sensor system relies on the basic strain sensing point: the strain patch. Based on a FBG of 4 mm length, a GFRP patch has been designed to be superficially installed to a hosting structure. This composite patch is manufactured using Vacuum assisted Resin Infusion (VaRI). The initial resin block is a strain FBG transducer for high precision applications that protects the bare optical fiber from breaking. This strain transducer has been embedded into a bigger patch with two protected optical fiber splices to optical fiber cable.

Each strain transducer has been manufactured by pouring epoxy resin into a nonstick mold. Using a Computer Numerical Control (CNC) cutting machine, the male mold has been mechanized following the proposed design (Fig. 4.53,

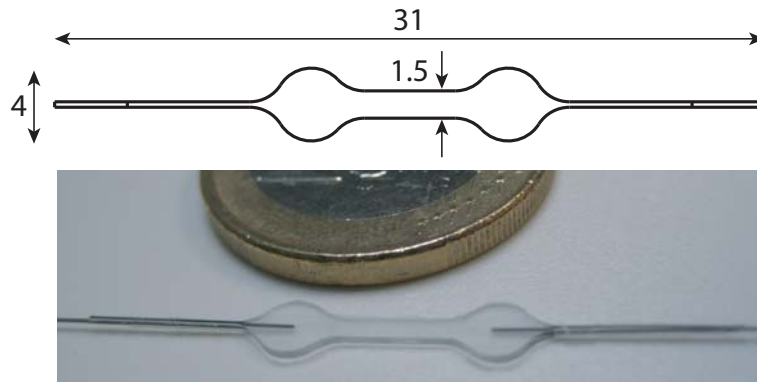


**Fig. 4.53.:** Final block dimensions in millimeters (top). Photo of the final transducer (bottom).

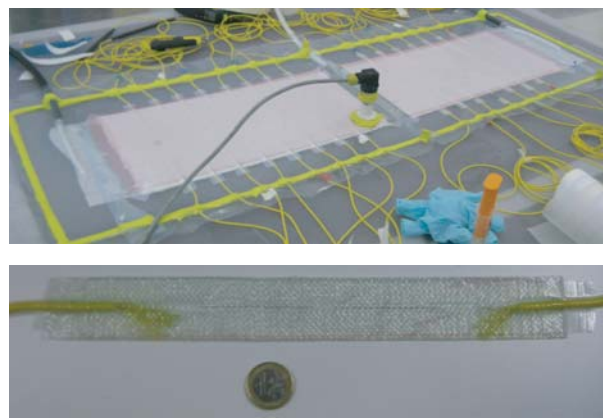


**Fig. 4.54.:** Patch manufacturing process (top). Final sensing patch (bottom). Courtesy of Aeroblade.

top) with a constant thickness of  $h \approx 0.5 \text{ mm}$ . This mold has been employed to build a female mold using nonstick silicone. The FBG is aligned with the middle axis before pouring low viscosity epoxy resin, followed by a vacuum stage to guarantee the homogeneity of the final block by removing the air bubbles. The epoxy resin is thermally cured for a few hours to obtain the final strain sensor. A photo of a manufactured strain transducer is depicted in Fig. 4.53 (bottom).

Each high precision strain transducer has been spliced to standard 3 mm optical fiber cable at fixed distance before protecting both weak points. Once spliced, each transducer was embedded into a two layer GFRP plate using a highly precise VaRI process, avoiding damages to the strain transducers. After finishing the GFRP plate, each individual patch has been mechanized

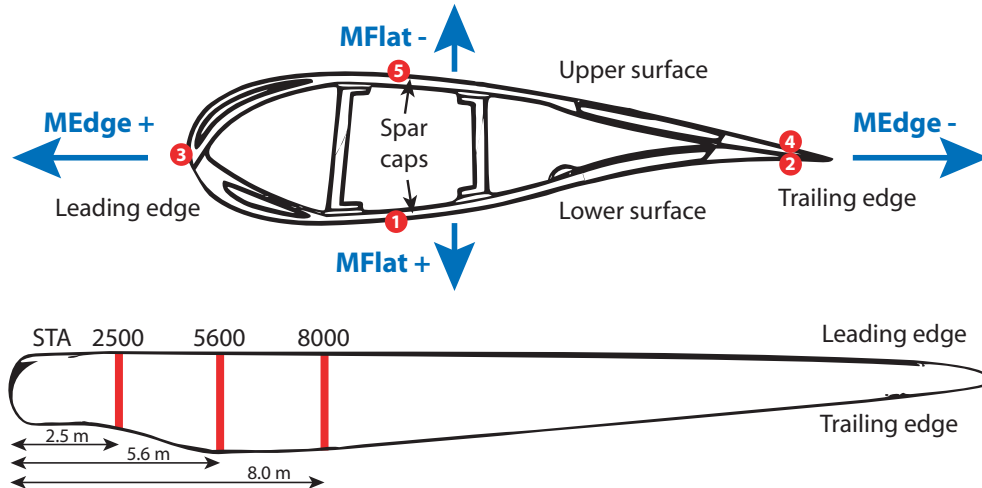


**Fig. 4.55.:** Wavelength patch distribution and test directions (top). Different station distances (bottom).

with a final dimension of  $w \approx 30 \text{ mm}$  by  $L \approx 250 \text{ mm}$  and a total thickness of  $h \approx 1.5 \text{ mm}$ . Details of the manufacturing process and the final patch are depicted in Fig. 4.54

## Installation

A total of 15 strain patches of 5 different wavelengths have been distributed into three optical fibers. Two commercial temperature transducers have been also included into a 4th optical fiber. Following the manufacturer's suggestions, the strain patches have been installed into three rings placed at different distances (stations) from the blade root. An installation scheme is depicted in Fig. 4.55.

Each sensing station has been monitored by an optical fiber channel with five strain patches. Each patch has been glued to the blade surface just in the central patch area, leaving both sides unglued to prevent splices breaking. After gluing each patch, a plastic sealer has been added to improve the patch protection and remove undesirable vibrations. The patch installation process is depicted in Fig. 4.56. The two temperature transducers have been installed in both spar caps (blade central areas) using thermal paste to compensate possible temperature drifts.

The optical fiber channels have been connected to a commercial unit (Si425 of Micron Optics) for their interrogation. An electric signal coming from a

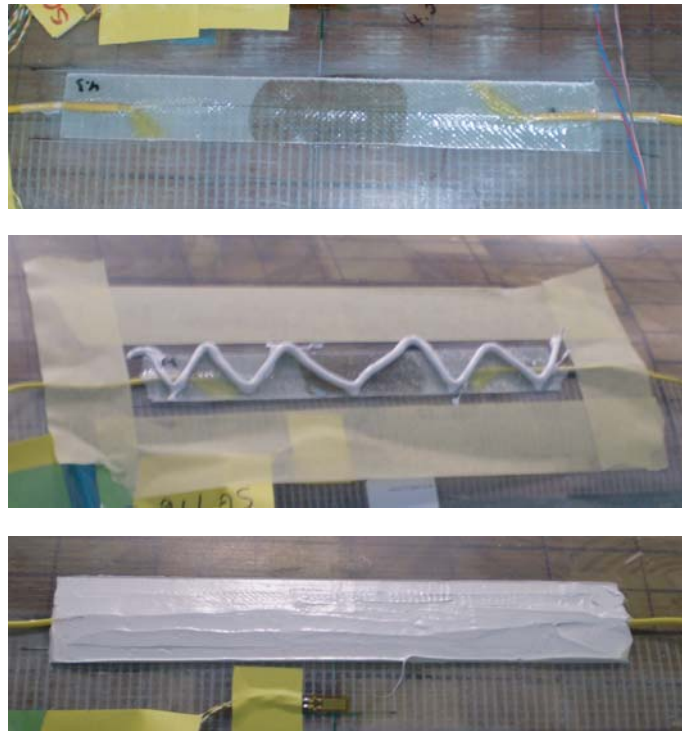


**Fig. 4.56.:** *A patch glued in its central area (top). Sealer application over a glued patch (middle). Patch finally installed (bottom). Courtesy of Aeroblade.*

loading cell has been recorded as reference signal using an Analog-Digital converter connected to a computer.

## Results

Several tests have been performed at the National Renewable Energy Center (Cener) at Navarra (Spain). The blade root was fixed to a concrete foundation while different wire ropes attached to pulling towers load the blade. A scheme of the loading facilities is depicted in Fig. 4.57.

Four loading tests to evaluate the blade response have been carried out: MEdge positive and negative and MFlat positive and negative (Fig. 4.55). In each test, one main direction of the blade is pulled while its root is fixed. Depending on the test, different start and end loads have been employed reaching a peak deformation above 101% of the designed maximum load. The achieved results are depicted in Fig. 4.58.

These results have been compared to loading cell signals and the maximum blade displacement is coherent with the measured peak deformations. In the

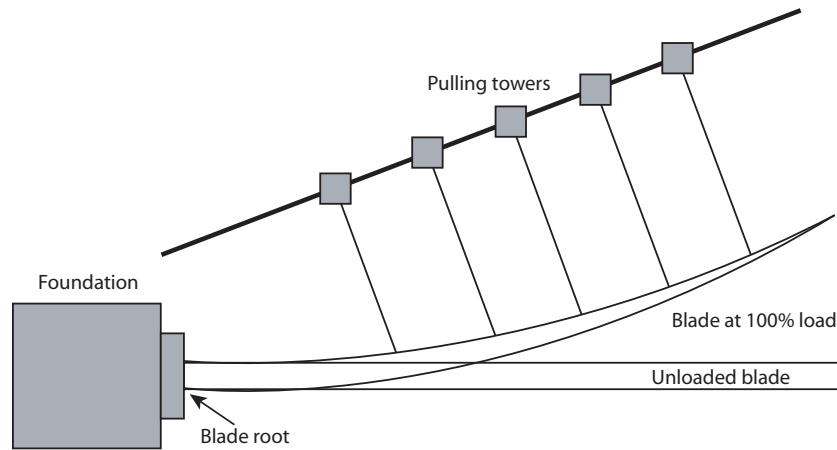


**Fig. 4.57.:** Scheme of the loading facilities at CENER (Navarra). Five towers pull from the blade fixed at root.

MEdge test, the most important measurements are given by the patches located at the leading and trailing edges (channels 2, 3 and 4). On the contrary, the spar caps patches (channels 1 and 5) provide useful data on MFlat tests achieving wavelength drifts above  $\Delta\lambda \geq 4 \text{ nm}$ . In Fig. 4.59, one of the most significant measurements (low spar cap patch) during the MFlat positive test is compared to the loading signal. The same linearity has been achieved in all of the loading tests.

### Specific remarks

A sensor system based on FBGs transducers has been employed to monitor the loading process of a full-scale wind turbine blade. FBG based strain gauges have been adapted to be installed on the structure surface by embedding them into a bigger composite patch. A total of 15 strain sensing points have been installed at three given distances from the blade root. Due to the short developing time of this work, the strain patches have been directly tested after their installation. However, the achieved results exhibited a great linearity and repeatability. Although the proposed solution has been adapted to its superficial installation, these results help to identify early problems of a full integrated sensing system.

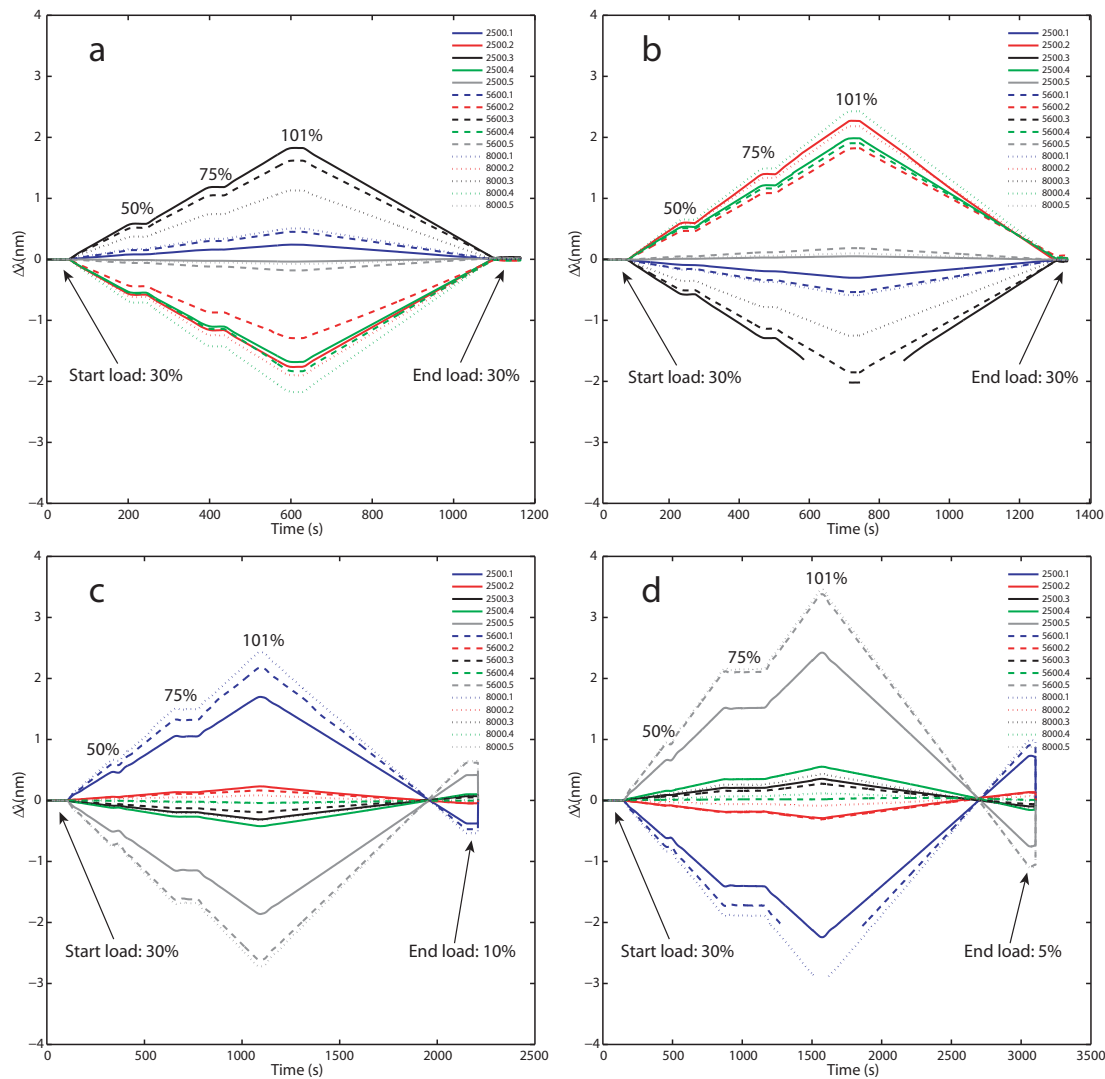


**Fig. 4.58.:** Measured deformations during *MEdge -* (a), *MEdge +* (b), *MFlat -* (c), *MFlat +* (d) tests.

### 4.3.5. Summary

In this section, different FBG based solutions have been proposed and verified to monitor specific properties of composite materials. Employing these new sensing capabilities, more complete models can be developed including new features beyond the usual ones (e.g. strain and temperature). Particularly, a new device to evaluate composite joints has been proposed to be employed in complex structures, detecting early failures. Another sensing head capable of monitoring the compaction pressure during the fabrication of a composite material and also capable of retrieving deformation values when

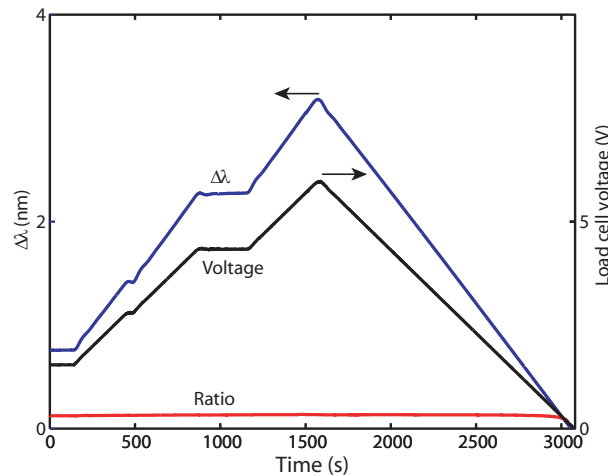


**Fig. 4.59.:** Measured strain on patch 2500.5 during the MFlat + test compared to the load cell signal.

the structure is under operation has also been developed. This new device allows a better tracking of composite materials, starting at their manufacturing process.

In addition to adding new sensing features to SHM models, a better implementation of existing FBG based strain sensors has also been addressed. By employing materials highly compatible with the hosting structure, a transducer design has been proposed and tested to bear real manufacturing conditions of large structures, dealing with high transverse pressures.

Finally, some of the technologies developed during this work have been tested in field applications. The first example was the embodiment of a FBG based transducer into a pre-stressed concrete beam to evaluate specific parameters. The second, and most challenging example, was the monitoring a full-scale wind turbine blade during loading tests.

## 4.4. Conclusions

Different aspects of FBG based sensors have been addressed in this chapter. Although this technology has been widely applied to many different engineering applications, there are still lots of new applications for these devices to be found. This chapter has been centered in three main sections where, starting from the improvement of traditional sensors, some final application examples

have been described.

Trying to improve the traditional interrogation methods of FBGs, different processing schemes have been proposed to retrieve the longitudinal axis deformation of FBGs just from the intensity of their reflection spectra. The proposed algorithms combine a custom defined error metric for spectral comparison and a Particle Swarm Optimization technique to get the deformation values of different FBG sections. This algorithm has been applied even to work with uniform FBGs, without spatial resolution limitations, by dividing the FBG length into  $N$  sections. This technique can be very useful for quasi-distributed sensing applications based on FBG technology by retrieving the individual intragrating strain distribution of several FBGs.

Also dealing with the improvement of the existing sensing methods, the following section was devoted to the widely addressed problem of temperature-strain discrimination. Although many different approaches have been reported to solve this problem based on composite materials, a wide set of solutions can be proposed to improve the discrimination. Using CFRP as host material, several sensing heads for strain-temperature discrimination based on embedding Fiber Bragg Gratings into composite plates have been designed and experimentally tested. The most interesting design relies on the drilling of two symmetrical holes to provoke different strain sensitivities to embedded FBGs. A temperature-independent strain sensor has also been manufactured and tested. By creating a non-uniform strain profile on an embedded long FBG, its spectral peak has been split into two, being its distance proportional to the plate deformation. Apart from applying the proposed designs as sensing elements, they can also be considered in the structure design to be included as structural parts, performing both tasks, mechanical reinforcement and sensing.

Considering that Smart Structures are very related to composite materials, OFS and particularly FBGs can be employed to measure specific parameters of composite structures. Employing these new sensing capabilities, more complete models can be developed including new features beyond the common used ones (i.e. strain and temperature). Different FBG based solutions were proposed regarding this point such as: a new device to evaluate composite joints of complex structures or a sensing head capable of monitoring the

compaction pressure during the fabrication of a composite material. These features can improve the existing structural models by detecting early stage failures.

Within the composite materials, a better implementation of existing FBG based strain sensors has also been addressed in addition to the measurement new features. By employing materials highly compatible with the hosting structure, a transducer design has been proposed and tested to bear real manufacturing conditions of large structures. Based on a resin block with two surrounding reinforcements, it has been designed to bear the high transverse pressures applied to the composite materials compaction. The achieved results exhibit a great repeatability and tolerance, enabling both design and process for industrial applications.

Employing some of the proposed FBG-based technologies for real challenges, different field applications have also been addressed. Related to civil engineering, a pre-stressed concrete beam has been monitored using embedded FBG transducers to measure specific parameters for a better understanding of the inner behavior of these materials. Another example was the monitoring of a full-scale wind turbine blade during its loading tests. This scenario deals with many challenges regarding actual Smart Structures and this experience gives rise to a better OFS development. Several conclusions can be retrieved from both examples but, in summary, both applications were useful for exhibiting the benefits of OFS techniques in the future Smart Structures development.

All the works described during this chapter are just a small increase to the existing state of the art, but several contributions have been obtained. Particularly, two emerging techniques for Smart Structures: composite materials and Fiber Bragg gratings have been merged and some benefits have arisen from their combination. As a result of this research, 5 journal articles, 4 international conference papers and 1 industrial patent have been published.



# Chapter 5

---

## Speckle based sensors using Polymer Optical Fibers

---

Polymer Optical Fiber (POF) based sensors claim to be a widespread technology in Smart Structures. Although optical losses in POFs are much higher than in conventional glass fibers, robustness, ease of handling and low cost have made them an attractive option for sensing applications in structural health monitoring [1, 2]. In this regard, POFs exhibit advantages including high elastic strain limits, high fracture toughness, and excellent flexibility and adaptability.

Based on multimode fibers, speckle interferometry has been studied and employed as a sensing tool by several authors [3–7]. These Fiber Speckle-gram Sensors (FSSs) based on speckle patterns and produced by coherent light within a multimode fiber, are known for their remarkable sensitivity to external perturbations. In addition, due to cost reductions in electronics, the FSS technique can be implemented as a low cost technology, but maintaining an extremely high sensitivity to different perturbations. Using FSS, several parameters have been successfully measured such as vibration [3, 7], micrometric displacements [4, 5], temperature [5] or angular alignments [6].

Combining POF and speckle approaches, different sensors and techniques

have been developed during this PhD work. Particularly, the sensitivity benefits of FSS have been studied for vibration sensing purposes (Section 5.2, *Vibration sensing*), demonstrating their applicability to heart rate measurements and even for seismic purposes. On the other hand, in Section 5.3 (*Strain sensing*) a processing scheme is proposed to extend the dynamic range of a speckle-based strain sensor. Finally, another processing scheme has been proposed to enhance the sensitivity of FSS, and it is detailed in Section 5.4 (*Radial speckle*).

## 5.1. Sensing principle

The speckle phenomenon in optical fibers has been treated by several authors [8–10]. It is generally considered that the number of speckles projected by a multimode optical fiber on a screen is approximately equal to the number of modes ( $M$ ) that the fiber supports [11]. For a step-index fiber, the number of modes is approximately  $M = V^2/2$  and for a graded-index fiber is  $M = V^2/4$ , where  $V$  is the normalized propagation constant. This value is defined as  $V = 2\pi a NA/\lambda$ , where  $NA$  is the numerical aperture of the fiber,  $\lambda$  the wavelength of the light source and  $a$  is the radius of the fiber core. For a multimode step-index fiber, the expression for  $M$  can be calculated by resolving the Helmholtz equation considering a plane wave rectilinearly polarized. Based on the ray model approximation, it can be considered that each mode has a different phase velocity caused by different optical paths, and at the output end of the fiber, each mode has a different spatial position.

When a coherent light is propagated through the fiber, the speckle phenomenon is defined as an interference between different modes and self-mode interaction [3]. The output speckle pattern (e.g. projected onto a screen) is composed of a large number of bright spots whose intensity varies slowly, mainly caused by environmental effects, but the total intensity of the speckle pattern remains constant.

Several changes in the fiber geometry and in the refraction index are caused when an external perturbation is applied to the fiber (such as temperature, pressure or strain). These changes also cause variations in the output speckle pattern distribution, but its total intensity remains constant. There is a model

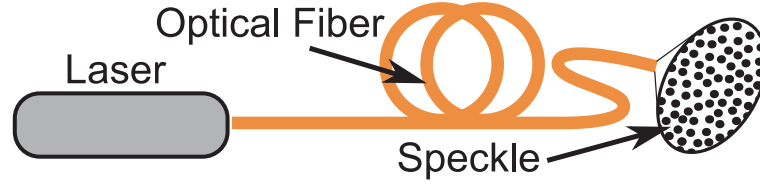


**Fig. 5.1.:** The speckle pattern (specklegram) of a multimode fiber projected to a screen.

[3] that determines the relation between the speckle pattern variation and the perturbation to be measured. This model considers that the mode propagation and the mode interference are both modified by the perturbation ( $F(t)$ ), that is reflected in the speckle intensity variation. This model is limited to small perturbations and the intensity of each speckle  $I_i$  can be calculated as the integration of the spatial intensity function for each speckle area:

$$I_i = A_i \cdot \{1 + B_i \cdot [\cos(\delta_i) - F(t) \cdot \phi_i \cdot \sin(\delta_i)]\}, \quad (5.1)$$

where  $A_i$  represents the self-mode interaction; and  $F(t)$ ,  $B_i$  and  $\delta_i$  define the interaction between different modes. Particularly,  $F(t)$  is the external perturbation of the fiber. The argument of the harmonic functions ( $\delta_i$ ) describes the difference in the propagation constant and the random phase of all the pairs of modes considered within the same speckle intensity  $I_i$ .  $A_i$ ,  $B_i$ ,  $\phi_i$  and  $\delta_i$  are constant values for any given  $i$ .

In order to extract the perturbation information ( $F(t)$ ), a differential processing method is applied to Eq. 5.1. The sum of the absolute value of the changes in all the signals is computed and can be described by:

$$\Delta I_T = \sum_{i=1}^N \left[ -A_i \cdot B_i \cdot \phi_i \cdot \frac{dF(t)}{dt} \cdot \sin(\delta_i) \right] = \left[ \sum_{i=1}^N C_i \cdot \sin(\delta_i) \right] \cdot \frac{dF(t)}{dt}. \quad (5.2)$$

In Eq. 5.2 the term within the brackets sums all the components of the speckle pattern, so the sum will remain constant despite local variations (the total energy is maintained). Eq. 5.2 can be written as:

$$\Delta I_T = \frac{dI_T}{dt} = C \cdot \frac{dF(t)}{dt} = C \cdot \Delta F. \quad (5.3)$$

Based on this approach, several sensors have been demonstrated [3, 12]. However, when the perturbation applied to the fiber is larger (not weak),

the approach required to achieve Eq. 5.3 is not valid, so the method is very limited in dynamic range. In the described model, only the self-mode and the mode-mode interactions are taken into account, while the physical process is much more complex. The influence of the radiated modes, propagation losses, bendings or micro-bendings has been ignored, so it can be assumed that more complex phenomena besides the self-mode and mode-mode interaction are produced. These effects in propagating waveguides have been analyzed by using the perturbation theory [13]. By observing a speckle pattern evolution, when a large perturbation is applied, the individual speckle area and position change, indicating a redistribution in the modal state energy. Obtaining an analytical description of all these phenomena is not a trivial task. However, a correlation between the speckle distribution and the external perturbation can be computed using the available computer methods.

## 5.2. Vibration sensing

The high speckle sensitivity to external perturbations has been studied for vibration sensing purposes. Although having a very high sensitivity increases the final noise, it also allows the FSS application to measure extremely low perturbations (e.g. heart monitoring or seismic activity). Several optical and physical parameters contribute to the final FSS sensitivity, requiring a specific POF selection for each application.

In this work, a differential processing scheme exploits the sensitivity of specklegram sensors based on different POFs. Employing a simple differential processing scheme, three different POFs have been tested to measure their vibration sensitivity using a CCD camera. This technique has been experimentally employed in two different applications: a heart rate sensor based on a cheap CCD camera and a low cost sensor system for seismic monitoring.

### 5.2.1. Differential processing

Trying to take advantage of the FSS sensitivity, a differential processing scheme is proposed to obtain vibration measurements. As detailed in the previous section and demonstrated in [12], the specklegram correlation is proportional to the strain but just when the perturbation ( $\Delta F$ ) is small enough.

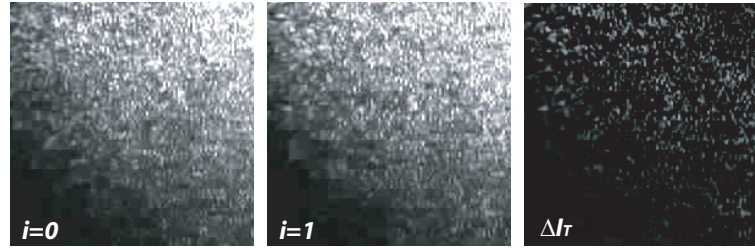


**Fig. 5.2.:** Two consecutive specklegrams and their differential processed image.

The correlation between specklegrams is useful within the same modal state when it is proportional to the external perturbation. Based on this approach and following the notation (Eq. 5.3), a differentially processed sequence for two specklegrams of  $N \times M$  pixels can be defined as follows:

$$D\{i\} = \Delta I_T\{i-1, i\} = \frac{1}{K \cdot N \cdot M} \sum_{n=1}^N \sum_{m=1}^M |p_{n,m}^{(i-1)} - p_{n,m}^i|, \quad (5.4)$$

where  $K$  is the full scale value of the specklegram colormap (e.g.  $K = 255$  for 8-bit grayscale) and  $p_{n,m}$  corresponds to the pixel of the  $n, m$  position of the specklegram  $i$ .

The differential intensity variation (Eq. 5.4) is proportional to the small variations caused by the perturbation between two consecutive specklegrams. Although the dynamic range of this approach is very limited [12], it is perfectly valid when the capturing sampling frequency is high enough (e.g. video standard: 30 Hz). Given that this method is only related to the current and previous specklegrams, all long term drifts (such as temperature) are removed from the sensor system.

### 5.2.2. Experiments and results

Several parameters contribute to the final sensitivity of a FSS, both optical and physical. Particularly, the speckle size is related to the FSS sensitivity. A fiber with a larger number of modes has smaller speckles, which is usually more sensitive and, therefore, more noisy. Trying to analyze the optical response of specklegram sensors and the influence of their mechanical properties to the final sensitivity, different POFs have been characterized for their application as sensing heads.

Manufacturer	Mitsubishi Rayon	Mitsubishi Rayon	Chromis Fiberoptics
Core diameter	980 $\mu m$	240 $\mu m$	50 $\mu m$
Fiber diameter	1 mm	250 $\mu m$	250 $\mu m$
Core material	PMMA	PMMA	PF
Profile	step-index	step-index	graded-index
Refractive index ( $n_{co}$ )	1.49	1.49	1.358
Numerical Aperture	0.5	0.5	0.2
Weight (mg/m)	1000	60	60
Number of modes <sup>a</sup>	3082691	184884	665

<sup>a</sup>for  $\lambda = 0.6328\mu m$

**Table 5.1.:** Characteristics of the tested optical fibers.

Two step-index and a graded-index POFs have been tested. With core diameters of 980, 240 and 50  $\mu m$  and external diameters of 1 mm, 250 and 250  $\mu m$  respectively, the two step-index are of different material (Polymethyl methacrylate, PMMA) than the graded-index (Perfluorinated polymer, PF). The different properties of the tested optical fibers are detailed in Table 5.1.

### 5.2.2.1. Experimental setup

Each fiber has been tested employing the same experimental setup: a cylindrical PZT actuator of 40 mm of external diameter (manufactured by PI) has been surrounded with the fiber under test with a single lap. A He-Ne laser ( $\lambda = 0.6328nm$ ) was attached to a fiber end while the other, that projects the speckle pattern, was connected to a high speed CCD camera (Pixelink PLA-741). A FBG has also been glued to the PZT surface to obtain its deformation. The camera, the PZT modulator and the FBG interrogation unit (Micron Si425-500) were connected to a computer to control the experiment as depicted in Fig. 5.3.

The PZT actuator was modulated by applying a sinusoidal wave varying its frequency and amplitude from 1 to 25 Hz and from 500 to 1000 peak to peak volts, respectively. A sweep of 6 steps in the amplitude range and for 5 different frequencies has been performed for each fiber (a total of 3 x 30 different cases). For each modulation step, the modulation wave was maintained for 30 seconds

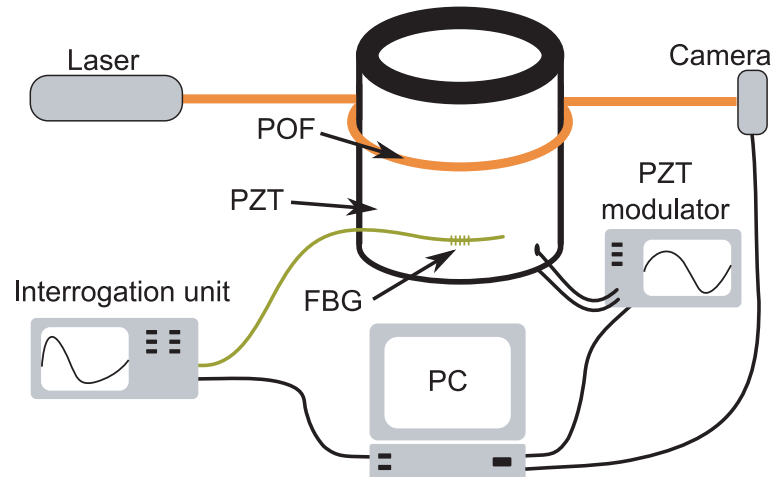


**Fig. 5.3.:** Experimental setup employed in the fiber characterization.

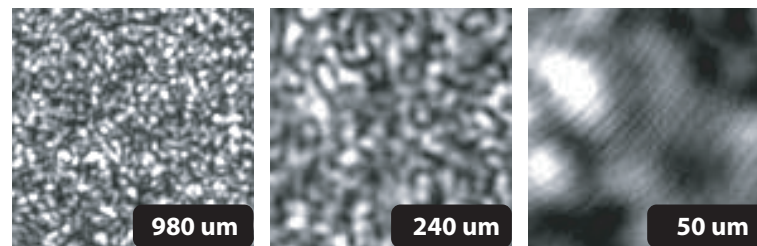


**Fig. 5.4.:** Different speckle patterns obtained with the tested POFs of 980  $\mu\text{m}$ , 240  $\mu\text{m}$  and 50  $\mu\text{m}$  core diameter, respectively. As the number of modes increases, the speckle becomes smaller.

to get an averaged value of the speckle value. The capturing rate of the CCD camera was set at 250 frames per second and its resolution limited to 96 by 96 pixels to reduce the amount of data. An example of three recorded specklegrams of the different fibers is depicted in Fig. 5.4

After capturing the video sequences, the same processing method has been employed for every tested case. A differential operation has been applied between two consecutive frames (Eq. 5.4) obtaining a sequence of the video length, whose values are related to the speckle pattern variation. This sequence has been low pass filtered to reduce the noise before detecting the peaks of the sinusoidal wave. The resulting peak-to-peak values have been averaged for several cycles to reduce the total noise. The same low-pass filter and peak detection schemes have been employed to the FBG signal to obtain the reference values. An example of the processing sequence is depicted in Fig. 5.5.

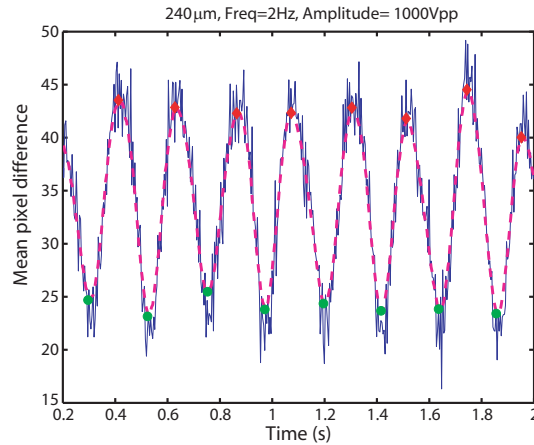


**Fig. 5.5.:** The differential sequence (solid line) is low-pass filtered (dotted line) before detecting the peaks of the sinusoidal wave (maximums with diamonds and minimums with circles).

### 5.2.2.2. Results

The PZT deformation is proportional to the control voltage. The computed pixel difference for each deformation and frequency is compared to the FBG measurements in Fig. 5.6. Due to the proposed differential processing scheme, this sensing method is more sensitive for higher frequencies, but always far from the maximum sampling rate of the camera. The two tested fibers with a higher number of modes have a very good linear response to the applied deformation, having a coefficient of determination ( $R^2$ ) above 0.99, being the higher frequency test the best scenario. On the contrary, the less sensitive fiber ( $50 \mu m$ ) fits worse the linear response even for the best case (at 25 Hz).

The amount of contained light granules (speckles) in a specklegram depends on the fiber core diameter (Fig. 5.4). The sensitivity of a FSS is related to the amount and size of speckles generated by multimode fibers. However, based on the achieved results, this is not the only reason because a fiber with less modes ( $240 \mu m$ ) exhibits a higher sensitivity than other with much more modes ( $980 \mu m$ ). Another interesting influence is given by the fiber mass: a light fiber is easily moved by a mechanical perturbation. The mass difference between the  $980$  and the  $240 \mu m$  contribute to their sensitivity variation. On the other hand, the other light fiber ( $50 \mu m$ ) also shows a low sensitivity due to its lower number of modes.

Although the achieved sensitivity depends drastically on the sampling rate

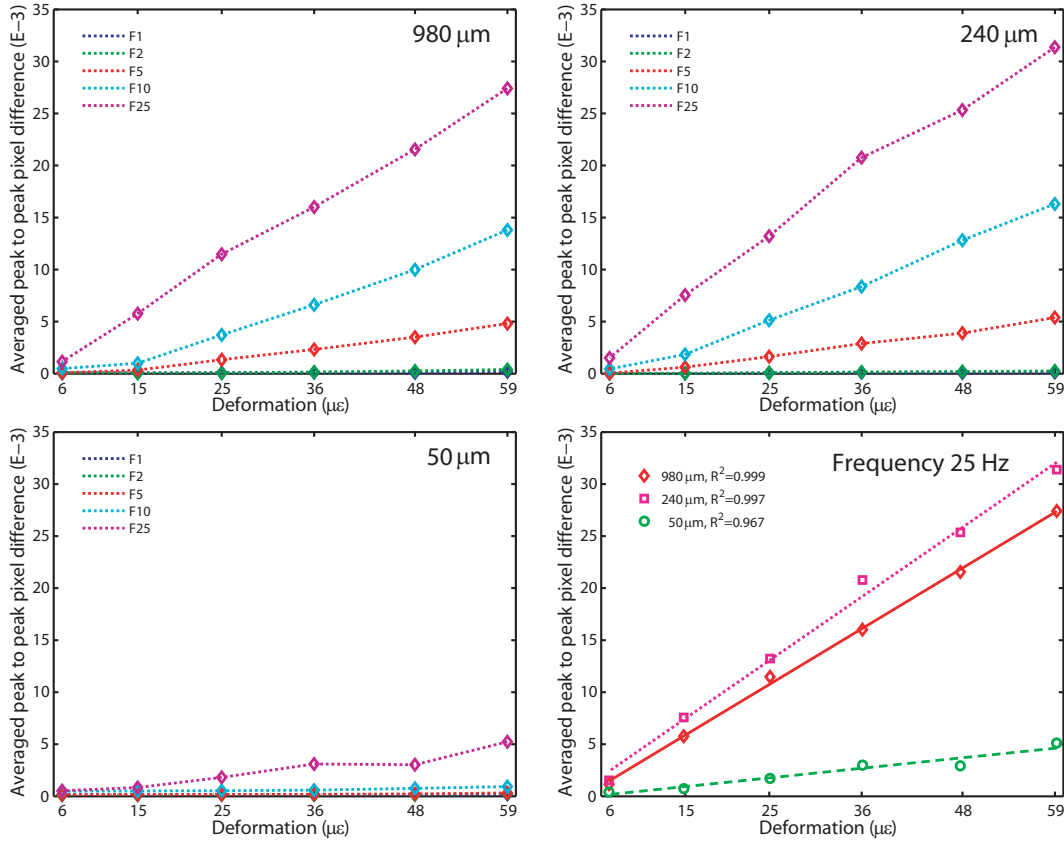


**Fig. 5.6.:** Measured response of the three tested fibers against the deformation measured by the FBG.

employed in the camera, the general response of each FSS must be maintained because it is related to their optical and mechanical parameters. Two fiber with a similar number of modes and mass should give rise to similar sensitivities, but when the chosen fiber is heavy, its mechanical response will become smoother, thus decreasing the sensor sensitivity. Regarding the number of modes, having a smaller speckle size (that is related to the number of modes) normally increases the sensor sensitivity to an external perturbation, but it also increases the final noise.

Based on the experimental characterization of different multimode fibers, two different benefits can be exploited in FSSs. Particularly, a low sensitive fiber ( $50 \mu m$ ) has been applied to the heart rate measurement, application where noise is a critical factor. On the other hand, a high sensitive fiber ( $240 \mu m$ ) has been employed to build a seismic sensor, where high frequency sensitivity is required.

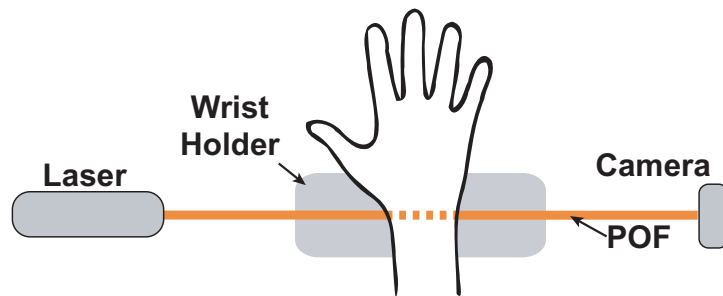


Fig. 5.7.: Setup employed for heart rate monitoring.

### 5.2.3. Heart rate detection

Employing the differential processing and having into account the experimental characterization of different POFs, a specklegram sensor has been proposed to monitor the human heart rate. FSSs have enough sensitivity to detect the pressure variation on wrists and also to deal with small movements of the wrist.

Based on the previous results, the low sensitivity fiber (GI,  $50 \mu m$ ) has been chosen for this application. Attaching a commercial web-cam to a fiber side and a cheap laser diode to the other, a short length of the fiber was placed into a plastic holder to house the wrist. The proposed setup is depicted in Fig. 5.7.

The bottom side of a wrist is placed on the top of the plastic holder, being the wrist directly in contact to the optical fiber. Pressure variations on wrist veins are transferred to the optical fiber, what modifies the projected speckle pattern. The sequences of 100 by 100 pixels specklegrams have been acquired at 30 frames per second and differentially processed. The heart rate of two different people have been measured using the proposed sensor and are depicted in Fig. 5.8

Both specklegram sequences have been differentially processed and normalized for viewing purposes. Based on the differential sequence, sharp peaks of each sequence have been identified to calculate both heart rates (43.5 and 78.9 bpm). Wrist position is a critical point, as can be noticed in the peak value variations due to slight wrist movements and on the noise background. Although these sequences can be enhanced employing low pass filters, the chosen low sensitivity POF and camera sampling rate are enough for achieving a

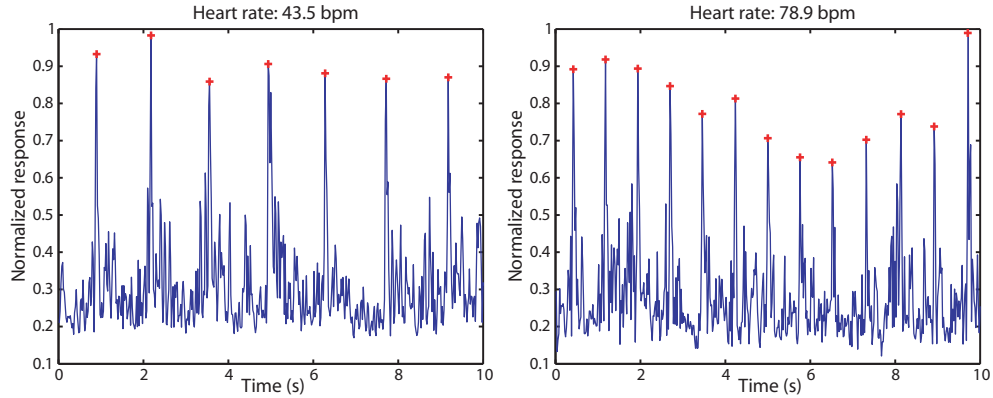


**Fig. 5.8.:** Heart rate of two people measured using the proposed POF-based sensor.

clean heart beat detection.

Several parameters contribute to the final performance: the employed POF or the camera sampling rate, but isolating the POF from other external perturbations is the greatest challenge. Particularly, the proposed setup has been designed to be easy to test, not to achieve a high performance. In a real scenario, a POF surrounding the wrist should be more sensitive to heart beat detection and both laser and camera can be included into the sensing head.

#### 5.2.4. Seismic sensor

Other different vibration monitoring application has also been addressed using FSSs. Based on the previous characterization, a high sensitive POF (240  $\mu\text{m}$ ) has been employed to build a highly sensitive sensor for environmental vibration. The proposed sensor is depicted in Fig. 5.9. A cheap laser diode for illumination and a standard web-cam to record the specklegram sequences have been combined to a piece of POF vertically suspended into a closed tube.

A fiber length of  $L \approx 40 \text{ cm}$  isolated from air vibrations has been glued to a plastic ring on its bottom edge. This ring has been also attached to an USB camera to center the speckle pattern directly to the CCD. The end of the fiber has been directly attached to the camera to reduce the CCD exposition time and get clearer images under moving conditions. The plastic ring also fixes the lower end of the fiber to the camera, maintaining the position of the speckle pattern over the camera. With the resulting setup, the suspended fiber is slightly tightened between the upper fixing point and the plastic ring.

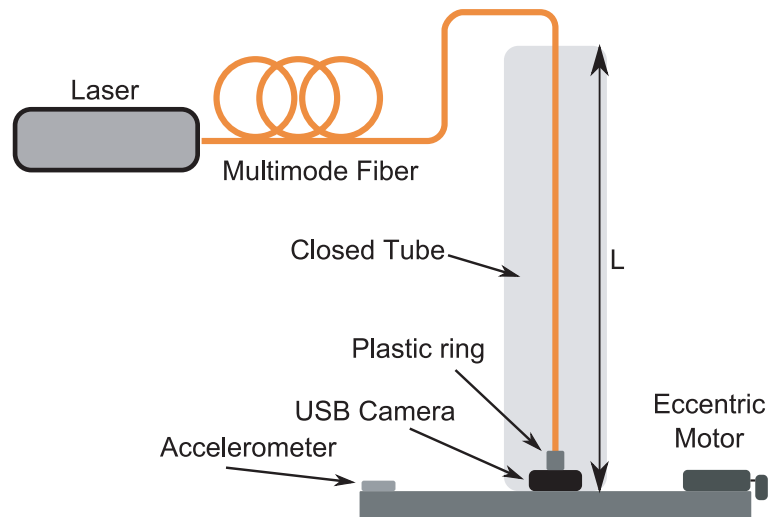


**Fig. 5.9.:** Setup employed for measuring environmental vibration.

Each vibration causes a little displacement between the top and bottom parts of the tube, what deforms the suspended POF and produces a speckle pattern variation.

The whole vertical tube has been attached to a table where an eccentric DC motor has also been fixed to generate small vibrations between 1 and 10 Hz. A commercial accelerometer (ADXL311) with a  $\pm 2 G$  range has been glued to the table surface to monitor the main axis vibration. Based on the described setup (Fig. 5.9), different sweeps have been performed varying the DC voltage of the eccentric motor and causing different accelerations. Due to the great amount of modes present in the chosen fiber, with a small section of the whole camera image is enough for the later processing. Particularly, in this application a 100 by 100 pixels resolution has been recorded at 30 frames per second.

All the specklegram sequences have been differentially processed and normalized for viewing purposes. In Fig.5.10 (left), a differentially processed sequence of 14 steps sweep is depicted. These differential values have been averaged (100 samples) for each vibration step and compared to the measured acceleration (Fig. 5.10, right).

The first and last speckle processed points have been measured under non vibration induced conditions, establishing the noise threshold. The same evolution is observed in both measurement sets, being remarkably linear against

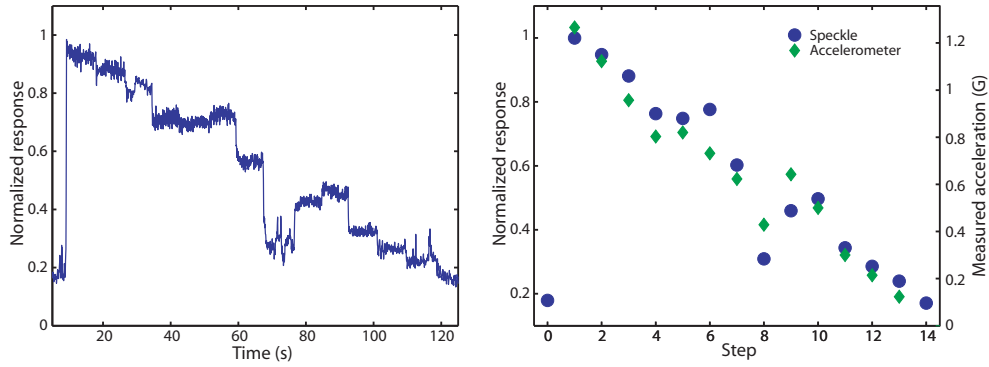


**Fig. 5.10.:** Normalized differential processed sequenced (left) and averaged differential values (circles) compared to measured acceleration (diamonds, right).

the motor control voltage (different steps). A drop on both sets can be noticed at  $t \approx 70$  s caused by the resonant frequency of the motor fixing piece. In addition to the mechanical response of the holding structure, the acceleration measurements show a high noise component introducing an uncertainty of  $\epsilon \approx \pm 0.05$  G.

Although different parameters of the proposed setup may vary the final sensitivity: type of fiber, fiber length, end ring dimensions and so on, the proposed sensing head has been experimentally tested, showing enough sensitivity to measure very low vibrations, exhibiting the benefits of FSS for vibration monitoring using low cost optoelectronics elements.

### 5.2.5. Summary

Different sensing heads for dynamic perturbations have been proposed and experimentally verified. A simple differential processing scheme has been applied to recover the perturbation from the measured specklegram sequences. Employing a relative high sampling rate (above 30 Hz), perturbations between two consecutive specklegrams can be considered low, being the speckle pattern variation proportional to the perturbation.

Three different multimode POFs have been characterized for their application to vibration sensing purposes. Different properties, both optical and mechanical, contribute to their final response, but different benefits of FSSs can be exploited for each application. Based on the achieved results, two vibration sensing applications have been proposed and experimentally verified.

A sensing head to measure the human heart rate and an experimental setup for environmental vibration monitoring have been successfully tested, employing cheap optoelectronic components. The proposed sensors exhibit high sensitivities to mechanical perturbations and can be implemented using low cost commercial devices.

### **5.3. Strain sensing**

FSSs have been successfully employed for high sensitivity applications in many different scenarios. However, most of the reported applications are far from measuring key parameters for structural monitoring (e.g. strain) due to the limited dynamic range or the over-sensitivity and cross-sensitivity of the FSS principle. Nevertheless, a strain measurement scheme based on FSS has been reported [12] by adhering multimode optical fibers to a cantilever beam and measuring the speckle intensity variation that is proportional to the applied strain. The achieved results exhibit a good linearity, but this scheme is limited in dynamic range because it is based on a weak perturbation approximation.

Specklegram based sensors have been also combined with some photorefractive materials to stabilize the processed sequences [14, 15]. This effect can be applied to reduce the extra noise due to the typical oversensitivity of specklegrams and to extend the dynamic range for slow varying perturbations. However, these kind of materials are not suitable for low cost applications.

Taking advantage of the cost reduction on computation technologies, a new processing scheme to extend the dynamic range of Fiber Specklegram Sensors is proposed and demonstrated. The designed algorithm employs the morphological differences between two specklegrams under very different perturbations to determine key-specklegrams as reference points. The speckle intensity variation is computed to the closest key-specklegram and the absolute strain can be obtained by employing this partial variation. A FSS has been embedded into a composite beam and several strain tests have been performed. The obtained specklegram sequence has been morphologically processed obtaining a very good performance. The proposed scheme is also suitable for applications where cost is a critical point.

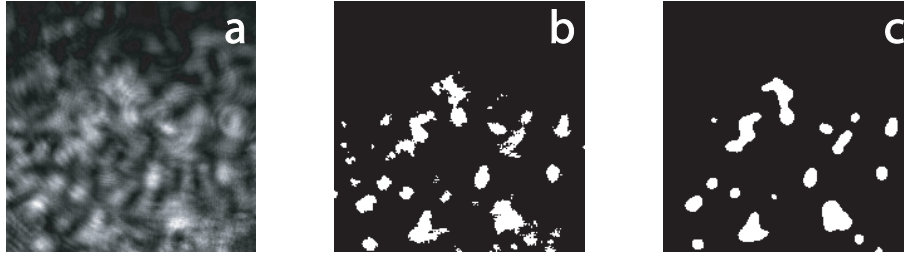


**Fig. 5.11.:** *Preprocessing steps. A 200x200 pixels gray level image of a specklegram (a). The same specklegram thresholded (b) and filtered (c).*

### 5.3.1. Morphological processing

The specklegram correlation is proportional to the strain but just when  $\Delta F$  is small enough [12]. The correlation between specklegrams is useful within the same modal state when it is proportional to the external perturbation. Given that the correlation is not a useful metric to compare two specklegrams of different modal states, a different approach is required. The morphological processing obtains the distribution of the different bright speckles and employs it to “define” the specklegram characteristics. Thus, to extend the dynamic range through different modal states, the correlation term may be computed to different Key-Specklegrams (KSs) associated with the different modal states. These KSs are determined during the sensor calibration ramp and they are associated with a strain value, establishing different local reference points corresponding to the different modal states. The incorrect determination of the KSs may lead to a wrong sensor performance.

In the morphological processing, the specklegram is converted to a binary image (using a threshold) and the different white spots (associated with bright speckles) are defined from their X-Y position and area. After the thresholding, a circular averaging filter is employed to reduce the sharpness of the obtained dots. This filtering creates a clustering effect by combining several small dots into a bigger one, reducing the final noise. This noise reduction is more significant when the bright speckles are close to the threshold, where a big spot can be decomposed into several smaller ones.

The obtained spots are sorted by area, making the larger ones more relevant. The list of sorted spots is the geometrical representation of a specklegram and it defines its high level morphological structure. Once the structure of a speck-

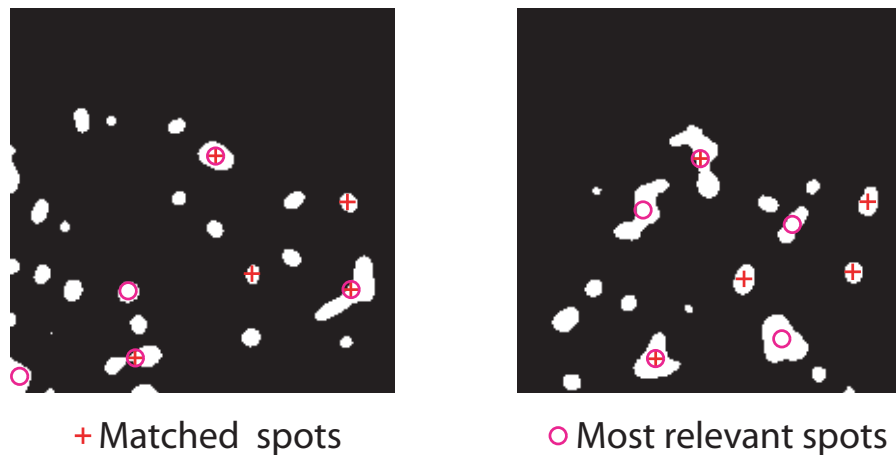


**Fig. 5.12.:** *Morphological comparison between two specklegrams of different modal states.*

legram has been determined, the spots with larger areas of both specklegrams are compared to the closest ones taking into account their position. After having established the spot correspondence, their area difference is calculated and normalized against the total area. This value is related to the amount of coincident bright speckles between the two specklegrams, which is also related to the coincidence (or not) of the modal state. A high error value indicates a completely different bright speckle distribution, what implies a different modal state.

In Fig.5.12 two specklegrams of different modal states are depicted. The five spots with the larger areas (most relevant) are marked with circles for both images. The five most relevant coincident spots between specklegrams are also marked with crosses. In this case, most of the bright speckle area is not coincident (three of the most relevant spots of the right specklegram are not matched) so the obtained value is high, indicating a different modal state.

Strain specklegram sensors need to be calibrated before their application and, consequently, a calibration procedure is required. During this step, a controlled strain ramp is applied to the POF while the specklegrams are acquired. When the applied perturbation (e.g. strain) is high enough, the modal state is not maintained and the speckle intensity variation ( $\Delta I_T$ ) does not replicate the perturbation. The morphological metric is employed to identify the different modal states during the calibration ramp and to establish their correspondent KSs to have local reference points (KSs), where the speckle intensity variation will be calculated. This parameter, for two specklegrams of

$N \times M$  pixels, can be defined as follows:

$$\Delta I_T\{i, j\} = \frac{1}{K \cdot N \cdot M} \sum_{n=1}^N \sum_{m=1}^M |p_{n,m}^i - p_{n,m}^j|, \quad (5.5)$$

where  $K$  is the full scale value of the specklegram colormap (e.g.  $K = 255$  for 8-bit grayscale) and  $p_{n,m}$  corresponds to the pixel of the  $n, m$  position of the specklegram  $i$  or  $j$ . Applying this notation to Eq. 5.3, the perturbation value of the  $i$ -th specklegram under a weak perturbation having the initial specklegram as reference can be obtained with:

$$\Delta F\{i\} = \frac{1}{C} \cdot \Delta I_T\{0, i\} = L_0 \cdot \Delta I_T\{0, i\}, \quad (5.6)$$

being  $L_0$  the proportionality constant (slope) between the speckle intensity variation (between the  $i$ -th and the first specklegram). During the sensor calibration step, different KSs are detected and their associated slopes ( $L_{KS(k)}$ ) and strain values ( $S_{KS(k)}$ ) are also saved. Consequently, when a new specklegram is available,  $I(i)$ , it can be evaluated in terms of its closest KS under the weak perturbation assumption. The speckle intensity variation of the incoming specklegram is calculated with all the stored KSs. The closest is employed as a strain reference and, with its slope, the strain value can be calculated. The second closest KS is employed to indicate the direction ( $d(i)$ ) of the calculated strain offset. The absolute strain value can be obtained as:

$$Strain(i) = \Delta F\{i\} = S_{KS(i)} + d(i) \cdot L_{KS(i)} \cdot I_T\{KS(i), i\}, \quad (5.7)$$

where  $KS(i)$  denotes the KS associated with the  $I(i)$  specklegram;  $S_{KS(i)}$  and  $L_{KS(i)}$  denote the strain value and slope correspondent to the KS associated with the  $i$ -th specklegram and  $d(i) \in [-1, 1]$  describes the intensity variation direction (positive or negative). However, for the incoming specklegrams falling in the middle of two KSs, the final strain value is obtained as the mean value of both references. This effect is detected when the two closest KSs intensity variations are very similar. The absolute strain value under this assumption is computed as:

$$Strain(i) = \frac{1}{2} \cdot \left[ S_{KS(i)_1} + d(i) \cdot L_{KS(i)_1} \cdot I_T\{KS(i)_1, i\} \right] + \frac{1}{2} \cdot \left[ S_{KS(i)_2} - d(i) \cdot L_{KS(i)_2} \cdot I_T\{KS(i)_2, i\} \right], \quad (5.8)$$

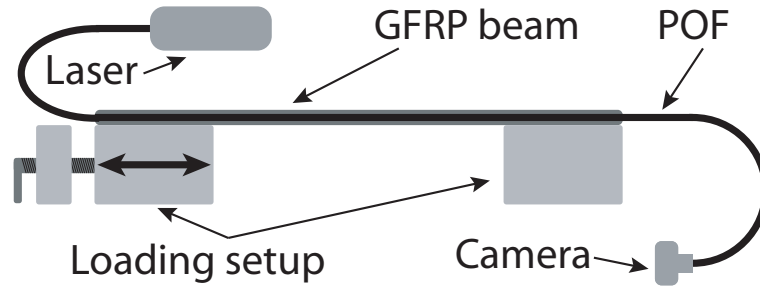


**Fig. 5.13.:** *Experimental setup. The POF is attached to a laser diode and a CCD camera. The FBG is interrogated using a commercial unit.*

where  $KS(i)_1$  and  $KS(i)_2$  denote the two KS with lower intensity variations with the  $i$ -th specklegram. This averaging step reduces the amount of noise in transition areas when the distance (intensity variation) between two specklegrams is very close.

### 5.3.2. Experiments and results

The described processing scheme has been tested with an experimental strain measurement. For this purpose, a Glass Fiber Reinforced Plastic (GFRP) beam has been manufactured with an embedded easy-to-handle POF. The chosen POF has a core diameter of  $d_c = 50 \mu m$  and an external diameter of  $d_o = 250 \mu m$ . A graded-index profile has been also chosen to reduce the number of modes, thus decreasing the noise. A Fiber Bragg Grating written in a standard telecommunications fiber has been also embedded to obtain the strain reference for the calibration ramp and further measurements. The beam has a constant thickness of 2 mm and a final size of 400x60 mm.

#### 5.3.2.1. Setup

The beam is fixed in one side and the other is attached to a mobile part connected to a screw that stretches the whole beam uniformly. An edge of the POF is connected to a cheap laser diode and the other side is connected to a CCD camera (Pixelink PL-A741). The FBG is attached to a Fibersensing FS4200 interrogation unit to obtain the reference strain value of each experiment. The whole setup is depicted in Fig. 5.13.

Several increasing and decreasing strain ramps were applied to the beam provoking a maximum deformation of  $\Delta s \approx 200 \mu\epsilon$ . The strain was uniformly

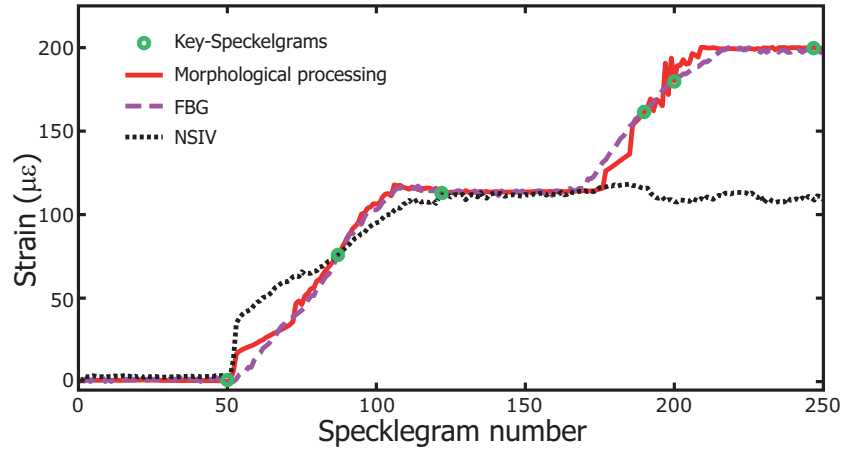


**Fig. 5.14.:** Calibration strain ramp. Strain values obtained with the morphological processing (solid line) are compared against the strain measured with the FBG (dashed line). The values proportional to the speckle intensity variation are also plotted (dotted line).

distributed along the 400 mm of the stretched beam. During the experiment, the first increasing ramp was employed for the sensor calibration. The rest of the measured values were used to study the performance of the sensor out of the calibration ramp. Specklegrams were captured at 25 frames per second.

### 5.3.2.2. Results and discussion

The morphological processing scheme was applied to obtain the KSs of an increasing strain ramp. For the analyzed data, the processing scheme obtained five KSs during the calibration step (the last one was added to determine the direction of the strain values above the last KS). Once the calibration procedure was finished, the same specklegrams sequence was employed to estimate the strain using the proposed method.

In Fig.5.14 the five identified KSs (circles) are plotted over the reference strain value (obtained with the FBG). The strain values obtained using the morphological processing are also depicted (solid line) and compared to the correlation processed ones (dotted line). The correlation method (Normalized Speckle Intensity Variation, NSIV) is described in [12] and it is limited to small deformations because it is only valid for the same modal state. As can be observed in Fig. 5.14, when the deformation is large enough to change the modal state, the correlation method is useless because specklegrams can not be

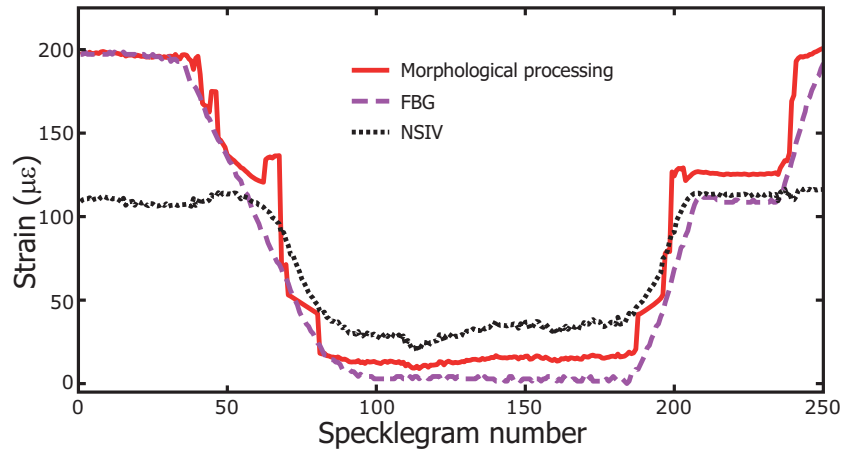


**Fig. 5.15.:** Strain values obtained with the morphological method (solid line) are compared against the strain measured with the FBG (dashed line) during strain ramps not included in the calibration. The values proportional to the speckle intensity variation are also plotted (dotted line).

directly compared. The achieved accuracy within the calibration ramp of the morphological scheme is remarkable, being always under  $\max(\Delta s) \approx 29.0\mu\epsilon$  with a mean error of  $\overline{\Delta s} \approx 5.6\mu\epsilon$ , good enough for the majority of structural applications. However, the case under analysis is an optimistic situation where the application scenario is exactly the same as the testing one. Consequently, the same calibration parameters have been also employed to test the sensor with other strain ramps.

A more realistic scenario is depicted in Fig. 5.15, where the calibration parameters obtained in the previous ramp (Fig. 5.14) have been applied to process specklegrams from other increasing and decreasing ramps. The KSs employed during this test are the same ones established during the calibration test. The morphological processed values (solid line) are plotted against the strain reference (dashed line) and the NSIV values (dotted line). The accuracy of the morphological method is not as good as the previous one, but it is still remarkably good for many structural applications, having a mean strain error of  $\overline{\Delta s} \approx 13.2\mu\epsilon$  and a maximum of  $\max(\Delta s) \approx 65.1\mu\epsilon$ . The worst cases are located during a transition between two reference KSs. This particular test indicates the suitability of the proposed processing scheme to work with a good response out of the calibration area, despite the noisy nature of the specklegram sensors. In addition, the maximum strain error is obtained during

the transition between KSs, when distances to both references are larger, but this error is not proportional to the sensor dynamic range. Several factors are contributing to the final error, but one of the most significant is to light up the sensor with a multimode POF what varies the modal state before reaching the sensing area. This problem can be reduced by using a monomode fiber to carry the light to the sensing area as proposed in [12], or by locating the CCD camera right at the end of the sensing area, reducing the extra perturbations.

Although the obtained accuracy, using the correlation term to calculate the strain deviation in the morphological processing, is good enough for many applications, it can be improved by employing other comparison methods less noise dependent. The morphological scheme has also been tried as a method to obtain the strain deviation over a KS, but, due to its noise immunity, it has proved to be useless to perform this task. Some trade-off between noise immunity (morphological scheme) and sensitiveness (correlation) is required for a metric to obtain strain from specklegrams in real scenarios.

The dynamic range of the proposed technique is mainly limited by the KSs detection, when two equal KSs arise from the calibration ramp. Having identical KSs may lead the strain reconstruction to a wrong value. The probability of reaching two equal KSs is given by several factors such as the number of speckles of the specklegrams (proportional to the number of modes of an optical fiber) or the captured spot area and resolution. Based on the experimental tests, the probability of reaching two equal KSs with the proposed setup is very low, enabling this technique to be applied to full-range applications (e.g. 5000  $\mu\epsilon$ ) without modifying the setup.

### 5.3.3. Summary

A morphological processing method to enhance the dynamic range of Specklegram strain sensors has been proposed and demonstrated. The proposed method analyzes the geometrical properties of the specklegram to determine if the modal state of the hosting multimode fiber remains unaltered. Once the working range of each modal state is established (given by its associated Key-Specklegram), the correlation between the incoming specklegram and the KS is employed to obtain the absolute strain value. The processing scheme has been experimentally checked, exhibiting a great accuracy even with speck-

legrams not considered in the calibration steps, obtaining a final mean error of  $\overline{\Delta s} \approx 13.2\mu\epsilon$ . A low cost implementation of the proposed scheme is possible, enabling this method for different sensing purposes.

## 5.4. Radial speckle

Different approaches to obtain external perturbations of FSS have been described in the previous sections. Based on different processing schemes, several sensing heads have been experimentally tested to retrieve dynamic (e.g. vibration) or static perturbations (e.g. strain). Nevertheless, all the described methods employ each specklegram as a sample and the retrieved information comes from the difference between specklegrams (either employing differential or morphological processing). However, from each individual specklegram, valuable statistical information regarding the POF modal distribution can be obtained.

Approximating the propagation within a multimode fiber by the ray model [16], some modal distributions in the speckle pattern can be established. Low order modes, whose optical path are close to the fiber longitudinal axis, will interfere (produce speckle dots or darks) centered in the middle of the speckle pattern. On the contrary, high order modes, whose optical path passes far from the longitudinal fiber axis, will produce speckle dots (or darks) all over the output speckle pattern. As the order of the modes decreases, their output positions change from being confined in the middle of the spot to be distributed all over the output speckle pattern. Thus, when the number of modes of the employed optical fiber is high, statistically, the outer speckle dots are caused by the interference of the higher order modes, which are more influenced by the perturbation to be measured. Otherwise, the speckle pattern center is mainly driven by low order modes that are less sensitive to external perturbations.

Based on this statistical approximation of mode propagation and its position within the output specklegram, the outer areas of the speckle pattern exhibit different sensitivities than those situated closer to the center. During this work, a processing method that tries to exploit this sensitivity difference has been proposed and experimentally verified. Based on a radial processing scheme, different sensitivities can be obtained from the same specklegram

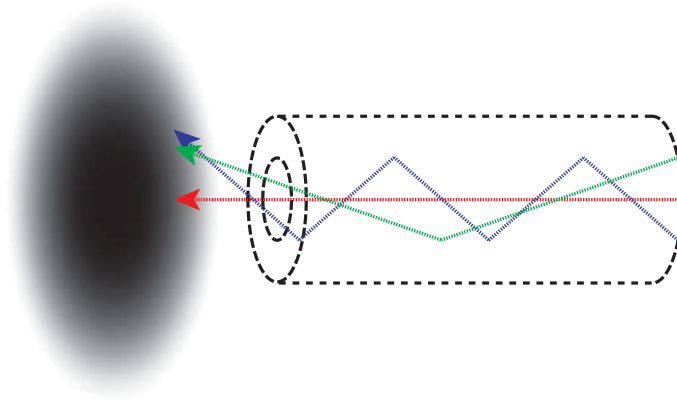


**Fig. 5.16.:** *Low order modes interfere in the speckle pattern center. High order modes are spread over the pattern.*

sequence, taking advantage of the spatial information within each individual speckle pattern.

### 5.4.1. Radial processing

Beyond extracting information only from differences between specklegrams, this method retrieves information from each specklegram. Based on the statistical relation between modal orders and speckle dot positions, the differential processing scheme has been adapted by employing rings of different radius instead of the whole speckle pattern. These rings are defined as a binary mask  $R_{n,m}$  that is non-zero for each pixel within the ring area  $(n, m)$ . Given that the number of pixels of each ring is not the same, the correlation value has to be scaled with the processed area to obtain the correlation per pixel. For any specklegram pair  $(i, j)$ , Eq. 5.4 can be scaled instead of considering the  $N$  by  $M$  pixels image:

$$\Delta I_T\{i, j\} = \frac{1}{K \cdot A \cdot I_{sc}} \sum_{n=1}^N \sum_{m=1}^M |p_{n,m}^i - p_{n,m}^j| \cdot R_{n,m}, \quad (5.9)$$

where  $A$  is the ring area in pixels,  $R_{n,m}$  the ring binary mask and  $I_{sc}$  the intensity scale of the ring. Since the amount of light of each pixel is not constant (lower intensities are located in outer regions), the averaged intensity ( $I_{sc}$ ) within each ring has been employed as a scale factor to correct this difference:

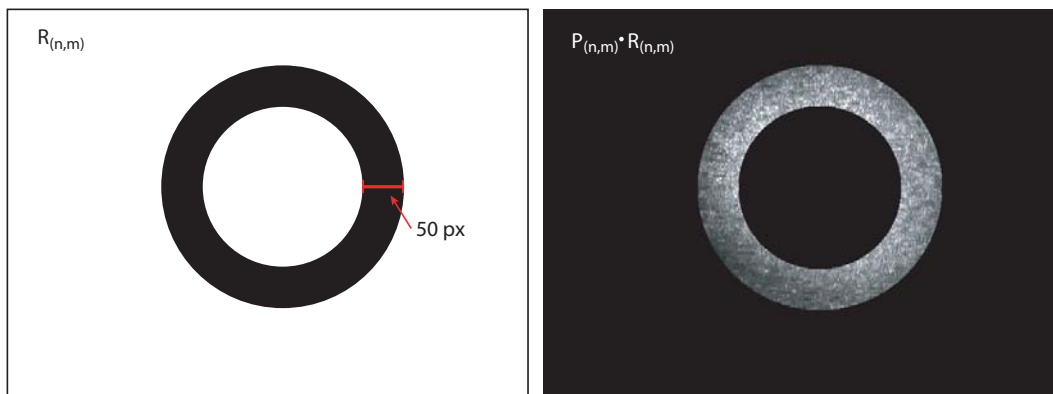


**Fig. 5.17.:** Example of a binary mask (left) and their combination with a specklegram (right).

$$I_{sc} = \frac{1}{L} \sum_{i=1}^L \sum_{n=1}^N \sum_{m=1}^M [p_{n,m}^i \cdot R_{n,m}], \quad (5.10)$$

being  $L$  the number of specklegrams of the sequence. The ring width must be greater than the speckle size to have enough speckle dots within the area of each ring to achieve a valid statistical behavior.

In Fig. 5.17, an example of a binary mask is depicted (left) and its combination with a speckle pattern (right). A high number of individual speckles are required within each ring area to get valid measurements. When the speckle pattern is modified, the energy within each ring must remain constant to have enough information. Having a large specklegram area (ring area in this case) will allow a pattern redistribution within the same area, maintaining its total energy (intensity).

## 5.4.2. Experiments and results

Radial speckle has been combined to the differential processing scheme to enhance its final sensitivity (Eq. 5.9). Based on a setup that provokes acoustic vibrations close to the fiber under test, two highly multimode POFs have been tested. Several rings of different radius but constant width have been employed as binary masks to compute the correlation between consecutive specklegrams.

### 5.4.2.1. Experimental setup

Two highly multimode POFs of  $240 \mu m$  and  $980 \mu m$  have been perturbed with a shaker that creates vibrations from 1Hz to 10Hz, employing a constant



**Fig. 5.18.:** A shaker has been placed close to the multimode fiber.

amplitude. Some characteristics of the employed fibers have already been detailed in Table 5.1. One side of the fiber under test has been connected to a cheap laser diode and the other to a USB camera capturing at 25 fps. A sequence of several specklegrams of 640 by 480 pixels has been captured for each fiber and frequency. The employed setup is detailed in Fig. 5.18.

Each video sequence has been processed using the described method (Eq. 5.9). Depending on the NA of the fiber and on the distance to the camera, different spot's sizes were achieved, so different radiuses have been considered for each fiber to have enough speckles within each ring.

#### 5.4.2.2. Results and discussion

Different specklegram sequences of both tested fibers have been processed and compared to a uniform differential processing scheme (considering the whole speckle pattern). Each sequence comprises a low perturbation section (mainly influenced by environmental conditions) and a high perturbation section (under the induced vibration) after  $t = 15$  s. Both sequences have been referenced to their initial specklegrams for viewing purposes. One processed sequence of each fiber is depicted in Fig. 5.19.

The central area of a sequence of each fiber has been normalized and depicted in Fig. 5.19. Different radiuses (measured in pixels) have been considered for each fiber maintaining the same width (50 pixels). The reference signal has been computed considering the whole spot: a circle (instead of a ring) with the maximum tested radio. As the radius is increased (maintaining its width), the obtained sensitivity also increases, because these areas are mainly influenced by higher order modes, which are also more exposed to the external perturbation. Particularly, for the maximum tested radio on the  $980 \mu\text{m}$  specklegrams (Fig. 5.19, right), the perturbation period can even be appreciated in the processed sequence. There is not enough capturing rate

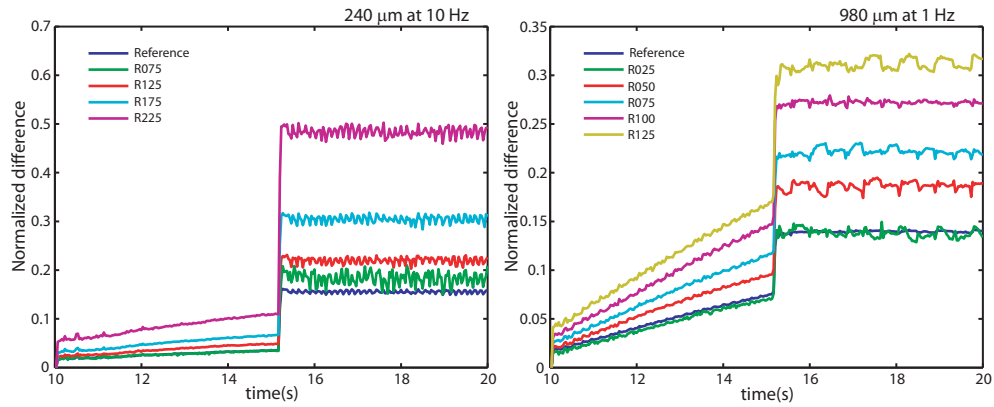


**Fig. 5.19.:** Normalized response for different radiuses of the 240  $\mu\text{m}$  fiber under 10 Hz perturbation (left) and of the 980  $\mu\text{m}$  fiber under 1 Hz perturbation (right).

to clearly appreciate the 10 Hz period in the first sequence. On the other hand, the sensitivity enhancement can also add extra noise to the measurements, because the environmental variations have more influence in the final sequence. This effect can be noticed in the slope of the sequences when no extra perturbation has been applied.

Since the proposed scheme is based on speckle statistics, it works properly in fibers with a very high number of modes, where speckle dots are smaller and when enough speckle dots are comprised within each ring. If small ring diameters are considered, there would not be enough speckles within each ring so, the total intensity within each ring would vary, adding extra noise to the sequence. However, both tested fibers are highly multimode, thus very narrow rings can be considered (few pixels) without having intensity instabilities.

### 5.4.3. Summary

A new processing scheme to enhance the speckle sensitivity to dynamic perturbation has been proposed and experimentally tested. Considering different areas of interest within a speckle pattern, each area is statistically related to higher modes that are more sensitive to external fiber perturbations. The radial processing scheme has been experimentally validated using two highly multimode POFs that have been subjected to an external vibration while their speckle pattern were recorded using an USB camera. The achieved results exhibit a sensitivity increase when areas far from the longitudinal fiber

axis (corresponding to higher order modes) were processed. This method enhances the FSS technique to applications where extremely high sensitivity is required, taking advantage of the spatial information within each individual specklegram.

## 5.5. Conclusions

In this chapter, several sensing systems based on specklegrams have been proposed. Employing polymer optical fibers as integral transducers, different approaches based on commercial CCD cameras have been tested to obtain reliable optical fiber sensors with a relative low cost. Combining the extremely high sensitivity of interferometric sensors with advanced processing schemes, both dynamic and static perturbations have been successfully measured taking advantage of the benefits offered by present computer systems.

Although there is a wide set of commercial POFs for FSS, a selection of three different multimode POFs have been characterized for sensing purposes. Two highly multimode fibers and one with a lower number of modes have been employed to measure dynamic and static perturbations, respectively. Based on a Piezoelectric Transducer, different properties, both optical and mechanical, have been studied to get the final response of the tested POFs for their application to vibration sensing. Employing cheap optoelectronic components, a sensing head to measure the human heart rate and an experimental setup for environmental vibration monitoring have been successfully tested. Both applications exploit the extremely high sensitivity to mechanical perturbations of highly multimode FSSs.

Maintaining the setup employed for vibration monitoring, static deformation measurements have also been performed despite their extremely high mechanical sensitivity. A processing scheme that extracts the general speckle pattern distribution (that is related to the modal state within the fiber) has been employed to enhance the dynamic range of Specklegram strain sensors. Dividing the whole dynamic range of the sensor in different sections (given by Key-Specklegrams, KS), an incoming specklegram is assigned to a section (given by the KS) and, within this range, the absolute strain value can be easily obtained. The processing scheme has been experimentally checked, exhibit-

ing a great accuracy even with specklegrams not considered in the calibration steps. This processing scheme can extend the application of FSSs for smart structures, being able to measure the deformation employing a very simple sensing head.

Taking advantage of the remaining spatial information within each speckle pattern, another different approach has been proposed to enhance the sensitivity of the existing FSSs. Based on the statistical relation between the modal order and specific areas of the speckle pattern, different sensitivities can be obtained. A processing scheme based on this approach has been proposed and tested (Radial Speckle) to verify the areas that offer higher sensitivities. The achieved results exhibit a sensitivity increase when areas corresponding to higher order modes (greater radiuses) were processed. This method improves the FSS technique for applications where extremely high sensitivity is required. Further investigations may lead this technique to new sensing methods based on multimode fibers taking advantage of the sensitivity difference between modes.

All the proposed techniques and sensing heads described during this chapter only exhibit the potential of POF-based sensors for sensing purposes. Fiber Specklegram Sensors (FSSs) combine two key advantages: an extremely high sensitivity to external perturbations and the possibility of developing a full sensor system employing low-cost commercial equipment. As a result of this research, 1 journal article and 4 international conference papers have been published.

# Chapter 6

---

## Fiber laser sensors

---

Fiber lasers are important for practical engineering applications, such as: remote sensing, communications, health diagnosis or structural monitoring [1]. In all of these scenarios, the quality of the light source may limit the final performance of the associated systems.

Although most photonic systems take benefit from a light source insensitive to environmental parameters, in particular scenarios, a source that depends on external perturbations can be useful as a sensing element by obtaining high precision measurements far from a host structure. Both requirements (high precision and long distances) can be satisfied by fiber laser sensors, where one or several wavelength matched FBGs can be employed to create an in-fiber cavity whose output is a laser signal. There are many applications for FBG based lasers but, when configured as sensing elements, changes in the environmental conditions (that affect the laser cavity, the FBGs or both) can be detected by monitoring the laser output.

In a simplified way, any fiber laser structure requires two key elements: an active medium to provide the amplification and an optical cavity that causes the positive feedback. Both elements, the active medium and the cavity design, determine the output power and the resulting laser modes. Usually, an extremely stable light source is required to feed optical fiber sensors in critical

applications. To achieve the necessary stability, laser sources (and particularly fiber lasers) should operate in single longitudinal mode (SLM) [2–4], because their output linewidth becomes narrower and the power stability improves. These conditions are particularly useful to achieve high resolutions in sensing systems based on fiber lasers. However, achieving a pure SLM operation in a fiber laser can be very difficult depending on the employed structure, and complex techniques are often required.

In a fiber laser, the optical cavity design determines the resulting laser modes and, basically, two parameters can be modified to reach SLM operation: shortening the cavity length or narrowing the optical filtering element. In ring configurations, complex optical filtering techniques are necessary to achieve the SLM operation because of the long active cavity where modal spacing is small [2, 5]. On the other hand, optical filtering is less restrictive in linear fiber lasers based on short cavities where modal spacing is larger [6, 7], but their output power is lower.

In this chapter, several aspects from the combination of Fiber Bragg Gratings and active fibers have been studied to improve laser structures. Particularly, the evolution of a passive filtering element (FBG) within a feedback structure has been modeled in Section 6.1 (*FBG spectral evolution in active fibers*), quantifying the narrowing process of a FBG within a ring laser. Trying to obtain fiber laser sensors, a filtering scheme based on a partial overlap of two FBGs has been evaluated in Section 6.2 (*Filtering technique based on spectral overlapping*) and, finally, the proposed filtering technique has been used to build a SLM sensing head based on a commercial Er-doped fiber (Section 6.3, *Single Longitudinal Mode Lasers*).

## 6.1. FBG spectral evolution in active fibers

The laser output spectral properties are usually estimated from the passive response of their filtering elements taking into account the gain constant in the filter bandwidth. The number of longitudinal modes operating within the cavity is usually determined by the filter bandwidth and the spectral spacing between them [8–10]. Although this approach can be useful in many scenarios, it may lead to inaccurate filtering requirements when extremely narrow

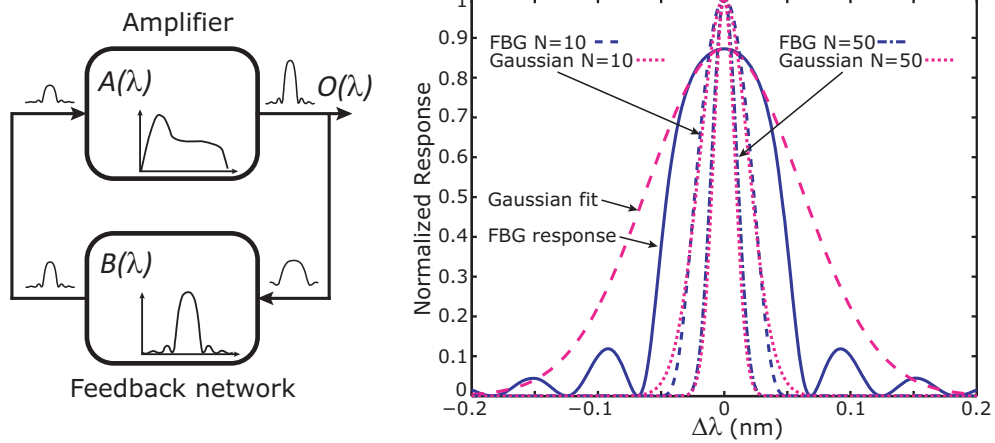


**Fig. 6.1.:** Block diagram of a feedback linear oscillator (left). Spectral response of a FBG and its Gaussian fit (right).

bandwidths are required.

The spectral evolution of the filter element of a laser structure (e.g. FBG) has been modeled and experimentally characterized in this work. The spectral distribution of the longitudinal modes in a laser structure have been studied taking into account not only the optical filter bandwidth, but also the properties of the feedback network. The laser output spectral properties have been studied using a feedback model based on the passive response of its filtering element. As the optical signal passes several times through the filtering element, its spectral shape becomes narrower, simplifying the requirements of the passive filter (FBG) within a laser structure. An experimental fiber ring laser has been employed to characterize different FBGs as filtering elements and the achieved laser outputs exhibit a good agreement to the proposed model.

### 6.1.1. Spectral narrowing principle

A laser scheme can be understood as a feedback linear oscillator where the output of the amplifying block is fed back to its input. The overall single-pass gain is quite small and usually a number of passes through the amplifier are required to generate a coherent output (Fig. 6.1, left). The feedback block gives the wavelength selectiveness and, typically, a passive filter is employed to perform this task.

The total frequency width, where all the longitudinal modes occur, is some-

what related to the filter bandwidth. Usually, the number of longitudinal modes can be obtained from the equation [10]  $N \approx FWHM_{FBG}/\Delta\lambda$ , where  $\Delta\lambda = \lambda^2/nL$  is the mode spacing between longitudinal modes of the cavity;  $n$  is the refractive index;  $L$  is the cavity length;  $\lambda$  is the central mode wavelength and  $FWHM_{FBG}$  is the bandwidth of the corresponding Fiber Bragg Grating (Full Width at Half Maximum). Nevertheless, the laser signal passes several times through the feedback block ( $\beta(\lambda)$ ), which is a spectrally discriminating element. Thus, this will have an influence in the laser emission spectrum. In order to understand how the spectral response evolves, the FBG spectral response can be approximated for a Gaussian function:

$$\beta(\lambda) \approx R \cdot e^{-\frac{(\lambda-\lambda_B)^2}{2\cdot\sigma^2}}, \quad (6.1)$$

where  $R$  is the FBG reflectivity;  $\lambda_B$  is the FBG Bragg wavelength and the variance ( $\sigma^2$ ) is related to the FBG bandwidth. Considering an ideal lossless system, the output power distribution  $O(\lambda)$  after  $N$  passes through the feedback network and its 3dB bandwidth can be defined as:

$$\begin{aligned} O(\lambda) &= A(\lambda)^N \cdot R^N \cdot e^{-N\frac{(\lambda-\lambda_B)^2}{2\cdot\sigma^2}} \\ W_{3dB} &= 2 \cdot \sqrt{2 \cdot \ln 2} \cdot \frac{\sigma}{\sqrt{N}}, \end{aligned} \quad (6.2)$$

where  $\sigma$  is a constant value for a chosen FBG and the gain distribution,  $A(\lambda)$ , remains constant for a given laser structure.

From Eq. 6.2, it can be deduced that the 3dB spectral selectiveness (bandwidth) is reduced by a factor of  $1/\sqrt{N}$  due to the feedback network. An example of a FBG response approximated by a Gaussian function is depicted in Fig. 6.1 (right). The normalized profile of both responses after  $N$  iterations is also depicted exhibiting their bandwidth reduction.

In Fig. 6.2, several simulated FBG spectra with different reflectivities have been employed as a filtering block and have been also iteratively processed to obtain their 3 dB equivalent bandwidth after  $N$  passes. These iterative 3 dB bandwidths have been compared to their fits ( $\propto 1/\sqrt{N}$ ) according to the Gaussian approximation described in Eq. 6.2. As the number of passes ( $N$ ) increases, the bandwidths decrease until given limits are reached.

As depicted in Fig. 6.2, the reduction expression obtained from the Gaussian approximation (Eq. 6.2) of a FBG spectrum works better for FBGs with lower

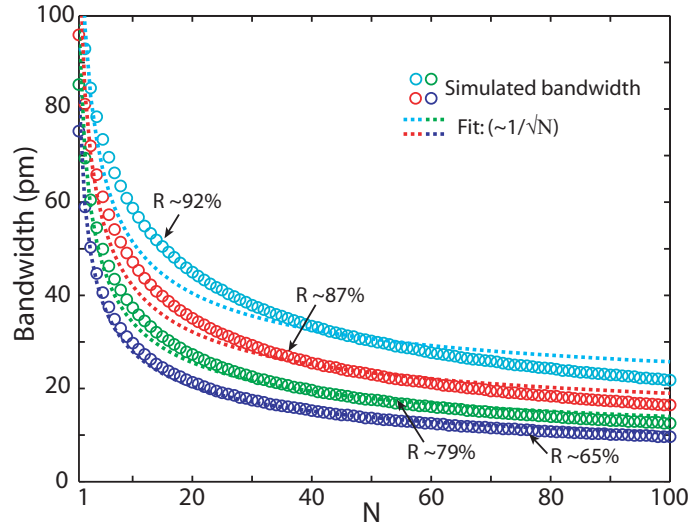


**Fig. 6.2.:** The bandwidth of the equivalent filters after  $N$  passes through FBG spectra as filtering element (circles) is compared to their Gaussian approximation (dotted line).

reflectivities. In this case, the Gaussian approximation remarkably agrees with the upper section of the FBG spectrum peak. When a FBG spectrum is iteratively multiplied by itself (several passes through a filtering block in a feed-back structure), only the higher values exceed zero, and thus the final spectral response is mainly driven by the peak upper shape.

In an experimental setup, the number of passes through the feedback filter ( $N$ ) is limited by several factors such as the saturation of the amplifying block, the feedback scheme or the passive filter response. Given that the feedback scheme and the saturation are usually constant for the same setup, the influence of the employed feedback filter in the laser output has been experimentally analyzed and tested for a particular fiber laser configuration.

### 6.1.2. Experiments

In order to experimentally verify the prediction of the last section, an erbium-doped fiber ring laser (EDFRL) has been mounted based on a commercial EDFA (Photonics BT-17), where a FBG has been included as a feedback element using a circulator (Fig. 6.3). Maintaining this setup and therefore maintaining the feed-back structure, the laser output has been characterized for different FBGs.

A high resolution Optical Spectrum Analyzer (BOSA-C Aragon Photon-

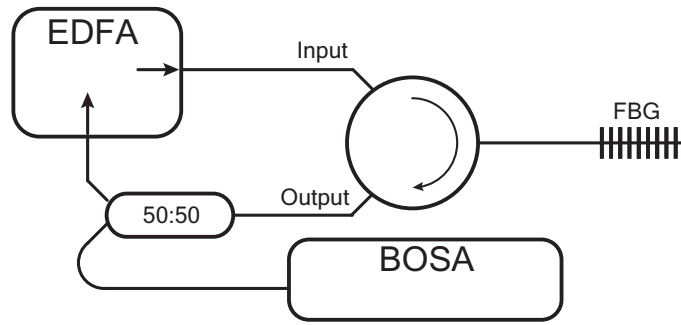


**Fig. 6.3.:** An EDFRL is mounted using a commercial EDFA. The feedback filtering is given by a FBG connected to the ring through a circulator.

ics) with a resolution of 0.08 pm has been employed. Its spectral resolution has a lower value than the mode spacing between the longitudinal modes. Consequently, the spectral distribution of the multilongitudinal-modes in the EDFRL can be determined. In order to measure the spectral range where the longitudinal modes can achieve the oscillation, the laser output has been held for a time interval, obtaining the probability distribution of the laser emission. These measurements are directly related to the equivalent spectral shape of the filtering device after  $N$  passes through the filter during the feedback process.

The laser output of this EDFRL (Fig. 6.3) was measured for a set of 18 different FBGs. These FBGs have lengths between 15 and 24 mm and reflectivities from 50% to 90%. The EDFA pump power has been set to 90 mW and the laser output signal has been held at BOSA during 15 minutes for each case.

The passive responses of the FBGs were also measured during the fabrication process using a white light source and an Optical Spectrum Analyzer (OSA). The iterative processing scheme has been applied to obtain the equivalent spectral shape of the FBG in the feedback network from its passive response. The iteration process is repeated until a given SNR is achieved. This value has been experimentally adjusted and can be considered constant for a given setup because it is mainly related to the amplification stage and the system losses.

Due to the low resolution of the OSA employed to characterize the FBG passive response (60 pm), each manufactured FBG structure (FBG length) has been simulated using the T-matrix method, adjusting its reflectivity based on

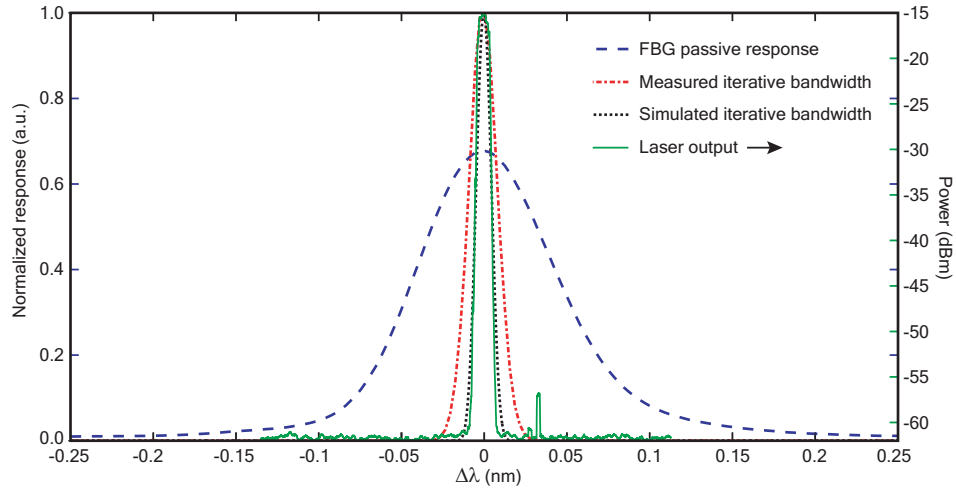


**Fig. 6.4.:** Example of a FBG passive response (dash-dot line) compared to its correspondent laser output (solid line). The two normalized iterative FBG spectra: measured (dashed line) and simulated (dotted line) are also depicted.

the measurements to improve the wavelength resolution. In Fig. 6.4, a comparison between a FBG spectrum, its processed bandwidths (both experimental and simulated) and the achieved laser output spectrum, has been depicted. Both processed (iterative) bandwidths have been obtained by multiplying each passive FBG spectrum (measured and simulated) by itself iteratively  $N$  times, trying to replicate the oscillation process. Although the passive response of the employed filtering element has a 3dB bandwidth greater than 100 pm, the measured laser bandwidth is much narrower ( $\approx 25$  pm). An explanation of this behavior lies in the feedback influence to the spectral selectiveness of the filter response.

In Fig. 6.5, the obtained laser bandwidths (measured using a more restrictive 20 dB criterion) are compared to the 3dB bandwidth of the passive response of each FBG. The iterative processed widths are also depicted. These values were calculated by empirically adjusting the number of iterations ( $N = 23$  for measured spectra). It can be observed that for all the measured FBGs, their passive bandwidths are much higher than the laser bandwidths. The two iterative bandwidths seem to fit better to the achieved laser bandwidths. Both methods (measured and simulated) remarkably agree with the measured laser outputs for the wider lasers (first five FBGs). However, for narrower lasers, the measured iterative bandwidth looks more flat while the

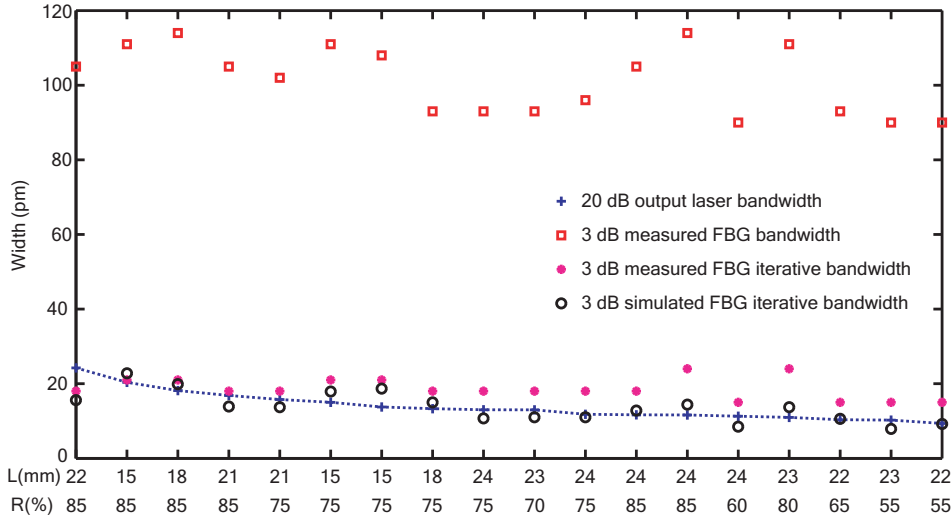


**Fig. 6.5.:** Example of a FBG passive response (dash-dot line) compared to its correspondent laser output (solid line). The two normalized iterative FBG spectra: measured (dashed line) and simulated (dotted line) are also depicted.

simulated iterative widths follow better the laser width trend. This effect is caused by the limited resolution of the measured passive response (60 pm) that decreases in a slow way while the filter iterates. The simulated iterative bandwidth fits better to the laser width trend because it is not limited in resolution. However, there are still small errors between the measured laser widths and the iterative predicted ones, what can be attributed to some implementation issues such as connection losses or slight instabilities of the filter during its characterization.

### 6.1.3. Summary

The improvement of the spectral selectiveness of a passive filtering element (FBG) in a feedback laser structure has been measured and theoretically modeled. The spectral width where all the longitudinal modes can oscillate in a fiber laser for 18 different FBGs has been experimentally characterized and compared to an iterative model that obtains the final laser bandwidth from the passive FBG response. The iterative model multiplies the filter response so many times as required to obtain the effective narrowing of the filtering block in a feed-back structure. The proposed method simply tries to obtain the general properties of the filter block in a feed-back structure; however, the

achieved results exhibit a very good agreement with the empirically trimmed number of iterations and they are far from the typical 3 dB bandwidth of the passive FBG response (5 times lower for the employed setup). In other works, the requirements for a laser device, especially when single-mode operation is required, are generally specified based on the passive bandwidth of the filtering element (typically the 3 dB bandwidth). Nevertheless, with the present study and experimental results, it has been demonstrated that these filtering requirements are not so strict for a particular spectral bandwidth requirement.

## 6.2. Filtering technique based on spectral overlapping

Although a simplification in the filtering stages of laser cavities has been demonstrated in the previous section, very narrow filtering techniques are still required for many applications, particularly for Single longitudinal mode (SLM) devices. SLM fiber lasers are an interesting alternative in many applications (wavelength division multiplexing (WDM) communications, fiber optic sensors, spectroscopy and microwave photonic systems [1, 11, 12]), where high resolutions are required. However, achieving a SLM behavior is highly conditioned by the chosen laser configuration.

Specifically, Erbium doped fiber lasers usually present multiple longitudinal modes closely spaced due to their long cavity length, necessary to achieve an optimum amplification. As a consequence, an ultra-narrow optical filter has to be incorporated in the cavity to eliminate the multiple longitudinal mode oscillations and ensure SLM operation. Different techniques have been presented to achieve ultra-narrow filtering: saturable absorbers, multi-ring loops, the use of FBGs as self-injection feedback elements, random distributed feedback based on Rayleigh backscattering (RBS) or phase shifted FBGs [2, 3, 13–15]. Some of these techniques add complexity to the setups, exhibiting a lack of flexibility to achieve multiwavelength lasers.

In this work, a narrow filtering technique based on the spectral overlapping of two uniform Fiber Bragg Gratings (FBG) to achieve a SLM operation in fiber lasers is described. The spectral overlapping of strange FBGs has been

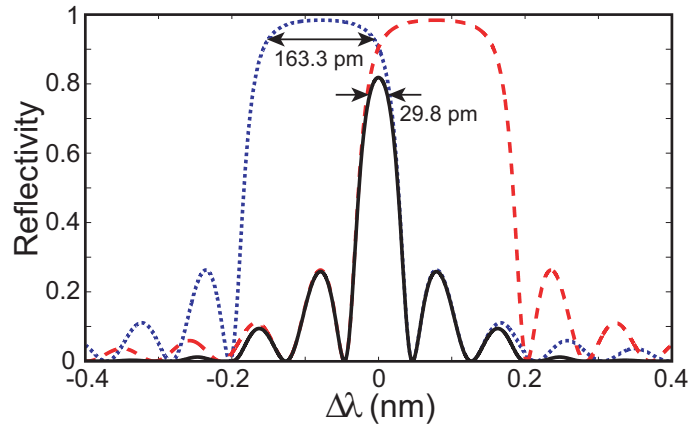


**Fig. 6.6.:** One FBG is detuned (dashed line) in terms of the other (dotted line). The overlapped spectrum (solid line) gives rise to a filter narrower than both individual FBGs.

already applied [16, 17], but, to the best of our knowledge, this is the first time that two uniform FBGs are combined to reduce the final bandwidth of the achieved filter. Due to the flexibility of this technique, ultra-narrow equivalent filter bandwidths can be achieved to be employed in different fiber laser configurations. Several aspects of the FBG spectral overlapping are studied both theoretically and experimentally. From these results, an erbium doped fiber ring laser with a cavity length of  $L \approx 8$  m is also analyzed to experimentally verify that it operates in the SLM condition due to the spectral selectivity of the filtering technique.

### 6.2.1. Spectral overlapping

As depicted in Fig. 6.6, a very narrow filter can be obtained by combining a pair of FBGs partially overlapped. The narrowing effect is produced by detuning a FBG, but keeping it partially overlapped with the other. In this way, the two filters are matched just when the wavelength of the optical signal is within the overlapped section, thus narrowing the whole spectral response. Using a very narrow filter in an active structure, the resulting laser output becomes narrower (lower bandwidth), reducing the number of active longitudinal modes and even allowing to reach the Single Longitudinal Mode (SLM) operation.

As can be noticed in Fig. 6.6, the resulting bandwidth depends on the detuning factor (DF) or wavelength difference between FBGs. Two uniform

FBGs of  $L=9\text{mm}$  length with a 1 dB bandwidth of  $W_{1dB} = 163.3 \text{ pm}$  are detuned  $DF = \Delta\lambda \approx 156.4 \text{ pm}$  obtaining an equivalent filter of  $W_{1dB} = 29.8 \text{ pm}$ . As demonstrated in the previous section (*FBG spectral evolution in active fibers*), there is an improvement on the spectral selectiveness of a FBG within a feedback structure. Trying to replicate this improvement, a  $1dB$  criterion has been employed to measure the passive FBG bandwidth.

By employing this structure, as the detuning factor increases (maintaining some spectral overlapping) the narrowing of the equivalent filter also improves. The main drawback of this scheme is the power drop due to the equivalent reflection reduction of the overlapped filter. This effect can be minimized by employing FBGs with a higher reflectivity (even being saturated), because their side slopes are steeper thus, maintaining the same bandwidth, a higher equivalent reflectivity can be achieved. However, their tuning process becomes more challenging. This spectral filtering scheme can be applied to different fiber laser structures, although a trade-off between reflectivity (limited by the medium gain) and bandwidth (limited by the modal spacing) needs to be reached to get SLM operation.

Several simulations have been performed to analyze the evolution of the combined filter response when different FBGs pairs and detuning factors are employed.

### 6.2.2. Simulations

The combined filter response is mainly driven by the edges of the main lobe of both FBG spectra and their relative wavelength displacement. By employing FBGs with steeper edges (e.g. high reflectivity or longer FBGs), their overlapped response bandwidth will experiment a fast drop as their wavelength displacement increases. Thus, lower bandwidths can be achieved when using FBGs with steeper edges.

One of the two matched FBGs has been displaced until the main peaks overlap becomes lower than the secondary lobes. These displacements have been calculated for two FBG pairs of  $L = 10 \text{ mm}$  length, but with different reflectivities ( $R_1 \approx 99\%$  and  $R_2 \approx 84\%$  as shown in Fig. 6.7, left). At lower detuning factors, the combined filter reflectivity and bandwidth are still comparable to a single FBG; however, when the edges of the main lobes are

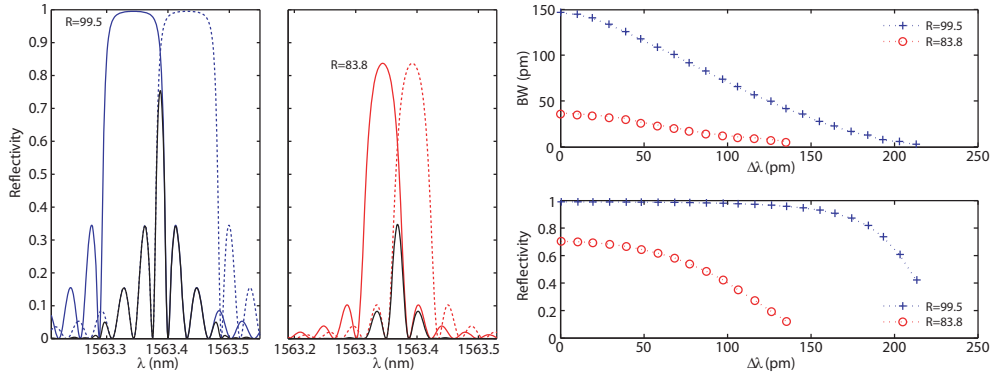


**Fig. 6.7.:** Illustration of the spectral overlapping of FBGs with different reflectivities (left). Achieved bandwidth (top) and reflectivity (bottom) during the wavelength displacement (right).

close, a great reduction in bandwidth and reflectivity is produced. This effect is more drastic when high reflectivity FBGs are employed as can be noticed in Fig. 6.7 (right), where the achieved 95% bandwidth and reflectivity of the combined filters have been plotted as a function of their wavelength displacement (difference between Bragg wavelength of both FBGs). As can be noticed, the achieved bandwidth of the combined filter is lower for higher reflectivity FBG pairs, allowing a best spectral selectivity (filter narrowing) when working with saturated FBGs. Particularly, in the depicted simulations, the minimum achieved bandwidth for  $L = 10 \text{ mm}$  FBGs is  $BW_H \approx 4 \text{ pm}$  for the higher reflectivity FBG pair and  $BW_L \approx 6 \text{ pm}$  for the lower reflectivity pair. But, as the reflectivity of the main FBG lobe increases, this effect is also reproduced for the secondary lobes, what limits the maximum wavelength displacement and, consequently, also limits the filter narrowing. This effect can be reduced by employing apodized FBGs, although apodization functions usually give rise to smoother main lobe edges, what also limits the filter narrowing.

In addition to the reflectivity, the FBG length has to be also considered in the design process. Longer FBGs of the same reflectivity have steeper main lobes, but their secondary lobes have the same reflectivity, what benefits the filter narrowing. In Fig. 6.8 (left) several FBGs of different lengths but same reflectivity ( $R \approx 95\%$ ) are depicted. When the FBG length increases, the main lobe of the FBG becomes narrower and steeper, increasing its edges slope. This situation can be useful for filtering purposes because their combination can be also steeper.

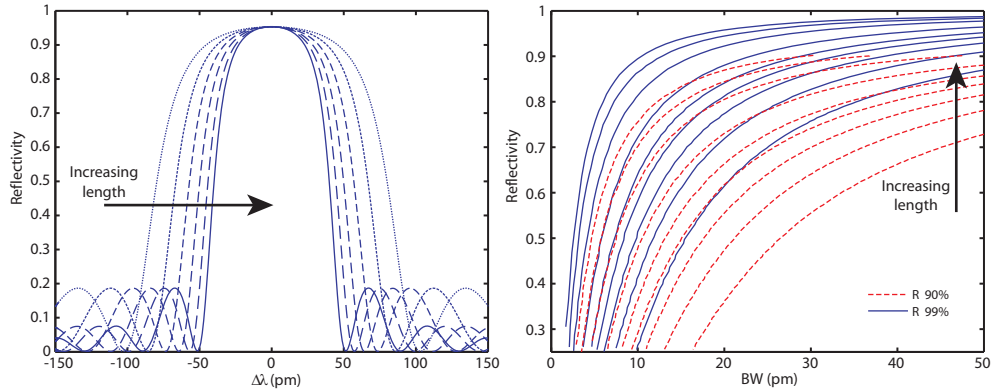


**Fig. 6.8.:** Reflection spectra of FBGs of different lengths (left). Relation between the achieved bandwidth and its reflectivity for different FBG lengths from 4 to 22 mm (right).

Although narrower combined filter bandwidths can be achieved by employing long FBGs with high reflectivities, as their main lobes become steeper, their tuning process can be more complicated; given that there is a huge reflectivity variation for a small wavelength displacement. In Fig. 6.8 (right), the achieved filter bandwidth is compared to its reflectivity for different FBG lengths. This graph gives an idea of how abrupt is the tuning process depending on the chosen FBGs. On the contrary, when the filtering requirements are not so strict, lower FBG lengths (and/or reflectivities) can be employed to make the manufacturing process easier and improve the final laser stability against external perturbations (such as vibrations).

### 6.2.3. Experiments

A ring laser scheme has been employed for the experimental verification of the proposed technique (Fig. 6.9, left). In order to reach the best performance (narrower laser bandwidth) and based on simulations, a combination of two long FBGs of  $L = 24$  mm with a high reflectivity have been employed as the filtering element of this laser. Two circulators, connected in series, have been spliced to both FBGs to get the combination of their reflection spectra. The resulting filter is the partial overlap of both FBG reflection spectra. The employed FBGs have been characterized using a high resolution Optical Spectrum Analyzer (BOSA-C, Argon-Photonics) and one spectrum is depicted against its simulated fitted model in Fig. 6.9 (right).

A FBG has been stretched using a motor stage (Newport MM4005) while

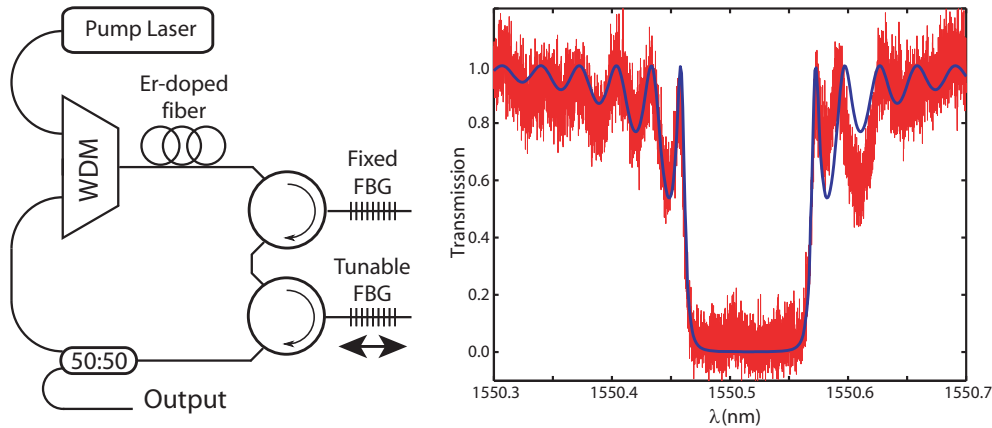


**Fig. 6.9.:** Ring laser setup based on the overlapping of two FBGs (left). Experimental spectrum of one FBG and its associated simulation (right).

the other was fixed. Several stretching sweeps have been performed using different pump powers. Since determining the Bragg wavelength difference of two partially overlapped FBGs is difficult, all sweeps have been started at the minimum overlapped point, where the cavity starts lasing. For the employed FBG pair, this point corresponds to the SLM operation. Based on a fixed wavelength displacement of  $\Delta\lambda \approx 2.5 \text{ pm}$ , several increments have been applied to a FBG as both spectra became more overlapped. In order to measure the spectral range where the longitudinal modes can oscillate, the laser output has been held for a time interval, obtaining the probability distribution of the laser emission. These measurements are directly related to the equivalent spectral shape of the filtering device. For each step, the laser output has been held by the BOSA for  $t = 3 \text{ min}$ . This time has been set large enough to obtain the statistical behavior of the laser, but also short enough to minimize the errors due to environmental changes such as vibrations or temperature drifts. Several factors contribute in these bandwidth measurements such as the number of modes, mode hopping or external vibrations that can influence the final laser performance.

In Fig. 6.10 (left), the measured laser bandwidth is depicted as a function of the wavelength displacement of the FBG for different pump powers. As the overlapped spectral area is reduced, the output laser bandwidth also becomes narrower. The same behavior has been noticed for different pump powers, being the main difference in the starting point: a lower pump power

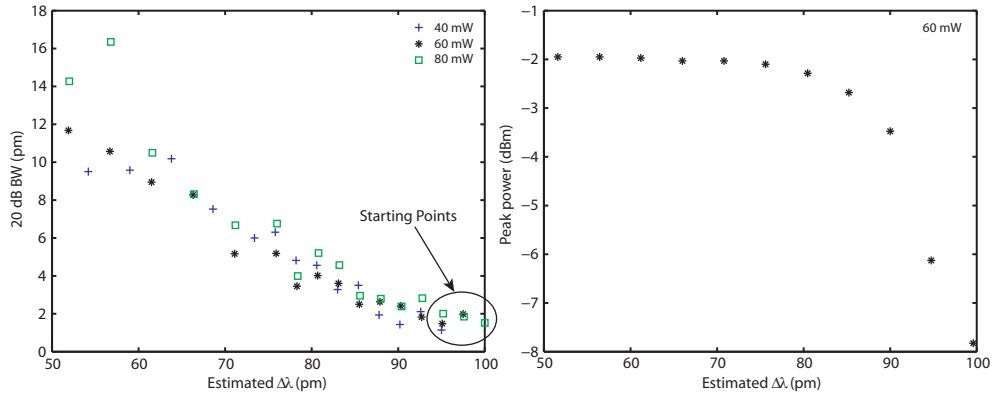


**Fig. 6.10.:** 20 dB laser bandwidth against the wavelength difference between FBGs for different pump powers (left). Output laser power against the wavelength difference (right).

requires a higher equivalent reflectivity, thus, the starting displacement must be lower. The evolution of the laser power during the strain sweep is also depicted in Fig. 6.10 (right) for a constant pump power. As the reflectivity of the combined filter decreases (while the laser bandwidth is also reduced) the output power also decreases. This power reduction is higher at lower laser bandwidths (higher displacements).

Although the laser output power drops due to the combined filter reflectivity reduction, when FBGs with a very steep spectral response are employed, extremely narrow filters can be achieved based on this technique. Particularly, for the chosen ring laser structure (with a total length of  $L \approx 8$  m), SLM operation has been achieved for different pump powers. The SLM operation was verified with a heterodyne detection system using an Optical Converter (HP11982A) and an Electric Spectrum Analyzer (HP8592L). The laser output was combined with the signal of a Tunable Laser Source (TLS, Agilent 8164B) using a 3 dB coupler, whose wavelength has been placed close to the laser output. In Fig. 6.11 (left), a capture with a single peak is shown associated with the different tested pump powers, proving the SLM operation of the laser. However, when both FBGs are more overlapped, the laser begins to operate in multimode regime, as shown in Fig. 6.11 (right).

The achieved results exhibit the capability of the spectral overlapping technique to reach very narrow filters for laser structures. Particularly, by employing FBGs with steeper main lobes, extremely narrow filters capable of reach SLM operation even with very low modal spacing ( $\Delta\lambda \approx 0.1$  pm) can be ob-

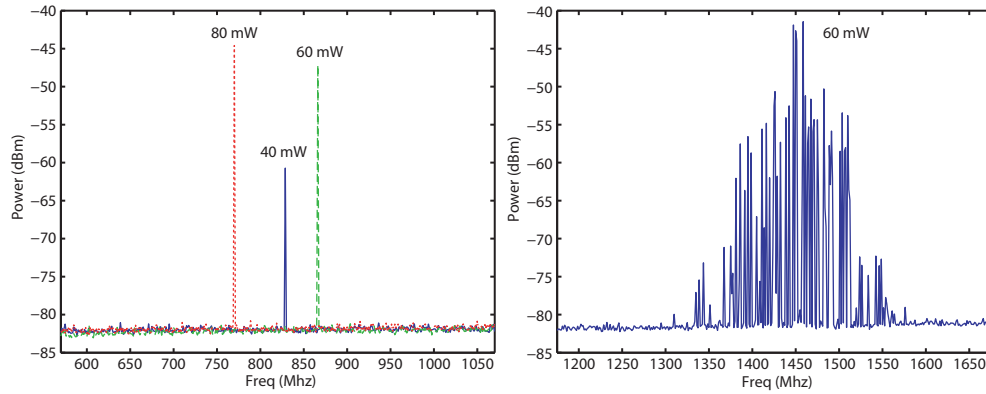


**Fig. 6.11.:** SLM operation at different pump powers (left) and multimode operation (right) of the ring laser measured with the heterodyne detection system.

tained. However, in order to improve the laser stability, when working with very narrow filters, additional strategies are required to isolate the vibration and/or temperature variations of the FBGs, such as fixing both FBGs to a host material.

#### 6.2.4. Summary

A simple filtering technique based on the spectral overlap of two uniform FBG has been proposed both by means of simulations and experimentally for its application to laser structures. The achieved results can help on the design of new laser structures by showing the final performance of two uniform FBGs employed as a combined filtering element. Despite the fact that both output power and bandwidth are the most important features in the laser design, other practical issues must be taken into account in the manufacturing process such as external noise isolation (e.g. vibration) or flexibility of the tuning process. The simulated results have been confirmed during the experimental tests, where the same bandwidths and power evolutions have been measured using a ring laser configuration employing two partially overlapped FBGs as the filtering element. This technique has also been tested for very narrow filtering purposes by achieving the Single Longitudinal Mode operation in a ring cavity of  $L \approx 8\text{ m}$  only using two uniform FBGs. In addition, the spectral overlapping is a flexible technique that can be employed in DBR structures and it is capable of achieving high performance Fiber Lasers, with the suitable manufacture and packaging processes.

## 6.3. Single Longitudinal Mode Lasers

Many laser configurations have been proposed to ensure a stable SLM operation. A ring cavity configuration is often employed, but complex techniques are required to achieve the SLM operation, thus resulting unsuitable for applications that require a small size [2, 3, 13]. A linear fiber laser becomes another option to achieve this operation mode. Short SLM linear fiber lasers using fiber Bragg grating (FBG) have been demonstrated in erbium doped fibers [6, 18–20], although the cavity length must be short to obtain a SLM operation. The fiber shortening implies the use of rare-earth ion doped fibers with a high gain to achieve a high output power. The phosphate glass fiber with a high Er-doping concentration (5dB/cm) was designed to short linear SLM fiber lasers [7]. However, this glass is expensive and the required splices to standard fiber introduce high losses and mechanical weakness. A different custom made Er-doped silica fiber has also been employed [4] in a linear cavity obtaining a SLM laser, but this fiber exhibits the same drawbacks as the phosphate one.

Moreover, for real sensor systems, relying on custom made doped fibers is not a practical solution and using commercial Er-doped fibers (with lower gains) implies a larger cavity. The achievement of SLM operation with a larger cavity implies the employment of a very narrow optical filter. Based on the filtering technique described in the previous section (*Filtering technique based on spectral overlapping*), a proof-of-concept laser has been manufactured by writing two uniform and spectrally displaced FBGs into an Er-doped fiber creating a DBR structure. An experimental characterization has also been performed exhibiting the benefits of the spectral overlapping technique to achieve stable SLM fiber lasers with temperature and strain variations. The achieved laser sensor combines the same benefits of FBGs: linearity with strain and temperature with a better Signal to Noise ratio due to the power increase.

### 6.3.1. Laser manufacturing

The two matched FBGs were written into a commercial erbium doped fiber (Fibercore M12, which has an absorption ratio of 12dB/m at 980 nm) using the phase mask technique with a continuous laser emitting at 244 nm. A small

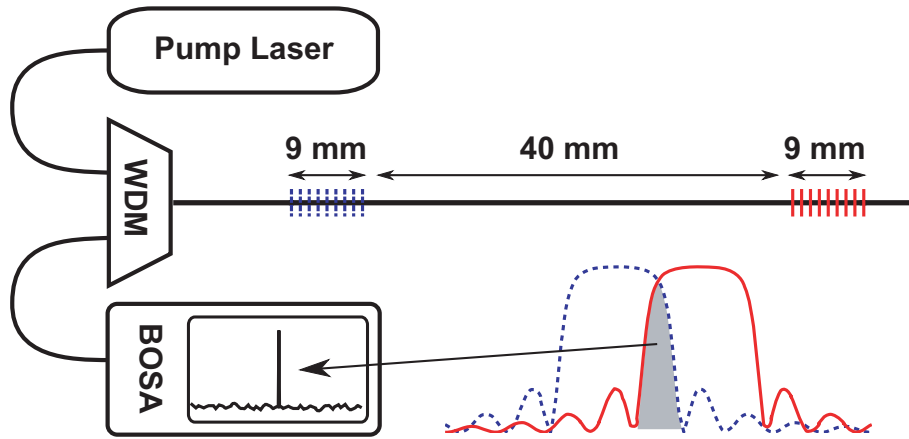


**Fig. 6.12.:** Characterization setup during the DBR laser fabrication process. Two uniform FBGs of 9 mm length were inscribed into Er-doped fiber with a distance between them of 40 mm.

Gaussian apodizing function has been applied to reduce the secondary lobes of both FBGs. In comparison to the laser structures where two FBGs are spliced to the active fiber, the writing of the FBGs directly to the Er-doped fiber reduces the power losses (lower threshold power) and avoids mechanical weak points. Once the FBGs have been written, one of them was post-exposed to drift its Bragg wavelength and reduce the overlapping area, narrowing consequently the equivalent filter bandwidth. The achieved FBGs exhibit a reflectivity of 99% with a FWHM bandwidth of 240 pm and the final wavelength drift is 180 pm.

During the FBGs post-exposition, the DBR fiber laser has been pumped at 1480 nm to generate the laser emission. As shown in Fig. 6.12, the laser signal has been monitored by using a high resolution optical spectrum analyzer (BOSA-C Aragon Photonics) to measure the behavior of the longitudinal modes. The FBG drift has been stopped when the SLM behavior has been measured at the BOSA.

### 6.3.2. Laser characterization

Since the wavelength selective effect is given by the equivalent filter bandwidth that results from the partial FBG's reflection bands overlapping, the wavelength of the obtained laser is centered at the Bragg wavelength of the equivalent filter. This value matches the upper and lower edges from the lower

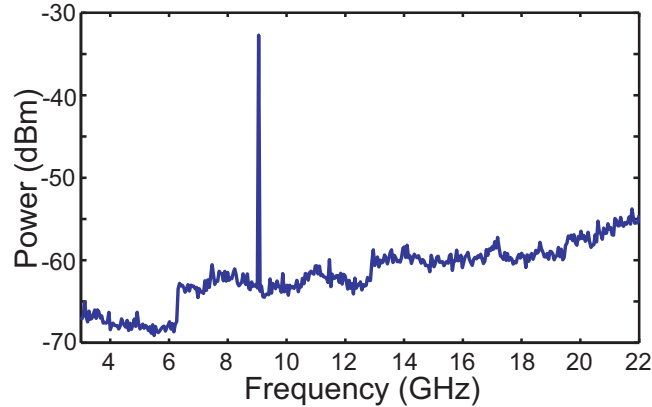


**Fig. 6.13.:** *SLM operation measured at 25°C. The laser signal is mixed with a TLS source obtaining a single peak.*

and upper FBG's bands respectively (1552.2 nm).

The SLM operation was verified with a heterodyne detection system. A polarization splitter has been connected to the laser output to remove one of the orthogonal polarization modes. The measurements have been performed using an Optical Converter (HP11982A) and an Electric Spectrum Analyzer (HP8592L). A single polarization mode of the lasing signal from the manufactured laser was combined with the signal of a Tunable Laser Source (TLS) using a 3 dB coupler. The TLS (Agilent 8164B) has a full-width at half maximum (FWHM) linewidth of 100 kHz and its wavelength has been placed close to the manufactured laser. In Fig. 6.13, a single peak is shown proving the SLM operation of the tested device

### 6.3.2.1. FWHM linewidth and wavelength stability

In order to measure the FWHM linewidth of the emitted light, the setup is changed to the delayed self-heterodyne detection scheme [21]. A phase modulator (Avanex IM10-P) has been employed to perform the 1GHz modulation. A 100 km length of standard optical fiber has been employed as the delayed line. An EDFA (MPB-EFA-P18F) has been introduced in the setup to amplify the delayed line. According to [21], the measured (FWHM) linewidth was the square root of two times the real linewidth, so this was less than 5 kHz as shown in Fig. 6.14. This narrow linewidth indicates a stable SLM operation of the fiber laser, being this very important to achieve high resolution in sens-

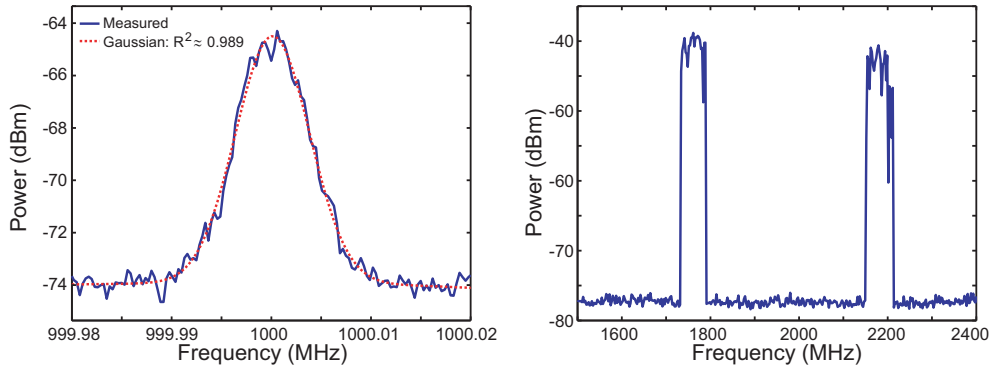


**Fig. 6.14.:** Linewidth of 4.5 kHz (3dB) measured using self-heterodyne detection with a modulation frequency of 1GHz (left). Wavelength stability (62.2MHz) of both orthogonal polarization modes measured during 10 minutes (right).

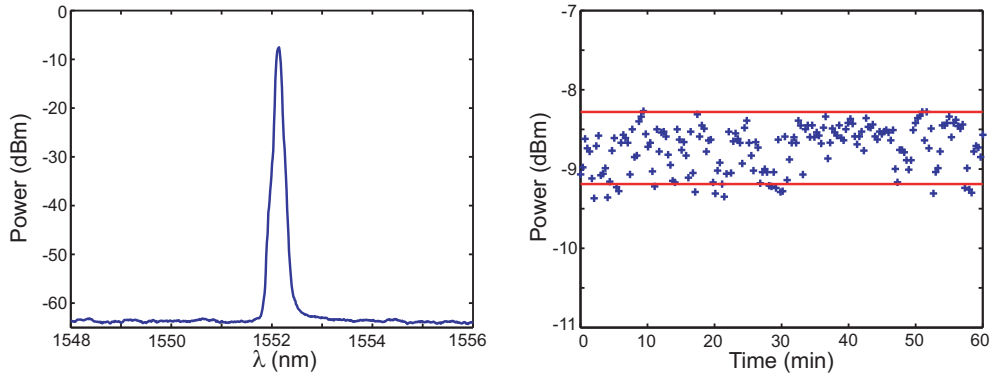
ing systems that depend on the linewidth and stability of the emitted laser wavelength.

Fig. 6.14 (right) also shows the wavelength stability measured using the heterodyne detection method (without the polarization splitter). The laser signal is mixed with the TLS and both polarization modes are held in the ESA during 10 minutes. The orthogonal polarization mode spacing of 400 MHz (3.2 pm) corresponds to the typical fiber birefringence. The higher wavelength drift of both polarization modes is under 65 MHz (0.52 pm).

### 6.3.2.2. OSNR and power stability

The output laser signal was connected directly to an OSA (HP70952B) to study the power behavior of the fabricated laser. Maintaining the pump power emitting at 26 dBm, the generated output optical power was monitored during 1 hour using the OSA.

In Fig. 6.15, the output spectra (monitored with an Optical Spectrum Analyzer) of the proposed laser emitting at the Bragg wavelength of the equivalent filter is depicted (left) exhibiting an optical signal-to-noise ratio (OSNR) higher than 55 dB. The power stability measured each 20 seconds (right) is also depicted. The achieved stability was 0.91 dB with a 90% confidence interval during 1 hour.



**Fig. 6.15.:** Measured OSNR for a 26dBm power pump (left) and power stability measured during 1 hour (right).

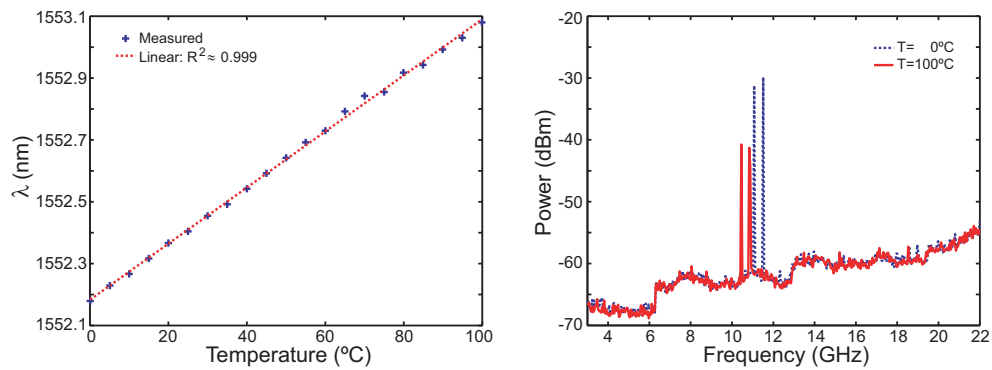


**Fig. 6.16.:** Emitted wavelength displacement during the temperature sweep (left) and the two orthogonal polarization modes at the extreme temperatures ( $0^{\circ}\text{C}$  and  $100^{\circ}\text{C}$ ) (right).

### 6.3.2.3. Temperature response

As the laser wavelength is given by the spectral overlapping of the reflected bandwidths of the FBGs, the wavelength laser response should follow the FBG thermal response. A temperature sweep between  $0$  and  $100^{\circ}\text{C}$  has been performed while the laser wavelength was measured using the OSA.

The laser response to the temperature sweep is depicted in Fig. 6.16 (left). The whole DBR structure behaves as its mirror FBGs, exhibiting linear response with a  $0.9$  nm drift within the  $100^{\circ}\text{C}$  sweep (similar to a FBG written into standard fiber). The SLM operation has been also studied during the temperature sweep. The measurements associated with the sweep limits are depicted in Fig. 6.16 (right). The same single modal behavior (polarization modes) can be observed at both temperature limits.

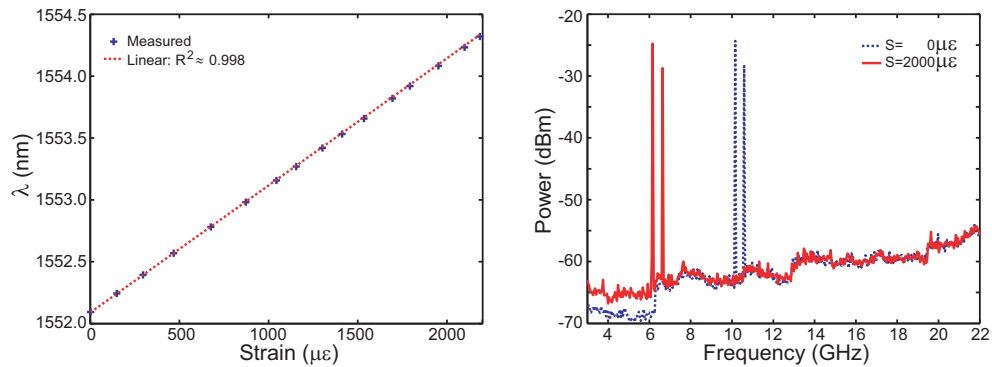


**Fig. 6.17.:** Emitted wavelength displacement during the strain sweep (left). The two orthogonal polarization modes are depicted in both extremes (right).

#### 6.3.2.4. Strain response

The manufactured device is attached to a micrometric linear motor stage to perform a strain sweep. If the applied strain is the same for both FBGs, the laser properties should be maintained while the structure is being stretched.

A strain sweep up to  $2000 \mu\epsilon$  has been performed while the laser wavelength was measured obtaining a peak drift of 2.2 nm. These results are shown in Fig. 6.17 (left) and they exhibit the same linear behavior as a single FBG. The SLM condition has also been evaluated during the sweep using the heterodyne detection. Results are shown in Fig. 6.17 (right) and the SLM is maintained for the highest achieved deformation.

### 6.3.3. Summary

The Spectral overlap technique has been applied to manufacture a DBR fiber laser by directly inscribing the two spectral overlapped FBGs in a commercial erbium doped fiber. The total length of the fiber laser, including the two FBGs, was 58 mm. This laser operated in robust SLM regime for different working conditions and in two orthogonal polarization modes. The FWHM was less than 5 kHz and the higher signal wavelength variation was under 65 MHz (0.52 pm). The OSNR was better than 55 dB and the power stability of 0.91 dB for a pump power of 26 dBm. It has also been confirmed that the fiber laser maintains a SLM behavior over the whole temperature and strain range discussed.

From the experimental results, it can be concluded that the proposed narrow

filtering technique provide a simple approach to achieve a stable SLM fiber laser where a precise control for the cavity length and a custom made erbium doped fibers are not required. These fiber lasers can be particularly appealing for applications requiring high resolution and small size sensors.

## 6.4. Conclusions

Different aspects of fiber laser sensors have been addressed in this chapter. Based on the combination of FBGs with active fibers (typically Erbium-doped fibers), several studies regarding the spectral evolution of filtering elements within a feedback structure have been performed. Extending these filtering requirements to obtain sensing heads, different filtering techniques based on FBGs have been evaluated for laser structures and particularly for local generated laser sensors based on commercial Er-doped fibers.

Since FBG are widely employed as filtering elements, the spectral evolution of a FBG within a laser structure has been modeled and experimentally characterized. The equivalent spectral response of the filter is modified depending on the chosen feedback structure. Particularly, when employing Fiber Bragg Gratings (FBGs), an improvement of the spectral selectiveness of the equivalent filter can be observed in the laser output spectrum. A new model that fits this spectral evolution has been proposed and experimentally tested. The achieved results exhibit a simplification on the requirements of the passive filtering element that are mainly related to its passive response and to the feedback structure.

Although some simplification regarding filtering elements has been experimentally confirmed for laser structures, for specific applications, very narrow filtering technique are still required. Also based on uniform FBGs, a simple filtering technique based on the partial overlap of two uniform FBG has been proposed and studied both by means of simulations and experimentally. The achieved results offer a detailed view of this filtering method, taking into account several factors such as the filter bandwidth or the tuning process. Based on a ring laser setup, this filtering technique has been experimentally tested, being able to reach the SLM regime even with a long cavity.

Finally, also based on this filtering scheme, a very stable fiber sensor that

locally generates a laser signal within the sensing head has been manufactured and experimentally tested. Employing a commercial Er-doped fiber, two uniform FBGs have been directly written, being one of them slightly displaced during the writing process. The achieved results exhibit a great stability confirming that the fiber laser maintains a SLM behavior over the whole temperature and strain range discussed. These kinds of sensing heads where a laser signal is directly generated on the sensing area can be very useful for improving the FBG interrogation distance.

The proposed studies and techniques can improve present quasidistributed transducers by introducing locally generated laser signals. This kind of sensing heads exhibits a great improvement regarding the available optical power and the same linearity of sensing FBGs.

As a result of the research about combining FBGs and Er-doped fibers, 3 journal articles and 1 international conference paper have been obtained.

# Chapter 7

---

## Hybrid Fiber Bragg Grating Shape Memory Alloy techniques

---

Hybrid materials with shape-modification capabilities have been commonly employed in a wide set of different scenarios [1]. Particularly, shape memory materials [2] exploit different physical and chemical properties to modify their inner structure under particular circumstances, what allows the design of new devices adaptable to external changes in temperature, stress, magnetic or electrical field.

Within this shape memory materials, Shape Memory Alloys (SMAs) [3, 4] are notable for their widely application to very different fields. Changing the crystallographic phase of metallic alloys, these materials offer large deformations and high recovering forces that can add reaction capabilities to many materials, both for sensors or active structures. Although combining OFSSs and SMAs in the same structure has already been addressed [5, 6], the reported applications are focused on preventing particular conditions instead of adding real time reaction capabilities by merging both technologies.

With a proper combination of Fiber Bragg Gratings and Shape Memory Alloys, several hybrid sensing devices and structures that combine sensing and reaction means have been developed during this PhD work. The sensi-

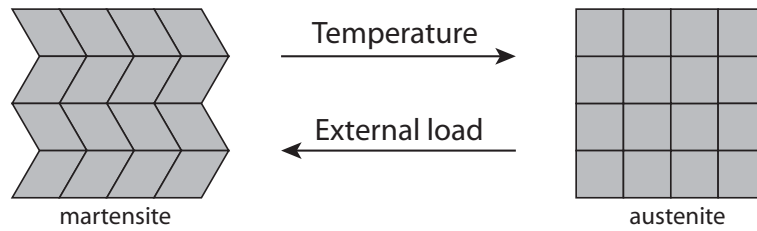


**Fig. 7.1.:** Schematic illustration of the deformation process of a SMA.

tivity enhancement to different parameters of SMAs have been exploited for the development of temperature transducers with temporal memory (Section 7.2, *Hybrid temperature level transducer*). A truly Smart Material based on these technologies has been also developed and is described in Section 7.3 (*Smart material based on SMA*). A smart material able to react to different operational conditions has been developed by means of a feedback loop that employs a SMA and a FBG as actuation and sensing means respectively.

## 7.1. Shape Memory Alloy

In a simple way, a Shape Memory Alloy (SMA) is a mixture of different metals that remembers its forged (original) shape [3]. The original shape is returned by heating the alloy above a threshold temperature. Basically, a SMA changes from a crystallographic phase (the martensite state) to other phase (the austenite state) as its temperature rises. The movement caused during the transition from the “cool” state (martensite) to the “hot” state (austenite) is caused by the material crystallographic restructuring. By increasing the temperature above a transition threshold, the original structure is recovered. Once the SMA is cooled again, the original shape is maintained until an external mechanical deformation is applied over it. Shape memory alloys derive their unique transducer capabilities from the fact that they can recover from up to 10% of the strain provoked by external loads. The stability of the austenite and martensite phases provides SMA with the capability for “remembering” different shapes constructed in the austenite phase (“high” temperature). A schematic illustration of the transition between phases is depicted in Fig. 7.1.

The thermal response of the SMA actuators is usually very abrupt, causing

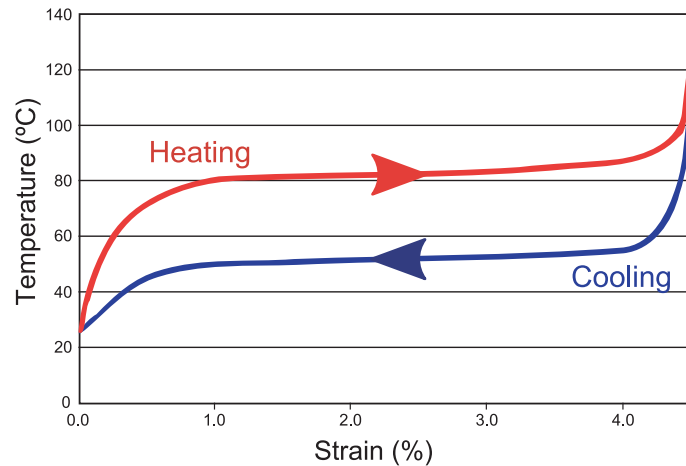


**Fig. 7.2.:** Thermal response of a loaded SMA wire with a central temperature transition of 70 °C.

a very strong deformation in a very short time. On the other hand, the cooling process depends on the actuator configuration, but it is usually slower than the heating process. Since the actuation movement is caused by the thermal evolution of the SMA, different external parameters such as air movements or surrounding materials may affect the whole system accuracy, making it more difficult to get high precision actuators. An example of the thermal response of a commercial actuator wire is depicted in Fig. 7.2.

Many different shape memory products are commercially available and are widely employed in other research environments, from mechanical structures to biomedical applications. Based on the combination of these shape memory products with other hosting materials, many different structures can be designed both for sensing and to react to external events.

## 7.2. Hybrid temperature level transducer

OFS-based temperature transducers are a widely addressed problem [7] and particularly those based on FBGs [8, 9]. Although FBG based technologies can be considered a mature research field, the availability of new materials enables the development of new fiber sensing devices exploiting specific benefits of different hosting materials to enhance their final performance.

Particularly, during the last decades, the appearance of shape memory materials [2] has allow the development of new hybrid transducers that take

advantage of their shape-varying condition. Within these materials, Shape Memory Alloys [3] offer a very high deformation range that can be employed for many different applications from biomedical [10] to structures [11]. Despite its pseudo-plastic response that can be interesting for many applications, SMA can also be modulated by their temperature. When the surrounding temperature increases above its transition threshold (that can be selected varying alloy concentrations), a SMA piece will recover its forged shape. Particularly, for a SMA whose forged shape was a wire and it is under strain, when the temperature rises, the SMA wire will shrink, recovering its original length.

A new approach to obtain temperature level measurements has been developed combining FBGs with SMA actuation wires. The achieved device combines the advantages of both technologies and the optical fiber device can be easily employed as on/off sensing system. The proposed device has been conceived to be a maximum detector that is activated when some measurands (temperature or current) go above a given threshold. Both, point or quasi-distributed fiber sensors systems can be based on these devices, enabling their application in a wide set of industrial applications. In this work, this new device has been described and experimentally characterized to analyze its main advantages/drawbacks for its employment as a quasi-distributed sensor system.

### 7.2.1. Transducer architecture

The proposed device is based on a nickel-titanium SMA forged in wire shape with a diameter of 0.25 mm [12]. Applying a pre-stressing force by a small spring, the SMA wire is strained at room temperature. A typical deformation ( $\Delta L/L$ ) for this kind of SMA actuators lies between 2% and 5% and, particularly, the chosen wire has a transition temperature of  $70^{\circ}C$ , so by heating the wire above this temperature it will recover its original length ( $L$ ). A scheme of the proposed device is depicted in Fig. 7.3 (top).

The proposed device has been manufactured employing a  $L = 4 \text{ mm}$  FBG written into a standard telecommunications optical fiber. The FBG has been embedded into a glue block, placed directly in contact to the SMA actuator wire. A thermal resistant glue capable of reaching temperatures up to  $150^{\circ}C$  has been employed to form the sensing block, comprised by a SMA wire glued

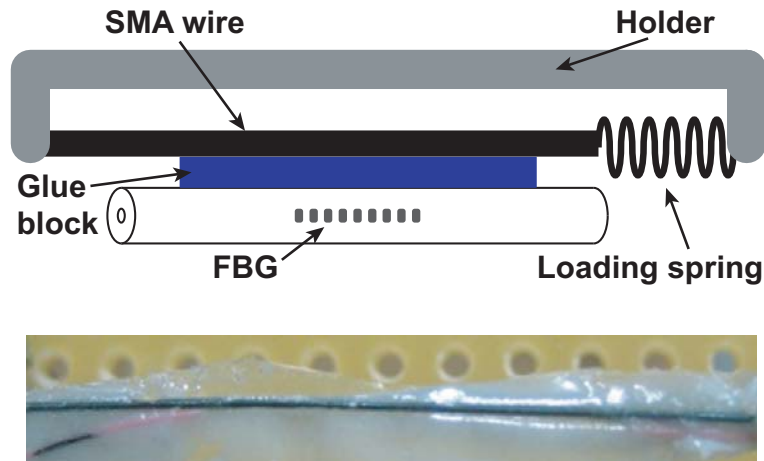


**Fig. 7.3.:** Scheme of the proposed transducer (top) and a detailed photo of the SMA-FBG interface (bottom).

to the FBG and a pre-loading spring mounted to an external holder.

Many effects contribute to the final FBG wavelength drift of the proposed device: the SMA wire shrinkage, the thermal expansion of the base materials and also the thermo-optic effect. However, based on different contributions, the most important is given by the SMA shrinkage, which determines the sensing response: as the temperature rises, the compression of the FBG given by the SMA wire shrinkage exceeds the other two contributions, achieving a lower FBG central wavelength.

### 7.2.2. Experiments

The manufactured proof-of-concept device has been experimentally characterized. Trying to avoid undesired thermal responses (e.g. overheating or temperature differences between SMA parts), the device has been heated by passing a controlled DC current through the SMA wire (Joule heating). Given that the SMA wires have a relative high electrical impedance, they can be easily heated employing DC currents. The setup employed during the characterization is depicted in Fig. 7.4.

Employing a commercial FBG interrogation unit (Si425-500 from Micron Optics), the FBG signal was acquired while different currents were applied to the SMA wire. Setting a peak current in 1.5 Amp, a custom PWM driver has been employed to apply different equivalent currents to the device. A

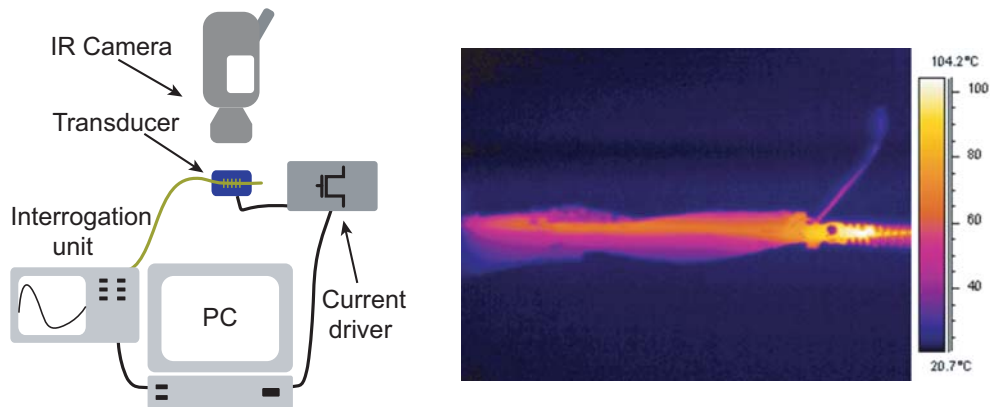


**Fig. 7.4.:** Setup employed for the experimental characterization of the proposed device (left) and a thermogram of the working device (right).

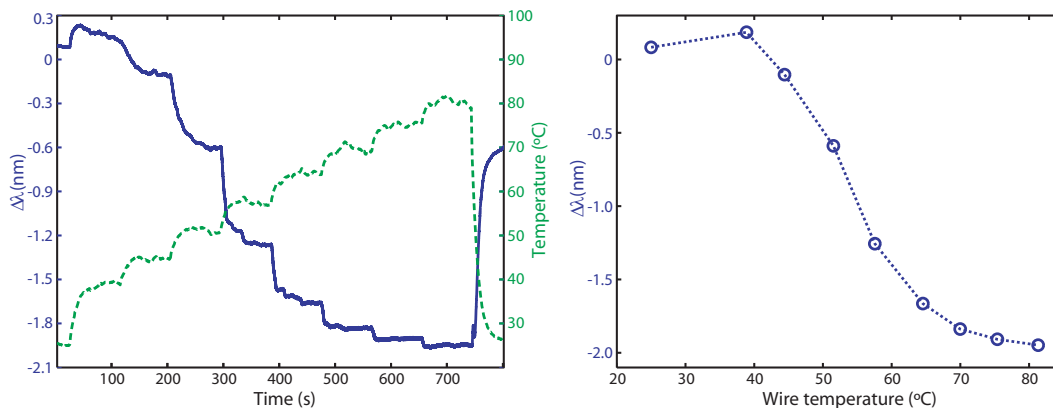


**Fig. 7.5.:** FBG wavelength drift (solid line) and wire temperature (dotted line) during the current sweep (left). Temperature response of the device (right).

thermographic IR camera (FLIR ThermaCam SC2000) has been also employed to measure the device temperature evolution. A current sweep (that provoked a temperature increase) has been applied to obtain the thermal response of the transducer.

In Fig. 7.5 (left), both measurements: the FBG wavelength and the wire temperature (obtained with the IR camera) are depicted. Their relation has also been extracted by averaging both signals for each sweep step and it is depicted in Fig. 7.5 (right). At lower temperatures, the whole sensing block responds positively to the temperature rise because the thermal expansion and the thermo-optic process overcome the SMA shrinkage. On the contrary, when the temperature increases, the SMA starts its transition to recover its forged shape, offering a steeper response. This process ends above the tran-

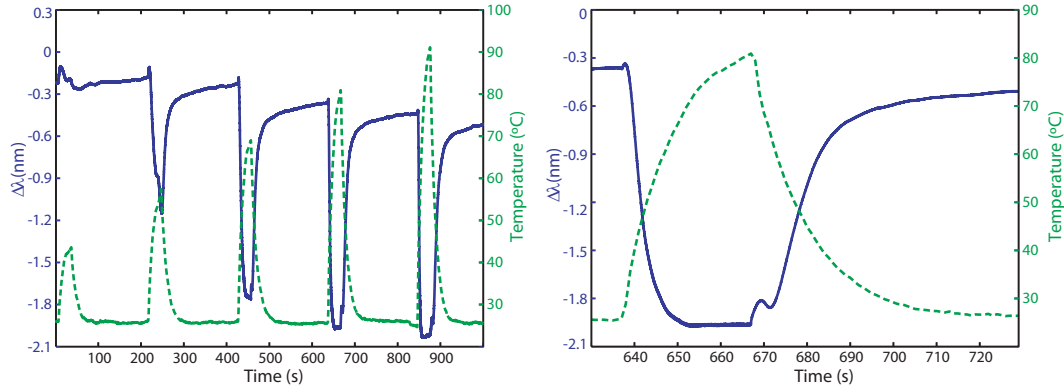


**Fig. 7.6.:** Train of pulses during the FBG accommodation (left). Single pulse after the FBG accommodation (right).

sition temperature ( $70\text{ }^{\circ}\text{C}$ , for the employed wire) when the process starts to stabilize.

In order to evaluate the repeatability of the manufactured sensor, different temperature peak trains have been provoked using different currents. In Fig. 7.6, both measurements during the first sequence of pulses are depicted (left). The accommodation effect of the FBG to the housing glue block can be noticed by the remaining compression on the FBG (besides the remaining thermal effect within the block). However, after a long pulse sequence (above 100 pulses) this accommodation effect is removed, achieving more repetitive peaks. When the reached temperature is far from the transition area, the FBG wavelength drift is very low. On the contrary, after exceeding a threshold, this drift becomes greater, being easily detectable by different means.

An example of a single peak after the accommodation effect is depicted in Fig. 7.6 (right). In this pulse, some thermal memory can be noticed, requiring extra time to reach the initial FBG wavelength. The transducer also exhibits a slow thermal recovering that is highly dependent on the surrounding materials and working conditions, but it can be useful to simplify the interrogation.

### 7.2.3. Quasi-distributed transducer

A quasi-distributed temperature sensor has been proposed formed by several connected temperature level transducers. The same sensing element can be connected in-series to an optical fiber and be interrogated using OTDR techniques. Employing FBGs of very low reflectivity with the same central

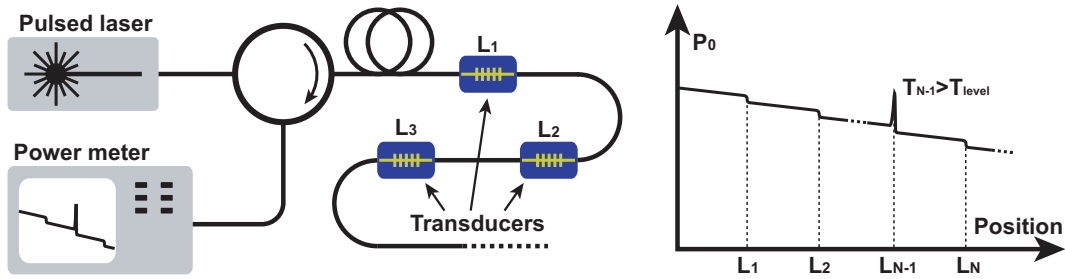


**Fig. 7.7.:** Illustration of the sensor network setup (left). Visualization of the position of each sensing point within the fiber (right).

wavelength, a laser pulse with a lower wavelength can be launched into the optical fiber while the return light is collected.

Based on the time of arrival, different spatially modulated sensing heads can be interrogated using the proposed scheme (Fig. 7.7, left). An example of an expected trace of the proposed system is depicted in Fig. 7.7 (right). When the temperature of a sensing point exceeds the designed threshold, this point becomes active, being detected by the OTDR technique.

#### 7.2.4. Summary

In this work, different technologies (FBG and SMA) have been merged to develop a new hybrid temperature sensing head. Based on the special properties of SMA wires, a transducer with a steep and negative temperature response has been experimentally verified. A proof-of-concept sensing head has been manufactured formed by commercial SMA actuation wires. Its experimental characterization exhibits its benefits for its application to quasi-distributed temperature sensing. In addition, just by adding extra means to hold the SMA wire into its short position after exceeding the designed temperature threshold, it could improve the device functionality, as it will not require an on-line monitoring of the transducer.

### 7.3. Smart material based on SMA

Although different technologies have been combined on the development of new sensing devices, industrial applications usually require very complex structures beyond only sensing devices. However, these hybrid sensor systems

can be an intermediate step towards a fully operative smart material where both sensing and actuation means are required.

As explained before, different technologies must be joined to achieve a Smart Structure: sensing, decision and actuation. At a lower scale, a Smart Material can be defined as a material with sensing and actuation capabilities. The main differences in comparison to a integral Smart Structure lie in the decision making. A smart material must be able to adapt itself as a part of something bigger; on the contrary, a Smart Structure must have a global knowledge about itself and its surrounding environment and, consequently, the decision step becomes more challenging.

Several proposals of Smart Materials based on feedback structures have been reported using Fiber Bragg Gratings (FBG) [13], such as reducing vibration in a metallic beam with piezoelectric actuators [14] or in a working structure by modifying a mass position [15]. Even in the robotics field FBG sensors have been reported providing signals to feed a control loop to reduce the vibration of a robot arm [16]. On the other hand, Shape Memory Alloy (SMA) actuators have also been applied to smart materials in different fields such as crack suppression in carbon fiber reinforced plastics [5] or to adapt wing geometries [6]. These cases combine both FBG transducers and SMA actuators, but performed in an offline way, with no feedback process during the structure operation.

Based on the technologies addressed in the development of sensing heads (FBGs and SMAs), a Smart Material has been developed during this work. Taking advantage of both sensing and actuation properties of these different technologies, an auto-stabilized GFRP structure has been developed. Employing a closed PID control loop, the position given by the FBG has been employed to adapt the actuation wire (SMA) to a precise position. The resulting material can adapt its response to different operational conditions and loads to follow a pre-established target position.

### **7.3.1. Material description**

A simple structure to evaluate the control scheme has been designed based on an arc-shaped Glass Fiber Reinforced Plastic beam. A glued FBG has been employed to provide the position measurements and a SMA wire attached to

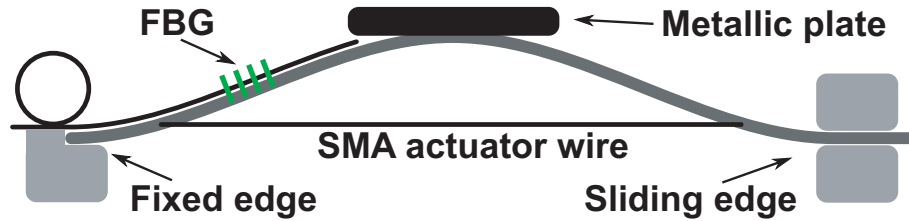


Fig. 7.8.: Experimental setup employed to test the proposed smart material.

the bottom has been employed as actuator. A metallic plate has also been attached to the center of the structure to provoke a vertical load, allowing the SMA wire to recover its original length. The structure has been designed to obtain a stable vertical position on the metallic plate attached to the top of the beam. This vertical position is measured by the FBG through the deformation in the outer surface of the arc beam. The actuator wire has been designed to reduce its length, provoking a vertical displacement of the metallic plate.

In Fig. 7.8, the proposed smart material is detailed. The combination of fixed and sliding edges allows the vertical movement of the central arc-section. The actuator wire is driven by a custom circuit that controls the current delivered to the wire and, consequently, the SMA temperature.

However, as described in previous sections, the activation curve of the SMA is very abrupt and offers a low control. Since the actuation movement is provoked by the thermal evolution of the SMA, different external parameters such as air movements or surrounding materials affect the whole system accuracy, making it more difficult to get high precision actuators. In addition, the cooling process depends on the actuator wire conditions, but it is usually slower than the heating process, achieving a slower movement in one direction. All these contributions cause a poor repeatability on the actuation system. Trying to overcome this lack of control, a Proportional Integral Derivative (PID) control loop has been employed to determine the current boosted to the SMA wire.

### 7.3.2. Experiments

The left end of the arc-shaped beam is fixed and the movement of the other one is limited in one axis and free in the longitudinal axis. When the SMA actuator wire becomes shorter, it raises the metallic plate on the top. Due to

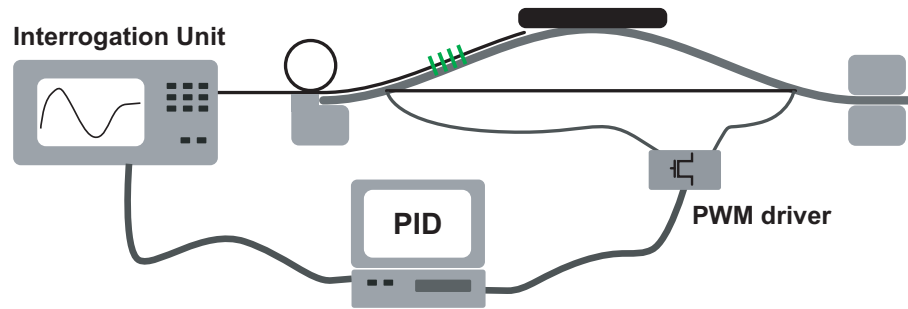


**Fig. 7.9.:** *Designed smart material with a FBG transducer and a SMA actuator wire.*

the pull down load caused by the metallic plate, the arc-shaped beam recovers its initial position when the SMA is relaxed.

The FBG transducer has been interrogated using a commercial unit (Si425-500 from Micron Optics) connected to a PC over Ethernet. The SMA actuator wire has been connected to the same PC using a custom PWM driver that boosts a controllable current to increase the SMA actuator temperature. The FBG feedback signal and the actuator driver are linked to the PID control loop that has been implemented on Matlab.

The sampling frequency of the FBG signals was set to 2 Hz and the PWM update period was 2 seconds. In order to get a smoother SMA response, the total current offered to the PWM driver has been limited to 1 Amp. The PID control loop gain factors have been empirically adjusted. Based on the setup depicted in Fig. 7.9, the proposed smart material has been driven to different target positions measured by the FBG transducer. Once the position of the structure became stable, different extra loads applied to the metallic plate were provoked to study the material response to varying environmental conditions.

Different FBG deformations have been employed as PID target positions to evaluate the smart material “static” response. During these tests, the load applied to the metallic plate has been maintained while the smart material must compensate the temperature variations in the SMA wire due to not-controlled environmental conditions (e.g. air flow or vibration) that influence the heating and cooling process of the SMA wire. The “dynamic” response of the proposed material has also been studied. Employing a static target position on the PID loop, different loads have been applied to the arc-shaped beam by changing the weight supported by the metallic plate. Trying to benefit this dynamic

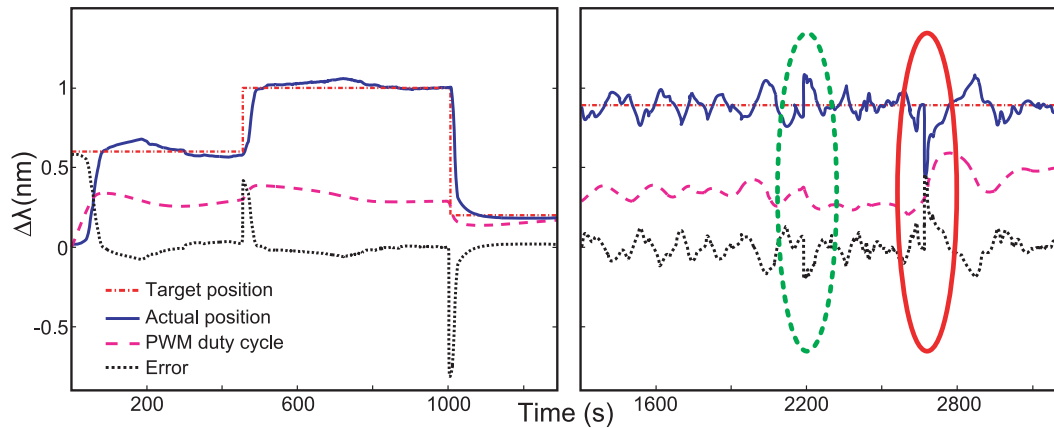


**Fig. 7.10.:** Smart material under 3 stable positions (left) and a target position with variable loads (right).

situation, the PID loop gains have been empirically modified to achieve a fast response.

The response of the smart material to both tested situations is depicted in Fig. 7.10. Three different target positions (specified in  $\Delta\lambda$ ) have been employed to feed the PID control (left). The control loop has been trimmed to generate a slow varying PWM duty cycle (dashed line) that reaches the target position based on the error evolution (dotted line). The measurements of the FBG wavelength shift (solid line) exhibit a smooth smart material movement to its new target position.

The material response to environmental varying conditions has been analyzed by trimming the PID loop to get a fast response and the achieved results are depicted in Fig. 7.10 (right). Employing a constant target position, different weights have been placed on the metallic plate. When a 100 grams load (dotted circle) was removed, the control loop reduced the PWM duty cycle (dashed line) to maintain the target position.

The smart material response to varying load conditions was also analyzed with a PID faster response configuration, shown in Fig. 7.10 (right). After the material stabilization, an extra load of 200 grams was added (solid circle) and the material became stable again. The reaction speed of the structure depends on the PID control parameters offering the possibility of favoring static or dynamic responses. Particularly, the overshoot achieved during the second test was higher than the first because of the PID “dynamic” configuration.

### 7.3.3. Summary

In this work a new smart material based on a glass fiber reinforced plastic instrumented with FBG transducers and SMA actuators under a PID control has been proposed and tested. The feedback signal coming from the FBGs was employed by a PID loop to achieve a high precision actuator based on SMA actuator wires. The achieved results exhibit the smart material stabilization capabilities even under varying working conditions. The final material response can be slightly adapted to react with high precision or high speed responses by changing the PID control parameters. Both tested situations show a good response of the proposed material despite the sharp activation curve of the SMA actuator wires.

## 7.4. Conclusions

Reflecting the actual interest in merging sensing and reaction technologies, two widely employed techniques (FBGs and SMAs) have been combined in this chapter to demonstrate new smart materials and hybrid sensors. Based on commercial actuation wires of a low transition temperature, different FBG based structures have been addressed both for sensing and actuation purposes.

SMA has been employed to build a temperature level transducer. Connecting both sides of a small piece of a SMA actuator wire to a loading spring, the whole structure was strained until the temperature increased over the given threshold ( $70^{\circ}\text{C}$ ), when the SMA wire was shrank. One of the FBG was glued to the actuation wire employing high temperature glue to translate the temperature variation to the optical domain. The achieved transducer can be easily interrogated by employing OTDR methods, achieving a simple optic temperature level sensor system.

Beyond improving the existing FBG based transducers, a small step towards a working Smart Structure has also been taken by combining both technologies into a feedback structure. Employing a FBG as a position reference, a SMA actuation wire has been added to an arc-shaped GFRP beam that supports a metallic plate. The SMA temperature has been controlled by applying different currents to the wire. Employing a closed PID loop, the position of the metallic plate has been corrected in response to different operational

conditions following a preset location.

Although the described approaches are just proof-of-concept devices, both developments have been employed to detect integration problems between very different technologies. Some weak points such as temperature dependence of the material properties and the integration problems of active materials, had to be solved before achieving working devices. The obtained conclusions will help on the development of improved smart sensors and structures. As a result of these studies, 3 international conference papers have been published based on the work summarized within this chapter.

# Chapter 8

---

## Data managing and decision making

---

With the quick development of sensing techniques, the available amount of data has been drastically increased, allowing more complex Structural Health Monitoring (SHM) models. However, this increase in sensing data gives rise to another problem: retrieving the useful information from large datasets. SHM models must usually provide a direct output regarding the whole status of the monitored structure. This direct output is required for a possible actuation within a Smart Structure or to externally take a decision regarding the structural status (e.g. stop the operation or make maintenance works).

In spite of the fact that SHM simple models are typically well defined, more complex models may not have an a-priori perfect definition, given that too many parameters have to be taken into account. Thus, achieving a reliable solution in these complex scenarios may be an extremely challenging problem. The improvement in sensing techniques has been widely supported by the fast development of Information and Communication Technologies (ICT), that also offer different means to solve data managing and decision making problems. Particularly, dealing with complex problems hard to replicate using pre-established models, Machine learning (ML) algorithms exhibit certain

benefits when some a-priori knowledge is not available. Nowadays, due to the processing capacity growth, a wide set of complex algorithms can be employed to simplify the decision task to be directly implemented into the Smart Structure.

Although ML approaches have not been widely applied to smart structures, there are several scenarios showing their benefits to deal with complex problems and large datasets. Examples such as pattern recognition, automatic navigation [1] or job analysis [2] have been successfully addressed using ML algorithms without an a-priori knowledge of the problem to be solved.

An important goal when using ML approaches is to let the algorithm learn the a-priori knowledge by itself, allowing a correct response of the system. To perform this task, these algorithms are usually trained with data to be classified indicating the correct output. There are lots of different machine learning algorithms applied to engineering fields [3], but they do not evolve in the same way when the incoming data are modified due to noise or environmental conditions changes, making one of them more suitable than the rest for a given application. This suitability can be studied by changing the environmental parameters of the problem such as the amount of acquired data, the pre-processing scheme, etc... These kinds of studies can show some clues to improve the final application by establishing the number of acquisition points or determining their best location and pre-processing scheme.

A small contribution to data managing and decision making has been performed during this PhD work by applying Machine Learning algorithms to solve SHM problems. A brief introduction to the two evaluated Machine learning techniques, Hierarchical Temporal Memories (HTM) and Artificial Neural Networks (ANN), has been detailed in Section 8.1, (*Machine learning approaches*). A reference algorithm (ANN) has been compared to a new computing paradigm (HTM) to study their final performance under different working conditions based on a well-known SHM problem, described in Section 8.2 (*Application to Smart Structures: Impact detection*), Both approaches have been employed to discover the a-priori knowledge of the proposed scenario to detect low energy impacts in a GFRP beam.

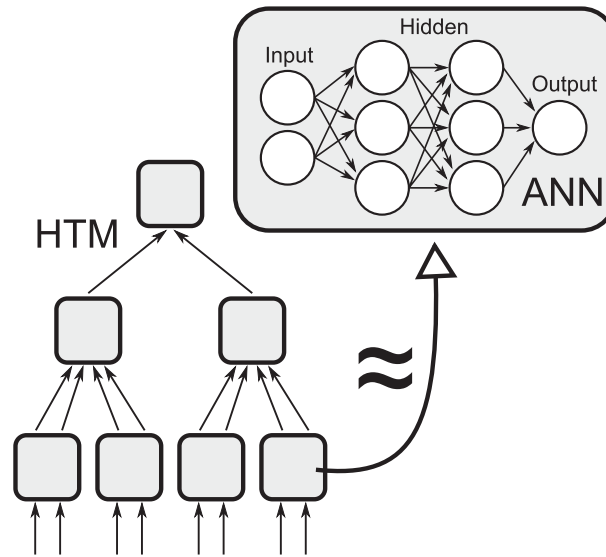


Fig. 8.1.: Schematic complexity of ANNs and HTMs.

## 8.1. Machine learning approaches

Although there are many machine learning algorithms, two of them have been evaluated for SHM purposes during this work. The widely applied approach known as Artificial Neural Networks (ANN) has been employed as a reference algorithm to be compared to a new approach: Hierarchical Temporal Memories (HTM). Introduced by Hawkins [4] and formalized by George [5], HTM is a high level computation model inspired in the human neocortex, and a software implementation called NuPic developed by the company Numenta, Inc is offered.

ANN is a well known, widely used supervised learning algorithm capable of modeling highly non-linear problems. The ANN learning algorithm [6] is inspired in the functional aspects of biological neural networks. It is a supervised learning algorithm where a group of interconnected neurons compute the same non-linear function (typically the sigmoid function) of the weighted inputs. ANNs have been widely used in many different fields including machine vision tasks [7] or industrial process control [8]. Both algorithms require a training phase before performing the classification tasks to allow the required problem modeling.

The HTM algorithm can be described as a hierarchy of interconnected high-level identical nodes that are able to process and store information from their

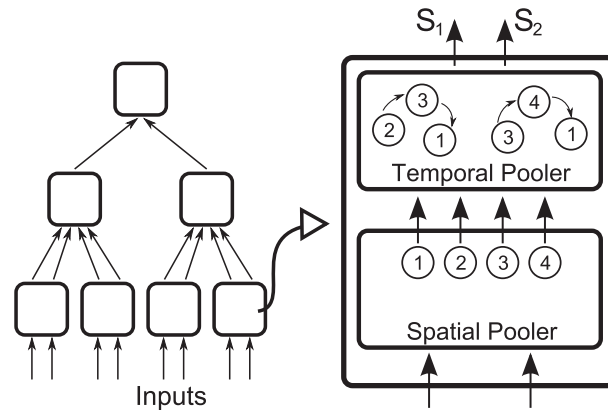


Fig. 8.2.: Architecture of HTMs. Detail of a HTM node.

data inputs. Each high-level node of this model mimics the behavior of the cortical columns of the biological brain ( $\approx 60,000$  neurons). Unlike ANNs, time is a very important aspect of HTMs: in the training phase, they are precisely the time variations of the input data what allows to identify their invariant patterns and to categorize them. HTMs have been used for different applications such as recognition of hand-written digits [9] or image retrieval [10], being most of them within the machine vision field.

As happens in ANNs, each node of a HTM computes the same algorithm, but it has two differentiated stages. As shown in Fig. 8.2 (right), the first stage is the spatial pooler where a set of coincidence patterns (four at the figure) is created during the training phase. To get the coincidence patterns during the training phase, every time that new data arrive, their Euclidean distance is calculated against the set of already created quantization centers. If the distance of the new data is larger than a configuration parameter, Max Distance, the pattern is added to the spatial pooler as a new center of quantization. The output provided by the spatial pooler is a vector with the probability distribution over the quantization centers, where the maximum of the output vector is the most probable pattern for a given input.

After the spatial pooler training phase, the training phase of the temporal pooler follows, where the temporal evolution of its input vectors (the probability distribution over the quantization centers of the spatial pooler) is used to progressively build a probabilistic transition matrix between the patterns. A set of the most probable pattern transitions (temporal sequences) is built, which is the training result in the temporal pooler. The training phase in the

temporal pooler is mainly controlled by 2 parameters: Top Neighbors, which specifies the maximum number of coincidence patterns that are added simultaneously to a temporal sequence; and Transition Memory, which specifies how many input vector transitions are kept in the temporal pooler to track the time structure of coincidences while learning the time adjacency matrix.

The output of the temporal pooler is a vector with the probability distribution over the space of temporal sequences, being the maximum of this vector the most probable sequence found in the training phase. This information is passed to the upper nodes in the hierarchy.

Once the HTM is trained, the inference mode can be used to perform the classification task. There are several algorithms for the inference mode, the Gaussian algorithm is commonly chosen and it works as follows: for every new set of data at the inputs of the bottom nodes, the probability of being any of the already stored patterns of the spatial poolers is calculated assuming a Gaussian function of the Euclidean distance. The parameter of this Gaussian function can be also configurable for each node (Sigma). After that, the probability vector is passed to the temporal pooler and the probability of being any of the stored temporal sequences is computed. The classification output computed by this algorithm is the vector with the probability of belonging to one of the temporal sequences.

Both approaches have particular advantages for the application discussed in the following section (*Application to Smart Structures: Impact detection*). On the one hand, ANNs are a relatively simple algorithm, but with capabilities of modeling highly non-linear patterns. On the other hand, HTMs are a more complex algorithm where a lot of parameters have to be set (apart from the architecture). HTMs can better process temporal sequences by using the temporal pooler, but they also need very high dimensional input vectors to work properly. On the contrary, ANNs work perfectly with small dimension input vectors, but they do not exhibit memory capabilities to process temporal sequences.

## 8.2. Application to Smart Structures: Impact detection

The ability of both machine learning approaches (ANN and HTM) to map non-linear problems from experimental data is evaluated under controlled experiments. The chosen scenario is the detection of impacts in a cantilever beam under vibration instrumented with Fiber Bragg Gratings [11]. The installation procedure and position of the FBGs has been modified to obtain different points of view of the same test. Although there are several deterministic approaches that solve this problem [12–14], even using machine learning approaches [15, 16]; all of them employ an a-priori knowledge of the problem to be solved.

In this work, the main characteristics of both machine learning approaches have been analyzed by varying environmental parameters such as the number of sensing points or their location. From the achieved results, some clues can be extracted about dealing with noisy or partial data when using machine learning approaches to create a complex model without a-priori knowledge.

### 8.2.1. Application scenario

Detection of low energy impacts in a composite beam under vibration has been chosen to test both machine learning algorithms. This is a widely addressed problem in the literature where, by analyzing strain signals of different sensors, the impacts can be detected [12] and even located [14]. In this work, a Glass Fiber Reinforced Plastic (GFRP) beam of 640 by 80 mm has been manufactured including 8 strain sensors located at different positions. One edge of the beam was fixed while the other one was attached to an electromagnetic shaker (TIRAvib 51110). The shaker was employed to periodically deform the beam adding extra noise to the measurements, hiding the low energy impacts. An electromagnetic actuator was also placed under the beam in 4 different positions to generate the impacts.

The 8 strain sensors were located at four different positions in the longitudinal axis, but at two different depths: 4 of them were embedded into the composite beam and the other 4 were glued to the beam surface. The

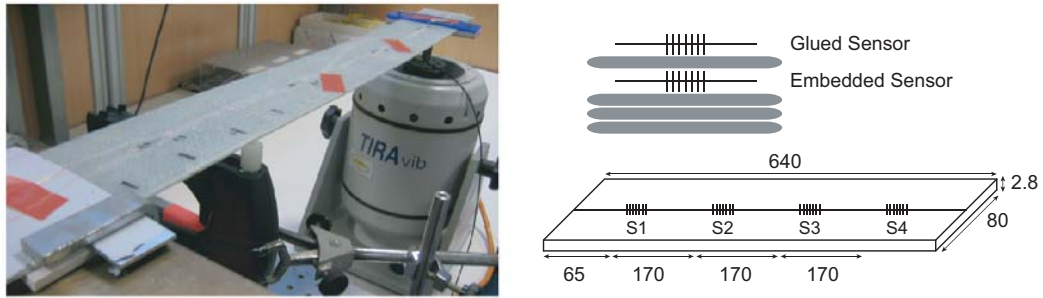


**Fig. 8.3.:** Photo of the experimental setup (left). Installation details of FBG sensors (right). Dimensions are in millimeters.

selected strain sensors are based on optical fiber technology, particularly on Fiber Bragg Gratings (FBGs) [11], a technology highly compatible with composite materials [13]. All the strain sensors have been interrogated using a commercial unit (si425 of Micron Optics) with a sampling frequency of 250 Hz, what limits the high frequency response of the impacts. To obtain the data, the shaker has been fed with a sinusoidal wave with a constant amplitude and a frequency varying between 1 and 20 Hz. For each frequency, an electromagnetic actuator was employed to hit the beam 6 times in 4 different positions for each frequency (a total of 480 impacts) with a measured energy of 0.2-0.3J.

### 8.2.2. Experiments

The addressed application could be easily resolved by pre-processing the incoming data using a high-pass filter to remove the added noise. In this way, impacts can be easily detected by simply employing a threshold (Fig. 8.4), but this solution implies an a-priori knowledge of noise and perturbation frequency contents. Within this application scenario, characteristics of the available data were studied in two different machine learning schemes. The amount of fed data as well as their sensitivity have been evaluated taking into account the final performance.

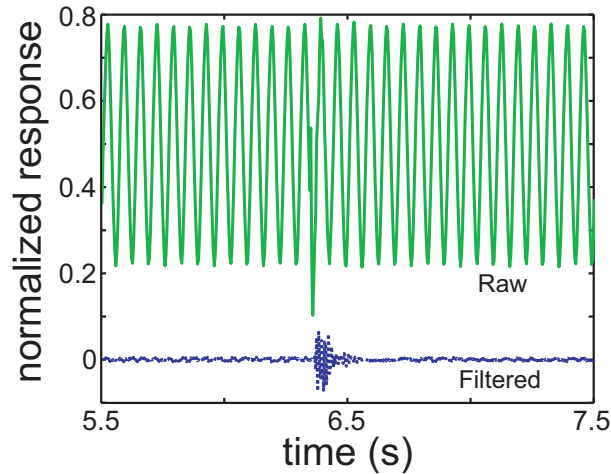


**Fig. 8.4.:** *High pass filtered FBG signal. Impacts can be detected using a threshold.*

### 8.2.2.1. Data processing

Before the training phase of both algorithms, a labeling step identifies each hit with a fixed duration of 0.36 seconds (90 samples at 250Hz). This value has been obtained by averaging the impact durations during a pre-processing step. All the strain data were scaled between 0 and 1 to allow a good numeric convergence of the algorithms. The available data have been split into 3 datasets for cross-validation. For each case, both algorithms were trained with 2 datasets and tested with the remaining one. The process was repeated 3 times, developing all the possible combinations, and the final performance was averaged. In each dataset, 2 of the 6 recorded hits for each situation were employed.

Impact detection is usually an asymmetric classification problem: there are more data in the “negative” state (non impact) than in the “positive” state (impact). In particular, in this work, there are 22.5% of samples labeled as impacts, so employing the classification rate metric can be confusing. In these cases, “precision”, “recall” and its harmonic mean “F1-score” [17] are useful metrics, and can be defined as:

$$precision = \frac{true\ positives}{true\ positives + false\ positives}$$

$$recall = \frac{true\ positives}{true\ positives + false\ negatives}$$

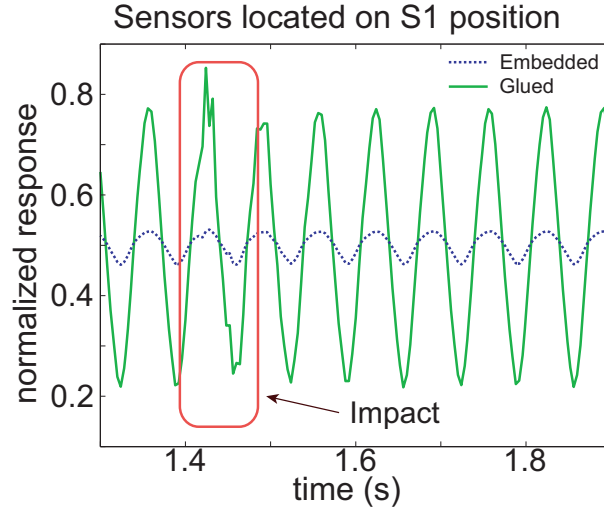


**Fig. 8.5.:** Deformation of S1 position sensors during an impact with  $Freq=15\text{Hz}$ .

$$F1_{score} = 2 \cdot \frac{precision \cdot recall}{precision + recall} \quad (8.1)$$

In a simple way, a high recall means that the algorithm returns most of the “positive” states (impacts). High precision means that the algorithm returns more “true positive” states (impacts) than “false negative” states (non impacts).

After defining the metric, both algorithms, ANN and HTM, were fed with the same input data in three different scenarios: employing the data from the 8 FBG sensors, just employing the data from the 4 sensors glued to the surface and just employing the data from the 4 embedded sensors. By using different ways to feed the data, particular advantages of each approach are highlighted. In these applications, those sensors placed on the surface are more sensitive to structural deformation, but they are also more exposed to environmental conditions (noise). On the contrary, embedded sensors are more protected but they exhibit a lower sensitivity. The sensitivity difference between embedded and glued sensors can be noticed in Fig. 8.5, where the signals from two sensors at the S1 location during an impact are depicted.

It must be noticed that the frequency sweep includes the resonant frequency of the structure (measured to be 16.4 Hz). Close to the resonant frequency, the vibration amplitude increases significantly, making more difficult the impact detection task. Trying to better understand both approaches, different data strategies were followed and the characteristics of each case are explained

below.

- Case A: Feeding with the 8 sensors data: In this situation, both surface-glued sensors and embedded sensors are included in the data fed to both algorithms. Therefore, there are highly redundant data in the non-impact state, but for impact states there is additional information due to the signal desynchronization between different sensors.
- Case B: Feeding with the 4 surface glued sensors data: By using the surface-glued sensors, there is still highly sensitive data from each position, but less redundant data.
- Case C: Feeding with the 4 embedded sensors data: The most sensitive signals (coming from the 4 glued sensors) are discarded and just the signals from the 4 embedded sensors are employed. As happens in Case B, with 4 sensors the data redundancy is lower.

In addition to the different feeding data strategies, the algorithm architecture and parameters have been also swept trying to find an optimum configuration. The ANN performance has been tested using 1 and 2 hidden layers, with a number of hidden neurons in each layer varying between 10 and 40 neurons (in steps of 10). The tested HTM architectures always consider 2 levels (as shown in Fig. 8.1, above the top node), and the number of nodes in each level varies from 4 to 8 nodes for the first level and from 2 to 8 for the second level. The remaining HTM parameters have been empirically adjusted based on previous works for other classification problems [18].

### 8.2.3. Results

The performance of both algorithms has been evaluated using the described metric (F1-score). The impact condition has been defined as a window of 64 samples of the vibration signal around the real instant of the impact. As there is not a clear end-of-impact indication within the vibration signal, and due to the presence of noise, a positive detection of the algorithms is considered when 16 of those 64 samples are labeled as “impact” in the output of the algorithm. In Fig. 8.6, a positive impact response of both algorithms is depicted (black line) against the desired output (solid line) and the individual decision of the

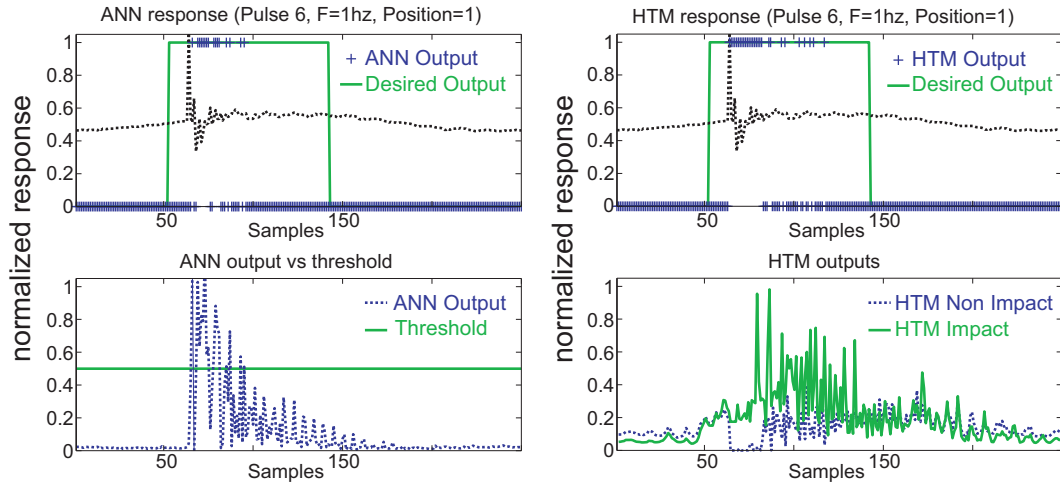


**Fig. 8.6.:** Positive output of both algorithms for an impact.

algorithm (crosses) for each sample. In the HTM case, the individual decision is taken by selecting the higher output (non-impact and impact). For the ANN, the individual decision is taken by comparing the single exit against a given threshold. This threshold has been modified for each configuration in order to improve the F1-score.

As shown in Fig. 8.6, the ANN tends to label less individual samples as an “impact” than HTM does. ANN is a memory-less algorithm where the present output just depends on the current sample fed to the algorithm. This lack of memory causes a more impulsive response of the ANN, in contrast to HTMs, where the output depends on the previous and current samples. The achieved responses of both algorithms under the three different approaches are described below:

### 8.2.3.1. Case A: Feeding with data from 8 sensors (both embedded and surface-glued)

In this case, there are 4 data sources with a high sensitivity (sensors glued to the surface) and other 4 with less sensitivity (sensors embedded into the GFRP). During the non-impact state, the less sensitive sensors almost do not add extra information to the others but, during the impact state, the embedded sensors add an extra point-of-view to the algorithms, making easier the classification task. The ANN works rather well with a 2 level architecture of 30 hidden neurons per level by having an averaged F1score of 0.967 establish-

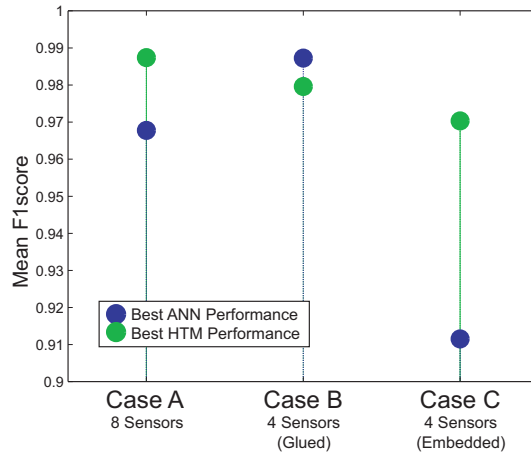


**Fig. 8.7.:** Best ANN and HTM performance achieved for each case.

ing the threshold in 0.5. The HTM seems to also exhibit a good performance with an averaged F1score of 0.987 for a 8-8 architecture (8 nodes in level 1 and 8 nodes in level 2).

As shown, both approaches work correctly in this case. Although ANNs do not have memory to work with temporal sequences, there are still enough different points of view of each “impact”, thus the algorithm is able to properly detect this situation. In general, HTMs classify temporal sequences better when an enough amount of data is available. For this case, the raw samples coming from the 8 sensors are fed into the algorithm, so there are few inputs for making spatial patterns in lower nodes. This fact establishes a limit in the hierarchy complexity to a few nodes in level 1; in fact, simpler architectures such as 4-2 works also rather well with an F1score of 0.971.

### 8.2.3.2. Case B: Feeding with the 4 surface glued sensor data

The most sensitive sensors are still used for the classification task. However, the amount of redundant data coming from the embedded sensors is reduced, but with the higher sensitive sensor samples there are enough data for the classification problem.

The ANN algorithm is directly fed with the 4-dimension vectors. On the contrary, for the HTM the same 4-dimension input vector is repeated reversed to give extra information allowing more complex architectures to find the spatial patterns. This step has been skipped for the ANN because no improvement

is obtained by repeating the same data. The best performance with the ANN approach is achieved for this scenario, as shown in Fig. 8.7. In this case, the most sensitive data from the glued sensors have been used having enough points of view of the impact state and reducing the noise data coming from the embedded ones. The best achieved F1score is 0.987 with 2 hidden layers of 30 nodes each one, and by establishing the threshold to 0.5.

In the case of the HTM, there are still very meaningful data coming from the 4 glued sensors, but the number of inputs is very low to get advantage of the spatial inference of this approach. However, the HTM seems to work pretty well by achieving a F1score of 0.979 with complex architectures such as 8-8. With a 8-8 architecture the spatial patterns are mostly discarded to benefit the temporal sequences (8 nodes in level 2). The other approach also exhibits a good performance: having into account the spatial patterns by using less nodes in level 1 with a simpler architecture (4-2). The obtained F1score is 0.970 for this architecture.

### **8.2.3.3. Case C: Feeding with the 4 embedded sensor data**

In this case, the data are coming from the 4 embedded sensors, which have a lower strain sensitivity and higher noise. As in Case B, for the HTM tests, the same 4-dimensional input vector has been repeated in the input space in reverse order to allow architectures with more input nodes. Case C is the worst case for both algorithms because only the less sensitive and noisiest data are available. For a memory-less algorithm such as ANNs, working with less sensitive data is more complicated because it is not possible to separate the noise component from the true information. Using the ANN, the best achieved F1score is 0.911 with 2 hidden layers of 20 nodes each one and by establishing the threshold to 0.4.

On the other hand, the HTM seems to work better than the ANN: the capability of this algorithm to manage temporal sequences is reflected in the obtained averaged F1score of 0.970. This performance has been achieved with an architecture of a few nodes in the first level and more in the second one (4-8). By having few nodes in the first level, the spatial patterns can be grouped in order to create clearer temporal sequences with less noise feeding the second level, where the main classification task is performed over the

temporal sequences of the first level.

In summary, with high sensitive and redundant data, both approaches exhibit a good performance, despite the errors caused by noisy redundant data on ANNs. With the data from the surface-glued sensors (higher sensitivity and less noise), both approaches still work well and the ANN works even better by not having the noise coming from the redundant data. Finally, with the data from the embedded sensors, the HTM still have a very good classification performance due to its memory capabilities, what can be noticed in the number of nodes of the second level.

#### **8.2.4. Summary**

Two machine learning algorithms have been tested using a controlled scenario. A GFRP beam instrumented with optical fiber strain sensors has been hit 480 times at 4 different locations while some extra noise were added using an electromagnetic shaker. A high level temporal algorithm (Hierarchical Temporal Memories) has been compared to the well known Artificial Neural Networks to detect these impacts. Different ways of feeding the experimental data to both algorithms exhibit their benefits and disadvantages when dealing with noisy data. Several configurations of both algorithms have been tested to achieve their best performance. Particular benefits of each approach can be exploited in order to reduce the number of sensors and/or to locate them in critical positions when installed in a real structure. The obtained data have been employed to train and test several architectures of both approaches. The achieved results exhibit an improvement in the detection ratio for the HTM just when partial data are employed. When there are enough sensing points, simpler approaches such as ANN are better to model the problem without a-priori knowledge.

### **8.3. Conclusions**

Based on the application of Machine Learning approaches, a proof-of-concept structural monitoring problem has been solved without requiring any previous modeling. Although the chosen scenario can be easily solved having into account the nature of the artifacts to be detected (e.g. impacts), this application

of ML exhibits the benefits of employing blind algorithms to solve problems without an appropriate modeling.

Blind modeling can be easily adapted to SHM purposes, where models are becoming more difficult to develop. Based on the actual computing technologies, complex ML algorithms (e.g. HTMs) can take advantage of their temporal modeling capabilities to create an abstract model of a working structure simply from the raw data directly obtained from the sensing network. This abstract model can be employed to analyze the current status of a working structure (one of the key factors of SHM) and to decide the possible actuation; achieving an on-line diagnosis tool capable of reacting to environmental and structural variations, in summary: a Smart Structure.

Beyond the final application of ML approaches, a new computing method (HTMs) based on retrieving the temporal invariant patterns within the input data has been proposed in this work. This model has been analyzed and compared to a reference ML approach (ANN) for their application to real scenarios, where partial or noisy data have to be employed to obtain a final response. Although both approaches exhibit specific benefits, HTMs work better with partial data showing their potential towards a fully operative structural model based on complex data. As a result of this study, 1 journal article has been published.



## **Part III.**

# **Conclusions and future lines**

The R&D works performed towards the improvement of optical sensing devices and techniques for Smart Structures have been briefly summarized in this part. The most significant conclusions have been extracted and, finally, the present open investigations and future R&D lines have been also detailed.

- Chapter 9: Summary and Conclusions
- Chapter 10: Open Future Lines



# Chapter 9

---

## Summary and Conclusions

---

A Smart Structure must combine three main characteristics: sensing, decision making and actuation, to be able to adapt its own condition and to react to environmental changes. Although Optical Fiber Sensors have been widely employed on Smart Structures, there are still many unsolved challenges. After reviewing the present state-of-the-art, several open challenges have been identified and grouped regarding their application field.

1. **To improve the existing sensing technologies and to develop sensing heads for new structural parameters:** Based on the requirements of new SHM models, many different parameters have to be detected and measured to obtain more complex structural models.
2. **To achieve more suitable OFSs for low cost applications:** There are still particular application scenarios where cost is a limiting factor. In this regard, achieving reliable solutions at lower costs would help their introduction in a wider variety of applications.
3. **To obtain high precision remote measurements for environmental monitoring:** A truly Smart Structure must be also aware of its surrounding environment, thus, obtaining high precision measurements

beyond the structure itself may help the structure to react.

4. **To combine OFSs techniques with actuation systems:** Although sensing technologies have been widely addressed using OFSs, additional approaches based on other technologies are required to make the structure reaction possible.
5. **To employ different algorithms to process OFS data:** Taken a decision from raw data is a main characteristic of Smart Structures, thus, several approaches should be explored to extract valuable information from these data.

Following the identified challenges, different contributions in each group have been addressed in the course of this PhD. Mainly related to the development of complex structures based on composite materials, different sensing devices have been proposed to be merged with these widely developed materials. Employing Fiber Bragg Gratings as the main technology. Both sensing techniques and devices have been developed to improve their application to structures.

A new technique to retrieve the inner strain distribution of Sampled and Uniform FBGs only employing the intensity of their reflection spectra, has been proposed and experimentally verified. Trying to improve typical interrogation methods of FBGs, the proposed algorithms combine a custom defined error metric for spectral comparison and a Particle Swarm Optimization technique to get the deformation values of different FBG sections.

Based on composite materials, different solutions have been proposed to improve the widely studied problem of temperature-strain discrimination. Several sensing heads for strain-temperature discrimination based on Fiber Bragg Gratings embedded into composite plates have been designed and experimentally tested. The most interesting approach relies on drilling two symmetrical holes to provoke different strain sensitivities to embedded FBGs. The proposed designs can be considered during the structure design to be included as structural parts, performing both tasks, mechanical reinforcement and sensing areas.

Also related to composite materials, a better implementation of the existing FBG based strain sensors has been also addressed. A transducer design

---

has been proposed to support real manufacturing conditions of large structures, making it suitable for industrial applications. Apart from improving the traditional sensing heads, different FBG based solutions have been proposed for composite materials such as a new device to evaluate composite joints of complex structures or a sensing head capable of monitoring the compaction pressure during the fabrication of a composite material.

All the FBG approaches have been verified within the laboratory. However, in addition to these experiments, several devices have been also tested under field conditions. Particularly, a full-scale wind turbine blade has been monitored during its loading tests exhibiting some of the benefits of OFS techniques in the development of Smart Structures. Although many solutions based on FBG technology have been proposed for Smart Structures, other approaches can be also studied to be included into this multidisciplinary research field.

Speckle interferometry within multimode optical fibers has been also studied to enlarge the applicability of OFS technologies by achieving low cost sensors based on commercial devices. Combining cheap sensing heads with processing schemes, different physical parameters have been successfully detected and measured, exhibiting some of the benefits of this technique.

Combining the extremely high sensitivity of interferometric sensors with advanced processing schemes, both dynamic and static perturbations have been successfully measured taking advantage of the benefits offered by the current computer systems. Employing cheap optoelectronic components, a sensing head to measure the human heart rate and an experimental setup for environmental vibration monitoring have been successfully tested. Both applications exploit the extremely high sensitivity to mechanical perturbations of highly multimode Fiber Specklegram Sensors (FSSs).

Although FSSs exhibit an extremely high mechanical sensitivity, static deformation measurements have been also studied, overcoming the noise. A processing scheme that extracts the general speckle pattern distribution (related to the modal state within the fiber) has been employed to enhance the dynamic range of Specklegram strain sensors. A fully operative sensor system for structural monitoring based on POFs and cheap optoelectronic components has been proposed and successfully tested.

A different approach has been proposed to improve the sensitivity of existing FSSs. By taking advantage of the remaining spatial information within each speckle pattern, their sensitivity can be improved because each area is statistically related to different order modes. A processing scheme has been proposed and tested, achieving a sensitivity increase when areas corresponding to higher order modes are processed. Further investigations may lead this technique to new sensing methods based on multimode fibers using their sensitivity difference between modes.

In order to reach far sensing points, different contributions to fiber lasers have been also addressed during this work. Employing commercial Erbium doped fibers, several studies regarding laser topologies and filtering requirements have been analyzed to improve the design of new active sensing heads based on fiber lasers.

Particularly, a simple filtering technique based on the partial overlap of two uniform FBGs has been studied. The achieved results offer a detailed view of this filtering method to be employed in Fiber Lasers, taking into account several factors such as the filter bandwidth or the tuning process. Based on this filtering scheme, a very stable fiber sensor working on the Single Longitudinal Mode regime has been manufactured employing a commercial Er-doped fiber. Experiments confirmed the laser stability and that a SLM behavior was maintained over the whole temperature and strain range considered. This laser sensor locally generates a strong laser signal within the sensing head that can be very useful to improve the FBG interrogation distance.

Different materials with actuation capabilities have been studied to be employed in the development of new hybrid sensing-actuation systems. Particularly, merging two widely developed techniques, FBGs and Shape Memory Alloys (SMAs), different structures have been addressed both for sensing and actuation purposes. Based on commercial actuation wires, a temperature level transducer has been proposed to be interrogated by OTDR methods, achieving a simple optic temperature level sensor system.

Going beyond the development of sensing systems, SMA wires have been also employed to build a Smart Material, as an intermediate step towards a working Smart Structure. Employing a FBG as position reference, a SMA actuation wire has been added to an arc-shaped beam that places a metallic

---

plate into any particular location. Employing a closed PID loop, the position of the metallic plate has been corrected in response to different applied forces that move the structure from the target location. Although the described approaches are just proof-of-concept devices, both developments have been employed to identify possible problems during the integration of very different technologies.

A working Smart Structure must be able to react to its environment, thus, on-line decisions have to be taken to determine the actuation (or not) based on the raw data coming from the sensing system. Complex Machine Learning (ML) algorithms can be employed to analyze the raw data and take a decision. Employing blind algorithms to solve problems without an appropriate modeling can be very useful for SHM purposes, where models are becoming more difficult to develop.

Regarding this issue, a proof-of-concept structural monitoring problem has been solved without requiring any previous modeling by employing two ML approaches: Artificial Neural Networks (ANN) and Hierarchical Temporal Memories (HTM). Both algorithms have been applied to a real scenario, where partial or noisy data has been employed to obtain a final response. Although this particular problem can be solved by other means, the application of ML approaches exhibit the benefits of blind modeling when dealing with complex models. These abstract models can be employed to analyze the status of a working structure and to decide the possible actuation; achieving an on-line diagnosis tool capable of reacting to environmental and structural variations, in summary: a Smart Structure.

The majority of the results obtained during this R&D work and included in this document have been validated by the international sensing community. The industrial application of the achieved results has been previously analyzed to be protected before their communication on specialized international conferences and journals. An industrial patent, 15 journal articles and more than 40 contributions to conferences have been achieved as a result of this thesis work. In addition, different R&D works are currently being prepared to their submission.



# Chapter 10

---

## Open Future Lines

---

The ultimate goal of this research is the contribution to the technology platform that makes possible the development of working Smart Structures that endure autonomously. Although several topics have been addressed during this PhD work, there are still lots of open challenges to be solved.

Regarding each of the main blocks, specific challenges can be identified. Starting for the sensing area, and particularly for the most employed technology, FBGs, different lines can be identified. Many different sensing solutions have been proposed based on FBG technology, however, as the complexity of working structures increases, different high order parameters have to be measured. The developing of new sensing heads for specific purposes must be reinforced with mechanical and structural knowledge, having into account high level mechanical responses during the development.

Other drawback of OFSs that can be improved is their associated cost. Although FBGs are significantly more accessible than a few years ago, there are still very expensive for many applications, thus working on cost reduction could improve their spreading over different fields. Related to this issue, other addressed technology, speckle interferometry in multimode POFs, may contribute by achieving practical implementations using inexpensive devices. However, a compact and robust implementation of these devices is required

to be employed in real scenarios. Besides, based on the same components, different wavelengths can be employed for different channels and extra means, based on modulating the laser source or improving the processing schemes, what can also enhance the spatial resolution and sensitivity of these sensors.

The other addressed sensing technology, Fiber Laser Sensors, can be very useful to face particular problems of large structures. However, a better understanding of fiber laser configurations to determine the filtering requirements would help the design of these devices. From an implementation point of view, the development of sensing heads improving the existing packages for field applications can be a great impulse for the real application of these devices, that can offer the same benefits of FBGs but improving their working range.

Going beyond sensing areas, there are lots of current challenges to be solved, within actuation and decision making. Particularly, regarding actuation systems, very different materials with actuation capabilities may be combined to OFS techniques on the design of new sensing heads for different measurands, what could improve the complex structural models. The same idea can be applied for actuation systems, where the introduction of new materials such as Shape Memory Polymers could improve drastically the material performance, having native means to react to its environment.

All these new materials with sensing and actuation capabilities must be controlled by sophisticated approaches, thus, following the structures design, more complex algorithms must be employed to determine the health of the structure, being able to work with very large datasets. Although this has been a poorly addressed problem, with the processing capacity increase this research field should become more active, achieving truly intelligent systems, capable of protecting the monitored structure.





# Part IV.

## References

This part includes all the references cited in the document, separated by chapters and also ordered alphabetically. Finally, the list of publications obtained during this PhD period is shown, classified both as the ones close related with the PhD work and the ones obtained as a consequence of collaborations with other members of Photonic Engineering Group. Chapters included in this section are:

- Chapter 11: References by chapter
- Chapter 12: References in alphabetical order
- Chapter 13: List of publications



# Chapter 11

---

## References by chapter

---

### 11.1. References of Chapter 2

- [1] Brian Culshaw. *Smart structures and materials*. Artech House Boston, 1996.
- [2] Jose Miguel Lopez-Higuera. *Handbook of optical fibre sensing technology*. Wiley Chichester, 2002.
- [3] Tsuneo Horiguchi, Alan Rogers, WC Michie, George Stewart, and Brian Culshaw. Distributed sensors- recent developments. In *Optical fiber sensors.*, volume 4, pages 309–368.
- [4] F Luo, J Liu, N Ma, and TF Morse. A fiber optic microbend sensor for distributed sensing application in the structural strain monitoring. *Sensors and Actuators A: Physical*, 75(1):41–44, 1999.
- [5] Clay K Kirkendall and Anthony Dandridge. Overview of high performance fibre-optic sensing. *Journal of Physics D: Applied Physics*, 37(18):R197, 2004.

- [6] CI Merzbacher, AD Kersey, and EJ Friebele. Fiber optic sensors in concrete structures: a review. *Smart materials and structures*, 5(2):196, 1996.
- [7] Daniele Inaudi, Adil Elamari, and Samuel Vurpillot. Low-coherence interferometry for the monitoring of civil engineering structures. In *Smart Structures and Materials: Second European Conference*, pages 216–219. International Society for Optics and Photonics.
- [8] Wolfgang R Habel and Detlef Hofmann. Determination of structural parameters concerning load capacity based on fibre fabry-perot interferometers. In *Smart Structures and Materials: Second European Conference*, pages 176–179. International Society for Optics and Photonics.
- [9] Dryver R Huston, Peter L Fuhr, Timothy P Ambrose, and David A Barker. Intelligent civil structures-activities in vermont. *Smart materials and structures*, 3(2):129, 1994.
- [10] Peter L Fuhr, Timothy P Ambrose, Dryver R Huston, and Adam P McPadden. Fiber optic corrosion sensing for bridges and roadway surfaces. In *Smart Structures & Materials' 95*, pages 2–8. International Society for Optics and Photonics.
- [11] Stephane R Teral. Vehicle weighing in motion with fiber optic sensors. In *First European Conference on Smart Structures and Materials: Proceedings of the International Conference Held in Glasgow, 12-14 May 1992*, volume 1777, page 139. CRC Press.
- [12] Raman Kashyap. *Fiber bragg gratings*. Access Online via Elsevier, 1999.
- [13] Andreas Othonos and Kyriacos Kalli. *Fiber Bragg gratings: fundamentals and applications in telecommunications and sensing*. Artech House Boston, 1999.
- [14] Jose Miguel Lopez-Higuera, Luis Rodriguez Cobo, Antonio Quintela Incera, and Adolfo Cobo. Fiber optic sensors in structural health monitoring. *Lightwave Technology, Journal of*, 29(4):587–608, 2011.

- 
- [15] Turan Erdogan. Fiber grating spectra. *Lightwave Technology, Journal of*, 15(8):1277–1294, 1997.
- [16] Yun-Jiang Rao. In-fibre bragg grating sensors. *Measurement science and technology*, 8(4):355, 1997.
- [17] A Ezbiri, A Munoz, SE Kanellopoulos, and VA Handerek. High resolution fibre bragg grating sensor demodulation using a diffraction grating spectrometer and ccd detection. 1997.
- [18] AB Lobo Ribeiro, LA Ferreira, JL Santos, and DA Jackson. Analysis of the reflective-matched fiber bragg grating sensing interrogation scheme. *Applied optics*, 36(4):934–939, 1997.
- [19] M. Lopez-Amo and J.M. Lopez-Higuera. *Multiplexing Techniques for FBG*, volume 1, chapter 6, pages 99–115. 2011.
- [20] YJ Rao, AB Lobo Ribeiro, DA Jackson, L Zhang, and I Bennion. Simultaneous spatial, time and wavelength division multiplexed in-fibre grating sensing network. *Optics Communications*, 125(1):53–58, 1996.
- [21] Glynn D Lloyd, Lorna A Everall, Kate Sugden, and Ian Bennion. Resonant cavity time-division-multiplexed fiber bragg grating sensor interrogator. *Photonics Technology Letters, IEEE*, 16(10):2323–2325, 2004.
- [22] Bo Dong, Shiya He, Shuyang Hu, Dawei Tian, Junfeng Lv, and Qida Zhao. Time-division multiplexing fiber grating sensor with a tunable pulsed laser. *Photonics Technology Letters, IEEE*, 18(24):2620–2622, 2006.
- [23] S Abad, M Lopez-Amo, FM Araujo, LA Ferreira, and JL Santos. Fiber bragg grating-based self-referencing technique for wavelength-multiplexed intensity sensors. *Optics letters*, 27(4):222–224, 2002.
- [24] RC Tennyson, AA Mufti, S Rizkalla, G Tadros, and B Benmokrane. Structural health monitoring of innovative bridges in canada with fiber optic sensors. *Smart materials and structures*, 10(3):560, 2001.

- [25] Jose Miguel Lopez-Higuera, Antonio Quintela, and Juan Echevarria. Fiber optic civil structure monitoring system. *Optical Engineering*, 44(4):044401–044401–10, 2005.
- [26] Sandeep Vohra, Gregg Johnson, TODD Michael, Bruce Danver, and Bryan Althouse. Distributed strain monitoring with arrays of fiber bragg grating sensors on an in-construction steel box-girder bridge. *IEICE Transactions on Electronics*, 83(3):454–461, 2000.
- [27] THT Chan, L Yu, HY Tam, YQ Ni, SY Liu, WH Chung, and LK Cheng. Fiber bragg grating sensors for structural health monitoring of tsing ma bridge: Background and experimental observation. *Engineering structures*, 28(5):648–659, 2006.
- [28] G Kister, D Winter, YM Gebremichael, J Leighton, RA Badcock, PD Tester, S Krishnamurthy, WJO Boyle, KTV Grattan, and GF Fernando. Methodology and integrity monitoring of foundation concrete piles using bragg grating optical fibre sensors. *Engineering Structures*, 29(9):2048–2055, 2007.
- [29] HY Tam, T Lee, SL Ho, T Haber, T Graver, A Mendez, KCRC House, and Sha Tin. Utilization of fiber optic bragg grating sensing systems for health monitoring in railway applications. *Struct. Health Monit.: Quantification, Validat., Implement*, 1:2, 2007.
- [30] Chung-Yue Wang, Hao-Lin Wang, and Ming-Hung Chen. Structural health monitoring activities of applying optical fiber sensors in taiwan. In *Optical Fiber Sensors*. Optical Society of America.
- [31] Maurice P Whelan, Daniel Albrecht, and Antonio Capsoni. Remote structural monitoring of the cathedral of como using an optical fiber bragg sensor system. In *SPIE’s 9th Annual International Symposium on Smart Structures and Materials*, pages 242–252. International Society for Optics and Photonics.
- [32] Jin-Hak Yi, Kwang-Soo Lee, Jin-Soon Park, and Woo-Sun Park. Structural health monitoring system for “uldolmok” tidal current power pilot plant and its applications. ASME.

- 
- [33] IJ Read and PD Foote. Sea and flight trials of optical fibre bragg grating strain sensing systems. *Smart materials and structures*, 10(5):1085, 2001.
- [34] G Wang, K Pran, G Sagvolden, GB Havsgard, AE Jensen, GA Johnson, and ST Vohra. Ship hull structure monitoring using fibre optic sensors. *Smart materials and structures*, 10(3):472, 2001.
- [35] Christopher Baldwin, Jason Kiddy, Toni Salter, Peter Chen, and Jack Niemczuk. Fiber optic structural health monitoring system: Rough sea trials testing of the rv triton. In *OCEANS'02 MTS/IEEE*, volume 3, pages 1806–1813. IEEE.
- [36] Wolfgang Ecke, Ines Latka, Reinhardt Willsch, Arnd Reutlinger, and Roland Graue. Fibre optic sensor network for spacecraft health monitoring. *Measurement science and technology*, 12(7):974, 2001.
- [37] MK Barnoski and SM Jensen. Fiber waveguides: a novel technique for investigating attenuation characteristics. *Applied optics*, 15(9):2112–2115, 1976.
- [38] Mitsuhiro Tateda and Tsuneo Horiguchi. Advances in optical time domain reflectometry. *Lightwave Technology, Journal of*, 7(8):1217–1224, 1989.
- [39] AA Boiarski, G Pilate, T Fink, and N Nilsson. Temperature measurements in power plant equipment using distributed fiber optic sensing. *Power Delivery, IEEE Transactions on*, 10(4):1771–1778, 1995.
- [40] Toshio Kurashima, Tsuneo Horiguchi, Hisashi Izumita, Shin-ichi Furukawa, and Yahei Koyamada. Brillouin optical-fiber time domain reflectometry. *IEICE Transactions on Communications*, 76(4):382–390, 1993.
- [41] Hiroshige Ohno, Hiroshi Naruse, Mitsuru Kihara, and Akiyoshi Shimada. Industrial applications of the botdr optical fiber strain sensor. *Optical fiber technology*, 7(1):45–64, 2001.
- [42] Wei Zhang, Junqi Gao, Bin Shi, Heliang Cui, and Hong Zhu. Health monitoring of rehabilitated concrete bridges using distributed optical

- fiber sensing. *Computer-Aided Civil and Infrastructure Engineering*, 21(6):411–424, 2006.
- [43] J Gao, B Shi, W Zhang, and H Zhu. Monitoring the stress of the post-tensioning cable using fiber optic distributed strain sensor. *Measurement*, 39(5):420–428, 2006.
- [44] Fabio Matta, Filippo Bastianini, Nestore Galati, Paolo Casadei, and Antonio Nanni. Distributed strain measurement in steel bridge with fiber optic sensors: validation through diagnostic load test. *Journal of performance of constructed facilities*, 22(4):264–273, 2008.
- [45] Assaf Klar, Peter J Bennett, Kenichi Soga, Robert J Mair, Paul Tester, Rab Fernie, Hugh D St John, and G Torp-Peterson. Distributed strain measurement for pile foundations. *Proceedings of the ICE-Geotechnical Engineering*, 159(3):135–144, 2006.
- [46] Bin Shi, Hongzhong Xu, Bin Chen, Dan Zhang, Yong Ding, Heliang Cui, and Junqi Gao. A feasibility study on the application of fiber-optic distributed sensors for strain measurement in the taiwan strait tunnel project. *Marine Georesources and Geotechnology*, 21(3-4):333–343, 2003.
- [47] Hiroshi Naruse, Koji Komatsu, Kazuhiko Fujihashi, and Masaru Okutsu. Telecommunications tunnel monitoring system based on distributed optical fiber strain measurement. In *Bruges, Belgium-Deadline Past*, pages 168–171. International Society for Optics and Photonics.
- [48] Hiroshi Naruse, Hideki Uehara, Taishi Deguchi, Kazuhiko Fujihashi, Masatoshi Onishi, Raul Espinoza, Cesar Guzman, Cesar Pardo, Cesar Ortega, and Manuel Pinto. Application of a distributed fibre optic strain sensing system to monitoring changes in the state of an underground mine. *Measurement science and technology*, 18(10):3202, 2007.
- [49] Vincent Lanticq, Emmanuel Bourgeois, P Magnien, L Dieleman, G Vincelas, A Sang, and S Delepine-Lesoille. Soil-embedded optical fiber sensing cable interrogated by brillouin optical time-domain reflectometry (B-OTDR) and optical frequency-domain reflectometry

- (OFDR) for embedded cavity detection and sinkhole warning system. *Measurement science and technology*, 20(3):034018, 2009.
- [50] Toshio Kurashima, Tsuneo Horiguchi, Nobuyuki Yoshizawa, Hidenobu Tada, and Mitsuhiro Tateda. Measurement of distributed strain due to laying and recovery of submarine optical fiber cable. *Applied optics*, 30(3):334–337, 1991.
- [51] Nils Nother, Aleksander Wosniok, Katerina Krebber, and Elke Thiele. A distributed fiber optic sensor system for dike monitoring using brillouin optical frequency domain analysis. In *The 15th International Symposium on: Smart Structures and Materials & Nondestructive Evaluation and Health Monitoring*, pages 69330T–69330T–9. International Society for Optics and Photonics.
- [52] Ye Qiu, Quan-bao Wang, Hai-tao Zhao, Ji-an Chen, and Yue-ying Wang. Review on composite structural health monitoring based on fiber bragg grating sensing principle. *Journal of Shanghai Jiaotong University (Science)*, 18:129–139, 2013.
- [53] AL Kalamkarov, SB Fitzgerald, and DO MacDonald. The use of fabry perot fiber optic sensors to monitor residual strains during pultrusion of frp composites. *Composites Part B: Engineering*, 30(2):167–175, 1999.
- [54] T Liu, D Brooks, A Martin, R Badcock, B Ralph, and GF Fernando. A multi-mode extrinsic fabry-perot interferometric strain sensor. *Smart materials and structures*, 6(4):464, 1997.
- [55] Jinsong Leng and Anand Asundi. Structural health monitoring of smart composite materials by using EFPI and FBG sensors. *Sensors and Actuators A: Physical*, 103(3):330–340, 2003.
- [56] Xiaoyi Bao, Chao Huang, Xiaodong Zeng, Antoine Arcand, and Pearl Sullivan. Simultaneous strain and temperature monitoring of the composite cure with a brillouin-scattering-based distributed sensor. *Optical Engineering*, 41(7):1496–1501, 2002.

- [57] Y Ito, K Fujimoto, S Minakuchi, T Mizutani, N Takeda, H Koinuma, and T Shimizu. Cure monitoring of carbon/epoxy composite by optical-fiber-based distributed strain/temperature sensing. 2010.
- [58] E Bocherens, S Bourasseau, V Dewynter-Marty, S Py, M Dupont, P Ferdinand, and H Berenger. Damage detection in a radome sandwich material with embedded fiber optic sensors. *Smart Materials and Structures*, 9:310, 2000.
- [59] Takashi Yari, K Nagai, and K Hotate. Monitoring aircraft structural health using optical fiber sensors. *Mitsubishi Heavy Ind. Tech. Rev.*, 45(4):5–8, 2008.
- [60] Hideaki Murayama, Kazuro Kageyama, Isao Kimpara, Shimada Akiyoshi, and Hiroshi Naruse. Structural health monitoring of iacc yachts using fiber optic distributed strain sensors: A technical challenge for america’s cup 2000. In *SPIE’s 7th Annual International Symposium on Smart Structures and Materials*, pages 312–323. International Society for Optics and Photonics.
- [61] E. J. Friebele, C. G. Askins, M. A. Putnam, Jr. Fosha, A. A., Jr. Florio, J., R. P. Donti, and R. G. Blosser. Distributed strain sensing with fibre bragg grating arrays embedded in crtm composites. *Electronics Letters*, 30(21):1783–1784, 1994.
- [62] VM Murukeshan, PY Chan, LS Ong, and LK Seah. Cure monitoring of smart composites using fiber bragg grating based embedded sensors. *Sensors and Actuators A: Physical*, 79(2):153–161, 2000.
- [63] KScea Kuang, R Kenny, MP Whelan, WJ Cantwell, and PR Chalker. Embedded fibre bragg grating sensors in advanced composite materials. *Composites Science and Technology*, 61(10):1379–1387, 2001.
- [64] Yoji Okabe, Shigeki Yashiro, Ryohei Tsuji, Tadahito Mizutani, and Nobuo Takeda. Effect of thermal residual stress on the reflection spectrum from fiber bragg grating sensors embedded in CFRP laminates. *Composites Part A: Applied Science and Manufacturing*, 33(7):991–999, 2002.

- [65] Shin-ichi Takeda, Jun Koyanagi, Shin Utsunomiya, Yuto Kinoshita, Yoshihiko Arao, and Hiroyuki Kawada. Monitoring of internal residual strain changes in CFRP using FBG sensors. In *Fourth International Conference on Experimental Mechanics*, pages 75223N–75223N–7. International Society for Optics and Photonics.
- [66] EJ Friebele, CG Askins, AB Bosse, AD Kersey, HJ Patrick, WR Pogue, MA Putnam, WR Simon, FA Tasker, and WS Vincent. Optical fiber sensors for spacecraft applications. *Smart materials and structures*, 8(6):813, 1999.
- [67] Yoji Okabe, Shigeki Yashiro, Tatsuro Kosaka, and Nobuo Takeda. Detection of transverse cracks in CFRP composites using embedded fiber bragg grating sensors. *Smart Materials and Structures*, 9(6):832, 2000.
- [68] Yoji Okabe, Ryohei Tsuji, and Nobuo Takeda. Application of chirped fiber bragg grating sensors for identification of crack locations in composites. *Composites Part A: Applied Science and Manufacturing*, 35(1):59–65, 2004.
- [69] Nobuo Takeda, Yoji Okabe, Junichiro Kuwahara, Seiji Kojima, and Toshimichi Ogisu. Development of smart composite structures with small-diameter fiber bragg grating sensors for damage detection: Quantitative evaluation of delamination length in CFRP laminates using lamb wave sensing. *Composites Science and Technology*, 65(15):2575–2587, 2005.
- [70] WJB Groupe, L Warnet, A De Boer, R Akkerman, and J Vlekken. Delamination detection with fibre bragg gratings based on dynamic behaviour. *Composites Science and Technology*, 68(12):2418–2424, 2008.
- [71] S Takeda, Y Okabe, and N Takeda. Monitoring of delamination growth in CFRP laminates using chirped FBG sensors. *Journal of Intelligent Material Systems and Structures*, 19(4):437–444, 2008.
- [72] J Palaniappan, SL Ogin, AM Thorne, GT Reed, AD Crocombe, TF Capell, SC Tjin, and L Mohanty. Disbond growth detection in

- composite-composite single-lap joints using chirped FBG sensors. *Composites Science and Technology*, 68(12):2410–2417, 2008.
- [73] A Propst, K Peters, MA Zikry, S Schultz, W Kunzler, Z Zhu, M Wirthlin, and R Selfridge. Assessment of damage in composite laminates through dynamic, full-spectral interrogation of fiber bragg grating sensors. *Smart Materials and Structures*, 19(1):015016, 2010.
- [74] Hiroaki Tsutsui, Akio Kawamata, Tomio Sanda, and Nobuo Takeda. Detection of impact damage of stiffened composite panels using embedded small-diameter optical fibers. *Smart Materials and Structures*, 13(6):1284, 2004.
- [75] Hiroshi Tsuda. Ultrasound and damage detection in CFRP using fiber bragg grating sensors. *Composites Science and Technology*, 66(5):676–683, 2006.
- [76] I McKenzie, Rhys Jones, IH Marshall, and S Galea. Optical fibre sensors for health monitoring of bonded repair systems. *Composite structures*, 50(4):405–416, 2000.
- [77] S Takeda, T Yamamoto, Y Okabe, and N Takeda. Debonding monitoring of composite repair patches using embedded small-diameter FBG sensors. *Smart Materials and Structures*, 16(3):763, 2007.
- [78] Farhad Ansari. State-of-the-art in the applications of fiber-optic sensors to cementitious composites. *Cement and Concrete Composites*, 19(1):3–19, 1997.
- [79] YM Gebremichael, W Li, WJO Boyle, BT Meggitt, KTV Grattan, B McKinley, GF Fernando, G Kister, D Winter, and L Canning. Integration and assessment of fibre bragg grating sensors in an all-fibre reinforced polymer composite road bridge. *Sensors and Actuators A: Physical*, 118(1):78–85, 2005.
- [80] HCH Li, I Herszberg, CE Davis, AP Mouritz, and SC Galea. Health monitoring of marine composite structural joints using fibre optic sensors. *Composite Structures*, 75(1-4):321–327, 2006.

- 
- [81] R Maaskant, T Alavie, G Tadros, SH Rizkalla, and A Guha-Thakurta. Fiber-optic bragg grating sensors for bridge monitoring. *Cement and Concrete Composites*, 19(1):21–33, 1997.
- [82] I Mckenzie and N Karafolas. Fiber optic sensing in space structures: the experience of the european space agency (invited paper). volume 5855, page 262.
- [83] JR Lee, CY Ryu, BY Koo, SG Kang, CS Hong, and CG Kim. In-flight health monitoring of a subscale wing using a fiber bragg grating sensor system. *Smart Materials and Structures*, 12:147, 2003.
- [84] Andrea Cusano, Patrizio Capoluongo, S Campopiano, Antonello Cuto, Michele Giordano, Ferdinando Felli, Antonio Paolozzi, and Michele Caponero. Experimental modal analysis of an aircraft model wing by embedded fiber bragg grating sensors. *Sensors Journal, IEEE*, 6(1):67–77, 2006.
- [85] K Chandler, S Ferguson, T Graver, A Csipkes, and A Mendez. On-line structural health and fire monitoring of a composite personal aircraft using an FBG sensing system. In *The 15th International Symposium on: Smart Structures and Materials & Nondestructive Evaluation and Health Monitoring*, pages 69330H–69330H–6. International Society for Optics and Photonics.
- [86] S Takeda, Y Aoki, T Ishikawa, N Takeda, and H Kikukawa. Structural health monitoring of composite wing structure during durability test. *Composite structures*, 79(1):133–139, 2007.
- [87] Hideki Sekine, Shin-Etsu Fujimoto, Tomonaga Okabe, Nobuo Takeda, and Toshimitsu Yokobori Jr. Structural health monitoring of cracked aircraft panels repaired with bonded patches using fiber bragg grating sensors. *Applied Composite Materials*, 13(2):87–98, 2006.
- [88] Alan D Kersey, Michael A Davis, Timothy A Berkoff, Anthony D Dandridge, RT Jones, Tsung-Ein Tsai, Gary B Cogdell, Gunnar Wang, GB Havsgaard, and Karianne Pran. Transient load monitoring on a composite hull ship using distributed fiber optic bragg grating sensors.

- In *Smart Structures and Materials' 97*, pages 421–430. International Society for Optics and Photonics.
- [89] Gregg A Johnson, Karianne Pran, G Sagvolden, O Farsund, GB Havs-gard, G Wang, AE Jensen, and J Taby. Surface effect ship vibro-impact monitoring with distributed arrays of fiber bragg gratings. *Proceedings of the 18th International Modal Analysis*, pages 1406–1411, 2000.
- [90] HCH Li, I Herszberg, AP Mouritz, CE Davis, and SC Galea. Sensitivity of embedded fibre optic bragg grating sensors to disbonds in bonded composite ship joints. *Composite Structures*, 66(1-4):239–248, 2004.
- [91] I Herszberg, HCH Li, F Dharmawan, AP Mouritz, M Nguyen, and J Bayandor. Damage assessment and monitoring of composite ship joints. *Composite structures*, 67(2):205–216, 2005.
- [92] Kara Peters. Polymer optical fiber sensors—a review. *Smart Materials and Structures*, 20(1):013002, 2011.
- [93] Sascha Liehr, Philipp Lenke, Mario Wendt, Katerina Krebber, Monika Seeger, Elke Thiele, Heike Metschies, Berhane Gebreselassie, and JC Munich. Polymer optical fiber sensors for distributed strain measurement and application in structural health monitoring. *Sensors Journal, IEEE*, 9(11):1330–1338, 2009.
- [94] Irwan Rawal Husdi, Kentaro Nakamura, and Sadayuki Ueha. Sensing characteristics of plastic optical fibres measured by optical time-domain reflectometry. *Measurement Science and Technology*, 15(8):1553, 2004.
- [95] Kentaro Nakamura, Irwan R Husdi, and Sadayuki Ueha. Memory effect of pof distributed strain sensor. In *Second European Workshop on Optical Fibre Sensors*, pages 144–147. International Society for Optics and Photonics.
- [96] Javier Gomez, Joseba Zubia, Gerardo Aranguren, Jon Arrue, Hans Poisel, and Idurre Saez. Comparing polymer optical fiber, fiber bragg grating, and traditional strain gauge for aircraft structural health monitoring. *Applied Optics*, 48(8):1436–1443, 2009.

- 
- [97] Gaizka Durana, Marlene Kirchhof, Michael Lubber, Idurre Saez de Ocariz, Hans Poisel, Joseba Zubia, and Carmen Vazquez. Use of a novel fiber optical strain sensor for monitoring the vertical deflection of an aircraft flap. *Sensors Journal, IEEE*, 9(10):1219–1225, 2009.
- [98] GD Peng, Z Xiong, and PL Chu. Photosensitivity and gratings in dyed-polymer optical fibers. *Optical Fiber Technology*, 5(2):242–251, 1999.
- [99] HY Liu, GD Peng, and PL Chu. Polymer fiber bragg gratings with 28-dB transmission rejection. *Photonics Technology Letters, IEEE*, 14(7):935–937, 2002.
- [100] Helen Dobb, David J Webb, Kyriacos Kalli, Alexander Argyros, Maryanne C Large, and Martijn A van Eijkelenborg. Continuous wave ultraviolet light-induced fiber bragg gratings in few- and single-mode microstructured polymer optical fibers. *Optics letters*, 30(24):3296–3298, 2005.
- [101] Yosuke Mizuno, Masato Kishi, Kazuo Hotate, Takaaki Ishigure, and Kentaro Nakamura. Observation of stimulated Brillouin scattering in polymer optical fiber with pump-probe technique. *Optics letters*, 36(12):2378–2380, 2011.
- [102] KSC Kuang, Ser Tong Quek, CY Tan, and SH Chew. Plastic optical fiber sensors for measurement of large strain in geotextile materials. *Advanced Materials Research*, 47:1233–1236, 2008.
- [103] KSC Kuang, WJ Cantwell, and C Thomas. Crack detection and vertical deflection monitoring in concrete beams using plastic optical fibre sensors. *Measurement Science and Technology*, 14(2):205, 2003.
- [104] Nobuo Takeda. Characterization of microscopic damage in composite laminates and real-time monitoring by embedded optical fiber sensors. *International Journal of Fatigue*, 24(2):281–289, 2002.
- [105] KSC Kuang and WJ Cantwell. The use of plastic optical fibre sensors for monitoring the dynamic response of fibre composite beams. *Measurement Science and Technology*, 14(6):736, 2003.

- [106] YM Wong, PJ Scully, RJ Bartlett, KSC Kuang, and WJ Cantwell. Plastic optical fibre sensors for environmental monitoring: biofouling and strain applications. *Strain*, 39(3):115–119, 2003.
- [107] Manuel Silva-Lopez, Amanda Fender, William N MacPherson, James S Barton, Julian DC Jones, Donghui Zhao, Helen Dobb, David J Webb, Lin Zhang, and Ian Bennion. Strain and temperature sensitivity of a single-mode polymer optical fiber. *Optics letters*, 30(23):3129–3131, 2005.
- [108] Sharon Kiesel, Kara Peters, Tasnim Hassan, and Mervyn Kowalsky. Large deformation in-fiber polymer optical fiber sensor. *Photonics Technology Letters, IEEE*, 20(6):416–418, 2008.
- [109] H Poisel. Pof strain sensor using phase measurement techniques. In *The 15th International Symposium on: Smart Structures and Materials & Nondestructive Evaluation and Health Monitoring*, pages 69330Y–69330Y–5. International Society for Optics and Photonics.
- [110] Matthew O’Donnell, Andrei R Skovoroda, Benjamin M Shapo, and Stanislav Y Emelianov. Internal displacement and strain imaging using ultrasonic speckle tracking. *Ultrasonics, Ferroelectrics and Frequency Control, IEEE Transactions on*, 41(3):314–325, 1994.
- [111] WB Spillman Jr, BR Kline, LB Maurice, and PL Fuhr. Statistical-mode sensor for fiber optic vibration sensing uses. *Applied Optics*, 28(15):3166–3176, 1989.
- [112] Francis TS Yu, Meiyuan Wen, Shizhuo Yin, and Chii-Maw Uang. Sub-micrometer displacement sensing using inner-product multimode fiber speckle fields. *Applied Optics*, 32(25):4685–4689, 1993.
- [113] Zhijun Zhang and Farhad Ansari. Fiber-optic laser speckle-intensity crack sensor for embedment in concrete. *Sensors and Actuators A: Physical*, 126(1):107–111, 2006.
- [114] Kun Pan, Chii-Maw Uang, Feng Cheng, and Francis TS Yu. Multimode fiber sensing by using mean-absolute speckle-intensity variation. *Applied Optics*, 33(10):2095–2098, 1994.

- 
- [115] Sharon Kiesel, Kara Peters, Tasnim Hassan, and Mervyn Kowalsky. Behaviour of intrinsic polymer optical fibre sensor for large-strain applications. *Measurement Science and Technology*, 18(10):3144, 2007.
- [116] Alexei A Kamshilin, Timo Jaaskelainen, and Yuri N Kulchin. Adaptive correlation filter for stabilization of interference-fiber-optic sensors. *Applied physics letters*, 73(6):705–707, 1998.
- [117] Felix Rodriguez-Barrios, Sonia Martin-Lopez, Ana Carrasco-Sanz, Pedro Corredera, Juan Diego Ania-Castanon, Luc Thevenaz, and Miguel Gonzalez-Herraez. Distributed brillouin fiber sensor assisted by first-order raman amplification. *Lightwave Technology, Journal of*, 28(15):2162–2172, 2010.
- [118] Xabier Angulo-Vinuesa, Sonia Martin-Lopez, Javier Nuño, Pedro Corredera, Juan Diego Ania-Castañon, Luc Thevenaz, and Miguel Gonzalez-Herraez. Raman-assisted brillouin distributed temperature sensor over 100 km featuring 2 m resolution and 1.2 c uncertainty. *Journal of Lightwave Technology*, 30(8):1060–1065, 2012.
- [119] Peng-Chun Peng, Hong-Yih Tseng, and Sien Chi. Long-distance FBG sensor system using a linear-cavity fiber raman laser scheme. *Photonics Technology Letters, IEEE*, 16(2):575–577, 2004.
- [120] Ju Han Lee, You Chang, Young-Geun Han, Haeyang Chung, Sang Kim, and Sang Lee. Raman amplifier-based long-distance remote, strain and temperature sensing system using an erbium-doped fiber and a fiber bragg grating. *Optics express*, 12(15):3515–3520, 2004.
- [121] Young-Geun Han, TVA Tran, Sang-Hyuck Kim, and Sang Bae Lee. Multiwavelength raman-fiber-laser-based long-distance remote sensor for simultaneous measurement of strain and temperature. *Optics letters*, 30(11):1282–1284, 2005.
- [122] Yun-Jiang Rao, Zeng-Ling Ran, and Rong-Rui Chen. Long-distance fiber bragg grating sensor system with a high optical signal-to-noise ratio based on a tunable fiber ring laser configuration. *Optics letters*, 31(18):2684–2686, 2006.

- [123] Yun-Jiang Rao, Sha Feng, Qi Jiang, and Zeng-Ling Ran. Ultra-long distance (300km) fiber bragg grating sensor system using hybrid edf and raman amplification. In *20th International Conference on Optical Fibre Sensors*, pages 75031Q–75031Q–4. International Society for Optics and Photonics.
- [124] GA Ball, WW Morey, and PK Cheo. Single-and multipoint fiber-laser sensors. *Photonics Technology Letters, IEEE*, 5(2):267–270, 1993.
- [125] Serge M Melle, A Tino Alavie, Shawn Karr, Trent Coroy, and Kexing Liu. A bragg grating-tuned fiber laser strain sensor system. *Photonics Technology Letters, IEEE*, 5(2):263–266, 1993.
- [126] JL Zyskind, V Mizrahi, DJ DiGiovanni, and JW Sulhoff. Short single frequency erbium-doped fibre laser. *Electronics Letters*, 28(15):1385–1387, 1992.
- [127] RA Perez-Herrera, S Chen, W Zhao, T Sun, KTV Grattan, and M Lopez-Amo. Stability performance of short cavity er-doped fiber lasers. *Optics Communications*, 283(6):1067–1070, 2010.
- [128] GA Ball, G Meltz, and WW Morey. Polarimetric heterodyning bragg-grating fiber-laser sensor. *Optics letters*, 18(22):1976–1978, 1993.
- [129] David A Grossman. *Information retrieval: Algorithms and heuristics*, volume 15. Springer, 2004.
- [130] Xiaoliang Zhao, Huidong Gao, Guangfan Zhang, Bulent Ayhan, Fei Yan, Chimam Kwan, and Joseph L Rose. Active health monitoring of an aircraft wing with embedded piezoelectric sensor/actuator network: I. defect detection, localization and growth monitoring. *Smart Materials and Structures*, 16(4):1208, 2007.
- [131] MM Reda Taha and J Lucero. Damage identification for structural health monitoring using fuzzy pattern recognition. *Engineering Structures*, 27(12):1774–1783, 2005.
- [132] GC Kahandawa, JA Epaarachchi, H Wang, D Followell, and P Birt. Use of fixed wavelength fibre-bragg grating (FBG) filters to capture time

- domain data from the distorted spectrum of an embedded FBG sensor to estimate strain with an artificial neural network. *Sensors and Actuators A: Physical*, 2013.
- [133] Masataro Amano, Yoji Okabe, Nobuo Takeda, and Tsuyoshi Ozaki. Structural health monitoring of an advanced grid structure with embedded fiber bragg grating sensors. *Structural Health Monitoring*, 6(4):309–324, 2007.
- [134] JM Ko and YQ Ni. Technology developments in structural health monitoring of large-scale bridges. *Engineering Structures*, 27(12):1715–1725, 2005.
- [135] Ch E Katsikeros and GN Labeas. Development and validation of a strain-based structural health monitoring system. *Mechanical Systems and Signal Processing*, 23(2):372–383, 2009.
- [136] XiaoLi Zhang, DaKai Liang, Jie Zeng, and Anand Asundi. Genetic algorithm-support vector regression for high reliability shm system based on FBG sensor network. *Optics and Lasers in Engineering*, 50(2):148–153, 2012.
- [137] K. Chau, B. Moslehi, G. Song, and V. Sethi. Experimental demonstration of fiber bragg grating strain sensors for structural vibration control. volume 5391, pages 753–764.
- [138] A. Cavallo, C. May, A. Minardo, C. Natale, P. Pagliarulo, and S. Pirozzi. Active vibration control by a smart auxiliary mass damper equipped with a fiber bragg grating sensor. *Sensors and Actuators A: Physical*, 153(2):180–186, 2009.
- [139] K.C. Chuang and C.C. Ma. Tracking control of a multilayer piezoelectric actuator using a fiber bragg grating displacement sensor system. *Ultrasonics, Ferroelectrics and Frequency Control, IEEE Transactions on*, 56(10):2036–2049, 2009.
- [140] M. Mieloszyk, L. Skarbek, M. Krawczuk, W. Ostachowicz, and A. Zak. Application of fibre bragg grating sensors for structural health monitor-

ing of an adaptive wing. *Smart Materials and Structures*, 20:125014, 2011.

## 11.2. References of Chapter 4

- [1] K.O. Hill and G. Meltz. Fiber bragg grating technology fundamentals and overview. *Lightwave Technology, Journal of*, 15(8):1263–1276, 1997.
- [2] J.M. Lopez-Higuera. *Handbook of optical fibre sensing technology*. John Wiley and Sons Inc, 2002.
- [3] Z.G. Zang and Y.J. Zhang. Low-switching power ( $\approx 45$  mw) optical bistability based on optical nonlinearity of ytterbium-doped fiber with a fiber bragg grating pair. *Journal of Modern Optics*, 59(2):161–165, 2012.
- [4] M. LeBlanc, SY Huang, M. Ohn, A. Guemes, and A. Othonos. Distributed strain measurement based on a fiber bragg grating and its reflection spectrum analysis. *Optics letters*, 21(17):1405–1407, 1996.
- [5] S. Huang, M. M. Ohn, M. LeBlanc, and R. M. Measures. Continuous arbitrary strain profile measurements with fiber bragg gratings. *Smart materials and structures*, 7(2):248–256, 1998.
- [6] J. Azana and M.A. Muriel. Reconstructing arbitrary strain distributions within fiber gratings by time–frequency signal analysis. *Optics letters*, 25(10):698–700, 2000.
- [7] X. Chapeleau, P. Casari, D. Leduc, Y. Scudeller, C. Lupi, R.L. Ny, and C. Boisrobert. Determination of strain distribution and temperature gradient profiles from phase measurements of embedded fibre bragg gratings. *Journal of Optics A: Pure and Applied Optics*, 8:775, 2006.
- [8] F. Casagrande, P. Crespi, A.M. Grassi, A. Lulli, R.P. Kenny, and M.P. Whelan. From the reflected spectrum to the properties of a fiber bragg grating: a genetic algorithm approach with application to distributed strain sensing. *Applied Optics*, 41(25):5238–5244, 2002.

- 
- [9] CC Cheng, Y.L. Lo, WY Li, CT Kuo, and HC Cheng. Estimations of fiber bragg grating parameters and strain gauge factor using optical spectrum and strain distribution information. *Applied Optics*, 46(21):4555–4562, 2007.
- [10] F. Teng, W. Yin, F. Wu, Z. Li, and T. Wu. Analysis of a FBG sensing system with transverse uniform press by using genetic algorithm. *Optoelectronics Letters*, 4(2):121–125, 2008.
- [11] Z.X. Wu, Q. Qiao, F. Wu, and L.L. Cai. Research on FBG spectral optimization with particle swarm optimization algorithm. *Applied Mechanics and Materials*, 128:690–693, 2012.
- [12] J. Kennedy and R. Eberhart. Particle swarm optimization. volume 4, pages 1942–1948 vol. 4. IEEE.
- [13] BJ Eggleton, PA Krug, L. Poladian, and F. Ouellette. Long periodic superstructure bragg gratings in optical fibres. *Electronics letters*, 30(19):1620–1622, 1994.
- [14] M.A. Muriel and A. Carballar. Internal field distributions in fiber bragg gratings. *Photonics Technology Letters, IEEE*, 9(7):955–957, 1997.
- [15] K.S.C. Kuang, R. Kenny, MP Whelan, WJ Cantwell, and PR Chalker. Embedded fibre bragg grating sensors in advanced composite materials. *Composites Science and Technology*, 61(10):1379–1387, 2001.
- [16] VM Murukeshan, PY Chan, LS Ong, and LK Seah. Cure monitoring of smart composites using fiber bragg grating based embedded sensors. *Sensors and Actuators A: Physical*, 79(2):153–161, 2000.
- [17] I. McKenzie, R. Jones, IH Marshall, and S. Galea. Optical fibre sensors for health monitoring of bonded repair systems. *Composite structures*, 50(4):405–416, 2000.
- [18] S. Takeda, T. Yamamoto, Y. Okabe, and N. Takeda. Debonding monitoring of composite repair patches using embedded small-diameter FBG sensors. *Smart materials and structures*, 16:763, 2007.

- [19] A. Propst, K. Peters, MA Zikry, S. Schultz, W. Kunzler, Z. Zhu, M. Wirthlin, and R. Selfridge. Assessment of damage in composite laminates through dynamic, full-spectral interrogation of fiber bragg grating sensors. *Smart materials and structures*, 19:015016, 2010.
- [20] Xuewen Shu, Yu Liu, Donghui Zhao, Bashir Gwandu, Filip Floreani, Lin Zhang, and Ian Bennion. Dependence of temperature and strain coefficients on fiber grating type and its application to simultaneous temperature and strain measurement. *Optics letters*, 27(9):701–703, 2002.
- [21] Bai-Ou Guan, Hwa-Yaw Tam, Xiao-Ming Tao, and Xiao-Yi Dong. Simultaneous strain and temperature measurement using a superstructure fiber bragg grating. *Photonics Technology Letters, IEEE*, 12(6):675–677, 2000.
- [22] SO Park, BW Jang, YG Lee, CG Kim, and CY Park. Simultaneous measurement of strain and temperature using a reverse index fiber bragg grating sensor. *Measurement Science and Technology*, 21(3):035703, 2010.
- [23] Wacław Urbanczyk, Ewa Chmielewska, and Wojtek J Bock. Measurements of temperature and strain sensitivities of a two-mode bragg grating imprinted in a bow-tie fibre. *Measurement Science and Technology*, 12(7):800, 2001.
- [24] O Frazao, JP Carvalho, LA Ferreira, FM Araujo, and JL Santos. Discrimination of strain and temperature using bragg gratings in microstructured and standard optical fibres. *Measurement Science and Technology*, 16(10):2109, 2005.
- [25] J.M. Lopez-Higuera, L. Rodriguez Cobo, A. Quintela Incera, and A. Cobo. Fiber optic sensors in structural health monitoring. *Journal of lightwave technology*, 29(4):587–608, 2011.
- [26] O Frazao, R Oliveira, and I Dias. A simple smart composite using fiber bragg grating sensors for strain and temperature discrimination. *Microwave and Optical Technology Letters*, 51(1):235–239, 2009.

- [27] MS Ferreira, J Vieira, C Frias, and O Frazão. Simultaneous measurement of strain and temperature using fiber bragg grating sensors embedded in hybrid composite laminates. *Measurement Science and Technology*, 22(4):045206, 2011.
- [28] Wei Jin, W Craig Michie, Graham Thursby, Maria Konstantaki, and Brian Culshaw. Simultaneous measurement of strain and temperature: error analysis. *Optical Engineering*, 36(2):598–609, 1997.
- [29] G Pereira, C Frias, H Faria, O Frazão, and AT Marques. On the improvement of strain measurements with FBG sensors embedded in unidirectional composites. *Polymer Testing*, 2012.
- [30] Jinsong Leng and Anand Asundi. Structural health monitoring of smart composite materials by using EFPI and FBG sensors. *Sensors and Actuators A: Physical*, 103(3):330–340, 2003.
- [31] IJ Read and PD Foote. Sea and flight trials of optical fibre bragg grating strain sensing systems. *Smart materials and structures*, 10(5):1085, 2001.
- [32] Nobuo Takeda, Yoji Okabe, Junichiro Kuwahara, Seiji Kojima, and Toshimichi Ogisu. Development of smart composite structures with small-diameter fiber bragg grating sensors for damage detection: Quantitative evaluation of delamination length in CFRP laminates using lamb wave sensing. *Composites Science and Technology*, 65(15):2575–2587, 2005.
- [33] WJB Groupe, L Warnet, A De Boer, R Akkerman, and J Vlekken. Delamination detection with fibre bragg gratings based on dynamic behaviour. *Composites Science and Technology*, 68(12):2418–2424, 2008.
- [34] S. Takeda, Y. Okabe, and N. Takeda. Monitoring of delamination growth in CFRP laminates using chirped FBG sensors. *Journal of Intelligent Material Systems and Structures*, 19(4):437–444, 2008.
- [35] J Palaniappan, SL Ogin, AM Thorne, GT Reed, AD Crocombe, TF Capell, SC Tjin, and L Mohanty. Disbond growth detection in composite–composite single-lap joints using chirped FBG sensors. *Composites Science and Technology*, 68(12):2410–2417, 2008.

- [36] E. J. Friebele, C. G. Askins, M. A. Putnam, Jr. Fosha, A. A., Jr. Florio, J., R. P. Donti, and R. G. Blosser. Distributed strain sensing with fibre bragg grating arrays embedded in crtm composites. *Electronics Letters*, 30(21):1783–1784, 1994.
- [37] Alan D Kersey, Michael A Davis, Timothy A Berkoff, Anthony D Dandridge, RT Jones, Tsung-Ein Tsai, Gary B Cogdell, Gunnar Wang, GB Havsgaard, and Karianne Pran. Transient load monitoring on a composite hull ship using distributed fiber optic bragg grating sensors. In *Smart Structures and Materials' 97*, pages 421–430. International Society for Optics and Photonics.
- [38] Gregg A Johnson, Karianne Pran, G Sagvolden, Ø Farsund, GB Havsgård, G Wang, AE Jensen, and J Taby. Surface effect ship vibro-impact monitoring with distributed arrays of fiber bragg gratings. *Proceedings of the 18th International Modal Analysis*, pages 1406–1411, 2000.
- [39] G Wang, K Pran, G Sagvolden, GB Havsgård, AE Jensen, GA Johnson, and ST Vohra. Ship hull structure monitoring using fibre optic sensors. *Smart materials and structures*, 10(3):472, 2001.
- [40] NP Avdelidis, BC Hawtin, and DP Almond. Transient thermography in the assessment of defects of aircraft composites. *NDT and E International*, 36(6):433–439, 2003.
- [41] J. Palaniappan, SL Ogin, AM Thorne, GT Reed, AD Crocombe, TF Capell, SC Tjin, and L. Mohanty. Disbond growth detection in composite-composite single-lap joints using chirped FBG sensors. *Composites Science and Technology*, 68(12):2410–2417, 2008.
- [42] T.J.R. Hughes. *The finite element method: linear static and dynamic finite element analysis*, volume 65. Dover Publications, 2000.
- [43] T. Erdogan. Fiber grating spectra. *Lightwave Technology, Journal of*, 15(8):1277–1294, 1997.
- [44] R. Kashyap. *Fiber bragg gratings*. Academic Pr, 1999.

- 
- [45] N. Chisholm, H. Mahfuz, V.K. Rangari, A. Ashfaq, and S. Jeelani. Fabrication and mechanical characterization of carbon/sic-epoxy nanocomposites. *Composite Structures*, 67(1):115–124, 2005.
- [46] B. Yenilmez, M. Senan, and E. Murat Sozer. Variation of part thickness and compaction pressure in vacuum infusion process. *Composites Science and Technology*, 69(11):1710–1719, 2009.
- [47] D. Modi, N. Correia, M. Johnson, A. Long, C. Rudd, and F. Robitaille. Active control of the vacuum infusion process. *Composites Part A: Applied Science and Manufacturing*, 38(5):1271–1287, 2007.
- [48] R. Matsuzaki, S. Kobayashi, A. Todoroki, and Y. Mizutani. Full-field monitoring of resin flow using an area-sensor array in a vartm process. *Composites Part A: Applied Science and Manufacturing*, 42(5):550–559, 2011.
- [49] SH Eum, K. Kageyama, H. Murayama, K. Uzawa, I. Ohsawa, M. Kanai, S. Kobayashi, H. Igawa, and T. Shirai. Structural health monitoring using fiber optic distributed sensors for vacuum-assisted resin transfer molding. *Smart Materials and Structures*, 16(6):2627, 2007.
- [50] D.L. Woerdeman, J.K. Spoerre, K.M. Flynn, and R.S. Parnas. Cure monitoring of the liquid composite molding process using fiber optic sensors. *Polymer composites*, 18(1):133–150, 1997.
- [51] R. Montanini and L. d’Acquisto. Simultaneous measurement of temperature and strain in glass fiber/epoxy composites by embedded fiber optic sensors: I. cure monitoring. *Smart Materials and Structures*, 16(5):1718, 2007.
- [52] TA Dawood, RA Shenoi, and M. Sahin. A procedure to embed fibre bragg grating strain sensors into GFRP sandwich structures. *Composites Part A: Applied Science and Manufacturing*, 38(1):217–226, 2007.
- [53] K. Lau, L. Yuan, L. Zhou, J. Wu, and C. Woo. Strain monitoring in frp laminates and concrete beams using FBG sensors. *Composite Structures*, 51(1):9–20, 2001.

- [54] S. Takeda, Y. Aoki, and Y. Nagao. Damage monitoring of CFRP stiffened panels under compressive load using FBG sensors. *Composite Structures*, 94(3):813–819, 2012.
- [55] RC Tennyson, AA Mufti, S Rizkalla, G Tadros, and B Benmokrane. Structural health monitoring of innovative bridges in canada with fiber optic sensors. *Smart materials and structures*, 10(3):560, 2001.
- [56] Jose Miguel Lopez-Higuera, Antonio Quintela, and Juan Echevarria. Fiber optic civil structure monitoring system. *Optical Engineering*, 44(4):044401–044401–10, 2005.
- [57] Jin-Hak Yi, Kwang-Soo Lee, Jin-Soon Park, and Woo-Sun Park. Structural health monitoring system for “uldolmok” tidal current power pilot plant and its applications. ASME.
- [58] UNE. Bond test of steels wires for prestressed concrete, 1982.

### 11.3. References of Chapter 5

- [1] Kara Peters. Polymer optical fiber sensors: A review. *Smart materials and structures*, 20(1):013002, 2010.
- [2] KSC Kuang, ST Quek, CG Koh, WJ Cantwell, and PJ Scully. Plastic optical fibre sensors for structural health monitoring: a review of recent progress. *Journal of sensors*, 2009, 2009.
- [3] WB Spillman Jr, BR Kline, LB Maurice, and PL Fuhr. Statistical-mode sensor for fiber optic vibration sensing uses. *Applied optics*, 28(15):3166–3176, 1989.
- [4] F.T.S. Yu, M. Wen, S. Yin, and C.M. Uang. Submicrometer displacement sensing using inner-product multimode fiber speckle fields. *Applied optics*, 32(25):4685–4689, 1993.
- [5] K. Pan, C.M. Uang, F. Cheng, and F.T.S. Yu. Multimode fiber sensing by using mean-absolute speckle-intensity variation. *Applied optics*, 33(10):2095–2098, 1994.

- 
- [6] S. Yin, P. Purwosumarto, and F.T.S. Yu. Application of fiber specklegram sensor to fine angular alignment. *Optics communications*, 170(1):15–21, 1999.
- [7] JS Leng and A. Asundi. Nde of smart structures using multimode fiber optic vibration sensor. *NDT and E International*, 35(1):45–51, 2002.
- [8] B. Crosignani, B. Daino, and P.D. Porto. Speckle-pattern visibility of light transmitted through a multimode optical fiber. *JOSA*, 66(11):1312–1313, 1976.
- [9] J.W. Goodman and E.G. Rawson. Statistics of modal noise in fibers: a case of constrained speckle. *Optics Letters*, 6(7):324–326, 1981.
- [10] Y. Tremblay, BS Kawasaki, and KO Hill. Modal noise in optical fibers: open and closed speckle pattern regimes. *Applied optics*, 20(9):1652–1655, 1981.
- [11] G. Kaiser. *Optical Fiber Communications*, chapter 2. McGraw-Hill, NY, second edition, 1991.
- [12] Z. Zhang and F. Ansari. Fiber-optic laser speckle-intensity crack sensor for embedment in concrete. *Sensors and Actuators A: Physical*, 126(1):107–111, 2006.
- [13] Dietrich Marcuse. Theory of dielectric optical waveguides. *New York, Academic Press, Inc., 1974. 267 p.*, 1, 1974.
- [14] A.A. Kamshilin, T. Jaaskelainen, and Y.N. Kulchin. Adaptive correlation filter for stabilization of interference-fiber-optic sensors. *Applied physics letters*, 73(6):705–707, 1998.
- [15] J.A. Gomez and Á. Salazar. Self-correlation fiber specklegram sensor using volume characteristics of speckle patterns. *Optics and Lasers in Engineering*, 2012.
- [16] Allan W Snyder and J Love. *Optical waveguide theory*, volume 190. Springer, 1983.

## 11.4. References of Chapter 6

- [1] JM Lopez-Higuera. *Handbook of Optical Fibre Sensing Technology 2002*. John Wiley & Sons, 2002.
- [2] Kang Zhang and Jin U Kang. C-band wavelength-swept single-longitudinal-mode erbium-doped fiber ring laser. *Optics Express*, 16(18):14173–14179, 2008.
- [3] M Angeles Quintela, Rosa Ana Perez-Herrera, Irene Canales, Monserrat Fernandez-Vallejo, Manuel Lopez-Amo, and Jose-Miguel Lopez-Higuera. Stabilization of dual-wavelength erbium-doped fiber ring lasers by single-mode operation. *Photonics Technology Letters, IEEE*, 22(6):368–370, 2010.
- [4] Yonghang Shen, Yanqing Qiu, Bo Wu, Weizhong Zhao, Shuying Chen, Tong Sun, and Kenneth TV Grattan. Short cavity single frequency fiber laser for in-situ sensing applications over a wide temperature range. *Optics Express*, 15(2):363–370, 2007.
- [5] Shilong Pan and Jianping Yao. A wavelength-switchable single-longitudinal-mode dual-wavelength erbium-doped fiber laser for switchable microwave generation. *Optics Express*, 17(7):5414–5419, 2009.
- [6] RA Perez-Herrera, S Chen, W Zhao, T Sun, KTV Grattan, and M Lopez-Amo. Stability performance of short cavity er-doped fiber lasers. *Optics Communications*, 283(6):1067–1070, 2010.
- [7] Christine Spiegelberg, Jihong Geng, Yongdan Hu, Yushi Kaneda, Shibin Jiang, and N Peyghambarian. Low-noise narrow-linewidth fiber laser at 1550 nm (june 2003). *Journal of Lightwave Technology*, 22(1):57, 2004.
- [8] Yuri O Barmenkov, Dobryna Zalvidea, Salvador Torres-Peiro, Jose L Cruz, and Miguel V Andres. Effective length of short fabry-perot cavity formed by uniform fiber bragg gratings. *Opt. Express*, 14(14):6394–6399, 2006.

- 
- [9] William T Silfvast. *Laser fundamentals*. Cambridge University Press, 2004.
- [10] Montserrat Fernandez-Vallejo, Silvia Diaz, Rosa Ana Perez-Herrera, Ruth Unzu, Maria Angeles Quintela, Jose Miguel Lopez-Higuera, and Manuel Lopez-Amo. Comparison of the stability of ring resonator structures for multiwavelength fiber lasers using raman or Er-doped fiber amplification. *Quantum Electronics, IEEE Journal of*, 45(12):1551–1557, 2009.
- [11] Antoine Bellemare. Continuous-wave silica-based erbium-doped fibre lasers. *Progress in Quantum Electronics*, 27(4):211–266, 2003.
- [12] L Talaverano, S Abad, S Jarabo, and M Lopez-Amo. Multiwavelength fiber laser sources with bragg-grating sensor multiplexing capability. *Journal of lightwave technology*, 19(4):553, 2001.
- [13] Shilong Pan, Xiaofan Zhao, and Caiyun Lou. Switchable single-longitudinal-mode dual-wavelength erbium-doped fiber ring laser incorporating a semiconductor optical amplifier. *Optics letters*, 33(8):764–766, 2008.
- [14] Guolu Yin, Bhavaye Saxena, and Xiaoyi Bao. Tunable Er-doped fiber ring laser with single longitudinal mode operation based on rayleigh backscattering in single mode fiber. *Optics Express*, 19(27):25981–25989, 2011.
- [15] Xiangfei Chen, Jianping Yao, Fei Zeng, and Zhichao Deng. Single-longitudinal-mode fiber ring laser employing an equivalent phase-shifted fiber bragg grating. *Photonics Technology Letters, IEEE*, 17(7):1390–1392, 2005.
- [16] M Ibsen, BJ Eggleton, MG Sceats, and F Ouellette. Broadly tunable DBR fibre laser using sampled fibre bragg gratings. *Electronics Letters*, 31(1):37–38, 1995.
- [17] Xiaoying He, Xia Fang, Changrui Liao, Dongning Wang, and Junqiang Sun. A tunable and switchable single-longitudinalmode dual-wavelength fiber laser with a simple linear cavity. *Optics Express*, 17(24):21773–21781, 2009.

- [18] JL Zyskind, V Mizrahi, DJ DiGiovanni, and JW Sulhoff. Short single frequency erbium-doped fibre laser. *Electronics Letters*, 28(15):1385–1387, 1992.
- [19] Gary A Ball and WW Morey. Continuously tunable single-mode erbium fiber laser. *Optics letters*, 17(6):420–422, 1992.
- [20] Shilpa Pradhan, Graham E Town, and Ken J Grant. Dual-wavelength DBR fiber laser. *Photonics Technology Letters, IEEE*, 18(16):1741–1743, 2006.
- [21] T Okoshi, Ki Kikuchi, and A Nakayama. Novel method for high resolution measurement of laser output spectrum. *Electronics Letters*, 16(16):630–631, 1980.

## 11.5. References of Chapter 7

- [1] Ralph C Smith. *Smart material systems: Model developments*, volume 32. Siam, 2005.
- [2] Kazuhiro Otsuka and Clarence Marvin Wayman. *Shape memory materials*. Cambridge University Press, 1999.
- [3] L McDonald Schetky. Shape-memory alloys. *Kirk-Othmer Encyclopedia of Chemical Technology*, 1982.
- [4] Hiroyasu Funakubo and JB Kennedy. Shape memory alloys. *Gordon and Breach, xii+ 275, 15 x 22 cm, Illustrated*, 1987.
- [5] M. Amano, Y. Okabe, and N. Takeda. Evaluation of crack suppression effect of TiNi SMA foil embedded in CFRP cross-ply laminates with embedded small-diameter FBG sensor. *JSME International Journal Series A*, 48(4):443–450, 2005.
- [6] M. Mieloszyk, L. Skarbek, M. Krawczuk, W. Ostachowicz, and A. Zak. Application of fibre bragg grating sensors for structural health monitoring of an adaptive wing. *Smart Materials and Structures*, 20:125014, 2011.

- [7] JM Lopez-Higuera. *Handbook of Optical Fibre Sensing Technology 2002*. John Wiley & Sons, 2002.
- [8] Yun-Jiang Rao. In-fibre bragg grating sensors. *Measurement science and technology*, 8(4):355, 1997.
- [9] Yunqi Liu, Zhuanyun Guo, Ying Zhang, Kin Seng Chiang, and Xiaoyi Dong. Simultaneous pressure and temperature measurement with polymer-coated fibre bragg grating. *Electronics letters*, 36(6):564–566, 2000.
- [10] Fatiha El Feninat, Gaetan Laroche, Michel Fiset, and Diego Mantovani. Shape memory materials for biomedical applications. *Advanced Engineering Materials*, 4(3):91, 2002.
- [11] Craig A Rogers. Active vibration and structural acoustic control of shape memory alloy hybrid composites: experimental results. *The Journal of the Acoustical Society of America*, 88:2803, 1990.
- [12] Inc Dynalloy. <http://www.dynalloy.com/>, 2012.
- [13] Raman Kashyap. *Fiber bragg gratings*. Access Online via Elsevier, 1999.
- [14] K. Chau, B. Moslehi, G. Song, and V. Sethi. Experimental demonstration of fiber bragg grating strain sensors for structural vibration control. volume 5391, pages 753–764.
- [15] A. Cavallo, C. May, A. Minardo, C. Natale, P. Pagliarulo, and S. Pirozzi. Active vibration control by a smart auxiliary mass damper equipped with a fiber bragg grating sensor. *Sensors and Actuators A: Physical*, 153(2):180–186, 2009.
- [16] K.C. Chuang and C.C. Ma. Tracking control of a multilayer piezoelectric actuator using a fiber bragg grating displacement sensor system. *Ultrasonics, Ferroelectrics and Frequency Control, IEEE Transactions on*, 56(10):2036–2049, 2009.

## 11.6. References of Chapter 8

- [1] Dean A Pomerleau. Efficient training of artificial neural networks for autonomous navigation. *Neural Computation*, 3(1):88–97, 1991.
- [2] Daniel J Fonseca and Daniel Navarrese. Artificial neural networks for job shop simulation. *Advanced Engineering Informatics*, 16(4):241–246, 2002.
- [3] Yoram Reich and SV Barai. Evaluating machine learning models for engineering problems. *Artificial Intelligence in Engineering*, 13(3):257–272, 1999.
- [4] Jeff Hawkins and Sandra Blakeslee. *On Intelligence*. 2004.
- [5] D. George and J. Hawkins. Towards a mathematical theory of cortical micro-circuits. *PLoS computational biology*, 5(10):e1000532, 2009.
- [6] Kishan Mehrotra, Chilukur K Mohan, and Sanjay Ranka. *Artificial Neural Networks*. the MIT Press, 1997.
- [7] TWS Chow and Siu-Yeung Cho. Industrial neural vision system for underground railway station platform surveillance. *Advanced Engineering Informatics*, 16(1):73–83, 2002.
- [8] SF Masri, AW Smyth, AG Chassiakos, TK Caughey, and NF Hunter. Application of neural networks for detection of changes in nonlinear systems. *Journal of Engineering Mechanics*, 126:666, 2000.
- [9] S. Stolc and I. Bajla. On the optimum architecture of the biologically inspired hierarchical temporal memory model applied to the hand-written digit recognition. *Measurement Science Review*, 10(2):28–49, 2010.
- [10] B.A. Bobier and M. Wirth. Content-based image retrieval using hierarchical temporal memory. In *Proceedings of the 16th ACM international conference on Multimedia*, pages 925–928. ACM.
- [11] Kenneth O Hill and Gerald Meltz. Fiber bragg grating technology fundamentals and overview. *Lightwave Technology, Journal of*, 15(8):1263–1276, 1997.

- [12] H.J. Bang, S.W. Park, D.H. Kim, C.S. Hong, and C.G. Kim. Impact monitoring in smart composites using stabilization controlled FBG sensor system. In *Proceedings of SPIE*, volume 5384, pages 279–86.
- [13] J. Frieden, J. Cugnoni, J. Botsis, and T. Gmür. Low energy impact damage monitoring of composites using dynamic strain signals from FBG sensors-part i: Impact detection and localization. *Composite Structures*, 2011.
- [14] E. Kirkby, R. de Oliveira, V. Michaud, and JA Månson. Impact localisation with FBG for a self-healing carbon fibre composite structure. *Composite Structures*, 2011.
- [15] R. Dua, SE Watkins, DC Wunsch, K. Chandrashekhara, and F. Akhavan. Detection and classification of impact-induced damage in composite plates using neural networks. In *International Joint Conference on Neural Networks*, volume 1, pages 681–686 vol. 1. IEEE.
- [16] C.K. Coelho, C. Hiche, and A. Chattopadhyay. Machine learning approach to impact load estimation using fiber bragg grating sensors. In *Proceedings of SPIE*, volume 7648, page 764810.
- [17] Cyril Goutte and Eric Gaussier. *A probabilistic interpretation of precision, recall and F-score, with implication for evaluation*, pages 345–359. Springer, 2005.
- [18] Luis Rodríguez-Cobo, P Beatriz García-Allende, Adolfo Cobo, José Miguel Lopez-Higuera, and Olga M Conde. Raw material classification by means of hyperspectral imaging and hierarchical temporal memories. *Sensors Journal, IEEE*, 12(9):2767–2775, 2012.



# Chapter 12

---

## References in alphabetical order

---

**Abad, S., Lopez-Amo, M., et al. (2002).** Fiber Bragg grating based self-referencing technique for wavelength-multiplexed intensity sensors. *Optics letters* 27(4): 222-224.

**Amano, M., Okabe, Y., et al. (2005).** Evaluation of Crack Suppression Effect of TiNi SMA Foil Embedded in CFRP Cross-Ply Laminates with Embedded Small-Diameter FBG Sensor. *JSME International Journal Series A* 48(4): 443-450.

**Amano, M., Okabe, Y., et al. (2007).** Structural health monitoring of an advanced grid structure with embedded fiber Bragg grating sensors. *Structural Health Monitoring* 6(4): 309-324.

**Angulo-Vinuesa, X., Martin-Lopez, S., et al. (2012).** Raman-assisted Brillouin distributed temperature sensor over 100 km featuring 2 m resolution and 1.2 C uncertainty. *Journal of Lightwave Technology* 30(8): 1060-1065.

**Ansari, F. (1997).** State-of-the-art in the applications of fiber-optic sensors to cementitious composites. *Cement and Concrete Composites* 19(1): 3-19.

**Avdelidis, N., Hawtin, B., et al. (2003).** Transient thermography in the assessment of defects of aircraft composites. *NDT and E International* 36(6): 433-439.

**Azana, J. and Muriel, M. A. (2000).** Reconstructing arbitrary strain distributions within fiber gratings by time-frequency signal analysis. *Optics letters* 25(10): 698-700.

**Baldwin, C., Kiddy, J., et al. (2002).** Fiber optic structural health monitoring system: Rough sea trials testing of the RV Triton. *OCEANS'02 MTS/IEEE, IEEE*.

**Ball, G., Meltz, G., et al. (1993).** Polarimetric heterodyning Bragg-grating fiber-laser sensor. *Optics letters* 18(22): 1976-1978.

**Ball, G., Morey, W., et al. (1993).** Single-and multipoint fiber-laser sensors. *Photonics Technology Letters, IEEE* 5(2): 267-270.

**Ball, G. A. and Morey, W. (1992).** Continuously tunable single-mode erbium fiber laser. *Optics letters* 17(6): 420-422.

**Bang, H. J., Park, S. W., et al. (2004).** Impact monitoring in smart composites using stabilization controlled FBG sensor system. *Proceedings of SPIE, San Diego, CA, USA*.

**Bao, X., Huang, C., et al. (2002).** Simultaneous strain and temperature monitoring of the composite cure with a Brillouin-scattering-based distributed sensor. *Optical Engineering* 41(7): 1496-1501.

**Barmenkov, Y. O., Zalvidea, D., et al. (2006).** Effective length of short Fabry-Perot cavity formed by uniform fiber Bragg gratings. *Opt. Express* 14(14): 6394-6399.

---

**Barnoski, M. and Jensen, S. (1976).** Fiber waveguides: a novel technique for investigating attenuation characteristics. *Applied optics* 15(9): 2112-2115.

**Bellemare, A. (2003).** Continuous-wave silica-based erbium-doped fibre lasers. *Progress in Quantum Electronics* 27(4): 211-266.

**Bobier, B. A. and Wirth, M. (2008).** Content-based image retrieval using hierarchical temporal memory. *Proceedings of the 16th ACM international conference on Multimedia* New York, NY, USA, ACM.

**Bocherens, E., Bourasseau, S., et al. (2000).** Damage detection in a radome sandwich material with embedded fiber optic sensors. *Smart Materials and Structures* 9: 310.

**Boiarski, A., Pilate, G., et al. (1995).** Temperature measurements in power plant equipment using distributed fiber optic sensing. *Power Delivery, IEEE Transactions on* 10(4): 1771-1778.

**Casagrande, F., Crespi, P., et al. (2002).** From the reflected spectrum to the properties of a fiber Bragg grating: a genetic algorithm approach with application to distributed strain sensing. *Applied Optics* 41(25): 5238-5244.

**Cavallo, A., May, C., et al. (2009).** Active vibration control by a smart auxiliary mass damper equipped with a fiber Bragg grating sensor. *Sensors and Actuators A: Physical* 153(2): 180-186.

**Chan, T., Yu, L., et al. (2006).** Fiber Bragg grating sensors for structural health monitoring of Tsing Ma bridge: Background and experimental observation. *Engineering structures* 28(5): 648-659.

**Chandler, K., Ferguson, S., et al. (2008).** On-line structural health and fire monitoring of a composite personal aircraft using an FBG sensing system. *The 15th International Symposium on: Smart Structures and Materials*

& Nondestructive Evaluation and Health Monitoring, International Society for Optics and Photonics.

**Chapeleau, X., Casari, P., et al. (2006).** Determination of strain distribution and temperature gradient profiles from phase measurements of embedded fibre Bragg gratings. *Journal of Optics A: Pure and Applied Optics* 8: 775.

**Chau, K., Moslehi, B., et al. (2004).** Experimental demonstration of fiber Bragg grating strain sensors for structural vibration control.

**Chen, X., Yao, J., et al. (2005).** Single-longitudinal-mode fiber ring laser employing an equivalent phase-shifted fiber Bragg grating. *Photonics Technology Letters, IEEE* 17(7): 1390-1392.

**Cheng, C., Lo, Y. L., et al. (2007).** Estimations of fiber Bragg grating parameters and strain gauge factor using optical spectrum and strain distribution information. *Applied Optics* 46(21): 4555-4562.

**Chisholm, N., Mahfuz, H., et al. (2005).** Fabrication and mechanical characterization of carbon/SiC-epoxy nanocomposites. *Composite Structures* 67(1): 115-124.

**Chow, T. and Cho, S.-Y. (2002).** Industrial neural vision system for underground railway station platform surveillance. *Advanced Engineering Informatics* 16(1): 73-83.

**Chuang, K. C. and Ma, C. C. (2009).** Tracking control of a multilayer piezoelectric actuator using a fiber Bragg grating displacement sensor system. *Ultrasonics, Ferroelectrics and Frequency Control, IEEE Transactions on* 56(10): 2036-2049.

**Coelho, C. K., Hiche, C., et al. (2010).** Machine learning approach to impact load estimation using fiber Bragg grating sensors. *Proceedings of SPIE.*

---

**Crosignani, B., Daino, B., et al. (1976).** Speckle-pattern visibility of light transmitted through a multimode optical fiber. *JOSA* 66(11): 1312-1313.

**Culshaw, B. (1996).** Smart structures and materials, Artech House Boston.

**Cusano, A., Capoluongo, P., et al. (2006).** Experimental modal analysis of an aircraft model wing by embedded fiber Bragg grating sensors. *Sensors Journal, IEEE* 6(1): 67-77.

**Daghia, F., Giammarruto, A., et al. (2011).** Combined use of FBG sensors and SMA actuators for concrete beams repair. *Structural Control and Health Monitoring*.

**Dawood, T., Shenoi, R., et al. (2007).** A procedure to embed fibre Bragg grating strain sensors into GFRP sandwich structures. *Composites Part A: Applied Science and Manufacturing* 38(1): 217-226.

**De Oliveira, R., Ramos, C., et al. (2008).** Health monitoring of composite structures by embedded FBG and interferometric Fabry-Pérot sensors. *Computers & structures* 86(3): 340-346.

**Dobb, H., Webb, D. J., et al. (2005).** Continuous wave ultraviolet light-induced fiber Bragg gratings in few-and single-mode microstructured polymer optical fibers. *Optics letters* 30(24): 3296-3298.

**Dong, B., He, S., et al. (2006).** Time-division multiplexing fiber grating sensor with a tunable pulsed laser. *Photonics Technology Letters, IEEE* 18(24): 2620-2622.

**Dua, R., Watkins, S., et al. (2001).** Detection and classification of impact-induced damage in composite plates using neural networks. *International Joint Conference on Neural Networks, Washington, DC, IEEE*.

**Durana, G., Kirchhof, M., et al. (2009).** Use of a novel fiber optical strain sensor for monitoring the vertical deflection of an aircraft flap. *Sensors Journal, IEEE* 9(10): 1219-1225.

**Dynalloy, I. (2012).** <http://www.dynalloy.com/>. from <http://www.dynalloy.com/>.

**Ecke, W., Latka, I., et al. (2001).** Fibre optic sensor network for spacecraft health monitoring. *Measurement science and technology* 12(7): 974.

**Eggleton, B., Krug, P., et al. (1994).** Long periodic superstructure Bragg gratings in optical fibres. *Electronics letters* 30(19): 1620-1622.

**El Feninat, F., Laroche, G., et al. (2002).** Shape memory materials for biomedical applications. *Advanced Engineering Materials* 4(3): 91.

**Erdogan, T. (1997).** Fiber grating spectra. *Lightwave Technology, Journal of* 15(8): 1277-1294.

**Eum, S., Kageyama, K., et al. (2007).** Structural health monitoring using fiber optic distributed sensors for vacuum-assisted resin transfer molding. *Smart Materials and Structures* 16(6): 2627.

**Ezbiri, A., Munoz, A., et al. (1997).** High resolution fibre Bragg grating sensor demodulation using a diffraction grating spectrometer and CCD detection.

**Fernandez-Vallejo, M., Diaz, S., et al. (2009).** Comparison of the stability of ring resonator structures for multiwavelength fiber lasers using Raman or Er-doped fiber amplification. *Quantum Electronics, IEEE Journal of* 45(12): 1551-1557.

**Ferreira, M., Vieira, J., et al. (2011).** Simultaneous measurement of strain and temperature using fiber Bragg grating sensors embedded in hybrid

---

composite laminates. *Measurement Science and Technology* 22(4): 045206.

**Fonseca, D. J. and Navarrese, D. (2002).** Artificial neural networks for job shop simulation. *Advanced Engineering Informatics* 16(4): 241-246.

**Franke, R., Malzahn, J., et al. (2009).** Vibration control of a multi-link flexible robot arm with Fiber-Bragg-Grating sensors, *IEEE*.

**Frazao, O., Carvalho, J., et al. (2005).** Discrimination of strain and temperature using Bragg gratings in microstructured and standard optical fibres. *Measurement Science and Technology* 16(10): 2109.

**Frazao, O., Oliveira, R., et al. (2009).** A simple smart composite using fiber Bragg grating sensors for strain and temperature discrimination. *Microwave and Optical Technology Letters* 51(1): 235-239.

**Friebele, E., Askins, C., et al. (1999).** Optical fiber sensors for spacecraft applications. *Smart materials and structures* 8(6): 813.

**Friebele, E. J., Askins, C. G., et al. (1994).** Distributed strain sensing with fibre Bragg grating arrays embedded in CRTM composites. *Electronics Letters* 30(21): 1783-1784.

**Frieden, J., Cugnoni, J., et al. (2011).** Low energy impact damage monitoring of composites using dynamic strain signals from FBG sensors-Part I: Impact detection and localization. *Composite Structures*.

**Fuhr, P. L., Ambrose, T. P., et al. (1995).** Fiber optic corrosion sensing for bridges and roadway surfaces. *Smart Structures & Materials' 95*, International Society for Optics and Photonics.

**Funakubo, H. and Kennedy, J. (1987).** Shape memory alloys. Gordon and Breach, xii+ 275, 15 x 22 cm, Illustrated.

**Gao, J., Shi, B., et al. (2006).** Monitoring the stress of the post-tensioning cable using fiber optic distributed strain sensor. *Measurement* 39(5): 420-428.

**Gebremichael, Y., Li, W., et al. (2005).** Integration and assessment of fibre Bragg grating sensors in an all-fibre reinforced polymer composite road bridge. *Sensors and Actuators A: Physical* 118(1): 78-85.

**George, D. (2005).** A hierarchical Bayesian model of invariant pattern recognition in the visual cortex. *Neural Networks IJCNN '05. Proceedings.*

**George, D. and Hawkins, J. (2009).** Towards a mathematical theory of cortical micro-circuits. *PLoS computational biology* 5(10): e1000532.

**George, D. and Jaros, B. (2007).** The HTM Learning Algorithm. Numenta Inc. Whitepaper.

**Gomez, J., Zubia, J., et al. (2009).** Comparing polymer optical fiber, fiber Bragg grating, and traditional strain gauge for aircraft structural health monitoring. *Applied Optics* 48(8): 1436-1443.

**Gomez, J. A. and Salazar, á. (2012).** Self-correlation fiber specklegram sensor using volume characteristics of speckle patterns. *Optics and Lasers in Engineering.*

**Goodman, J. W. and Rawson, E. G. (1981).** Statistics of modal noise in fibers: a case of constrained speckle. *Optics Letters* 6(7): 324-326.

**Goutte, C. and Gaussier, E. (2005).** A probabilistic interpretation of precision, recall and F-score, with implication for evaluation. *Advances in Information Retrieval, Springer:* 345-359.

**Grossman, D. A. (2004).** *Information retrieval: Algorithms and heuristics,* Springer.

---

**Grouve, W., Warnet, L., et al. (2008).** Delamination detection with fibre Bragg gratings based on dynamic behaviour. *Composites Science and Technology* 68(12): 2418-2424.

**Guan, B.-O., Tam, H.-Y., et al. (2000).** Simultaneous strain and temperature measurement using a superstructure fiber Bragg grating. *Photonics Technology Letters, IEEE* 12(6): 675-677.

**Habel, W. R. and Hofmann, D. (1994).** Determination of structural parameters concerning load capacity based on fibre Fabry-Perot interferometers. *Smart Structures and Materials: Second European Conference, International Society for Optics and Photonics.*

**Han, Y.-G., Tran, T., et al. (2005).** Multiwavelength Raman-fiber-laser-based long-distance remote sensor for simultaneous measurement of strain and temperature. *Optics letters* 30(11): 1282-1284.

**He, X., Fang, X., et al. (2009).** A tunable and switchable single-longitudinalmode dual-wavelength fiber laser with a simple linear cavity. *Optics Express* 17(24): 21773-21781.

**Herszberg, I., Li, H., et al. (2005).** Damage assessment and monitoring of composite ship joints. *Composite structures* 67(2): 205-216.

**Hill, K. O. and Meltz, G. (1997).** Fiber Bragg grating technology fundamentals and overview. *Lightwave Technology, Journal of* 15(8): 1263-1276.

**Horiguchi, T., Rogers, A., et al. (1997).** Distributed sensors- Recent developments. *Optical fiber sensors.*

**Huang, S., Ohn, M. M., et al. (1998).** Continuous arbitrary strain profile measurements with fiber Bragg gratings. *Smart materials and structures* 7(2): 248-256.

**Hughes, T. J. R. (2000).** The finite element method: linear static and dynamic finite element analysis, Dover Publications.

**Husdi, I. R., Nakamura, K., et al. (2004).** Sensing characteristics of plastic optical fibres measured by optical time-domain reflectometry. *Measurement Science and Technology* 15(8): 1553.

**Huston, D. R., Fuhr, P. L., et al. (1994).** Intelligent civil structures-activities in Vermont. *Smart materials and structures* 3(2): 129.

**Ibsen, M., Eggleton, B., et al. (1995).** Broadly tunable DBR fibre laser using sampled fibre Bragg gratings. *Electronics Letters* 31(1): 37-38.

**Inaudi, D., Elamari, A., et al. (1994).** Low-coherence interferometry for the monitoring of civil engineering structures. *Smart Structures and Materials: Second European Conference, International Society for Optics and Photonics*.

**Inaudi, D. and López-Higuera, J. (2002).** Photonic sensing technology in civil engineering applications. *Handbook of Optical Fibre Sensing Technology* 25: 517-542.

**Ito, Y., Fujimoto, K., et al. (2010).** Cure Monitoring of Carbon/Epoxy composite by optical-fiber-based distributed strain/temperature sensing.

**Jeff Hawkins and Blakeslee, S. (2004).** On Intelligence.

**Jin, W., Michie, W. C., et al. (1997).** Simultaneous measurement of strain and temperature: error analysis. *Optical Engineering* 36(2): 598-609.

**Johnson, G. A., Pran, K., et al. (2000).** Surface effect ship vibro-impact monitoring with distributed arrays of fiber bragg gratings. *Proceedings of the 18th International Modal Analysis*: 1406-1411.

---

**Jung, K., Kang, T. J., et al. (2007).** Estimation of residual strain and stress in interply hybrid composite using fiber bragg grating sensor. *Fibers and Polymers* 8(4): 438-442.

**Kahandawa, G., Epaarachchi, J., et al. (2013).** Use of fixed wavelength Fibre-Bragg Grating (FBG) filters to capture time domain data from the distorted spectrum of an embedded FBG sensor to estimate strain with an Artificial Neural Network. *Sensors and Actuators A: Physical*.

**Kahandawa, G. C., Epaarachchi, J., et al. (2012).** Use of FBG sensors for SHM in aerospace structures. *Photonic Sensors* 2(3): 203-214.

**Kaiser, G. (1991).** *Optical Fiber Communications*. NY, McGraw-Hill.

**Kalamkarov, A., Fitzgerald, S., et al. (1999).** The use of Fabry Perot fiber optic sensors to monitor residual strains during pultrusion of FRP composites. *Composites Part B: Engineering* 30(2): 167-175.

**Kamshilin, A. A., Jaaskelainen, T., et al. (1998).** Adaptive correlation filter for stabilization of interference-fiber-optic sensors. *Applied physics letters* 73(6): 705-707.

**Kashyap, R. (1999).** *Fiber bragg gratings*, Academic Pr.

**Katsikeros, C. E. and Labeas, G. (2009).** Development and validation of a strain-based Structural Health Monitoring system. *Mechanical Systems and Signal Processing* 23(2): 372-383.

**Kennedy, J. and Eberhart, R. (1995).** *Particle swarm optimization*, IEEE.

**Kennedy, J. F., Kennedy, J., et al. (2001).** *Swarm intelligence*, Morgan Kaufmann Pub.

**Kersey, A. D., Davis, M. A., et al. (1997).** Transient load monitoring on a composite hull ship using distributed fiber optic Bragg grating sensors. *Smart Structures and Materials' 97*, International Society for Optics and Photonics.

**Kiesel, S., Peters, K., et al. (2007).** Behaviour of intrinsic polymer optical fibre sensor for large-strain applications. *Measurement Science and Technology* 18(10): 3144.

**Kiesel, S., Peters, K., et al. (2008).** Large deformation in-fiber polymer optical fiber sensor. *Photonics Technology Letters, IEEE* 20(6): 416-418.

**Kirkby, E., de Oliveira, R., et al. (2011).** Impact localisation with FBG for a self-healing carbon fibre composite structure. *Composite Structures*.

**Kirkendall, C. K. and Dandridge, A. (2004).** Overview of high performance fibre-optic sensing. *Journal of Physics D: Applied Physics* 37(18): R197.

**Kister, G., Winter, D., et al. (2007).** Methodology and integrity monitoring of foundation concrete piles using Bragg grating optical fibre sensors. *Engineering Structures* 29(9): 2048-2055.

**Klar, A., Bennett, P. J., et al. (2006).** Distributed strain measurement for pile foundations. *Proceedings of the ICE-Geotechnical Engineering* 159(3): 135-144.

**Ko, J. and Ni, Y. (2005).** Technology developments in structural health monitoring of large-scale bridges. *Engineering Structures* 27(12): 1715-1725.

**Kuang, K. and Cantwell, W. (2003).** The use of plastic optical fibre sensors for monitoring the dynamic response of fibre composite beams. *Mea-*

---

surement Science and Technology 14(6): 736.

**Kuang, K., Cantwell, W., et al. (2003).** Crack detection and vertical deflection monitoring in concrete beams using plastic optical fibre sensors. *Measurement Science and Technology* 14(2): 205.

**Kuang, K., Kenny, R., et al. (2001).** Embedded fibre Bragg grating sensors in advanced composite materials. *Composites Science and Technology* 61(10): 1379-1387.

**Kuang, K., Quek, S., et al. (2009).** Plastic optical fibre sensors for structural health monitoring: a review of recent progress. *Journal of sensors* 2009.

**Kuang, K., Quek, S. T., et al. (2008).** Plastic optical fiber sensors for measurement of large strain in geotextile materials. *Advanced Materials Research* 47: 1233-1236.

**Kuang, K. S. C., Kenny, R., et al. (2001).** Embedded fibre Bragg grating sensors in advanced composite materials. *Composites Science and Technology* 61(10): 1379-1387.

**Kurashima, T., Horiguchi, T., et al. (1993).** Brillouin optical-fiber time domain reflectometry. *IEICE Transactions on Communications* 76(4): 382-390.

**Kurashima, T., Horiguchi, T., et al. (1991).** Measurement of distributed strain due to laying and recovery of submarine optical fiber cable. *Applied optics* 30(3): 334-337.

**Lanticq, V., Bourgeois, E., et al. (2009).** Soil-embedded optical fiber sensing cable interrogated by Brillouin optical time-domain reflectometry (BOTDR) and optical frequency-domain reflectometry (OFDR) for embedded cavity detection and sinkhole warning system. *Measurement science and tech-*

nology 20(3): 034018.

**Large, M. C., Moran, J., et al. (2009).** The role of viscoelastic properties in strain testing using microstructured polymer optical fibres (mPOF). *Measurement Science and Technology* 20(3): 034014.

**Lau, K., Yuan, L., et al. (2001).** Strain monitoring in FRP laminates and concrete beams using FBG sensors. *Composite Structures* 51(1): 9-20.

**LeBlanc, M., Huang, S., et al. (1996).** Distributed strain measurement based on a fiber Bragg grating and its reflection spectrum analysis. *Optics letters* 21(17): 1405-1407.

**Lee, J., Ryu, C., et al. (2003).** In-flight health monitoring of a subscale wing using a fiber Bragg grating sensor system. *Smart Materials and Structures* 12: 147.

**Lee, J. H., Chang, Y., et al. (2004).** Raman amplifier-based long-distance remote, strain and temperature sensing system using an erbium-doped fiber and a fiber Bragg grating. *Optics express* 12(15): 3515-3520.

**Leng, J. and Asundi, A. (2002).** NDE of smart structures using multi-mode fiber optic vibration sensor. *NDT and E International* 35(1): 45-51.

**Leng, J. and Asundi, A. (2003).** Structural health monitoring of smart composite materials by using EFPI and FBG sensors. *Sensors and Actuators A: Physical* 103(3): 330-340.

**Li, H., Herszberg, I., et al. (2006).** Health monitoring of marine composite structural joints using fibre optic sensors. *Composite Structures* 75(1-4): 321-327.

**Li, H., Herszberg, I., et al. (2004).** Sensitivity of embedded fibre optic Bragg grating sensors to disbonds in bonded composite ship joints. *Composite*

---

Structures 66(1-4): 239-248.

**Liehr, S., Lenke, P., et al. (2009).** Polymer optical fiber sensors for distributed strain measurement and application in structural health monitoring. *Sensors Journal, IEEE* 9(11): 1330-1338.

**Liu, H., Peng, G., et al. (2002).** Polymer fiber Bragg gratings with 28-dB transmission rejection. *Photonics Technology Letters, IEEE* 14(7): 935-937.

**Liu, T., Brooks, D., et al. (1997).** A multi-mode extrinsic Fabry-Perot interferometric strain sensor. *Smart materials and structures* 6(4): 464.

**Liu, Y., Guo, Z., et al. (2000).** Simultaneous pressure and temperature measurement with polymer-coated fibre Bragg grating. *Electronics letters* 36(6): 564-566.

**Lloyd, G. D., Everall, L. A., et al. (2004).** Resonant cavity time-division-multiplexed fiber Bragg grating sensor interrogator. *Photonics Technology Letters, IEEE* 16(10): 2323-2325.

**Lobo Ribeiro, A., Ferreira, L., et al. (1997).** Analysis of the reflective-matched fiber Bragg grating sensing interrogation scheme. *Applied optics* 36(4): 934-939.

**Lopez-Amo, M. and Lopez-Higuera, J. M. (2011).** Multiplexing Techniques for FBG. *Fiber Bragg Grating Sensors: Recent Advancements, Industrial Applications and Market Exploitation*. 1: 99-115.

**Lopez-Higuera, J. M. (2002).** *Handbook of optical fibre sensing technology*, John Wiley and Sons Inc.

**Lopez-Higuera, J. M., Quintela, A., et al. (2005).** Fiber optic civil structure monitoring system. *Optical Engineering* 44(4): 044401-044401-

044410.

**Lopez-Higuera, J. M., Rodriguez Cobo, L., et al. (2011).** Fiber optic sensors in structural health monitoring. *Journal of lightwave technology* 29(4): 587-608.

**Luo, F., Liu, J., et al. (1999).** A fiber optic microbend sensor for distributed sensing application in the structural strain monitoring. *Sensors and Actuators A: Physical* 75(1): 41-44.

**Maaskant, R., Alavie, T., et al. (1997).** Fiber-optic Bragg grating sensors for bridge monitoring. *Cement and Concrete Composites* 19(1): 21-33.

**Marcuse, D. (1974).** *Theory of dielectric optical waveguides.* New York, Academic Press, Inc., 1974. 267 p. 1.

**Masri, S., Smyth, A., et al. (2000).** Application of neural networks for detection of changes in nonlinear systems. *Journal of Engineering Mechanics* 126: 666.

**Matsuzaki, R., Kobayashi, S., et al. (2011).** Full-field monitoring of resin flow using an area-sensor array in a VaRTM process. *Composites Part A: Applied Science and Manufacturing* 42(5): 550-559.

**Matta, F., Bastianini, F., et al. (2008).** Distributed strain measurement in steel bridge with fiber optic sensors: validation through diagnostic load test. *Journal of performance of constructed facilities* 22(4): 264-273.

**McKenzie, I., Jones, R., et al. (2000).** Optical fibre sensors for health monitoring of bonded repair systems. *Composite structures* 50(4): 405-416.

**Mckenzie, I. and Karafolas, N. (2005).** Fiber optic sensing in space structures: the experience of the European Space Agency (Invited Paper).

---

**Mehrotra, K., Mohan, C. K., et al. (1997).** Artificial Neural Networks, the MIT Press.

**Melle, S. M., Alavie, A. T., et al. (1993).** A Bragg grating-tuned fiber laser strain sensor system. *Photonics Technology Letters, IEEE* 5(2): 263-266.

**Merzbacher, C., Kersey, A., et al. (1996).** Fiber optic sensors in concrete structures: a review. *Smart materials and structures* 5(2): 196.

**Mieloszyk, M., Skarbek, L., et al. (2011).** Application of fibre Bragg grating sensors for structural health monitoring of an adaptive wing. *Smart Materials and Structures* 20: 125014.

**Mizuno, Y., Kishi, M., et al. (2011).** Observation of stimulated Brillouin scattering in polymer optical fiber with pump-probe technique. *Optics letters* 36(12): 2378-2380.

**Modi, D., Correia, N., et al. (2007).** Active control of the vacuum infusion process. *Composites Part A: Applied Science and Manufacturing* 38(5): 1271-1287.

**Montanini, R. and d Acquisto, L. (2007).** Simultaneous measurement of temperature and strain in glass fiber-epoxy composites by embedded fiber optic sensors: I. Cure monitoring. *Smart Materials and Structures* 16(5): 1718.

**Murayama, H., Kageyama, K., et al. (2000).** Structural health monitoring of IACC yachts using fiber optic distributed strain sensors: A technical challenge for America's Cup 2000. SPIE's 7th Annual International Symposium on Smart Structures and Materials, International Society for Optics and Photonics.

**Muriel, M. A. and Carballar, A. (1997).** Internal field distributions in fiber Bragg gratings. *Photonics Technology Letters, IEEE* 9(7): 955-957.

**Murukeshan, V., Chan, P., et al. (2000).** Cure monitoring of smart composites using fiber Bragg grating based embedded sensors. *Sensors and Actuators A: Physical* 79(2): 153-161.

**Nakamura, K., Husdi, I. R., et al. (2004).** Memory effect of POF distributed strain sensor. Second European Workshop on Optical Fibre Sensors, International Society for Optics and Photonics.

**Naruse, H., Komatsu, K., et al. (2005).** Telecommunications tunnel monitoring system based on distributed optical fiber strain measurement. Bruges, Belgium-Deadline Past, International Society for Optics and Photonics.

**Naruse, H., Uehara, H., et al. (2007).** Application of a distributed fibre optic strain sensing system to monitoring changes in the state of an underground mine. *Measurement science and technology* 18(10): 3202.

**Nother, N., Wosniok, A., et al. (2008).** A distributed fiber optic sensor system for dike monitoring using Brillouin optical frequency domain analysis. The 15th International Symposium on: Smart Structures and Materials & Nondestructive Evaluation and Health Monitoring, International Society for Optics and Photonics.

**Numenta.** . Documentation <http://numenta.com/archives/documentation.php>. from <http://numenta.com/archives/documentation.php>.

**O'Donnell, M., Skovoroda, A. R., et al. (1994).** Internal displacement and strain imaging using ultrasonic speckle tracking. *Ultrasonics, Ferroelectrics and Frequency Control, IEEE Transactions on* 41(3): 314-325.

**Ohno, H., Naruse, H., et al. (2001).** Industrial applications of the BOTDR optical fiber strain sensor. *Optical fiber technology* 7(1): 45-64.

---

**Okabe, Y., Tsuji, R., et al. (2004).** Application of chirped fiber Bragg grating sensors for identification of crack locations in composites. *Composites Part A: Applied Science and Manufacturing* 35(1): 59-65.

**Okabe, Y., Yashiro, S., et al. (2000).** Detection of transverse cracks in CFRP composites using embedded fiber Bragg grating sensors. *Smart Materials and Structures* 9(6): 832.

**Okabe, Y., Yashiro, S., et al. (2002).** Effect of thermal residual stress on the reflection spectrum from fiber Bragg grating sensors embedded in CFRP laminates. *Composites Part A: Applied Science and Manufacturing* 33(7): 991-999.

**Okoshi, T., Kikuchi, K., et al. (1980).** Novel method for high resolution measurement of laser output spectrum. *Electronics Letters* 16(16): 630-631.

**Othonos, A. and Kalli, K. (1999).** *Fiber Bragg gratings: fundamentals and applications in telecommunications and sensing*, Artech House Boston.

**Otsuka, K. and Wayman, C. M. (1999).** *Shape memory materials*, Cambridge University Press.

**Palaniappan, J., Ogin, S., et al. (2008).** Disbond growth detection in composite-composite single-lap joints using chirped FBG sensors. *Composites Science and Technology* 68(12): 2410-2417.

**Pan, K., Uang, C. M., et al. (1994).** Multimode fiber sensing by using mean-absolute speckle-intensity variation. *Applied optics* 33(10): 2095-2098.

**Pan, S. and Yao, J. (2009).** A wavelength-switchable single-longitudinal-mode dual-wavelength erbium-doped fiber laser for switchable microwave generation. *Optics Express* 17(7): 5414-5419.

**Pan, S., Zhao, X., et al. (2008).** Switchable single-longitudinal-mode dual-wavelength erbium-doped fiber ring laser incorporating a semiconductor optical amplifier. *Optics letters* 33(8): 764-766.

**Park, S., Jang, B., et al. (2010).** Simultaneous measurement of strain and temperature using a reverse index fiber Bragg grating sensor. *Measurement Science and Technology* 21(3): 035703.

**Peng, G., Xiong, Z., et al. (1999).** Photosensitivity and gratings in dye-doped polymer optical fibers. *Optical Fiber Technology* 5(2): 242-251.

**Peng, P.-C., Tseng, H.-Y., et al. (2004).** Long-distance FBG sensor system using a linear-cavity fiber Raman laser scheme. *Photonics Technology Letters, IEEE* 16(2): 575-577.

**Pereira, G., Frias, C., et al. (2012).** On the improvement of strain measurements with FBG sensors embedded in unidirectional composites. *Polymer Testing*.

**Perez-Herrera, R., Chen, S., et al. (2010).** Stability performance of short cavity Er-doped fiber lasers. *Optics Communications* 283(6): 1067-1070.

**Peters, K. (2010).** Polymer optical fiber sensors: A review. *Smart materials and structures* 20(1): 013002.

**Peters, K. (2011).** Polymer optical fiber sensors-a review. *Smart Materials and Structures* 20(1): 013002.

**Poisel, H. (2008).** POF strain sensor using phase measurement techniques. *The 15th International Symposium on: Smart Structures and Materials & Nondestructive Evaluation and Health Monitoring, International Society for Optics and Photonics*.

**Pomerleau, D. A. (1991).** Efficient training of artificial neural networks

---

for autonomous navigation. *Neural Computation* 3(1): 88-97.

**Pradhan, S., Town, G. E., et al. (2006).** Dual-wavelength DBR fiber laser. *Photonics Technology Letters, IEEE* 18(16): 1741-1743.

**Propst, A., Peters, K., et al. (2010).** Assessment of damage in composite laminates through dynamic, full-spectral interrogation of fiber Bragg grating sensors. *Smart materials and structures* 19: 015016.

**Qiu, Y., Wang, Q.-b., et al. (2013).** Review on composite structural health monitoring based on fiber Bragg grating sensing principle. *Journal of Shanghai Jiaotong University (Science)* 18: 129-139.

**Quintela, M., Perez-Herrera, R. A., et al. (2010).** Stabilization of dual-wavelength erbium-doped fiber ring lasers by single-mode operation. *Photonics Technology Letters, IEEE* 22(6): 368-370.

**Rao, Y., Jackson, D., et al. (1996).** Strain sensing of modern composite materials with a spatial/wavelength-division multiplexed fiber grating network. *Optics letters* 21(9): 683-685.

**Rao, Y., Lobo Ribeiro, A., et al. (1996).** Simultaneous spatial, time and wavelength division multiplexed in-fibre grating sensing network. *Optics Communications* 125(1): 53-58.

**Rao, Y.-J. (1997).** In-fibre Bragg grating sensors. *Measurement science and technology* 8(4): 355.

**Rao, Y.-J., Feng, S., et al. (2009).** Ultra-long distance (300km) fiber Bragg grating sensor system using hybrid EDF and Raman amplification. 20th International Conference on Optical Fibre Sensors, International Society for Optics and Photonics.

**Rao, Y.-J., Ran, Z.-L., et al. (2006).** Long-distance fiber Bragg grat-

ing sensor system with a high optical signal-to-noise ratio based on a tunable fiber ring laser configuration. *Optics letters* 31(18): 2684-2686.

**Read, I. and Foote, P. (2001).** Sea and flight trials of optical fibre Bragg grating strain sensing systems. *Smart materials and structures* 10(5): 1085.

**Reda Taha, M. and Lucero, J. (2005).** Damage identification for structural health monitoring using fuzzy pattern recognition. *Engineering Structures* 27(12): 1774-1783.

**Reich, Y. and Barai, S. (1999).** Evaluating machine learning models for engineering problems. *Artificial Intelligence in Engineering* 13(3): 257-272.

**Rodriguez Cobo, L., Quintela Incera, M. A., et al. (2013).** Single-longitudinal mode laser structure based on a very narrow filtering technique. *Optics Express* 21(8): 10289-10294.

**Rodriguez-Barrios, F., Martin-Lopez, S., et al. (2010).** Distributed Brillouin fiber sensor assisted by first-order Raman amplification. *Lightwave Technology, Journal of* 28(15): 2162-2172.

**Rodríguez-Cobo, L., García-Allende, P. B., et al. (2012).** Raw Material Classification by Means of Hyperspectral Imaging and Hierarchical Temporal Memories. *Sensors Journal, IEEE* 12(9): 2767-2775.

**Rogers, C. A. (1990).** Active vibration and structural acoustic control of shape memory alloy hybrid composites: experimental results. *The Journal of the Acoustical Society of America* 88: 2803.

**Rowley, H. A., Baluja, S., et al. (1998).** Neural network-based face detection. *Pattern Analysis and Machine Intelligence, IEEE Transactions on* 20(1): 23-38.

**Schetky, L. M. (1982).** Shape-Memory Alloys. *Kirk-Othmer Encyclope-*

---

dia of Chemical Technology.

**Schroeder, K., Ecke, W., et al. (2006).** A fibre Bragg grating sensor system monitors operational load in a wind turbine rotor blade. *Measurement Science and Technology* 17: 1167.

**Sekine, H., Fujimoto, S.-E., et al. (2006).** Structural health monitoring of cracked aircraft panels repaired with bonded patches using fiber Bragg grating sensors. *Applied Composite Materials* 13(2): 87-98.

**Shen, Y., Qiu, Y., et al. (2007).** Short cavity single frequency fiber laser for in-situ sensing applications over a wide temperature range. *Optics Express* 15(2): 363-370.

**Shi, B., Xu, H., et al. (2003).** A feasibility study on the application of fiber-optic distributed sensors for strain measurement in the Taiwan Strait Tunnel project. *Marine Georesources and Geotechnology* 21(3-4): 333-343.

**Shu, X., Liu, Y., et al. (2002).** Dependence of temperature and strain coefficients on fiber grating type and its application to simultaneous temperature and strain measurement. *Optics letters* 27(9): 701-703.

**Silfvast, W. T. (2004).** *Laser fundamentals*, Cambridge University Press.

**Silva-Lopez, M., Fender, A., et al. (2005).** Strain and temperature sensitivity of a single-mode polymer optical fiber. *Optics letters* 30(23): 3129-3131.

**Smith, R. C. (2005).** *Smart material systems: Model developments*, Siam.

**Snyder, A. W. and Love, J. (1983).** *Optical waveguide theory*, Springer.

**Spiegelberg, C., Geng, J., et al. (2004).** *Low-noise narrow-linewidth*

fiber laser at 1550 nm (June 2003). *Journal of Lightwave Technology* 22(1): 57.

**Spillman Jr, W., Kline, B., et al. (1989).** Statistical-mode sensor for fiber optic vibration sensing uses. *Applied Optics* 28(15): 3166-3176.

**Stolc, S. and Bajla, I. (2010).** On the Optimum Architecture of the Biologically Inspired Hierarchical Temporal Memory Model Applied to the Hand-Written Digit Recognition. *Measurement Science Review* 10(2): 28-49.

**Takeda, N. (2002).** Characterization of microscopic damage in composite laminates and real-time monitoring by embedded optical fiber sensors. *International Journal of Fatigue* 24(2): 281-289.

**Takeda, N., Okabe, Y., et al. (2005).** Development of smart composite structures with small-diameter fiber Bragg grating sensors for damage detection: Quantitative evaluation of delamination length in CFRP laminates using Lamb wave sensing. *Composites Science and Technology* 65(15): 2575-2587.

**Takeda, S., Aoki, Y., et al. (2007).** Structural health monitoring of composite wing structure during durability test. *Composite structures* 79(1): 133-139.

**Takeda, S., Aoki, Y., et al. (2012).** Damage monitoring of CFRP stiffened panels under compressive load using FBG sensors. *Composite Structures* 94(3): 813-819.

**Takeda, S., Okabe, Y., et al. (2008).** Monitoring of Delamination Growth in CFRP Laminates using Chirped FBG Sensors. *Journal of Intelligent Material Systems and Structures* 19(4): 437-444.

**Takeda, S., Yamamoto, T., et al. (2007).** Debonding monitoring of composite repair patches using embedded small-diameter FBG sensors. *Smart materials and structures* 16: 763.

---

**Takeda, S.-i., Koyanagi, J., et al. (2009).** Monitoring of internal residual strain changes in CFRP using FBG sensors. Fourth International Conference on Experimental Mechanics, International Society for Optics and Photonics.

**Talaverano, L., Abad, S., et al. (2001).** Multiwavelength fiber laser sources with Bragg-grating sensor multiplexing capability. *Journal of light-wave technology* 19(4): 553.

**Tam, H., Lee, T., et al. (2007).** Utilization of fiber optic Bragg Grating sensing systems for health monitoring in railway applications. *Struct. Health Monit.: Quantification, Validat., Implement* 1: 2.

**Tanaka, N., Okabe, Y., et al. (2003).** Temperature-compensated strain measurement using fiber Bragg grating sensors embedded in composite laminates. *Smart materials and structures* 12(6): 940.

**Tateda, M. and Horiguchi, T. (1989).** Advances in optical time domain reflectometry. *Lightwave Technology, Journal of* 7(8): 1217-1224.

**Teng, F., Yin, W., et al. (2008).** Analysis of a FBG sensing system with transverse uniform press by using genetic algorithm. *Optoelectronics Letters* 4(2): 121-125.

**Tennyson, R., Mufti, A., et al. (2001).** Structural health monitoring of innovative bridges in Canada with fiber optic sensors. *Smart materials and structures* 10(3): 560.

**Teral, S. R. (1992).** Vehicle weighing in motion with fiber optic sensors. *First European Conference on Smart Structures and Materials: Proceedings of the International Conference Held in Glasgow, 12-14 May 1992*, CRC Press.

**Tremblay, Y., Kawasaki, B., et al. (1981).** Modal noise in optical fibers: open and closed speckle pattern regimes. *Applied optics* 20(9): 1652-

1655.

**Triollet, S., Robert, L., et al. (2010).** Discriminated measures of strain and temperature in metallic specimen with embedded superimposed long and short fibre Bragg gratings. *Measurement Science and Technology* 22(1): 015202.

**Tsuda, H. (2006).** Ultrasound and damage detection in CFRP using fiber Bragg grating sensors. *Composites Science and Technology* 66(5): 676-683.

**Tsutsui, H., Kawamata, A., et al. (2004).** Detection of impact damage of stiffened composite panels using embedded small-diameter optical fibers. *Smart Materials and Structures* 13(6): 1284.

**UNE (1982).** Bond test of steels wires for prestressed concrete. 7-436-82. Madrid, Iranor.

**Urbanczyk, W., Chmielewska, E., et al. (2001).** Measurements of temperature and strain sensitivities of a two-mode Bragg grating imprinted in a bow-tie fibre. *Measurement Science and Technology* 12(7): 800.

**Vohra, S., Johnson, G., et al. (2000).** Distributed strain monitoring with arrays of fiber Bragg grating sensors on an in-construction steel box-girder bridge. *IEICE Transactions on Electronics* 83(3): 454-461.

**Wang, C.-Y., Wang, H.-L., et al. (2006).** Structural health monitoring activities of applying optical fiber sensors in Taiwan. *Optical Fiber Sensors*, Optical Society of America.

**Wang, G., Pran, K., et al. (2001).** Ship hull structure monitoring using fibre optic sensors. *Smart materials and structures* 10(3): 472.

**Whelan, M. P., Albrecht, D., et al. (2002).** Remote structural monitoring of the cathedral of Como using an optical fiber Bragg sensor system.

---

SPIE's 9th Annual International Symposium on Smart Structures and Materials, International Society for Optics and Photonics.

**Woerdeman, D. L., Spoerre, J. K., et al. (1997).** Cure monitoring of the liquid composite molding process using fiber optic sensors. *Polymer composites* 18(1): 133-150.

**Wong, Y., Scully, P., et al. (2003).** Plastic optical fibre sensors for environmental monitoring: biofouling and strain applications. *Strain* 39(3): 115-119.

**Wu, Z. X., Qiao, Q., et al. (2012).** Research on FBG Spectral Optimization with Particle Swarm Optimization Algorithm. *Applied Mechanics and Materials* 128: 690-693.

**Yari, T., Nagai, K., et al. (2008).** Monitoring aircraft structural health using optical fiber sensors. *Mitsubishi Heavy Ind. Tech. Rev* 45(4): 5-8.

**Yenilmez, B., Senan, M., et al. (2009).** Variation of part thickness and compaction pressure in vacuum infusion process. *Composites Science and Technology* 69(11): 1710-1719.

**Yi, J.-H., Lee, K.-S., et al. (2009).** Structural health monitoring system for Uldolmok tidal current power pilot plant and its applications, *ASME*.

**Yin, G., Saxena, B., et al. (2011).** Tunable Er-doped fiber ring laser with single longitudinal mode operation based on Rayleigh backscattering in single mode fiber. *Optics Express* 19(27): 25981-25989.

**Yin, S., Purwosumarto, P., et al. (1999).** Application of fiber specklegram sensor to fine angular alignment. *Optics communications* 170(1): 15-21.

**Yu, F. T., Wen, M., et al. (1993).** Submicrometer displacement sensing using inner-product multimode fiber speckle fields. *Applied Optics* 32(25):

4685-4689.

**Yu, F. T. S., Wen, M., et al. (1993).** Submicrometer displacement sensing using inner-product multimode fiber speckle fields. *Applied optics* 32(25): 4685-4689.

**Zang, Z. (2011).** Numerical analysis of optical bistability based on Fiber Bragg Grating cavity containing a high nonlinearity doped-fiber. *Optics Communications* 285(5): 521-526.

**Zang, Z. G. and Zhang, Y. J. (2012).** Low-switching power ( $\leq 45$  mW) optical bistability based on optical nonlinearity of ytterbium-doped fiber with a fiber Bragg grating pair. *Journal of Modern Optics* 59(2): 161-165.

**Zhang, K. and Kang, J. U. (2008).** C-band wavelength-swept single-longitudinal-mode erbium-doped fiber ring laser. *Optics Express* 16(18): 14173-14179.

**Zhang, W., Gao, J., et al. (2006).** Health monitoring of rehabilitated concrete bridges using distributed optical fiber sensing. *Computer-Aided Civil and Infrastructure Engineering* 21(6): 411-424.

**Zhang, X., Liang, D., et al. (2012).** Genetic algorithm-support vector regression for high reliability SHM system based on FBG sensor network. *Optics and Lasers in Engineering* 50(2): 148-153.

**Zhang, Z. and Ansari, F. (2006).** Fiber-optic laser speckle-intensity crack sensor for embedment in concrete. *Sensors and Actuators A: Physical* 126(1): 107-111.

**Zhao, X., Gao, H., et al. (2007).** Active health monitoring of an aircraft wing with embedded piezoelectric sensor/actuator network: I. Defect detection, localization and growth monitoring. *Smart Materials and Structures* 16(4): 1208.

---

**Zyskind, J., Mizrahi, V., et al. (1992).** Short single frequency erbium-doped fibre laser. *Electronics Letters* 28(15): 1385-1387.



# Chapter 13

---

## List of publications

---

### 13.1. Close related to the PhD work

#### 13.1.1. International Journals

1. **Rodriguez-Cobo, L., Marques, A. T. et al. (2013).** New design for temperature-strain discrimination using fiber Bragg gratings embedded in laminated composites. *Smart Materials and Structures*.
2. **Rodriguez-Cobo, L., Lomer, M. et al. (2013).** Optical fiber strain sensor with extended dynamic range based on specklegrams. *Sensors and Actuators A*.
3. **Rota-Rodrigo, S., Rodriguez-Cobo L. et al. (2013).** Switchable Erbium Doped Fiber Ring Laser System for Temperature Sensors Multiplexing. *Sensors Journal, IEEE 13(6): 2279 - 2283*.
4. **Rodriguez-Cobo, L., Cobo, A. et al. (2013).** Recovering a Fiber Bragg Grating axial strain distribution from its reflection spectrum. *Optics Letters 38(13): 2327-2329*.

5. **Rodriguez-Cobo, L., Quintela, M. A. et al. (2013).** Single-longitudinal mode laser structure based on a very narrow filtering technique. *Optics Express* 21(8): 10289-10294.
6. **Rodriguez-Cobo, L., Cobo, A. et al. (2013).** Bonding sensor based on simplified Fiber Bragg Grating spectral evolution. *Composites Part B: Engineering*.
7. **Rodriguez-Cobo, L., Cobo, A. et al. (2012).** Sampled Fiber Bragg Grating spectral synthesis. *Optics Express* 20(20): 22429-22441.
8. **Lopez-Higuera, J. M., Rodriguez-Cobo, L. , et al. (2011).** Currents and Trends on Fiber Sensing Technologies for Structural Health Monitoring. *NDT.net*.
9. **Lopez-Higuera, J. M., Rodriguez Cobo, L. , et al. (2011).** Fiber optic sensors in structural health monitoring. *Lightwave Technology, Journal of* 29(4): 587-608.

### 13.1.2. International conferences

1. **Rodriguez-Cobo, L., Quintela, M. A. et al. (2013).** Sensor system based on Single Longitudinal Mode lasers. *RIAO/OPTILAS 2013 (VIII Iberoamerican Conference on Optics - XI Latinamerican meeting on Optics, Lasers and Applications)*, Porto, Portugal.
2. **Rodriguez-Cobo, L., Marques, A. T. et al. (2013).** Design of carbon plates with embedded FBGs to strain measurements. *RIAO/OPTILAS 2013 (VIII Iberoamerican Conference on Optics - XI Latinamerican meeting on Optics, Lasers and Applications)*, Porto, Portugal.
3. **Rodriguez-Cobo, L., Lomer, M. et al. (2013).** Speckle pattern geometrical analysis for sensing applications. *RIAO/OPTILAS 2013 (VIII Iberoamerican Conference on Optics - XI Latinamerican meeting on Optics, Lasers and Applications)*, Porto, Portugal.
4. **Lomer, M., Rodriguez-Cobo, L. et al. (2013).** Characterization of multimode optical fibers parameters using speckle patterns. *RIAO/OPTILAS*

- 2013 (VIII Iberoamerican Conference on Optics - XI Latinamerican meeting on Optics, Lasers and Applications. Porto, Portugal.
5. **Rodriguez-Cobo, L., Lomer, M. et al. (2013).** Radial processing scheme of speckle patterns for sensing applications. Optical Sensors (SENSORS), Rio Grande, Puerto Rico.
  6. **Lopez-Higuera, J. M., Rodriguez-Cobo, L. et al. (2013).** Temperature Level Fiber Sensor Network. Optical Sensors (SENSORS), Rio Grande, Puerto Rico.
  7. **Rodriguez-Cobo, L., Marques, A. T. et al. (2013).** Simplified sensor design for temperature-strain discrimination using Fiber Bragg Gratings embedded in laminated composites. 5th European Workshop on Optical Fibre Sensors, Krakow, Poland.
  8. **Rota-Rodrigo, S., Rodriguez-Cobo, L. et al. (2013).** Switchable fiber optic laser system for high and low-strain fiber optic sensors remote multiplexing. 5th European Workshop on Optical Fibre Sensors, Krakow, Poland.
  9. **Rodriguez-Cobo, L., Quintela, A. et al. (2012).** Smart material using Fiber Bragg Grating transducers and Shape Memory Alloy actuators. OFS'22 (22nd International Conference on Optical Fiber Sensors), Beijin, China.
  10. **Rodriguez-Cobo, L., Quintela, M. A. et al. (2012).** Pipe flow speed sensor based on Fiber Bragg Gratings. OFS'22 (22nd International Conference on Optical Fiber Sensors), Beijin, China.
  11. **Rodriguez-Cobo, L., Lomer, M. et al. (2012).** POF vibration sensor based on speckle pattern changes. OFS'22 (22nd International Conference on Optical Fiber Sensors), Beijin, China.
  12. **Rodriguez-Cobo, L., Polanco, J. A. et al. (2012).** Quasidistributed fiber sensor for precast concrete structures monitoring. OFS'22 (22nd International Conference on Optical Fiber Sensors), Beijin, China.

13. **Lopez-Higuera, J. M., Rodriguez-Cobo, L. et al. (2012).** Temperature level optical fiber sensor using shape memory alloy wires. OFS'22 (22nd International Conference on Optical Fiber Sensors), Beijing, China.
14. **Rodriguez-Cobo, L., Lomer, M. et al. (2012).** Speckle characterization in multimode fibers for sensing applications. V International conference on Speckle Metrology, Vigo, Spain.
15. **Rodriguez-Cobo, L., Carrascal, I. A. et al. (2012).** Optical Fiber Sensor for Prestressed Concrete Structures Bond behaviors measurements. 6 European Workshop on Structural Health Monitoring, Dresden, Germany.
16. **Lomer, M., Rodriguez-Cobo, L. et al. (2012).** Plastic optical fiber sensor for measuring arterial pulse. POF 2012 (21st International Conference on Plastic Optical Fibers). Atlanta, EEUU.
17. **Lomer, M., Arozamena, J. et al. (2012).** Speckle patterns obtained in plastic optical fibers for sensing applications. POF 2012 (21st International Conference on Plastic Optical Fibers). Atlanta, EEUU.
18. **Lopez-Higuera, J. M., Rodriguez-Cobo, L. et al. (2010).** Fiber optics in structural health monitoring. Photonics Asia 2010, Beijing, China.
19. **Lopez-Higuera, J. M., Rodriguez-Cobo, L. et al. (2010).** Currents and Trends on Fiber Sensing Technologies for Structural Health Monitoring. The 2nd Mediterranean Photonics Conference.
20. **Lopez-Higuera, J. M., Madruga, F. et al. (2010).** Four Fiber Sensing Technologies for Structural Building Monitoring. 37 IAHS World Congress on Housing, Santander.

### **13.1.3. Industrial Publications**

1. **Rodriguez-Cobo, L., Lopez-Higuera, J. M. et al. (2011).** Sistema de Transducción basado en redes de difracción de fibra óptica. Patente nacional solicitada por Aeroblade (201100866).

## 13.2. Other contributions

### 13.2.1. International Journals

1. **Rodriguez-Cobo, L., Ruiz-Lombera, R. et al. (2013)**. Feasibility study of Hierarchical Temporal Memories applied to welding diagnostics. *Sensors and Actuators A*.
2. **Anabitarte, F., Rodriguez-Cobo, L. et al. (2012)**. Normalization of laser-induced breakdown spectroscopy spectra using a plastic optical fiber light collector and acoustic sensor device. *Applied optics* 51(34): 8306-8314.
3. **Rodriguez-Cobo, L., Garcia-Allende, P. B. et al. (2012)**. Raw Material Classification by Means of Hyperspectral Imaging and Hierarchical Temporal Memories. *Sensors Journal, IEEE* 12(9): 2767-2775.
4. **Ullan, A., Quintela, M. A. et al. (2012)**. Quasi distributed hybrid Brillouin fiber laser sensor system. *Measurement Science and Technology* 23(8): 85202-85207.
5. **Ullan, A., Quintela, M. A. et al. (2012)**. Sensor System Based on a Brillouin Fiber Laser for Remote in Series Fiber Bragg Gratings Interrogation. *Sensors Journal, IEEE* 12(12): 3480 - 3482
6. **Mirapeix, J., Ruiz-Lombera, R. et al. (2011)**. Defect detection with CCD-spectrometer and photodiode-based arc-welding monitoring systems. *Journal of Materials Processing Technology* 211(12): 2132-2139.

### 13.2.2. National Journals

1. **Mirapeix, J., Rodriguez-Cobo, L. et al. (2013)**. Clasificación de defectos de soldadura en tiempo real. *Soldadura y Tecnologías de Union:* 12-18.

### 13.2.3. International conferences

1. **Anabitarte, F., Rodriguez-Cobo, L. et al. (2013).** Laser Induced Breakdown Spectroscopy Induced Shockwave Detection by means of a Fiber Bragg Grating Transducer. EMSLIBS (7th Euro - Mediterranean Symposium on Laser Induced Breakdown Spectroscopy, Bari, Italy.
2. **Rodriguez-Cobo, L., Mirapeix, J. et al. (2013).** Fiber Bragg Grating sensors for on-line welding diagnostic. 5th European Workshop on Optical Fibre Sensors, Krakow, Poland.
3. **Castrellon-Uribe, J., Lomer, M. et al. (2013).** LPG in perfluorinated GI-POF for concentration measurement in liquids. Optical Sensors (SENSORS), Rio Grande, Puerto Rico.
4. **Mirapeix, J., Rodriguez-Cobo, L. et al. (2012).** Clasificacion de defectos de soldadura en tiempo real mediante tecnicas opticas y memorias jerarquicas temporales. 2 Congreso Internacional de Soldadura y Tecnologias de Union y 19as jornadas tecnicas de soldadura, Madrid.
5. **Anabitarte, F., Rodriguez-Cobo, L. et al. (2012).** Focal beam position detection in a laser Induced Breakdown Spectroscopy system by using a Fiber Bragg Grating sensor. OFS'22 (22nd International Conference on Optical Fiber Sensors), Beijin, China.
6. **Galindez, C., Rodriguez-Cobo, L. et al. (2012).** Integral temperature hybrid laser sensor. OFS'22 (22nd International Conference on Optical Fiber Sensors), Beijin, China.
7. **Galindez, C., Lomer, M. et al. (2012).** Influence of the refractive index of liquids in the speckle pattern of multimode fibers. V International conference on Speckle Metrology, Vigo, Spain.
8. **Lomer, M., Rodriguez-Cobo, L. et al. (2011).** Multiple Bending fiber sensor for measurement of liquid level. POF 2011 (The 20th International Conference on Plastic Optical Fibers), Bilbao, Spain.

9. **Lomer, M., Rodriguez-Cobo, L. et al. (2011).** Angular displacement sensor based on plastic optical fibers curved. POF 2011 (The 20th International Conference on Plastic Optical Fibers), Bilbao, Spain.
10. **Anabitarte, F., Rodriguez-Cobo, L. et al. (2011).** Laser Induced breakdown spectroscopy light collector based on coiled plastic optical fiber. POF 2011 (The 20th International Conference on Plastic Optical Fibers), Bilbao, Spain.
11. **Quintela, A., Rodriguez-Cobo, L. et al. (2011).** Optimal design and implementation of a temperature and strain optical transducer using FBGs and fiber taper hybrid structure. OFS'21 (21st International Conference on Optical Fiber Sensors), Ottawa, Canada.
12. **Cobo, A., Mirapeix, J. et al. (2011).** Optical Fiber Sensors for Welding Quality Monitoring. The seventeenth Microoptics Conference, Sendai, Japan.
13. **Conde, O. M., De-la-Cruz, J. et al. (2011).** Optimized Image Calibration for Spectroscopic Systems. IEEE Sensors 2011, Limerick, Ireland.
14. **Anabitarte, F., Mirapeix, J. et al. (2010).** Automatic classification of steel plates based on Laser Induced Breakdown Spectroscopy and Support Vector Machines. 4th European Workshop of Optical Fiber Sensors (EWOFS'10), Porto, Portugal.

#### 13.2.4. National conferences

1. **Quintela, A., Arribas, F. et al. (2013).** Transductor de temperatura y presión basado en redes de difracción en fibra óptica: diseño, implementación y caracterización. Optoel 2013, Alcalá de Henares, Madrid.
2. **Rodriguez-Cobo, L., Anabitarte, F. et al. (2011).** Acoustic Detection of laser-induced plasma emission by means of a fiber-Bragg grating sensor. Optoel 2011 (VII Reunión Española de Optoelectrónica), Santander.

3. **Lomer, M., Rodriguez-Cobo, L. et al. (2011).** Sensor de desplazamiento angular basado en perdidas de curvaturas de fibras opticas. Optoel 2011 (VII Reunion Española de Optoelectronica), Santander.
4. **Mirapeix, J., Garcia-Allende, P. B. et al. (2011).** Evaluacion de la calidad de soldadura mediante algoritmos de seleccion de características y de optimizacion. Optoel 2011 (VII Reunion Española de Optoelectronica), Santander.
5. **Mirapeix, J., Ruiz-Lombera, R. et al. (2011).** Estudio comparativo entre sistemas de monitorizacion on-line basados en espectrometros y fotodiodos para la deteccion en linea de defectos de soldadura. Optoel 2011 (VII Reunion Española de Optoelectronica), Santander.
6. **Ullan, A., Quintela, M. A. et al. (2011).** Laser en fibra de efecto Brillouin para interrogacion remota de multiples redes de difraccion de Bragg colocadas en serie. Optoel 2011 (VII Reunion Española de Optoelectronica), Santander.

## **13.3. Submitted contributions**

### **13.3.1. Journal articles close related to the PhD work**

1. **Rodriguez-Cobo, L., Cobo, A. et al. (2013).** Embedded compaction pressure sensor based on Fiber Bragg Gratings. Submitted to Composites Part B: Engineering.
2. **Rodriguez-Cobo, L., Quintela, M. A. et al. (2013).** Effective optical filtering in a feedback network. Submitted to Photonics Technology Letters.
3. **Rodriguez-Cobo, L., Quintela, M. A. et al. (2013).** Study of Fiber Bragg Grating spectral overlapping for laser structures. Submitted to Journal of Lightwave Technology.
4. **Rodriguez-Cobo, L., Mirapeix, J. et al. (2013).** Comparison of Hierarchical Temporal Memories and Artificial Neural Networks under noisy data. Submitted to Journal of Advanced Engineering Informatics.

5. **Rodriguez Cobo, L., Cobo, A. et al. (2013).** Optical strain gauge with high spatial resolution. Submitted to The Journal of Strain Analysis for Engineering Design.
6. **Rota-Rodrigo, S., Rodriguez-Cobo, L. et al. (2013).** Dual-Wavelength Single-Longitudinal Mode Fiber Laser using Phase-Shift Bragg Gratings. Submitted to IEEE Journal on Selected Topics in Quantum Electronics.

### **13.3.2. Other journal articles**

1. **Rodriguez Cobo, L., Mirapeix, J. et al. (2013).** Fiber Bragg Grating sensors for on-line welding diagnostics. Submitted to Journal of Materials Processing Technology.